

DISS. ETH NO.28156

# Towards solving the puzzle of ice crystal formation and growth in Arctic mixed-phase clouds

A thesis submitted to attain the degree of

DOCTOR OF SCIENCES of ETH ZURICH

(Dr. sc. ETH Zurich)

presented by

JULIE THÉRÈSE PASQUIER

MSc in Environmental Sciences, ETH Zurich

born on 05 March 1993

citizen of Switzerland

accepted on the recommendation of  
Prof. Dr. Ulrike Lohmann, examiner  
Prof. Dr. Alexis Berne, co-examiner  
Dr. Jan Henneberger, co-examiner

2022



# Abstract

Clouds influence the Earth's radiative budget in two competing ways. On the one side they reflect shortwave radiation back to space and thereby cool the atmosphere. On the other side they absorb and re-emit longwave radiation and thereby warm the atmosphere. The net cloud radiative effect depends largely on the cloud's temperature and microphysical properties and is still insufficiently understood. Indeed, cloud radiative effects are a major uncertainty in climate projections (IPCC, 2021). Clouds especially play a key role in the local radiative budget in the Arctic, a region vulnerable to climate warming (Goosse et al., 2018). The cloud droplet and ice crystal size distributions regulate the cloud radiative effects. Clouds consisting of many small cloud droplets have a larger optical thickness compared to clouds with fewer and larger ice crystals for the same cloud water path. This larger optical thickness leads to a larger albedo, hence a larger reflection of solar radiation on one side and on the other side to a larger emissivity leading to larger longwave radiation emittance. The changes caused by cloud microphysical processes on the phase partitioning and particle size distributions are not sufficiently understood in mixed-phase clouds containing cloud droplets and ice crystals.

The aim of this thesis is to improve the understanding of the microphysical processes shaping the phase partitioning in Arctic mixed-phase clouds with an extensive set of instruments operated during the Ny-Ålesund Aerosol Cloud Experiment (NASCENT) campaign. In-situ measurements retrieved from an holographic imager mounted on a tethered balloon system are employed, together with ground-based remote sensing observations, standard atmospheric parameters retrieval, and the determination of the concentration of aerosol particles acting as cloud condensation nuclei or as ice nucleating particles. The combination of many different measurement methods was highly beneficial to study the properties of aerosol and cloud and their interactions. In addition, the balloon-borne cloud microphysical observations were for the first time successfully supplemented with in-situ radiation observations, enabling the direct comparison between cloud microphysical and radiative properties.

A large variety of microphysical properties was identified during six days of measurements in low-level Arctic mixed-phase clouds. Many ice crystals with distinct shapes and sizes were observed. The habit of ice crystals allow to determine their histories as well as the atmospheric conditions prevailing in the clouds. For example, ice crystals recirculating in the cloud and thereby experiencing subsequently growth in plate and column environments, as well as aged-rimed particles were identified. Furthermore, a shallow stratocumulus with low updrafts and turbulence was characterized by comparable ice nucleating particles and ice crystal concentrations. Consequently, these ice crystals formed by nucleation on ice nucleating particles and no other process substantially contributed to their formation. The concentration of aerosols acting as ice nucleating particles in the pristine Arctic environment limited the ice crystal formation in this cloud. In warmer but more convective clouds, a large discrepancy between the concentration of small pristine ice crystals and concentration of ice nucleating particle was identified. Secondary ice production mechanisms causing the multiplication of ice crystals are proposed to be responsible for these discrepancies. We assume that small pristine ice crystals ( $< 100 \mu\text{m}$ ) were formed close to the measurement location, otherwise they would have grown to larger sizes or interacted with other cloud particles, thereby losing their pristine shapes. Due to their recent formation, these small ice crystals can be used as evidence for local secondary ice production. Local secondary

ice production prevailed during 40% of the six days of measurements in MPCs, and high secondary ice production events (small ice crystal number concentrations larger as  $10 \text{ L}^{-1}$ ) during 3.6%. Secondary ice production took place at all temperatures observed ( $-2 \text{ }^\circ\text{C}$  to  $-24 \text{ }^\circ\text{C}$ ). The concentration of small pristine ice crystals peaked between  $-3 \text{ }^\circ\text{C}$  and  $-5 \text{ }^\circ\text{C}$  and the frequency of occurrence of secondary ice production was highest between  $-18 \text{ }^\circ\text{C}$  and  $-24 \text{ }^\circ\text{C}$ , reaching between 76% and 96%.

The most investigated secondary ice processes are the rime-splintering or Hallett-Mossop process referring to the production of ice splinters during riming, the droplet shattering process occurring during freezing of supercooled droplets, and the collisional breakup process describing fragmentation during collision of two (or more) ice crystals. The direct observation of secondary ice production processes in natural clouds is practically impossible. Instead, we use the small pristine ice crystals as tracers for identifying regions with prevailing secondary ice production and examine the cloud properties at these locations. This allows to determine the possible mechanisms involved in ice multiplication. For example, the concentration of frozen drops increased simultaneously as the small pristine ice crystals concentration during one high secondary ice production event, indicative for the occurrence of droplet shattering. During another high secondary ice production event, the rime-splintering, the droplet shattering, and the collisional breakup processes likely all contributed partly to the formation of splinters growing to small pristine ice crystals.

During the six days of measurements, the ratio of occurrence of drizzle drops was enhanced by a factor of 2 during secondary ice production and by a factor of 4 during high secondary ice production. Moreover, frozen drops were measured during 87% of the high secondary ice production observations, indicating a likely considerable contribution from the droplet shattering mechanism. We advance that the formation of large drizzle drops initiating the secondary ice production is determined by the low concentration of aerosols acting as cloud condensation nuclei in the pristine Arctic environment.

In this thesis, we demonstrated the role of ice crystal formation on ice nucleating particles and cloud droplet activation on cloud condensation nuclei for initiating secondary ice production mechanisms, which are responsible for the increase the ice crystal number concentration by several order of magnitude. The interplay between these aerosols and secondary ice production, together with environmental conditions (temperature, updrafts), shape the microphysical and radiative properties of Arctic mixed-phase clouds, and should be represented accurately in atmospheric models to reduce the uncertainty related to cloud radiative effects in the Arctic.

# Résumé

Les nuages influencent le bilan radiatif de la Terre de deux manières. D'une part, ils réfléchissent le rayonnement à ondes courtes vers l'espace et refroidissent ainsi l'atmosphère. D'autre part, ils absorbent et émettent à leur tour le rayonnement à grande longueur d'onde et réchauffent ainsi l'atmosphère. L'influence des nuages sur le rayonnement dépend largement de leur température et de leurs propriétés microphysiques. Leur influence exacte n'est pas encore suffisamment comprise, et l'impact des nuages sur le bilan radiatif de la Terre constitue une grande source d'incertitude dans les projections climatiques (IPCC, 2021). Les nuages jouent notamment un rôle clé dans le bilan radiatif local de l'Arctique, une région particulièrement vulnérable au réchauffement climatique (Goosse et al., 2018). Les processus microphysiques se déroulant à l'intérieur des nuages arctiques restent difficiles à étudier, de par la rareté des mesures in-situ et la complexité du système. Les nuages à phases mixtes arctiques contiennent à la fois des gouttelettes d'eau et des cristaux de glace, et la distribution de ces deux types d'hydrométéores régule leurs propriétés optiques. En effet, les nuages composés de nombreuses petites gouttelettes d'eau ont une épaisseur optique plus importante ce qui cause une plus grande réflexion du rayonnement solaire, par rapport aux nuages composés en plus grande partie de cristaux de glace en générale moins nombreux et plus grands. Les nuages avec une plus grande épaisseur optique ont aussi une plus grande émissivité, c'est-à-dire une plus grande émission de rayonnement infrarouge. Les processus microphysiques qui se déroulent dans les nuages influencent la répartition des phases et la taille de particules d'eau et de glace, et méritent donc d'être étudiés plus en détail afin de réduire l'incertitude de l'impact radiatif des nuages dans la région arctique.

L'objectif de cette thèse est d'améliorer la compréhension des processus microphysiques qui déterminent la répartition des phases thermodynamiques dans les nuages à phases mixtes de l'Arctique à l'aide d'un large ensemble d'instruments employés pendant la campagne de mesure NASCENT (Ny-Ålesund Aerosol Cloud Experiment). En particulier, des mesures in-situ obtenues à partir d'un imageur holographique monté sur un ballon captif sont utilisées, ainsi que des observations de télédétection au sol, des mesures atmosphériques standards, et la détermination de la concentration de noyaux glaçogènes et de noyaux de condensation. La combinaison de nombreuses méthodes de mesure s'est montrée très utile à l'analyse des propriétés des aérosols, des nuages et de leurs interactions. De plus, les observations microphysiques de nuages effectués à l'aide du ballon captif ont été pour la première fois accompagnées par des mesures de rayonnement, ce qui a permis de comparer directement les propriétés microphysiques et optiques des nuages.

Une grande variété de propriétés microphysiques ont été identifiées à l'aide de six jours de mesures dans des nuages de basse altitude à phase mixte. Plusieurs formes de cristaux de glace particulières ont été observées. La forme des cristaux permet de déterminer leurs histoires ainsi que les conditions atmosphériques prévalant dans les nuages. Par exemples, des cristaux de glace qui ont grandi consécutivement dans des environnements avec différentes températures ambiantes ont été observés. Ces cristaux ont donc circulé dans les nuages et grandi consécutivement à des températures favorable au développement de colonnes puis de plaques hexagonales.

Par ailleurs, des concentrations comparables de noyaux glaçogènes et de cristaux de glace ont été mesurées dans un stratocumulus avec un faible courant ascendant et peu de turbulence. Par conséquent, ces cristaux de glace se sont formés par nucléation à partir de noyau glaçogène à environ  $-16$  °C et aucun autre processus n'a considérablement contribué à leur formation. La

faible concentration d'aérosols agissant comme des noyaux glaçogènes dans l'atmosphère propre de l'Arctique a donc limité la formation de cristaux de glace dans ce nuage. Au contraire, dans d'autres nuages plus chauds et plus convectifs, nous avons identifié un écart important entre la concentration de petits cristaux de glace et la concentration de noyaux glaçogènes. Il est postulé que des mécanismes de production de glace secondaire causant la multiplication de petits cristaux de glace sont responsables de ces écarts. Nous partons du principe que les petits cristaux de glace ( $< 100 \mu\text{m}$ ) se sont formés à proximité de l'instrument de mesure. Autrement, les cristaux auraient atteint de plus grandes tailles ou interagi avec d'autres gouttelettes ou cristaux de glace dans le nuage, et ainsi perdu leurs formes originales. En raison de leur formation récente, ces petits cristaux de glace peuvent être utilisés pour démontrer la production locale de glace secondaire. Durant les six jours de mesures, la production locale de glace secondaire a été observée dans 40% des observations dans les nuages à phase mixtes. Dans 3,6% des cas, des valeurs de production de glace secondaire particulièrement élevées (avec des concentrations de petits cristaux de glace supérieures à  $10 \text{ L}^{-1}$ ) ont été mesurées. La production de glace secondaire a eu lieu à toutes les températures observées ( $-2 \text{ }^\circ\text{C}$  à  $-24 \text{ }^\circ\text{C}$ ). Le maximum de la concentration de petits cristaux de glace a été observé entre  $-3 \text{ }^\circ\text{C}$  et  $-5 \text{ }^\circ\text{C}$ , tandis que la fréquence de la production de glace secondaire était la plus élevée entre  $-18 \text{ }^\circ\text{C}$  et  $-24 \text{ }^\circ\text{C}$ , atteignant des valeurs comprises entre 76% et 96%.

Plusieurs mécanismes de production de glace secondaire ont été identifiés dans la littérature. Le processus de Hallett-Mossop fait référence à la production d'éclats de glace lorsqu'un gros cristal de glace collecte des petites gouttelettes d'eau liquide surfondue qui gèlent au contact du cristal. Le mécanisme de congélation de grosse gouttes d'eau surfondues crée des cristaux de glace secondaire quand de grosses gouttes d'eau surfondues éclatent ou se fragmentent en gelant. Enfin, le processus de rupture par collision décrit la fragmentation d'un cristal suite à sa collision avec d'autres cristaux. L'observation des processus de production de glace secondaire directement dans les nuages naturels est pratiquement impossible. A la place, nous utilisons les petits cristaux de glace pour retracer les conditions environnementales à l'endroit de la production de glace secondaire. Cela permet de déterminer les mécanismes pouvant être impliqués dans la multiplication de la glace. Par exemple, nous avons observé un événement de production secondaire de glace particulièrement élevé au cours duquel la concentration de gouttes gelées a augmenté simultanément que les petits cristaux de glace. Cela indique la large contribution du processus de congélation de grosse gouttes surfondues. En revanche, les trois mécanismes de production de glace secondaire (le processus de Hallett-Mossop, le processus de rupture de cristaux de glaces et le processus de congélation de grosse gouttes surfondue) ont probablement tous contribué à la formation d'éclats de glace lors d'un autre événement de production de glace secondaire élevé. Sur l'ensemble des six jours de mesures, le rapport de fréquence des gouttes d'eau surfondue a doublé pendant la production de glace secondaire et a même quadruplé pendant les événements de production de glace secondaire élevée. De plus, des gouttes gelées ont été observées durant 87% des mesures de production de glace secondaire élevée, indiquant probablement la contribution considérable du mécanisme de congélation de grosses gouttes surfondues. Nous avançons l'hypothèse que la formation de grosses gouttes surfondues initiant la production de glace secondaire est déterminée par la faible concentration d'aérosols agissant comme des noyaux de condensation dans l'environnement Arctique peu pollué.

Dans cette thèse, nous avons démontré le rôle de la formation de cristaux de glace grâce aux noyaux glaçogène et l'importance de l'activation d'une faible quantité de gouttelettes par des noyaux de condensation pour initier les mécanismes de production de glace secondaire qui augmentent la concentration de cristaux de glaces dans les nuages à phase mixte de l'Arctique. Les interactions entre ces aérosols et la production de glace secondaire façonne les propriétés microphysiques et optiques des nuages à phase mixte de l'Arctique, et devraient être représentées avec plus de précision dans les modèles atmosphériques afin de réduire les incertitudes liées aux effets des nuages sur le rayonnement en Arctique.

# Contents

<b>Abstract</b>	<b>ii</b>
<b>Résumé</b>	<b>v</b>
<b>1 Introduction</b>	<b>1</b>
1.1 The Arctic amplification of climate warming . . . . .	1
1.2 Cloud microphysics . . . . .	2
1.2.1 Cloud types . . . . .	2
1.2.2 Cloud droplet formation and growth . . . . .	3
1.2.3 Ice crystal formation on INPs . . . . .	4
1.2.4 Secondary ice crystal formation . . . . .	4
1.2.5 Ice crystal growth . . . . .	5
1.2.6 Seeder-feeder process . . . . .	6
1.2.7 Wegener-Bergeron Findeisen process . . . . .	7
1.2.8 Aerosol-cloud interaction . . . . .	7
1.2.9 Persistence of Arctic MPCs . . . . .	7
1.2.10 Cloud radiative effects . . . . .	8
1.3 Atmospheric observations . . . . .	8
1.3.1 In-situ cloud observations . . . . .	8
1.3.2 Remote sensing cloud observations . . . . .	11
1.3.3 Other ground based measurements . . . . .	12
1.3.4 Meteorological and radiation observations . . . . .	12
1.4 Objectives of this thesis . . . . .	13
<b>2 The Ny-Ålesund Aerosol Cloud Experiment (NASCENT): Overview and First Results</b>	<b>15</b>
2.1 Motivation . . . . .	16
2.2 NASCENT study design . . . . .	18
2.2.1 Measurement site . . . . .	18
2.2.2 Experimental set-up . . . . .	18
2.3 Seasonality of meteorological, aerosol, and cloud parameters during NASCENT .	19
2.3.1 Temperature . . . . .	19
2.3.2 Wind . . . . .	20
2.3.3 Aerosols . . . . .	21
2.3.4 Clouds . . . . .	23
2.4 First research highlights from the NASCENT study . . . . .	23
2.4.1 Chemical and physical properties of aerosols, cloud residuals, and ice nucleating particles . . . . .	23
2.4.2 Cloud microphysical properties . . . . .	28
2.4.3 Model comparison . . . . .	32
2.5 Summary and Future Work . . . . .	33

<b>3</b>	<b>Conditions favorable for secondary ice production in Arctic mixed-phase clouds</b>	<b>37</b>
3.1	Methods . . . . .	40
3.1.1	Measurement location . . . . .	40
3.1.2	Instrument setup . . . . .	40
3.1.3	SIP identification . . . . .	41
3.1.4	Determination of INP concentrations . . . . .	43
3.2	SIP occurrence during six days of MPC measurements in Arctic MPCs . . . . .	43
3.2.1	Overview of the six days with MPCs . . . . .	43
3.2.2	High SIP event on 11 November 2019 . . . . .	46
3.2.3	Seeder-feeder event on 1 April 2020 . . . . .	50
3.3	Environmental conditions favorable for SIP . . . . .	52
3.3.1	Role of the hydrometeor types for SIP . . . . .	53
3.3.2	Temperature . . . . .	55
<b>4</b>	<b>Understanding the history of complex ice crystal habits deduced from a holographic imager</b>	<b>61</b>
4.1	Introduction . . . . .	62
4.2	Methods . . . . .	63
4.3	Results . . . . .	63
4.3.1	Observation of recirculation particles . . . . .	63
4.3.2	Observation of aged-rimed particles . . . . .	66
4.4	Summary . . . . .	67
<b>5</b>	<b>Collocated in-situ measurements of radiation and cloud microphysical properties in Arctic mixed-phase clouds with the tethered balloon system HoloBalloon</b>	<b>69</b>
5.1	Introduction . . . . .	70
5.2	Methods . . . . .	71
5.2.1	Main instrumentation . . . . .	71
5.2.2	Radiation measurements . . . . .	71
5.3	Results & Discussion . . . . .	73
5.3.1	Longwave radiative cooling at cloud top . . . . .	74
5.3.2	Influence of ice crystal concentration on shortwave radiation . . . . .	75
5.4	Conclusion . . . . .	79
<b>6</b>	<b>Conclusion and outlook</b>	<b>81</b>
6.1	Summary and conclusion of the results . . . . .	81
6.1.1	Ice crystal formation from secondary ice processes . . . . .	81
6.1.2	Ice crystal habits as indicator for environmental properties . . . . .	82
6.1.3	Arctic cloud and radiation . . . . .	83
6.2	Outlook . . . . .	83
6.2.1	Further analysis of dataset from the NASCENT campaign . . . . .	83
6.2.2	Technical improvements of HoloBalloon . . . . .	84
6.2.3	Automatic classification of ice crystal habits . . . . .	86
6.2.4	Need for a more accurate SIP process characterization . . . . .	87
	<b>Appendices</b>	<b>89</b>
<b>A</b>	<b>Supplementary Material: The Ny-Ålesund Aerosol Cloud Experiment (NASCENT): Overview and First Results</b>	<b>89</b>
A.1	Meteorological situation on 12 November 2019 . . . . .	90
A.2	Swiss Site . . . . .	92



A.2.1	Aerosol measurements at the container . . . . .	92
A.2.2	HoloBalloon . . . . .	92
A.3	Zeppelin Observatory . . . . .	93
A.3.1	GCVI sampling and aerosol instrumentation . . . . .	93
A.3.2	CRAFT . . . . .	95
A.3.3	Hawkeye & MPS . . . . .	96
A.3.4	HOLIMO3G . . . . .	97
A.4	AWIPEV . . . . .	97
A.4.1	CPS Sonde . . . . .	97
A.4.2	Forward simulation with PAMTRA . . . . .	97
A.5	Gruvebadet . . . . .	99
A.6	Climate Change Tower . . . . .	99
A.7	WRF Modeling . . . . .	99
<b>List of symbols and abbreviations</b>		<b>105</b>
<b>List of Figures</b>		<b>107</b>
<b>List of Tables</b>		<b>115</b>
<b>References</b>		<b>117</b>
<b>Acknowledgments</b>		<b>137</b>
<b>Curriculum Vitae</b>		<b>139</b>



# Chapter 1

## Introduction

### 1.1 The Arctic amplification of climate warming

Average temperatures over the Arctic region have increased more than twice as much as in the global average in the past decades (e.g., Meredith et al., 2019). This stronger warming is known as Arctic Amplification (AA) and is responsible for the increasing rate of sea ice retreat (Kay and Gettelman, 2009; Serreze et al., 2009; Bennartz et al., 2013; Cohen et al., 2014). Several feedback mechanisms associated with temperature, water vapour, and clouds contribute to the AA (Goosse et al., 2018). Their relative importance in different regions in the Arctic is however still under debate (e.g., Hall et al., 2021).

The sea-ice albedo feedback characterizes the increased absorption of solar radiation at the surface when snow and ice retreat and more ocean surface is exposed, that has a much lower albedo than the highly reflective ice and snow surfaces. This positive feedback process is often proposed as the main contributor to the AA (e.g., Deser et al., 2000; Screen and Simmonds, 2010), but AA was also observed in simulation without changes in snow cover (Graversen and Wang, 2009; Bekryaev et al., 2010).

The positive lapse-rate feedback is also a large contributor to the AA (Pithan and Mauritsen, 2014) and is connected to the vertical structure of the atmosphere. Because the lower troposphere is stably stratified in the Arctic, mixing of cold dense air close to the surface with the lighter air aloft is inhibited. This confines the surface warming to the lower layers of the troposphere (Bintanja et al., 2012). This larger warming of the lower than of the upper troposphere reduces the increase in outgoing terrestrial radiation compared to uniform warming of the entire troposphere profile, and thus leads to further warming (Goosse et al., 2018). Note that this feedback is, on the contrary, negative in the tropics where unstable conditions favor convection and mixing and distribute the warming throughout the entire troposphere.

The physics behind the positive water vapor feedback are that a warmer atmosphere can contain a larger amount of water vapor as described by the Clausius-Clapeyron equation, which amplifies the greenhouse effect of water vapor and further increases the warming (Gordon et al., 2013). The advection of warm moist air from lower latitude was found to have a large impact on the AA (e.g., Moore, 2016; Dahlke and Maturilli, 2017).

Finally, the cloud radiative feedbacks contribute to the AA in two competing ways (e.g. Curry et al., 1996; Goosse et al., 2018). On the one hand, clouds absorb longwave radiation and emit it back to the surface and therefore have a longwave warming effect. On the other hand, clouds scatter solar radiation back to space, leading to a shortwave cooling effect at the surface (e.g. Ebell et al., 2020). The shortwave cooling effect is only prevailing during the polar days and depends strongly on the surface below. Additionally, the cloud particle concentration and its thermodynamical phase influence the cloud radiative effect as discussed in Section 1.2.10. The feedbacks related to clouds are the most uncertain of all the radiative feedbacks (Goosse et al., 2018) and therefore require further research. In particular, a comprehensive understanding of the

processes shaping the cloud particle concentrations and phase partitioning is essential to reduce the uncertainties about the impact of Arctic clouds on the AA. The present thesis takes a step towards enhancing our understanding about the microphysical and radiative properties of Arctic clouds.

## 1.2 Cloud microphysics

### 1.2.1 Cloud types

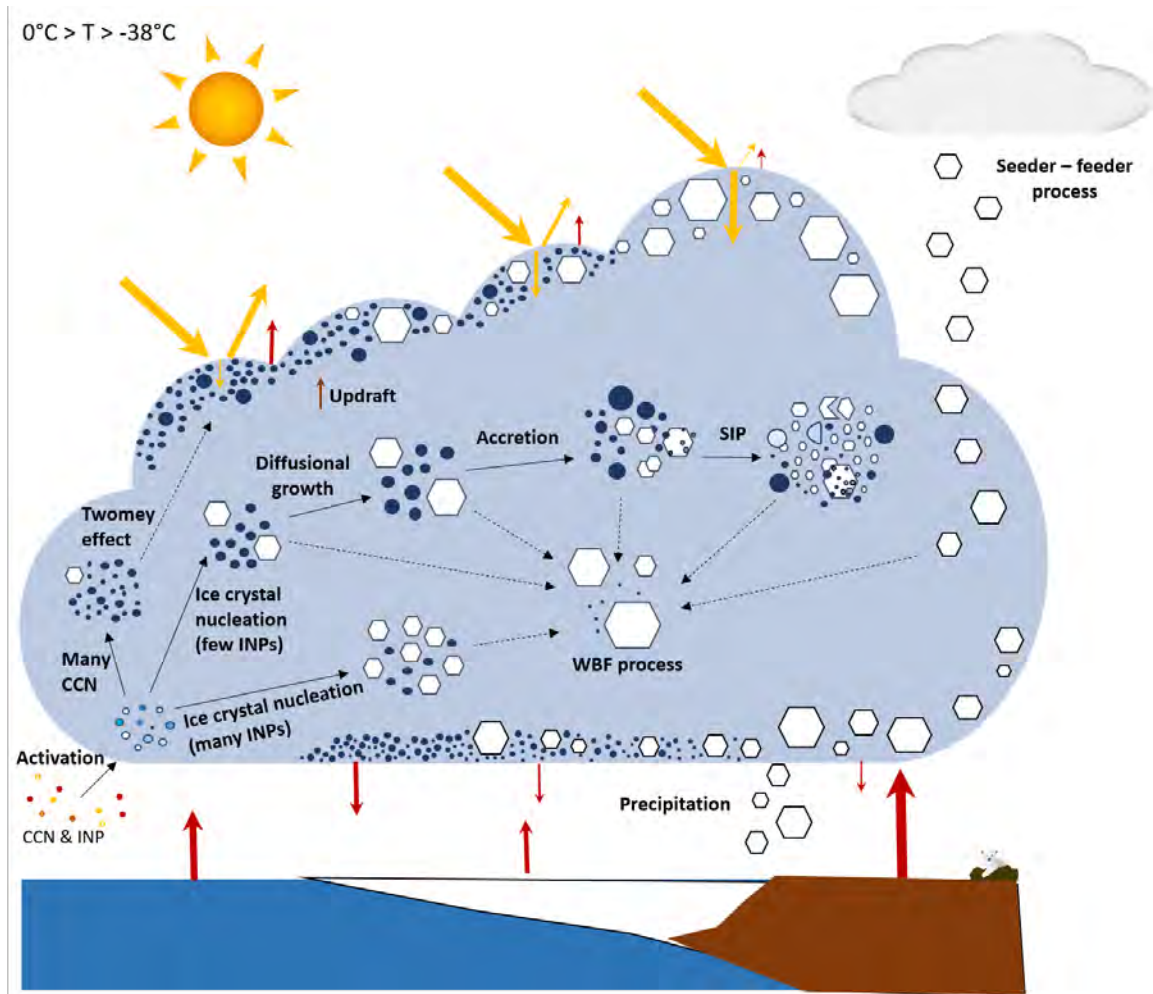


Figure 1.1: Schematic of the microphysical processes occurring in Arctic MPCs. Yellow and red arrows indicate the magnitude of shortwave and longwave radiation fluxes, respectively. Black arrows represent cloud processes.

Clouds consist of water vapor, together with cloud droplets, and/or ice crystals. Clouds consisting solely of water vapor and cloud droplets are called warm clouds and occur at temperature above 0 °C. In addition, cloud droplets can be supercooled down to -38 °C. Below this temperature they freeze homogeneously (i.e. without the need of an ice nucleating particles (INPs)). Typical warm clouds are fair-weather cumuli observed at our latitudes in summer time. At temperatures below -38 °C clouds consist solely from ice crystals and water vapor. The ice crystals form by homogeneous freezing of liquid or solution droplets and relative humidities with respect to ice above 140% (Kanji et al., 2017), or by heterogeneous nucleation of INPs (e.g., DeMott et al., 2010; Hoose and Möhler, 2012; Murray et al., 2012). Typical ice clouds are cirrus observed at

altitudes  $>7000$  m. At temperatures between  $0$  °C and  $-38$  °C, mixed-phase clouds (MPCs) consisting of water vapor, supercooled droplets, and ice crystals can exist. Typical MPCs at mid-latitudes are precipitating clouds in the winter-half of the year, or cumulonimbus in the summer time. Low-level MPCs are typically found in the Arctic and are the focus of this thesis. The main processes relevant for Arctic MPCs are introduced in the following subsections and displayed in the schematic of Arctic MPCs in Figure 1.1. Nevertheless, one should keep in mind that because of the lack of measurements in the Arctic and the complexity of the interplay between the microphysical processes, Arctic MPCs are still neither fully understood nor accurately represented in models (e.g., Mioche et al., 2015; Lloyd et al., 2015).

### 1.2.2 Cloud droplet formation and growth

Cloud droplets form by activation of aerosol particles acting as cloud condensation nuclei (CCN). The CCN concentration (CCNC) depends on the aerosol type and concentration, and on the supersaturation. Good CCN are particles that are hygroscopic to form an aqueous solution drop, such as sea salt NaCl (Wang, 2013). Droplets grow by diffusion of water vapor molecules towards the liquid droplets and condensation of the molecules on the surface of the droplet (Lohmann et al., 2016b). The linear growth rate, i.e. the increase in radius, of the diffusion and condensation process decreases with increasing droplet size. Starting from approximately  $15$   $\mu\text{m}$ , the collision and subsequent coalescence of multiple liquid droplets is a more efficient growth process. This process is initiated by the sedimentation of droplets which collide with smaller droplets in their path (Lohmann et al., 2016b). The collision-coalescence process can produce precipitation-sized particles of a few millimeters within  $\sim 20$  min and is the dominant precipitation formation pathway in warm clouds (Rogers and Yau, 1989).

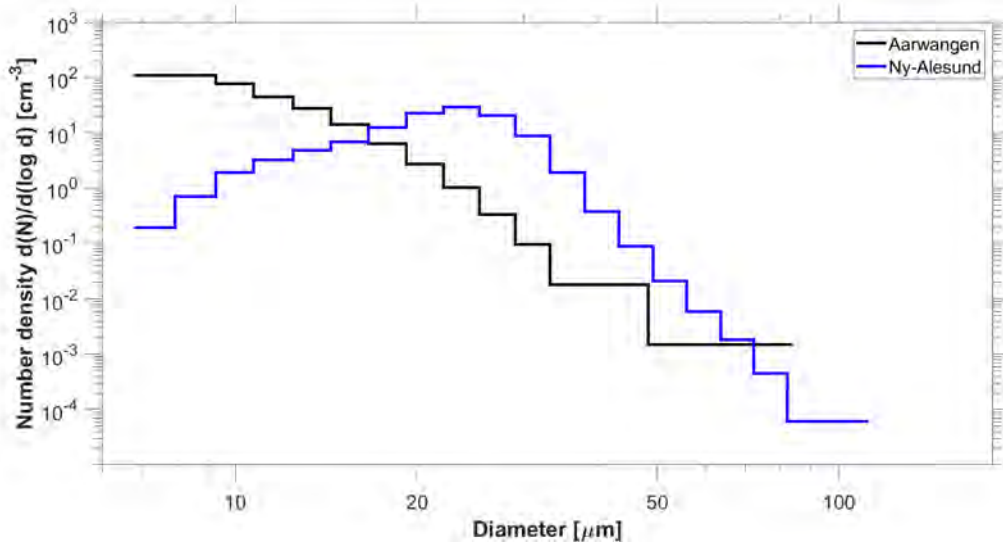


Figure 1.2: Cloud droplet size distributions measured by HoloBalloon in a stratocumulus cloud on 10 November 2019 in Ny-Ålesund, Svalbard (blue line) and on 24 February 2018 in Aarwangen, Switzerland (black line).

The size distributions of an Arctic stratocumulus measured in Ny-Ålesund, Svalbard and one continental stratocumulus measured in Aarwangen, over the Swiss plateau are shown in Figure 1.2 illustrate the influence of the CCNC on the droplet's growth. The Arctic stratocumulus cloud shows fewer but larger droplets compared to the continental stratocumulus. The size distribution peaks at around  $25$   $\mu\text{m}$  in the Arctic, compared to  $7$   $\mu\text{m}$  in the continental case. The reason for this difference is that the air in the Arctic is cleaner than over the Swiss plateau. Fewer CCN are available in the ambient air, thus fewer cloud droplets form by CCN activation but each drop

can grow to a larger size due to less competition with other droplets (i.e. the same amount of condensed water is distributed over fewer cloud droplets).

### 1.2.3 Ice crystal formation on INPs

Ice crystals form via heterogeneous nucleation with the help of INPs at temperatures between 0 °C and -38 °C in MPCs (e.g., DeMott et al., 2010; Hoose and Möhler, 2012; Boose et al., 2016). Fewer aerosol particles act as INPs than as CCN in the atmosphere and the INP concentration (INPC) depends strongly on the ambient temperature and supersaturation. Solid insoluble particles with a large surface area such as biological particles or mineral dust are the most prevailing INPs (Kanji et al., 2017). Heterogeneous nucleation can occur via four different modes: (1) immersion freezing refers to the freezing of a cloud or solution droplet in which an INP is already immersed and initiates freezing upon cooling, (2) condensation freezing describes the condensation of water that subsequently freezes on an INP, (3) contact freezing occurs when an INP collides with a supercooled droplet and initiates its freezing, (4) deposition nucleation characterizes the direct deposition of vapor on an INP (Lohmann et al., 2016b). Recent studies proposed the actual process behind deposition nucleation is liquid water condensation and freezing in pores (pore condensation and freezing), where liquid water condensation can occur below water saturation (Marcolli, 2014; David et al., 2019b). Contact freezing and immersion freezing are the relevant nucleation modes for ice crystal formation in Arctic MPC (Ansmann et al., 2008). Ice forming directly from INPs is called primary ice, in contrast to secondary ice crystals produced from multiplication of ice particles and discussed in the following section. The origin of ice crystals (primary versus secondary ice) is still insufficiently quantified, especially in Arctic MPCs, and is therefore a focus of this thesis.

### 1.2.4 Secondary ice crystal formation

Observations in MPCs have shown that the ice crystal number concentration (ICNC) is frequently several orders of magnitude larger and shows more temporal fluctuations than the estimated INPC (e.g., Hobbs and Rangno, 1985; Lloyd et al., 2015; Lohmann et al., 2016a). Secondary ice production (SIP) which refers to the formation of additional ice particles from the prevailing ice crystals can explain this discrepancy. SIP is expected to play an important role in the formation of ice crystals in MPCs (e.g., Korolev et al., 2020; Korolev and Leisner, 2020). Because ice crystals are required for the initiation of SIP processes, the first ice crystals will always form by nucleation on INPs and only thereafter SIP processes can become active. Several SIP processes have been documented over the past decades: (1) droplet fragmentation during freezing, (2) splintering during riming (Hallett–Mossop process), (3) fragmentation during ice-ice collision, (4) ice fragmentation during thermal shock, and (5) fragmentation during sublimation. The knowledge gained from laboratory experiments on SIP processes is shortly describe here. Please see Korolev and Leisner (2020) for a complete review of the results from laboratory experiments related to SIP processes.

The production of secondary ice during riming is referred as rime-splintering or Hallett-Mossop (HM) process named after the studies by Hallett and Mossop (1974) and Mossop and Hallett (1974) who observed splinters formation during riming in a cloud chamber. However, the underlying physical mechanism of this process is still not well understood. It is considered to occur when cloud droplets with diameters larger than 25  $\mu\text{m}$  and smaller than 13  $\mu\text{m}$  coexist and freeze upon collision with a larger ice particles (Field et al., 2017; Korolev and Leisner, 2020). Despite the lack of physical understanding of the HM process, there is a scientific consensus that this process occurs in a temperature range between -8 °C and -3 °C when heavily rimed particles and cloud droplets smaller 13  $\mu\text{m}$  and larger 25  $\mu\text{m}$  are prevailing. This SIP process is the one which received the most attention and is the only SIP mechanism for which parametrizations are widely used in numerical weather prediction models. However, as the HM process is constrained

to the temperature range between  $-8\text{ }^{\circ}\text{C}$  and  $-3\text{ }^{\circ}\text{C}$ , its impact on the cloud microphysics in seems limited.

Droplet fragmentation during freezing can be initiated by the collision of a cloud droplet with an INP or with an ice crystal in most cases. An ice shell can form which trap the liquid water inside. When the ice shell expands, an internal pressure builds up because of the lower density of ice compared to liquid water. If the pressure reaches a critical point, the ice shell may crack to relieve the internal pressure, and thereby produces secondary ice crystals (e.g., Langham et al., 1958; Mason and Maybank, 1960; Korolev and Leisner, 2020). Lauber et al. (2018) found that the production of splinters increases with liquid droplets size. The maximum rate of fragments produced was found at around  $-15\text{ }^{\circ}\text{C}$ , but the process was observed at temperatures from  $-20\text{ }^{\circ}\text{C}$  up to  $-0.5\text{ }^{\circ}\text{C}$  (Korolev et al., 2020; Keinert et al., 2020).

Ice crystals can fragment and create splinters during collisions with other ice crystals. Only two laboratory studies investigated SIP during ice-ice collisions (Vardiman, 1978; Takahashi et al., 1995). Therefore the efficiency of this SIP process is still poorly described. It seems to be favored by large rimed ice crystals (Vardiman, 1978) and the number of fragments generated to depend additionally on the air temperature, and on the relative fall speed of the colliding particles (Takahashi et al., 1995; Korolev and Leisner, 2020).

Thermal-shock fragmentation may take place during riming (King and Fletcher, 1976). When the drop freezes on the surface of the ice crystal, its temperature rises to the melting point and a part of the latent heat released is transmitted to the ice crystal. This may cause a thermal shock, producing a stress that can cause the cracking or splintering of the ice crystal because of the differential expansion of ice (Koenig, 1965). Thermal shock fragmentation was found to be able to occur at temperatures below  $-5\text{ }^{\circ}\text{C}$  (King and Fletcher, 1976). However, this SIP mechanism obtained only little investigation and is still badly understood and described.

Fragmentation during sublimation can occur in subsaturated regions, for example below cloud base. Laboratory studies have shown that the number of fragments produced varies depending on the shape of the initial ice crystal. In addition, the temperature and the relative humidity influence the fragment numbers (Dong et al., 1994; Bacon et al., 1998). The fragments need to re-enter back into saturated regions (i.e. in cloud) to growth to larger ice crystals and thus to be counted for as SIP particles. If the fragments remain in subsaturated air, they will sublimate completely.

Large gaps in knowledge as well as contradictory results emerged from laboratory experiments. Thus, further laboratory work is needed to improve the physical understanding and develop quantitative descriptions of the SIP processes. Furthermore, a increased knowledge of the occurrence of all SIP mechanism as well as the environmental conditions favorable for SIP occurrence is crucially needed in clouds, but this is difficult because direct measurement of SIP processes is practically impossible in natural clouds. One goal of this thesis is to obtain a better description of environmental conditions favorable for SIP processes. To this aim, we compare the concentrations of INP and small ice crystal to determine regions of SIP occurrence, and investigate the environmental conditions prevailing in these regions.

### 1.2.5 Ice crystal growth

Once an ice crystal has formed, it will grow by vapor diffusion, similarly to cloud droplets. The ice crystals growth by deposition is more efficient than the condensational growth of cloud droplets because higher supersaturations with respect to ice are encountered and the water vapor gradient at the particle's surface is larger for ice crystals than for cloud droplets. The ice crystals need a few minutes to reach a size of many tens of micrometers (Lohmann et al., 2016b). The arrangement of water molecules in the ice crystal lattice is responsible for the hexagonal shape of the ice crystals and the temperature and supersaturation further determine the habit of ice crystals. Simple ice crystals have the form of an hexagonal prism with two basal faces and six prism face (Lohmann et al., 2016b).

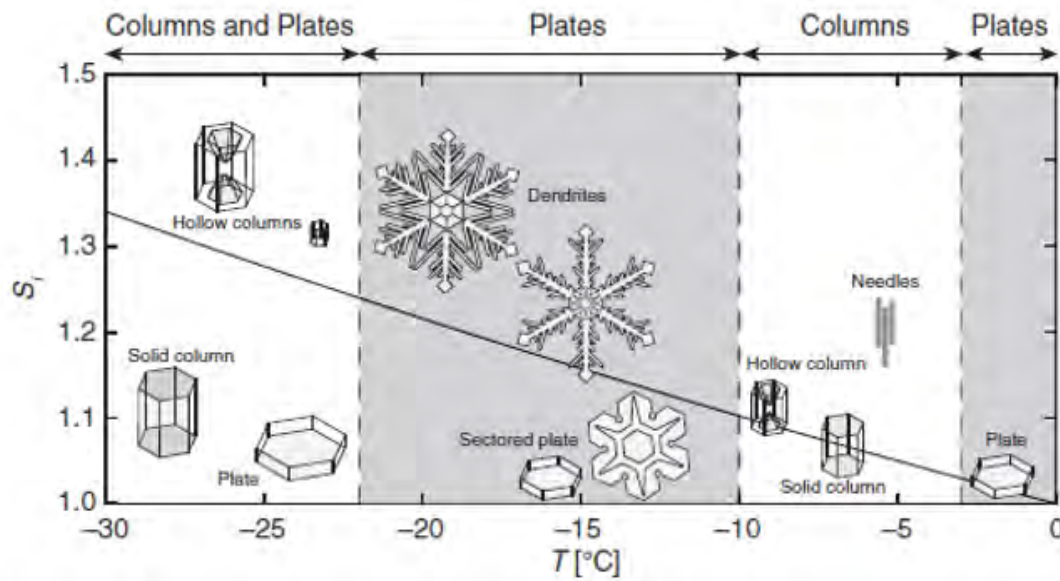


Figure 1.3: Ice crystal habit diagram, showing to which habit ice crystals grow as a function of temperature ( $T$ ) and saturation ratio with respect to ice ( $S_i$ ). The solid black line represents saturation with respect to liquid water. Figure taken from (Lohmann et al., 2016b)

The growth in the basal (column-like) or prism (plate-like) face is favored depending on the ambient temperature. Results from laboratory experiments have shown that plate-like ice habits are the predominant ice habit in the temperature range between  $0\text{ }^{\circ}\text{C}$  and  $-3\text{ }^{\circ}\text{C}$  and between  $-10\text{ }^{\circ}\text{C}$  and  $-22\text{ }^{\circ}\text{C}$ , whereas columnar ice crystals are mostly prevailing at temperatures between  $-3\text{ }^{\circ}\text{C}$  and  $-10\text{ }^{\circ}\text{C}$ , as well as at temperatures below  $-22\text{ }^{\circ}\text{C}$  (Fig. 1.3) (e.g., Libbrecht, 2005). At  $-3\text{ }^{\circ}\text{C}$  and  $-10\text{ }^{\circ}\text{C}$ , ice crystals with an aspect ratio of close to 1 are observed. In this thesis, we use the knowledge about these favored growth regimes to investigate the history of the ice particles in natural clouds.

In addition to growth by deposition, ice crystal can growth by accretion when colliding with other ice particles (aggregation) or cloud droplets (riming). Aggregation is larger at higher temperatures because of the thicker quasi-liquid layer on their surface that increases their stickiness (Lohmann et al., 2016b). This is most effective at temperature higher than  $-10\text{ }^{\circ}\text{C}$ . Riming occurs when a supercooled droplet collides and freezes on the surface of an ice crystal. Because the droplet is likely to freeze upon collision, the sticking efficiency is close to unity. Rather, the riming efficiency depends the collision efficiency between ice crystals and cloud droplets and therefore on the cloud droplet size distribution and the CCNC. The ice crystals shape and size gives information about its origin and growth history.

### 1.2.6 Seeder-feeder process

In addition to the formation of ice crystals by homogeneous and heterogeneous nucleation, and from SIP processes, the seeder-feeder process can increase the ICNC in low-level MPCs. The seeder-feeder mechanism refers to sedimenting ice particles from a higher cloud into a separate lower cloud or a lower part of the same cloud (Proske et al., 2021). Even though the seeder-feeder mechanism was originally proposed over orographic terrain, it was found to be frequently occurring also in Arctic multilayer clouds (Vassel et al., 2019). The higher ICNC can enhance the Wegener-Bergeron-Findeisen process (WBF) explained below and/or the precipitation amount.



### 1.2.7 Wegener-Bergeron Findeisen process

The mixture of water vapor, supercooled liquid droplets, and ice crystals found in MPC is thermodynamically unstable because the equilibrium vapor pressure over ice is lower than over supercooled water. This causes ice crystals to grow faster by diffusion of water vapor than the liquid droplets. The ice crystal growth reduces the water vapor pressure and can lead to the evaporation of cloud droplets if the water vapor saturation drops below saturation with respect to liquid. This process is called the WBF process (Wegener, 1911; Bergeron, 1935; Findeisen, 1938). The WBF can cause a complete glaciation of the MPC within a few minutes to hours depending on the ice crystal concentration and liquid water content (Harrington et al., 1999; Korolev and Isaac, 2003). However, the efficiency of the WBF depends on the spatial distribution of cloud droplets and ice crystals, and is limited if the ice crystals and cloud droplets are inhomogeneously distributed (Korolev et al., 2017). Additionally, if sufficient updrafts are prevailing to sustain water vapor saturation, both cloud droplet and ice crystals can growth simultaneously. In the contrary, if updrafts are too low, the saturation with respect to ice may not be sustained which would cause the sublimation of the ice crystals.

### 1.2.8 Aerosol-cloud interaction

Aerosol particles exert a direct effect on the Earth's radiation budget because they absorb or scatter shortwave radiation and absorb and re-emit longwave radiation. This is referred to as the effective radiative forcing due to aerosol-radiation interactions ( $ERF_{ari}$ ) (Boucher et al., 2013). In addition, aerosol particles acting as CCN and INPs change the microphysical properties of clouds, thus influencing their radiative properties as will be discussed in Section 1.2.10. The effect of aerosol particles on cloud properties is nowadays called the effective radiative forcing due to aerosol-cloud interaction ( $ERF_{aci}$ ) (Boucher et al., 2013). For example, three such effects arise from an increase in CCNC leading to an increase in cloud droplet number concentration (CDNC): (1) the cloud-albedo or Twomey effect stating that more cloud droplets increase the albedo the cloud, (2) the riming indirect effect stating that it results in a decrease in the sizes of cloud droplets and thus in a less efficient riming process reducing the mass of the ice crystals and hence the ice water content (Borys et al., 2003), (3) the thermodynamic indirect effect that states that the decrease in the sizes of cloud droplets delay the onset of freezing and thus decrease the ice crystal number concentration (Lohmann and Feichter, 2005; Jackson et al., 2012). Regarding the  $ERF_{aci}$  on INPC, the glaciation indirect effect states that an increase in INPC increases the ICNC and thus enhances the amount of ice phase precipitation (Lohmann, 2002). The interplay between cloud and aerosol particles is complex and especially important in the Arctic atmosphere, where increases in aerosol concentration can have a large impact on the otherwise clean atmosphere. There is a need to obtain better characterisation of the aerosol-cloud interactions in the Arctic climate, to better constrain their impact in the current and future on the Arctic climate.

### 1.2.9 Persistence of Arctic MPCs

Despite all processes contributing to the formation and growth of ice crystals and thus favoring the glaciation of MPCs, Arctic MPCs regularly persist for several hours or days (e.g., Pinto, 1998; Shupe et al., 2008a; Morrison et al., 2011). This persistence requires that the environment remains saturated with respect to liquid water, otherwise the cloud droplets would evaporate. This can be achieved by sufficiently large updrafts (Heymsfield, 1977; Pinto, 1998; Korolev et al., 2017) if the condensate supply rate exceeds the diffusional growth rate of ice crystals (Raubert and Tokay, 1991). In Arctic MPC, it was found that the radiative cooling enhanced by the frequently observed supercooled liquid layer at cloud top (e.g., Hobbs and Rangno, 1998; Shupe et al., 2008a; McFarquhar et al., 2011) drives updraft and turbulence, which help maintaining liquid water saturation needed for sustaining the cloud top liquid layer (Morrison et al., 2011).

The current understanding is that this feedback process is responsible for the persistence of Arctic MPCs (Morrison et al., 2011). In addition, low ICNC regions (e.g. in an INP-limited cloud) need lower updrafts to remain supersaturated with respect to liquid water because of the lower competition for water vapor and because the few ice crystals grow rapidly by vapor deposition and sediment out of the cloud without causing its entire glaciation (Girard et al., 2013).

### 1.2.10 Cloud radiative effects

In general, clouds influence the Earth’s radiation budget in two competing ways: they cool the surface by scattering solar radiation back to space, and warm the surface by absorbing and re-emitting longwave radiation (Shupe and Intrieri, 2004; Lohmann et al., 2016b). Because of their high frequency of occurrence in the Arctic (e.g., Intrieri et al., 2002; Shupe et al., 2006; Nomokonova et al., 2019), MPCs largely influence the surface and the top-of-atmosphere radiative budgets (e.g., Zuidema et al., 2005b; Shupe and Intrieri, 2004; Korolev et al., 2017). The radiation properties depend largely on the cloud optical depth which is defined as the extinction coefficient integrated over the thickness of the cloud. Cloud droplets have a larger extinction coefficient and thus a larger optical depth than ice crystals for a given cloud water path because they are smaller and more numerous. For this reason, the cloud droplets are mainly controlling the MPC’s shortwave and longwave radiative properties. On one side, more cloud droplets in the MPC mean a higher albedo and thus a larger surface cooling effect. This is furthermore enhanced by the difference in scattering properties between spherical water droplets and nonspherical ice crystals (e.g., Järvinen et al., 2018). On the other side, the emissivity of MPC is larger when they contain more cloud droplets. Therefore, their longwave warming effect is stronger. It was found from combined remote sensing and modelling studies and that the radiative forcing from Arctic clouds exhibit a strong seasonality (Dong et al., 2010; Ebell et al., 2020). Clouds induce a surface warming during most of the year and a short period of surface cooling in the summer, when the shortwave cooling dominates over the longwave warming effect. However, the impact of the cloud radiative feedbacks on the AA remain largely uncertain. More observations of cloud microphysical and radiative properties are needed to better constrain models and reduce these uncertainties. In this thesis, we introduce an innovative approach, where we combine collocated in-situ microphysical and radiative measurements to directly infer the effect of the cloud particles concentrations and phase on the radiative fluxes.

## 1.3 Atmospheric observations

Observations of cloud properties can be obtained by in situ and remote sensing measurements. In situ instruments sample the cloud properties directly at the instruments location and provide a detailed characterization of the cloud properties at a given point in time and space, but lack information on the rest of the cloud structure. On the contrary, remote sensing instrumentation profile atmosphere continuously, but relies on retrieval algorithms based on assumption about the cloud microphysics. Additional essential information about the entire atmosphere profile such as temperature, wind speed and direction, and relative humidity is most frequently obtained from radiosondes. Therefore, the combination of cloud in-situ and remote sensing observations, together with radiosonde profiles is optimal to acquire a thorough understanding of the cloud microphysical properties. In the following sections, we describe in situ instrumentation (Section 1.3.1) and remote sensing instrumentation (Section 1.3.2), which are relevant for this thesis.

### 1.3.1 In-situ cloud observations

In situ observations of clouds have been performed on mountain tops (e.g., Borys et al., 2003; Henneberger et al., 2013; Beck et al., 2018; Koike et al., 2019), on cable cars (e.g. Beck et al.,

2017; Lauber et al., 2021), on aircrafts (e.g., Lawson et al., 2001; McFarquhar et al., 2011; Lloyd et al., 2015; Korolev et al., 2020), and less frequently on tethered balloon systems (e.g., Duda et al., 1991a; Ramelli et al., 2020, 2021a,b). All measurement platforms have advantages and caveats. Mountain top measurements can provide continuous measurements of clouds for long time period but the measurements can be influenced by the surface-based processes (Beck et al., 2018). Measurements performed with aircrafts offer flexibility on the choice of the flight path, which is useful for the characterization of specific cloud regions (e.g., cloud top), but the high traveling speed of aircraft limits the spatial distribution the measurements and the high aspiration speed may generate ice crystal shattering at the tips of the instrument’s inlet (Korolev et al., 2011). Cable car platforms have lower aspiration speeds compared to aircrafts, but their location and travel altitude is restricted. Tethered balloon platforms have even lower aspiration speeds, are more flexible in term of measurement locations, the altitude of measurements can be varied and the instruments orient themselves automatically in the direction of the wind. However, the maximum altitude of such measurements is limited to the lower part of the atmosphere. This makes tethered balloon systems an ideal platform to measure low-level clouds in remote regions like the Arctic. In this thesis, the tethered balloon system HoloBalloon (Fig. 1.4) was utilized to sample Arctic MPCs. HoloBalloon consists of a 175 m<sup>3</sup> helikite and an instrument platform and is able to fly up to ~1200 m above ground (when launched from sea level). The HOLOGraphic Imager for Microscopic Objects (HOLIMO 3B) is the main instrument on this platform.



Figure 1.4: HoloBalloon flying with the instrument platform hanging 12 m below the helikite. The container where aerosol measurements were performed is visible on the left. Photography taken by Jan Henneberger.

HOLIMO3B works on the principle of digital in-line holography using a coherent light source from a laser and a digital camera (Ramelli et al., 2020). First, a hologram is recorded from the interference pattern of the reference wave emitted by the laser and the scattered waves from cloud particles in the sample volume (Fig. 1.5). Second, the HoloSuite software package

is used to extract the particle images and the cloud properties (Fugal et al., 2009; Schlenczek, 2018). For this, layers are reconstructed in the sampling volume. An amplitude threshold is used to detect particles inside the sample volume and the 3D in-focus position as well as the 2D shadowgraphs of the particles are extracted. More information about the holographic method used can be found in Fugal et al. (2009) and Henneberger et al. (2013). Thereafter, particles are classified into cloud droplets, ice crystals, and artefacts using supervised machine learning (e.g., Fugal et al., 2009; Beck et al., 2017) or a convolutional neural network trained and fine-tuned on cloud particles from holographic imagers (Touloupas et al., 2020; Lauber, 2020). One major advantage of HOLIMO3B compared to other cloud microphysical probes is that it has a well-defined sample volume independent of particle size and air speed, which enable the use of an open path configuration, i.e. no inlets are needed.

A better understanding of the role of the phase partitioning within MPCs on their radiative properties is needed to reduce the uncertainties related to the cloud radiative feedbacks on the AA. To be able to directly relate the cloud microphysical and radiative properties, I installed two pyrgeometers (upward and downward looking) and two pyranometers (upward and downward looking) on the backside of HOLIMO3B. These measurements are discussed in Chapter 5. Another new implementation was the change of the communication system between the monitoring computer on the ground and HOLIMO3B in the clouds. This provisory adaptation was implemented because it is forbidden to use wavelengths above 2 GHz in Ny-Ålesund as this region is part of a radio silent zone. Finally, HOLIMO3B was for the first time installed on a new platform hanging below the tethered balloon system. HOLIMO3B had so far been attached directly to the keel of the helikite. However, it was found during previous campaigns that this may have generated a turbulent flow possibly influencing the observation of large ice particles due to shielding effects of the balloon. Thus, we mounted HOLIMO3B for the first time on a new hanging platform 12 m below the tethered balloon system (see Fig. 1.4), instead of being attached to its keel.

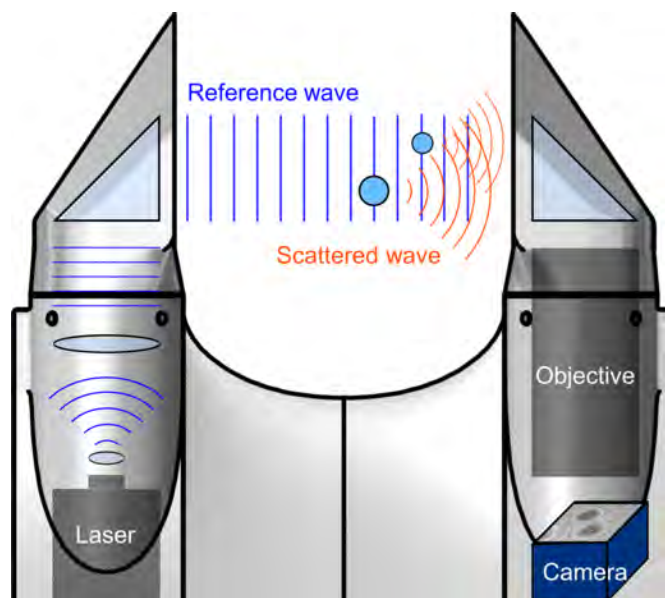


Figure 1.5: Schematic of the working principle of HOLIMO3B. A collimated laser beam generate a reference wave which is scattered by two cloud droplets. The scattered waves interfere with the reference wave. This forms the interference pattern called a hologram, which is recorded by a digital camera. Figure taken from Ramelli et al. (2020)

### 1.3.2 Remote sensing cloud observations

There are two types of remote sensing techniques: passive and active sensors. Passive remote sensing methods (e.g., radiometers) measure radiation that is naturally emitted or reflected by atmospheric particles. Active remote sensing methods (e.g., radar, lidar) emit radiation towards the targets of interest and measure the radiation scattered back. In the following, we describe the principles of active remote sensing instruments relevant for this thesis.

Ceilometers are elastic backscattering LIDARs (LIght Detection And Ranging). They are active remote sensing instruments that emit an electromagnetic wave in the visible frequency range and measure the photons scattered back by atmospheric targets. The instantaneous magnitude of the return signal gives information on the backscatter properties of the atmosphere (COST, 2013). The travel time and the speed of light are used to determine the height of the atmospheric targets. Ceilometers are mostly employed to automatically identify the cloud base altitude. The backscattered power is a function of the area of the target illuminated by the ceilometer beam. Therefore backscatter from larger targets like cloud particles will be of a greater magnitude than backscatter from aerosol particles and threshold criteria are used to discriminate if the signal originates from clouds or aerosol particles (COST, 2013). The obstruction of vision by precipitation below cloud base may lead to too low cloud base detection by ceilometer.

The RADAR (RAdio Detection And Ranging) technique works in a similar way as the lidar technique, but uses electromagnetic waves in the radar frequency range (1 - 100 GHz). This enables cloud radars to retrieve information from inside the clouds even if they are optically thick. As for the lidar technique, a part of the electromagnetic wave emitted is scattered back by atmospheric particles and their distance is calculated from the run time of the pulse. The received signal provides information about the received power, from which the reflectivity of the target can be derived, together with the Doppler shift in frequency, which is indicative of target's velocity along the radar beam (radial velocity). In addition, some cloud radars provide information about the polarization of the signal, from which information of the particle shape and orientation can be derived (Houze Jr, 2014). The power received by the antenna averaged over a time interval of 0.01-0.1 s is given by

$$\bar{P}_r = C_R \frac{Z|K|^2}{r^2} \quad (1.1)$$

where  $Z$  is the radar reflectivity,  $|K|^2$  is the square of the absolute value of the complex index of refraction,  $r$  is the distance between the scattering target and the radar, and  $C_R$  consists of constants and radar parameters (Lohmann et al., 2016b). If the Rayleigh scattering criterion is fulfilled (i.e. the size of the scattering cloud particles is much smaller than the wavelength of the electromagnetic wave), the radar reflectivity factor  $Z$  can be calculated from the sixth moment of the size distribution of the hydrometeors in the volume of air scanned (Houze Jr, 2014):

$$Z = \int_0^{\infty} D^6 N(D) dD \quad (1.2)$$

where  $N(D)$  is the size distribution of the hydrometeors and  $D$  is the particle diameter. The  $Z$  signal is largely dominated by large particles because  $Z$  is proportional to the particle's diameter to the power of six. Thus, if hydrometeors of different sizes are present in the volume measured, the largest hydrometeors will dominate the return signal. It is therefore more convenient to display  $Z$  on a logarithmic scale with the units (Lohmann et al., 2016b):

$$\text{dBZ} = Z[\text{dB}] = 10 \log_{10} \left( \frac{Z}{\text{mm}^6 \text{ m}^{-3}} \right) \quad (1.3)$$

Typical values of  $Z$  for various hydrometeors and precipitation types are displayed in Table 1.1.

In addition to the reflectivity information, the Doppler shift of frequency occurring between the transmitted and received signal can be used to obtain information about the motions of

Table 1.1: Typical values of Z for various hydrometeors and precipitation types (adapted from Lohmann et al. (2016b)).

Scatterer	Z values [dBZ]
Cloud droplets	- 40 to -20
Mixed-phase clouds	- 20 to -10
Drizzle	- 20 to 0
Very light rain or light snow	0 to 10
Moderate rain and heavier snow	10 to 30
Melting snow	30 to 45
Moderate to heavy rain	30 to 60
Hail	> 60

the air and the hydrometeors. The so-called Doppler velocity is the sum of the fall speed of the hydrometeors and the vertical wind. A Doppler velocity vector away from the cloud radar indicates a region where updrafts dominate over the fall speed of the hydrometeors.

Many hydrometeors are present in the sample volume of the radar and each hydrometeor generates a Doppler shift in frequency. This gives a distribution of Doppler radial velocities (i.e., Doppler spectrum). From the Doppler spectrum, the mean Doppler velocity (1<sup>st</sup> moment) and the width of the Doppler spectrum (2<sup>nd</sup> moment) can be calculated. The width of the Doppler spectrum, or spectral width, represents its standard deviation. Small spectral widths values indicate a narrow distribution, and large values a larger spread of Doppler velocities within the sampled volume. Such larger spectral widths can result from turbulent motion and/or from the presence of multiple particle populations with different fall speeds.

In the present thesis, a vertically-pointing (non-polarimetric) 94 GHz cloud radar (JOYRAD-94, K uchler et al., 2017), and a ceilometer (Vaisaila-CL51, Maturilli and Ebell, 2018) are used together with in-situ measurements on HoloBalloon to study the microphysics of Arctic MPCs.

### 1.3.3 Other ground based measurements

#### 1.3.3.1 Aerosol measurements

Aerosol particles, especially when acting as CCN or INPs, are crucial for the cloud microphysical properties. Thus, accurate measurements of CCNC and INPC are needed to understand the cloud microphysical properties. Several online and offline measurement techniques exist to measure the INPC at different temperatures. In offline techniques, the sampling and testing for the ice nucleation ability of the aerosol particles is separated. The air is first sampled through an aerosol-to-liquid cyclone impinger, or through a filter exposed to a defined volume of ambient air during several hours or days. Then the INPC is derived, using for example drop-freezing instruments such as the DRoplet Ice Nuclei Counter Zurich (DRINCZ, David et al., 2019a), where aerosol particles are cooled in an ethanol bath and freezing is automatically detected with a camera. In contrast, online techniques sample and test INPs quasi-simultaneously. The Horizontal Ice Nucleating Chamber (HINC, Lacher et al., 2017) is an example of an online technique. This continuous flow diffusion chamber uses a temperature gradient to generate supersaturation in the chamber to measure the INPC at -30 °C. Supersaturation generated by a thermal gradient and hence vapor can also be used to measure CCNC in continuous flow diffusion chamber called CCN counters (Roberts and Nenes, 2005).

#### 1.3.4 Meteorological and radiation observations

The irradiances at the Earth’s surface are important to understand the radiative processes. State of the art radiation measurements are performed at measurement sites of the Baseline Surface

Radiation Network (BSRN) around the world. The goal behind the radiation measurements performed at BSRN fields is to detect important changes in Earth's radiation at the Earth's surface which could be linked to climate change. In addition to radiation measurements, collocated surface meteorological observations of temperature, wind speed and direction and pressure are essential to obtain a complete picture of the state of the atmosphere. A BSRN field site is installed in Ny-Ålesund (Maturilli et al., 2015; Maturilli, 2020c). These measurements were used to gain understanding about the prevailing meteorology and as ground truth to compare with the newly installed radiation sensors on HoloBalloon.

## 1.4 Objectives of this thesis

Whereas it has been identified that MPCs play an important role for the radiative budget in the Arctic (e.g., Shupe et al., 2006; Korolev et al., 2017), the uncertainties related to their impacts are still large Goosse et al. (2018). A better understanding of the microphysical and radiative properties of MPCs is needed to reduce these uncertainties. Especially, the mechanisms shaping the ice crystals and cloud droplets concentrations and sizes need to be better understood and related to the radiative properties of the MPCs. This includes obtaining a more precise characterization of the aerosol properties and their interaction with clouds, as well as increasing the knowledge about other processes leading to cloud particle formation, such as SIP processes. With this aim, extensive aerosol and cloud observations were retrieved during the Ny-Ålesund Aerosol Cloud Experiment (NASCENT) campaign. In the present thesis, observations from this multidimensional set of instruments including remote sensing instrumentation, balloon-borne in situ observations, and ground-based aerosol measurements are analyzed to obtain a more comprehensive understanding of the microphysical and radiative properties of Arctic MPCs.

With the aim to extend the current knowledge and understanding of microphysical properties and processes in Arctic MPCs, especially on ice crystal formation, the objectives of the present thesis are:

1. *To organise and perform two field campaigns in October-November 2019 and March-April 2020 in the framework of NASCENT:* This includes the implementation of a new communication system in HOLIMO3B and adaptations for a new measurement platform hanging below the balloon, as well as being the principal investigator of the project on-site and being in charge of the HoloBalloon measurements.
2. *To combine the measurements performed by 19 institutions worldwide in an overview paper describing the main instrumentation and highlights of the NASCENT campaign:* After extensive field campaigns were completed, I took the lead on writing an overview paper of NASCENT combining all the measurements collected (see Chapter 2). My role was to coordinate the work of all the co-authors, and to write the more general parts of the paper such as the introduction and description of the climatology, as well as parts related to the cloud microphysical properties observed in-situ with HoloBalloon, by remote-sensing instrumentation, and modelled by the Weather Research and Forecasting (WRF) model (Chapter 2).
3. *To study the formation of ice crystals in Arctic MPCs measured during the NASCENT campaign with an holographic imager mounted on HoloBalloon:* The microphysical MPC measurements gathered during 6 days are used to assess the prevailing ice crystal formation mechanisms. On one day, the INPC limited the formation of ice crystals, whereas on three days, high SIP was observed. A special focus is given on the atmospheric conditions favorable for the occurrence of SIP (Chapter 3).

4. *To identify the growth history of ice crystals with complex habits in the observed Arctic MPCs:* The 2D images obtained with the holographic imager mounted on HoloBalloon are used to determine the growth history of two ice crystal types with complex shapes. Ice crystals growing at different temperature ranges indicate a recirculation within the cloud and ice crystals with particular faceted protuberance are indicative of riming at an early growth stage (Chapter 4).
5. *To install and validate upward and downward looking pyranometers and pyrgeometers measuring shortwave and longwave radiation on the backside of HOLIMO3B:* A comparison of the newly installed radiation measurements with the BSRN measurement field was performed. The radiation measurement setup on HoloBalloon was used to measure cloud top cooling, to obtain profiles of shortwave and longwave radiation in order to find possible connections with the cloud microphysical properties. This demonstrates the huge potential of the combined microphysical and radiation measurements on HoloBalloon. Finally, possibilities how to improve the quality of future measurements were identified (Chapter 5).



## Chapter 2

# The Ny-Ålesund Aerosol Cloud Experiment (NASCENT): Overview and First Results

J. T. Pasquier (1) and R. O. David (2) and G. Freitas (3,4) and R. Gierens (5) and Y. Gramlich (3,4) and S. Haslett (3,4) and G. Li (1) and B. Schäfer (2) and K. Siegel (3,4) and J. Wieder (1) and K. Adachi (17) and F. Belosi (14) and T. Carlsen (2) and S. Decesari (14) and K. Ebell (5) and S. Gilardoni (12,13) and M. Gysel-Beer (9) and J. Henneberger (1) and J. Inoue (6) and Z. A. Kanji (1) and M. Koike (7) and Y. Kondo (6) and R. Krejci (3,4) and U. Lohmann (1) and M. Maturilli (10) and M. Mazzolla (12,13) and R. Modini (9) and C. Mohr (3) and G. Motos (11) and A. Nenes (11, 19) and A. Nicosia (14) and S. Ohata (15, 16) and M. Paglione (14) and S. Park (8) and R. E. Pileci (9,21) and F. Ramelli (1) and M. Rinaldi (14) and C. Ritter (10) and K. Sato (18) and T. Storelvmo (2) and Y. Tobo (6) and R. Traversi (20) and A. Viola (12,13) and P. Zieger(3,4)

(1) Institute for Atmospheric and Climate Science, ETH Zürich, Zurich, Switzerland

(2) Department of Geosciences, University of Oslo, Oslo, Norway

(3) Department of Environmental Science, Stockholm University, Sweden

(4) Bolin Centre for Climate Research, Stockholm University, Sweden

(5) Institute for Geophysics and Meteorology, University of Cologne, Cologne, Germany

(6) National Institute of Polar Research (NIPR), Tachikawa, Tokyo, Japan

(7) Department of Earth and Planetary Science, Graduate School of Science, University of Tokyo, Tokyo, Japan

(8) Korea Polar Research Institute (KOPRI), Incheon, Korea

(9) Laboratory of Atmospheric Chemistry, Paul Scherrer Institute (PSI), Villigen PSI, Switzerland

(10) Alfred Wegener Institute, Helmholtz Centre for Polar and Marine Research (AWI), Potsdam, Germany

(11) Laboratory of Atmospheric Processes and their Impacts, Ecole Polytechnique Fédérale de Lausanne, Lausanne, Switzerland

(12) Institute for Polar Sciences, CNR, Bologna, Italy

(13) Institute for Polar Sciences, CNR, Rome, Italy

(14) National Research Council, Institute of Atmospheric Sciences and Climate, CNR-ISAC, Bologna, Italy

(15) Institute for Space–Earth Environmental Research, Nagoya University, Nagoya, Aichi, Japan

(16) Institute for Advanced Research, Nagoya University, Nagoya, Aichi, Japan

(17) Meteorological Research Institute, Tsukuba, Ibaraki, Japan

(18) Kitami Institute of Technology, Kitami, Hokkaido, Japan

(19) Center for Studies of Air Quality and Climate Change, Institute for Chemical Engineering Sciences, Foundation for Research and Technology Hellas, Patras, Greece

(20) Department of Chemistry, University of Florence, Florence, Italy

(21) U-Earth Biotech Ltd, London, United Kingdom

*This work is currently in review in the Bulletin of the American Meteorological Society.*

*\*JTP coordinated the work of all the co-authors, analyzed and interpreted airborne in-situ cloud observational data, and wrote the introduction, the description of the climatology, as well as sections related to the cloud microphysical properties with the help of other authors.*

---

## Abstract

The Arctic is warming at more than twice the rate of the global average. This warming is strongly influenced by clouds which modulate the solar and terrestrial radiative fluxes, and thus, determine the surface energy budget. However, the interactions among clouds, aerosols, and radiative fluxes in the Arctic are still poorly understood. To address these uncertainties, the Ny-Ålesund AeroSol Cloud ExperimeNT (NASCENT) study was conducted from September 2019 to August 2020 in Ny-Ålesund, Svalbard. The campaign’s primary goal was to elucidate the life cycle of aerosols in the Arctic and to determine how they modulate cloud properties throughout the year. In-situ and remote sensing observations were taken on the ground at sea-level and at a mountaintop station, and with a tethered balloon system. An overview of the meteorological and the main aerosol seasonality encountered during the NASCENT year is introduced, followed by a presentation of first scientific highlights. In particular, we present new findings on aerosol physicochemical properties which also include molecular properties. Further, the role of cloud droplet activation and ice crystal nucleation in the formation and persistence of mixed-phase clouds, and the occurrence of secondary ice processes, are discussed and compared to the representation of cloud processes within the regional Weather Research and Forecasting model. The paper concludes with research questions that are to be addressed in upcoming NASCENT publications.

## 2.1 Motivation

Average temperatures over the Arctic region have increased by a factor of 2 to 3 compared to the global average rate in the past few decades (e.g., Wendisch et al., 2017). This phenomenon is known as Arctic Amplification (AA) and causes the retreat of sea ice at the alarming rates currently observed (e.g., Bennartz et al., 2013; Cohen et al., 2014). Several feedback mechanisms contribute to AA, but their relative importance in different regions of the Arctic is still under discussion (e.g., Hall et al., 2021). The sea-ice albedo feedback is often proposed as the main driver of AA (e.g., Deser et al., 2000). However, model experiments have shown that AA occurs even in the absence of sea ice and snow cover changes (e.g., Graversen and Wang, 2009). Despite their potentially large impact on the AA, the feedback processes related to aerosols and clouds are especially poorly understood (e.g., Morrison et al., 2011; Wendisch et al., 2017; Goosse et al., 2018).

The role of aerosols in the Arctic climate is especially complex due to the diverse processes that control their abundance and their chemical and physical properties (e.g., Willis et al., 2018). Knowledge gaps in aerosol sources, sinks, transformation processes and uncertainties in aerosol-cloud interactions are among the reasons why current climate models have difficulties reproducing the current and future climate in the Arctic (Schmale et al., 2021). At Ny-Ålesund on Svalbard, the potential aerosol particle sources and sinks show a strong seasonality (Tunved et al., 2013; Ström et al., 2003). Primary particles can originate from natural sources such as oceans (e.g., sea spray, primary biological particles) or glaciers (e.g., soil dust) (Weinbruch et al., 2012; Tobo et al., 2019; Heslin-Rees et al., 2020). Particles from forest fires or anthropogenic emissions can be transported from lower latitudes to Svalbard (Stohl et al., 2007; Schacht et al., 2019). Secondary

particles can be formed locally from gas-to-particle conversion processes involving anthropogenic and natural precursor gases (e.g., Dall'Osto et al., 2017; Nielsen et al., 2019; Beck et al., 2020; Lee et al., 2020a; Brean et al., 2021; Choi et al., 2019). However, quantitative knowledge about the physicochemical properties of Arctic aerosols and precursor gases remains limited, especially during the Arctic winter, which renders an accurate source apportionment and the estimation of their impact unknown.

Clouds influence down-welling solar and terrestrial radiative fluxes that determine the surface energy budget (e.g., Curry et al., 1996; Shupe and Intrieri, 2004). On the one hand, clouds scatter solar radiation back to space, leading to a shortwave cooling effect at the surface. On the other hand, they emit longwave radiation to space and back to the surface, and therefore have a longwave warming effect (Lohmann et al., 2016b; Nomokonova et al., 2019; Ebell et al., 2020). The impact clouds have on the energy budget depends on their macro- and microphysical properties (e.g., Shupe and Intrieri, 2004; Dong et al., 2010; Sedlar et al., 2012). The optical thickness of a pure ice cloud is lower for a given cloud water path because ice particles are fewer and larger than corresponding liquid droplets and have a different refractive index, i.e. ice clouds have lower albedos and longwave emissivities (Sun and Shine, 1994; Korolev, 2007). Arctic mixed-phase clouds (MPCs), consisting of cloud droplets and ice crystals, particularly influences the Arctic climate due to the different radiative properties of liquid water and ice within them (e.g., Sun and Shine, 1994; Curry et al., 1996; Shupe and Intrieri, 2004). Their albedos and emissivities lie between the ones of pure ice and pure liquid clouds, and depend on the exact mixture of the phases (Sun and Shine, 1994) which is strongly influenced by aerosols. Indeed, aerosols acting as cloud condensation nuclei (CCN) are required to form cloud droplets and aerosols termed ice-nucleating particles (INPs) are needed to form primary ice crystals. Once primary ice crystals are formed, secondary ice production (SIP) can occur (e.g., Hallett and Mossop, 1974; Takahashi et al., 1995; Korolev et al., 2020; Korolev and Leisner, 2020) and enhance the ice crystal number concentration (ICNC) by several order of magnitudes (Korolev et al., 2020). Consequently, aerosol particles acting as CCN and INPs as well as SIP determine the phase partitioning within MPCs, which ultimately influences the radiation budget.

The phase partitioning within MPC further impacts the lifetime of Arctic MPCs. Indeed, the mixture of ice crystals and cloud droplets is thermodynamically unstable and the so-called Wegener-Bergeron-Findeisen (WBF) process (Wegener, 1911; Bergeron, 1935; Findeisen, 1938) can cause a complete glaciation of the cloud within a few hours (Harrington et al., 1999; Rangno and Hobbs, 2001; Korolev and Isaac, 2003). However, Arctic MPCs can surprisingly persist over several hours or days (e.g., Zuidema et al., 2005a; Morrison et al., 2011). The current understanding obtained from modelling and theoretical studies is that self-maintaining feedbacks between liquid water, radiation, and turbulent updrafts are responsible for the persistence of Arctic MPCs (Morrison et al., 2011). Although a number of studies have focused on the microphysical properties of Arctic MPCs (e.g., McFarquhar et al., 2011; Lloyd et al., 2015; Young et al., 2016; Wendisch et al., 2019), the processes controlling the life cycle of Arctic MPCs still remain poorly understood (e.g., Tjernström et al., 2014; Mioche et al., 2015).

The Ny-Ålesund AeroSol Cloud Experiment (NASCENT) campaign was conducted to enhance our knowledge on Arctic aerosols and clouds, and their complex interactions throughout the polar year. The former mining town of Ny-Ålesund, located on the western part of the Norwegian archipelago of Svalbard (Fig. A.1), is nowadays fully dedicated to research. Ny-Ålesund is an ideal place to study aerosols, clouds and their interactions since the Svalbard region experiences amongst the largest warming within the Arctic (Dahlke and Maturilli, 2017; Susskind et al., 2019) and MPCs are frequently observed (Mioche et al., 2015). The NASCENT study was designed to obtain a comprehensive set of cloud and aerosol observations to address the following questions:

- To what extent can aerosol particles act as CCN and INPs in the Arctic? What are the sources, precursor gases, chemical composition, molecular properties, and the seasonality of

these aerosols?

- Under which conditions do CCN and INPs or SIP dominantly influence the phase partitioning in Arctic MPCs?
- How are cloud droplets and ice crystals spatially distributed in Arctic MPCs, and how does this distribution influence cloud lifetime and radiative properties?
- To what extent does in-cloud scavenging influence the aerosol particle size distribution in the Arctic?

The general setup and main instrumentation of NASCENT are introduced in Section 2.2. An overview of the temperature, wind, aerosol, and cloud seasonality during NASCENT is given in Section 2.3. In Section 2.4, first research highlights on aerosol and cloud interactions are discussed. Finally, a summary of the paper is given in Section 2.5, including questions to be answered in the forthcoming data analyses of the NASCENT study.

## 2.2 NASCENT study design

### 2.2.1 Measurement site

The NASCENT study took place at the Ny-Ålesund research station (78.9° N, 11.9 ° E), located on the west coast of Svalbard, from September 2019 through August 2020. Ny-Ålesund is situated on the south side of Kongsfjorden and surrounded by glaciers, moraines, rivers, mountains, and a typical tundra ecosystem. During NASCENT, atmospheric measurements were performed at five locations close to Ny-Ålesund (Fig. A.1). The atmospheric observatory of the AWIPEV research base, a joint platform of the German Alfred Wegener Institute and the French Polar Institute Paul Emile Victor, and the Swiss Site are located at the southwestern edge of town. The Zeppelin Observatory is located 2 km southwest of Ny-Ålesund at 475 m a.s.l. Measurements by the Italian Institute for Polar Sciences were located in the Gruvebadet laboratory about 1 km southwestward and at the Amundsen-Nobile Climate Change Tower (CCT) 1 km southwestward of the town.

### 2.2.2 Experimental set-up

Aerosol, cloud, radiation and meteorological properties were characterized using a multifaceted suite of instrument ranging from in-situ to remote sensing techniques. An overview of the retrieved parameters at the different locations is given in Figure A.1 and in Table A.1. The specific instrumentation and further details to the set-up are described in the supplementary information (SI).

At the Zeppelin Observatory (see e.g., Platt et al., 2021, for a review of the last 30 years of observations), detailed aerosol and cloud in-situ observations and meteorological parameters were taken using a multitude of complementary instrument techniques. At the temporary Swiss Site, ambient aerosol, CCN, and INP concentrations (INPC) were sampled through an heated inlet mounted on top of the provisory observatory container. The holographic imager HOLIMO3B was mounted on the tethered balloon system HoloBalloon (Ramelli et al., 2020) to obtain in-situ phase-resolved particle size distributions up to an altitude of 1000 m a.s.l. At the AWIPEV Observatory, long-term measurements are operated to monitor the Arctic atmosphere including a cloud radar, a ceilometer, and a wind lidar, which were used in this study. During intensive observation periods, additional radiosondes were launched to supplement the standard daily launches. Furthermore, meteorological parameters, and surface based radiation data were monitored (Maturilli et al., 2013; Maturilli, 2020d). At Gruvebadet, aerosol properties (e.g., Becagli et al., 2019; Turetta et al., 2021), black carbon (BC) concentration, INPC, and chemical characterization of organic aerosol (PM1) were monitored. Meteorological parameters and radiation measurements were performed on the 33 m high CCT). Note that because of the distance between the five measurement locations, there are small spatial (up to 2 km) and temporal (up

to a few minutes) differences between the measurements at the different sites. Finally, we used the Advanced Weather Research and Forecasting (WRF) model, version 4.2.1 (Skamarock et al., 2019), to evaluate the model representation of a MPC when prescribing the measured CCN and INP concentrations.

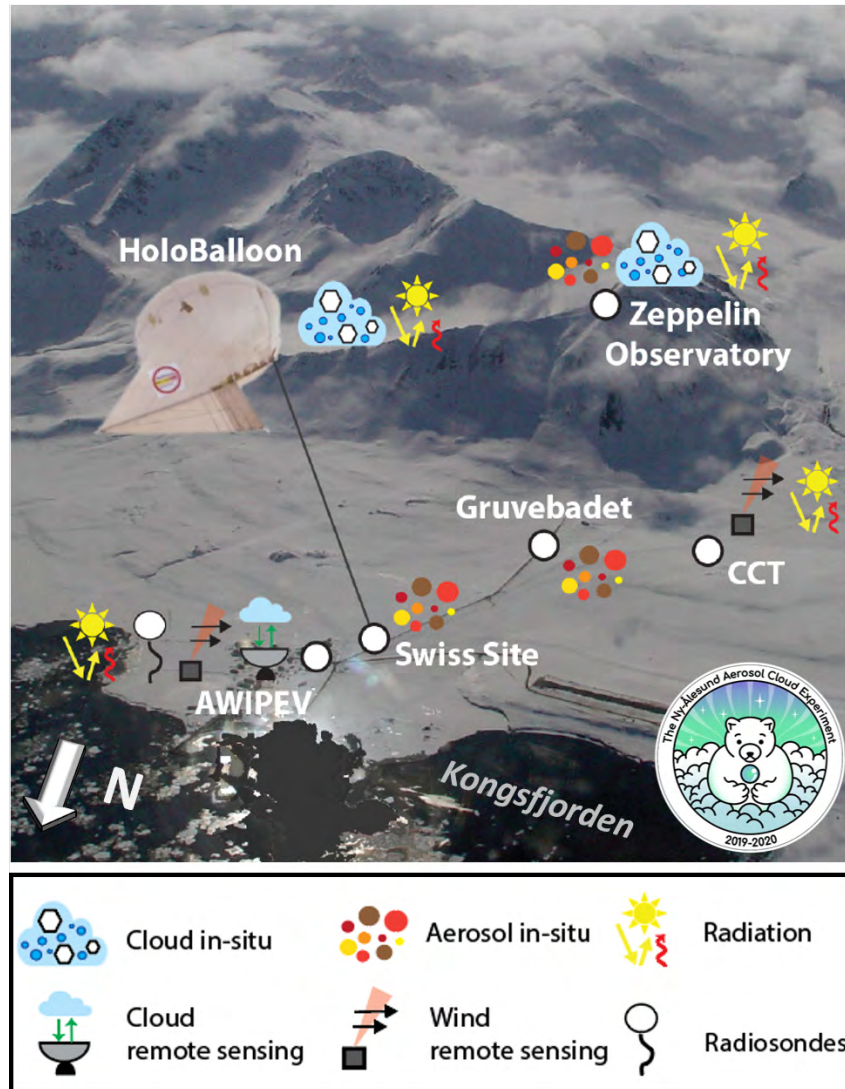


Figure 2.1: Overview of the NASCENT study set-up at Ny-Ålesund, Svalbard. Aerial photo with the five measurement locations and the respective instrumentation. The campaign logo is shown in the lower right corner.

## 2.3 Seasonality of meteorological, aerosol, and cloud parameters during NASCENT

### 2.3.1 Temperature

During NASCENT, the temperatures were colder in winter and spring (up to 6°C) and slightly warmer in summer (up to 2°C) than the climatological mean (Fig. 2.2a). Unusually low temperatures in February and March were observed in the entire Arctic and can be explained by an exceptionally strong and cold stratospheric polar vortex prevailing during the winter 2019-2020 (Lawrence et al., 2020; Lee et al., 2020b). The low temperatures caused the rare freezing of the Kongsfjorden from February to April 2020, which likely delayed the biological aerosol release from the fjord.

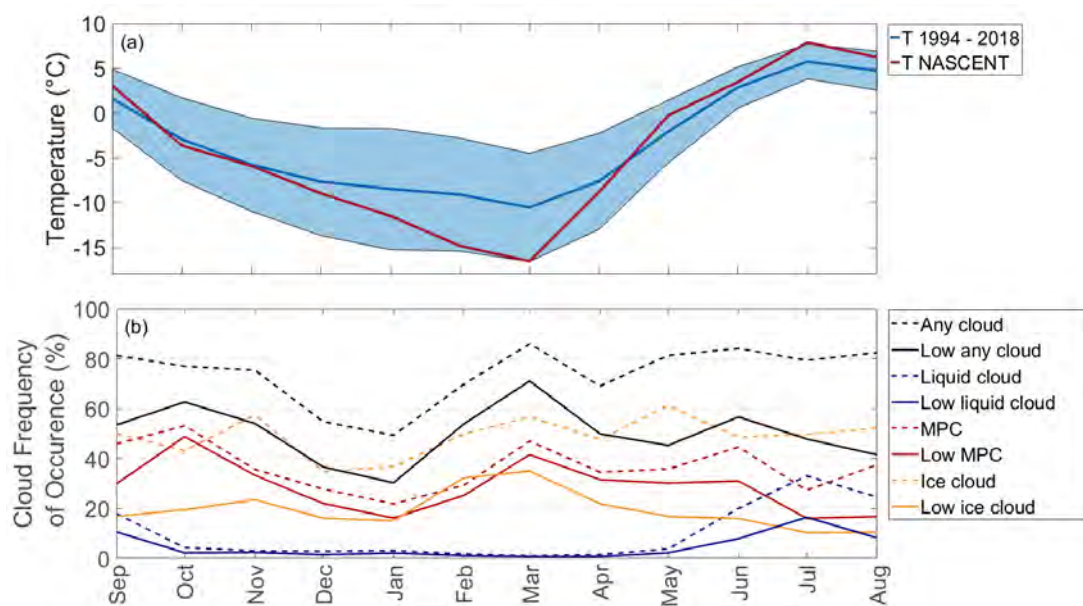


Figure 2.2: Temperature and cloud seasonality observed during NASCENT. (a) Average temperatures during NASCENT compared to the climatology of 1994 to 2018 (shading represents the standard deviation) measured at the AWIPEV weather mast 10 m above ground (Maturilli et al., 2013). (b) Monthly frequency of occurrence of cloud types derived from the Cloudnet data during NASCENT. Colors represent the different cloud types, while dashed lines show all clouds in the column and solid lines the low-level clouds with cloud tops below three kilometers. Note that multiple cloud layers of different kinds are accounted for separately, so that the sum of 'liquid', 'ice', and 'mixed-phase' does not equal the frequency of 'any' clouds.

### 2.3.2 Wind

The wind at Ny-Ålesund is strongly influenced by the surrounding topography, especially by the mountains, Kongsfjorden, and the glaciers. The wind measured 10 m above ground on the measurement field of the AWIPEV Observatory predominantly came from the southeast and less frequently from the southwest and northwest (Fig. 2.3). The wind speed was generally moderate (below  $9 \text{ m s}^{-1}$ ). These results are in agreement with previous studies showing that the wind is channeled along the Kongsfjorden (Beine et al., 2001; Maturilli et al., 2013; Maturilli and Kayser, 2017). The effect of topography can be seen when comparing the wind measurements at AWIPEV to the ones taken at the CCT where the main wind direction was also from the southeast but had more frequent periods of southwesterly wind (Fig. 2.3), which is related to the katabatic outflow from the Brøggerbreen glaciers channeled along the slopes of the Zeppelin mountain range (Maturilli et al., 2013).

At the Zeppelin Observatory, the prevailing wind showed more southerly components with occasional periods of north- to northwesterly wind (Fig. 2.3), which is in agreement with previous studies (Beine et al., 2001). This dominant wind component is due to the channeling between Zeppelin mountain on the southwest side and a smaller hill on the east side of the observatory. This mountains block the large-scale winds and are responsible for the relatively low wind speed at the observatory (mostly below  $6 \text{ m s}^{-1}$ ). Nevertheless, the air at Zeppelin Observatory may often reside within the free troposphere and would therefore be less influenced by local aerosol sources compared to the other sites around Ny-Ålesund.

In contrast to the surface winds, the radiosonde measurements between 3000 m and 3500 m a.s.l. show that southwesterly to northwesterly winds were most frequently observed above Ny-Ålesund (Fig. 2.3), in agreement with the climatological wind observed by Maturilli and Kayser (2017). This demonstrates that the topography determines the surface wind speed and direction around



Ny-Ålesund.

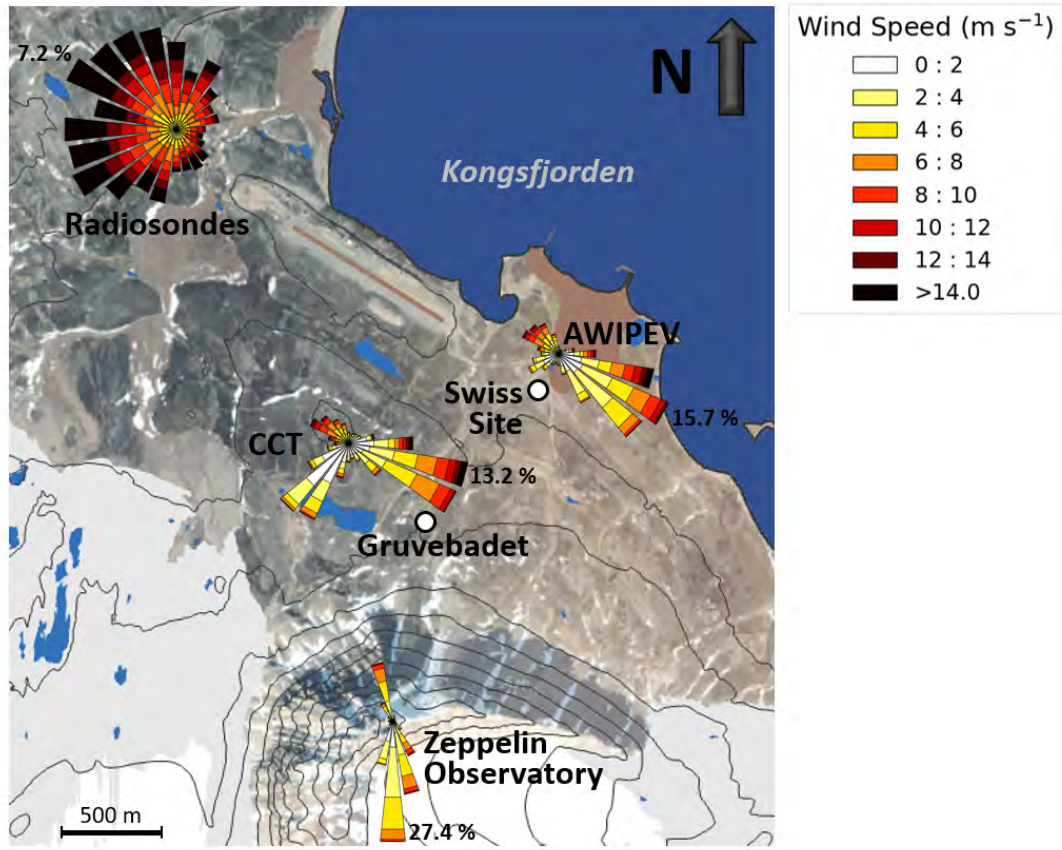


Figure 2.3: Wind measurements during NASCENT throughout the Ny-Ålesund area at the different locations and retrieved from radiosondes. Data is shown for the AWIPEV weather mast (10 m), the Zeppelin Observatory, the CCT (10 m), and from daily radiosondes between 3000-3500 m a.s.l.. The bar length gives the respective frequency of occurrence with the maximum frequency value specified at the end of the longest bar. Topographic map of the Ny-Ålesund region from (Norwegian Polar Institute, 2014).

### 2.3.3 Aerosols

Aerosol particles at Ny-Ålesund follow a typical seasonal cycle that is governed by the seasonality of the particles' respective sources and sinks (e.g., Tunved et al., 2013; Freud et al., 2017), and the seasonality in atmospheric transport patterns (e.g., Stohl, 2006). The summer months are marked by high number concentrations of small particles (i.e., with a diameter  $\leq 100$  nm) due to frequent new particle formation events (e.g., Tunved et al., 2013; Dall'Osto et al., 2017; Beck et al., 2020). In contrast, aerosol mass tends to reach a maximum in the winter and spring months (e.g., Ström et al., 2003) due to long-range transport of pollutants that form the well-known Arctic haze (e.g., Shaw, 1995; Quinn et al., 2007). BC concentrations follow the aerosol mass cycle and peak during winter and spring (Eleftheriadis et al., 2009; Sinha et al., 2017).

The typical seasonal cycle of aerosols loading was also observed during NASCENT, as can be seen in Figure 2.4, which shows the monthly distributions of daily-averaged particle number and BC mass concentrations measured at the Zeppelin Observatory and at Gruvebadet. The observed aerosol number concentrations (Fig. 2.4a) at both sites show the same seasonal cycle with a maximum in July and a minimum in the late fall and early winter months, similar to slightly higher than previous observations (Tunved et al., 2013). This difference, primarily during summer months, can be attributed to different measurement methods. Tunved et al. (2013) used

integrated particle number concentrations (using size-resolved measurements), while we used the direct particle concentration measurements using condensation particle counters (CPC) that have a lower particle cut-off diameter and are less influenced by particle diffusion losses.

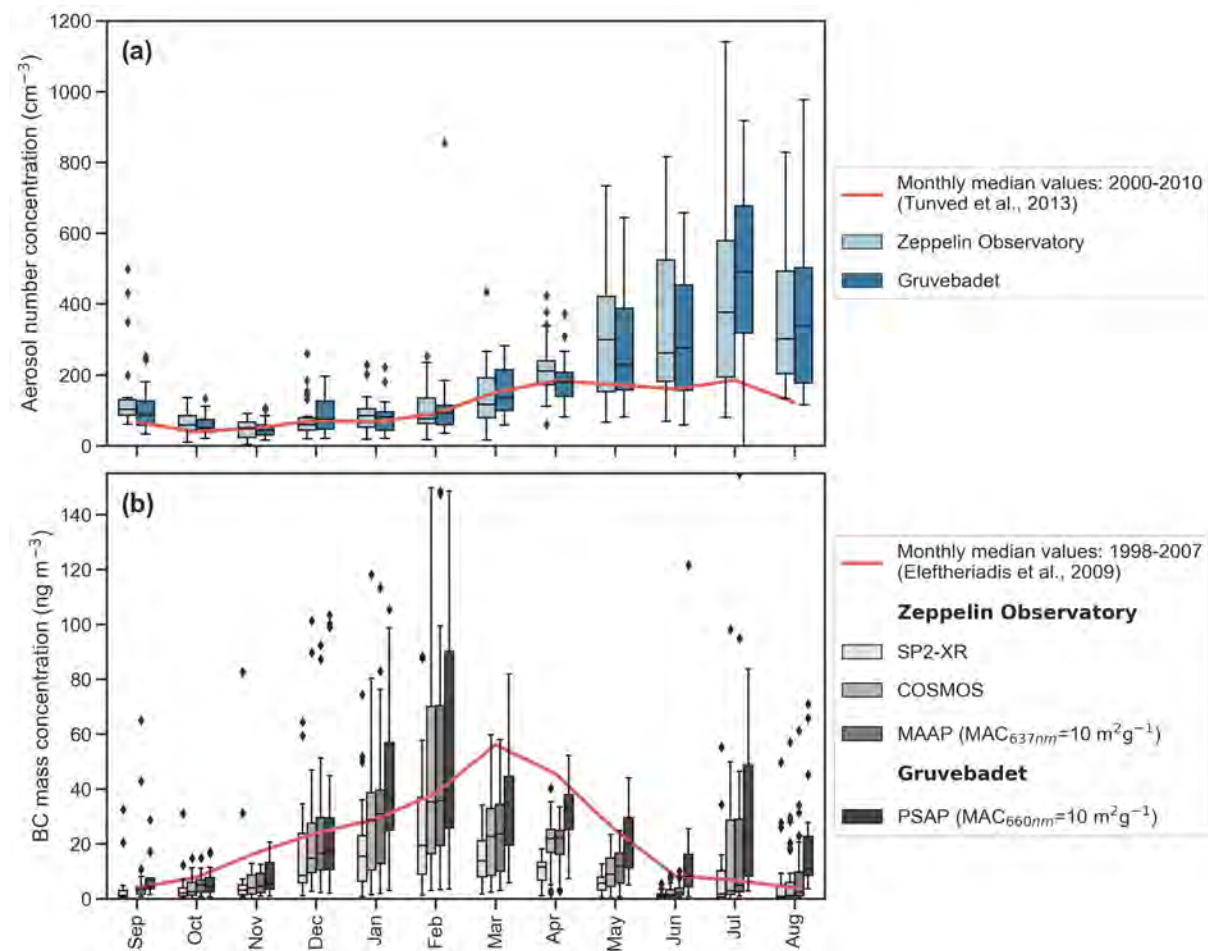


Figure 2.4: Monthly average distributions of (a) aerosol particle number and (b) black carbon (BC) mass concentrations measured during NASCENT at Gruebadet and at the Zeppelin Observatory in comparison to previous climatologies. The box-whisker plots show the quartiles and the 5th and 95th percentiles, respectively, while outliers are marked with diamonds. The particle number concentrations were measured using CPC's, while BC concentrations were measured by four different instruments: extended-range single-particle soot photometer (SP2-XR, Stephens et al., 2003; Schwarz et al., 2006), a multi-angle absorption photometer (MAAP, Petzold and Schönlinner, 2004), a continuous soot monitoring system (COSMOS, Kondo et al., 2011), and a Particle Soot Absorption Photometer (PSAP).

The BC concentrations were slightly higher in Gruebadet than at the Zeppelin Observatory, especially throughout 2020, which is most likely due to local emissions from the Ny-Ålesund settlement that impact the Gruebadet site but not necessarily the mountain-top site, especially during shallow boundary layers (Dekhtyareva et al., 2018; Platt et al., 2021).

As shown in Figure 2.4b, the BC levels measured during NASCENT were comparable to values reported previously at the Zeppelin Observatory (Eleftheriadis et al., 2009). For example, during the pristine summer and autumn, monthly-mean BC concentrations at the Zeppelin Observatory reached as low as a few  $\text{ng m}^{-3}$ , which are comparable to values measured over the remote southeast Pacific (Shank et al., 2012) and the Southern Ocean (Schmale et al., 2019).



### 2.3.4 Clouds

Clouds are frequently observed in the Arctic and Ny-Ålesund is no exception. During NASCENT, the monthly cloud cover assessed using the Cloudnet target classification product (Illingworth et al., 2007) ranged between 50% and 85%, out of which 30% to 70% were low-level clouds with a cloud top below 3 km (Fig. 2.2b). The low-level cloud occurrence peaked in March 2020 and was at a minimum in December 2019 and January 2020. Liquid-only clouds were primarily observed in the summer and early autumn months. Meanwhile, MPCs and ice clouds were present year round with ice clouds being the most abundant cloud type except for below 3 km where MPCs were dominant (Fig. 2.2b). These observations are in accordance with measurements of liquid droplets year-round at the Zeppelin Observatory (Koike et al., 2019). Previous studies investigating cloud cover in Ny-Ålesund have observed similar cloud occurrences albeit with slight differences in seasonality and cloud type contributions (Nomokonova et al., 2019; Gierens et al., 2020). Regardless of this year to year variability, MPCs are overall the most prevalent cloud type close to the surface at Ny-Ålesund. This highlights the importance of low-level MPCs year-round in the Arctic region and their potential to alter the Arctic climate.

## 2.4 First research highlights from the NASCENT study

First highlights are described in the following sections to demonstrate how the wide variety of observations contributes to the understanding of properties and interactions of Arctic aerosols and clouds. We use measurements mainly taken on 12 November 2019 to discuss the role of physical and chemical aerosol properties, cloud droplet activation, ice crystal nucleation, and SIP on the formation and evolution of a MPC, and finish with a comparison of the cloud structure representation in the WRF model with the in-situ cloud observations.

On 12 November 2019, a warm front influenced the weather around Ny-Ålesund (see section S1 and Fig. S2 in the SI). The temperature varied between  $-3^{\circ}\text{C}$  and  $0^{\circ}\text{C}$  at Ny-Ålesund and between  $-5^{\circ}\text{C}$  and  $-3.5^{\circ}\text{C}$  at the Zeppelin Observatory. A persistent MPC was observed until 2100 UTC, with cloud top rising from 1300 to 2000 m a.s.l and cloud top temperature varying between  $-13.5^{\circ}\text{C}$  and  $-11^{\circ}\text{C}$  (Fig. S3). The large-scale wind measured by the radiosondes (Fig. S8) and visible on the wind lidar measurements above 800 m a.s.l. (Fig. S3) was southwesterly.

### 2.4.1 Chemical and physical properties of aerosols, cloud residuals, and ice nucleating particles

On 12 November 2019, a cloud was present at Zeppelin Observatory with a cloud particle number concentration (CPNC) and liquid water content (LWC) up to  $17.5\text{ cm}^{-3}$  and  $0.3\text{ gm}^{-3}$ , respectively (Fig. A.5a). The visibility was on average 562 m and the Counterflow Virtual Impactor (CVI) inlet was in operation for most of the time (Fig. A.5b). The cloud residual number concentration was very low and, as expected, inversely proportional to the visibility, which acts as a measure for the optical density of the cloud. The cloud residual size distribution was dominated by small particles of around 10 to 30 nm (Fig. A.5c). These small particles were also present, although to a slightly lower extent, in the whole-air inlet, which samples both interstitial and cloud particles. It is also interesting that the accumulation mode particles (particles around 100 nm), as measured by the whole-air inlet, were found to a much lower extent within the cloud residuals and thus were probably not CCN and/or INPs. A possible explanation for this is that the WBF process has taken place and liquid droplets (activated accumulation mode particles) have evaporated in the presence of ice, which has been similarly observed in MPCs at other mountain sites (Verheggen et al., 2007).

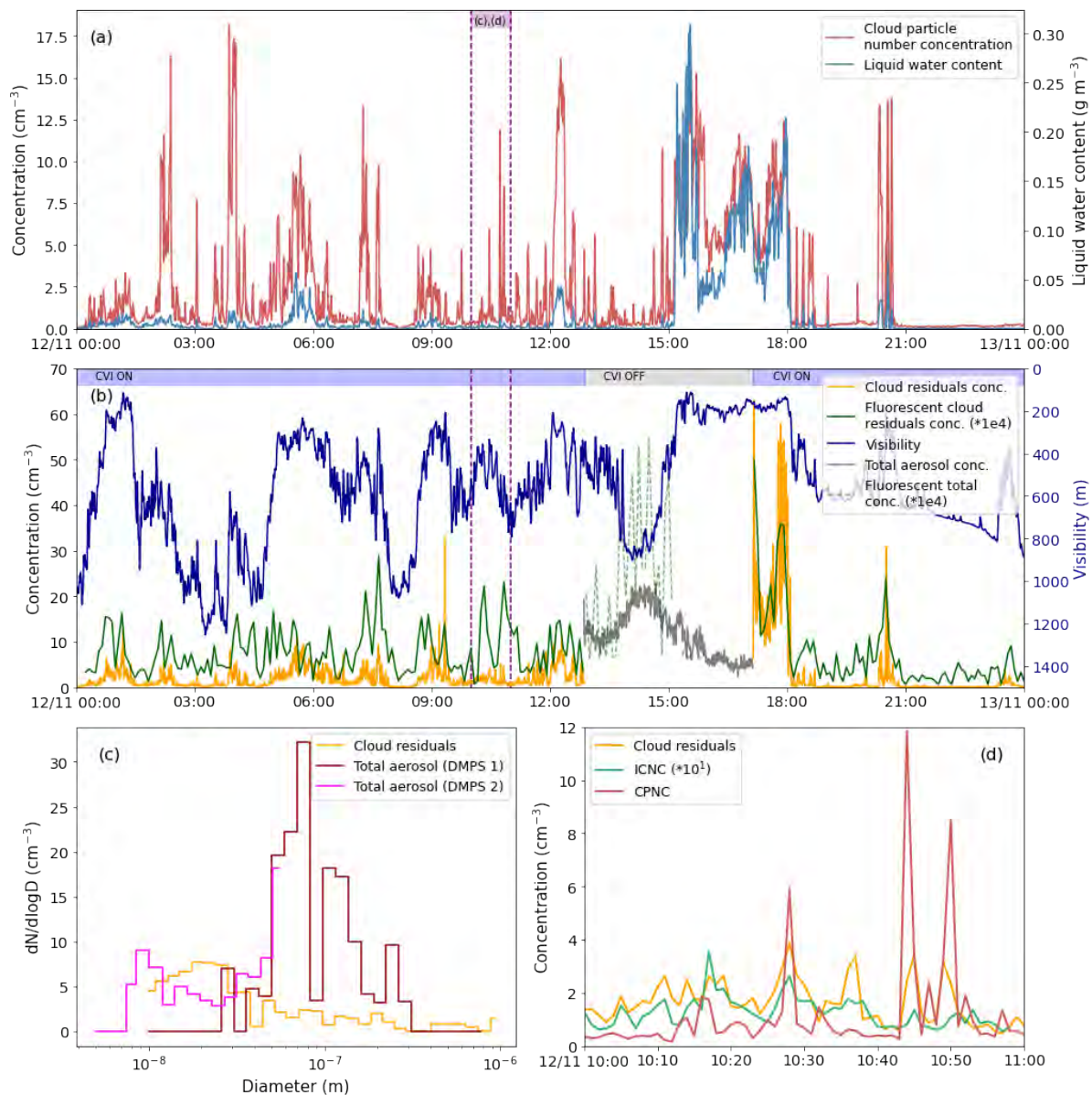


Figure 2.5: Cloud in-situ measurements on 12 November 2019 at Zeppelin Observatory. (a) Cloud particle number concentration and liquid water content measured by the fog monitor. The period selected for the lower panels (c) and (d) is indicated. (b) Cloud residual number concentration and ambient aerosol number concentration, together with the fluorescent particle concentration ( $\times 10^3$ ) within the cloud residuals/ambient aerosol number concentrations, and ambient visibility measured at the CVI inlet (note the reversed y-axis). The shading at the top of the figure indicates when the CVI was in operation/ON. (c) Particle number size distribution of the cloud residuals and whole-air aerosols (interstitial and activated aerosol) measured by a tandem-DMPS system. (d) Cloud residual number concentration measured by the CVI inlet, ambient ICNC ( $\times 10$ ) measured by HOLIMO3G, and CPNC measured by the fog monitor.

The origin of the enhanced number of small cloud residuals is not fully clear and a number of possibilities (e.g., SIP) and sampling artefacts are discussed in Karlsson et al. (2021). While previous studies (e.g., Karlsson et al., 2021) were missing detailed information on the cloud phase, the holographic imager HOLIMO3G (Beck et al., 2018) allows the determination of ICNC (between  $25 \mu\text{m}$  and  $2 \text{mm}$ ), and the fog monitor the determination of CPNC (between  $3 \mu\text{m}$  and  $50 \mu\text{m}$ ) in parallel to the CVI sampling during NASCENT. Even if the exact magnitude of

the CVI sampling efficiency still remains to be solved, a good temporal agreement of the ICNC and CPNC with the cloud residual number concentration (Fig. A.5d) indicates that sampling artefacts is an unlikely explanation for the small sizes of cloud residual and suggests that indeed SIP may cause such small cloud residuals. The cloud residual measurements observed during NASCENT, in combination with the high-resolution cloud probes, will provide new and unique evidence of the importance of sub-accumulation mode particles on cloud formation in the Arctic. Future work will shed further light into the importance of the WBF process and SIP throughout the seasons. In addition, the role of particle and gas phase chemistry and the role of biological particles in cloud formation is being investigated, as discussed shortly below.

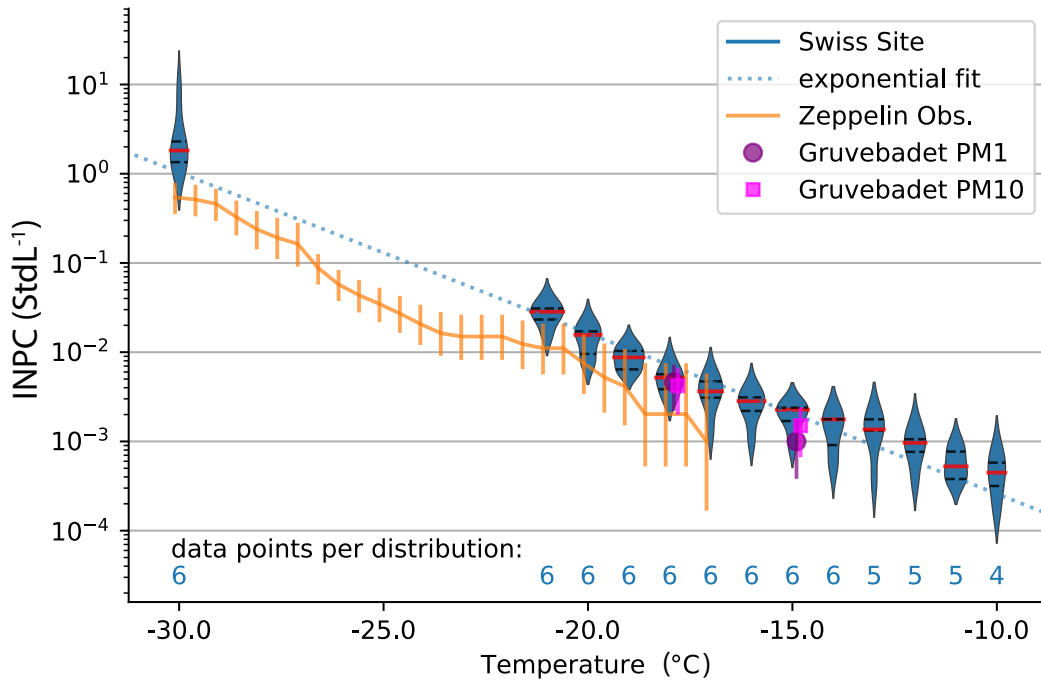


Figure 2.6: Overview of INPCs observed on 12 November 2019. Blue violin plots: six INP samples measured with DRINCZ between  $-10^{\circ}\text{C}$  and  $-21^{\circ}\text{C}$  and with HINC at  $-30^{\circ}\text{C}$  at the Swiss Site. The red lines indicate the median and the dashed black lines the 25th and 75th percentiles. The blue dashed line shows the corresponding exponential fit ( $INPC(T) = \exp(-0.4146 \cdot T - 12.4059)$ ) (cf. Li et al., 2022)). Purple and Magenta: one filter sample collected between 0900 - 1200 UTC at Gruvebadet analyzed by the DFPC on PM1 and PM10. Orange line: one filter sample collected from 10 - 16 November 2019 at the Zeppelin Observatory analyzed by CRAFT. The error bars represent the 95% confidence interval.

INP measurements were conducted at the Swiss Site with the Horizontal Ice Nucleating Chamber (HINC, Lacher et al., 2017) and the DRoplet Ice Nuclei Counter Zurich (DRINCZ, David et al., 2019a; Wieder et al., 2022b), at the Zeppelin Observatory with the Cryogenic Refrigerator Applied to Freezing Test (CRAFT, Tobo, 2016), and at Gruvebadet with the Dynamic Filter Processing Chamber (DFPC, Santachiara et al., 2010; Rinaldi et al., 2017). Despite the different techniques used, the INPCs as a function of temperature measured by the four methods agree within a factor of 5 (Fig. 2.6). This is substantial for a highly spatiotemporally varying quantity such as INPs, which occur at very low concentrations. The observed INPC ranged from  $\sim 2 \text{ StdL}^{-1}$  at  $-30^{\circ}\text{C}$  down to the lowest detectable concentration of  $\sim 10^{-4} \text{ StdL}^{-1}$  at  $-10^{\circ}\text{C}$ . While there is agreement between the INPCs measured in the overlap temperature range ( $-21^{\circ}$  to  $-15^{\circ}\text{C}$ ), on average the INPCs obtained with at the Zeppelin Observatory are slightly below those measured at Gruvebadet and at the Swiss Site (Fig. 2.6). This is likely because

the Zeppelin Observatory experiences less local influence from the the boundary layer and from the town of Ny-Ålesund (see Figure 2.7a). Moreover, the CRAFT measurements represent the INPCs averaged over three days, while at the Swiss Site INPCs were measured at higher frequency (10 min to 40 min averages). The use of two different filter cutoff sizes (PM1 and PM10) gives some information about the size of the INPs. At  $-18^{\circ}\text{C}$  ( $-15^{\circ}\text{C}$ ) the INPC retrieved from the PM10 filter were 10% (50%) higher than the one retrieved from the PM1 filter (squares and circles in Figure 2.6). This difference suggests that the observed INPs at  $-15^{\circ}\text{C}$  were larger than  $1\ \mu\text{m}$  and smaller than  $10\ \mu\text{m}$  whereas the observed INPs at  $-18^{\circ}\text{C}$  were smaller than  $1\ \mu\text{m}$ .

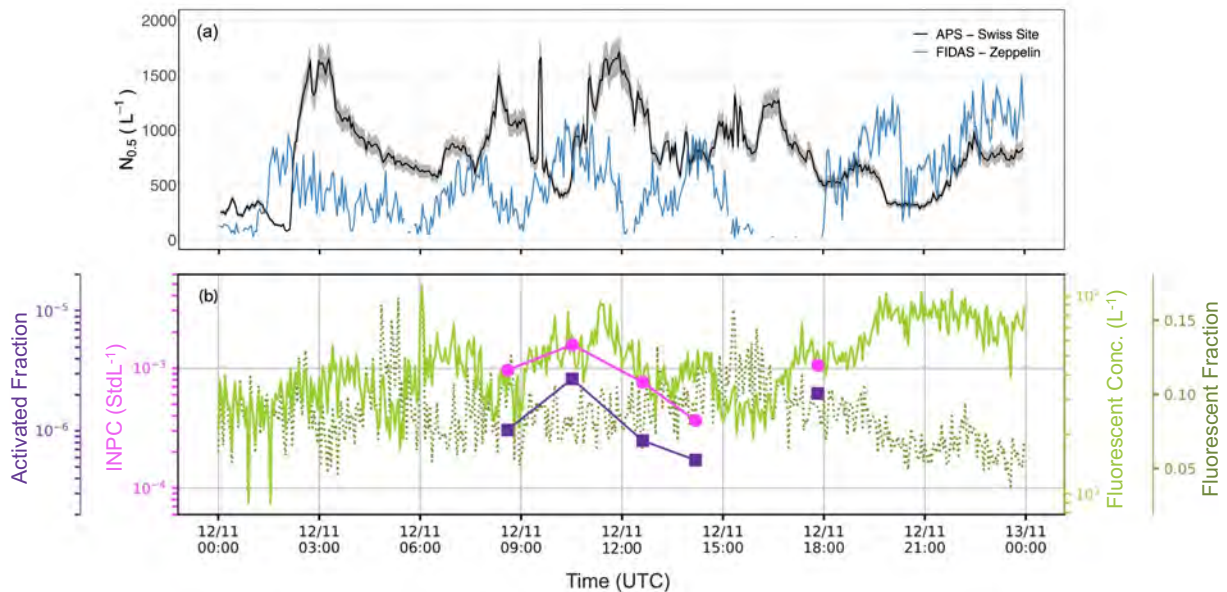


Figure 2.7: (a) Particle number concentration for sizes  $\geq 0.5\ \mu\text{m}$  measured by the APS (aerodynamic diameter) at the Swiss Site and by the FIDAS (optical diameter) at the Zeppelin Observatory, with a time resolution of 3 minutes for both instruments. (b) INPC and activated fraction ( $\text{INPC}/N_{0.5}$ ) at  $-12^{\circ}\text{C}$  (left axis), and fluorescent (particle) concentration and fluorescent (particle) fraction (right axis). We select a temperature of  $-12^{\circ}\text{C}$  to adequately evaluate the contribution from biological aerosol particles (Kanji et al., 2017, and references therein). The INPCs are measured by DRINCZ and the fluorescent particle concentration by an Wideband Integrated Bioaerosol Sensor (WIBS). The fractions are normalized to the particle fraction  $\geq 0.5\ \mu\text{m}$ .

For the most part of the day, higher aerosol concentrations  $\geq 0.5\ \mu\text{m}$  were measured at the Swiss Site than at the Zeppelin Observatory and an inverse trend is observed at the two sites (Fig. 2.7a). Only between 0300 and 0600 UTC and from 2000 UTC onward do the aerosol concentrations follow the same trend. Previous field measurements have suggested that biological particles are a key source of INPs in the Arctic (e.g., Bigg and Leck, 2001; Tobo et al., 2020; Hartmann et al., 2020). Therefore, the contribution of biological particles as INPs is investigated via the fluorescent aerosol concentration and fraction (Santander et al., 2021) at the Swiss Site. It is evident that the fluorescent aerosol fraction and concentration do not correlate (follow the same trend) and that the fluorescent particle concentration is highly variable in time (Fig. 2.7b). This implies that the fluorescent particles do not scale with aerosol concentrations  $\geq 0.5\ \mu\text{m}$ . In contrast, the INPC and activated fraction at  $-12^{\circ}\text{C}$ , follow the same trend as fluorescent aerosol concentration (Fig. 2.7b). This relationship suggests a correlation between the fluorescent particle concentrations and the observed INPC and INP activated fraction and therefore, provides additional evidence that biological particles could play an essential role in controlling cloud phase



in the Arctic.

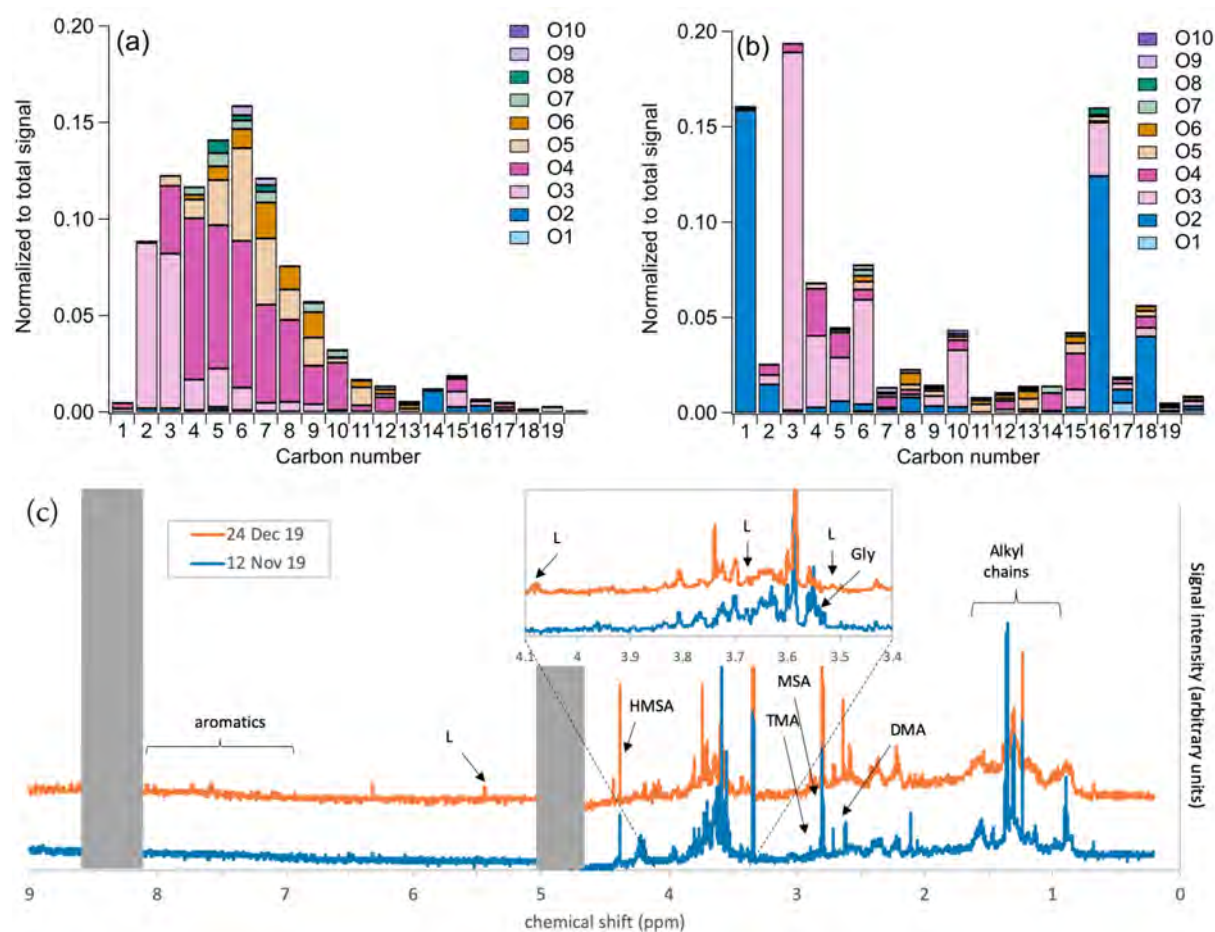


Figure 2.8: High-resolution chemical composition of (a) aerosol particles before a cloud event (whole-air inlet) and (b) of cloud residuals during the cloud measured by the FIGAERO-CIMS on 24 December 2019. Shown is the background-corrected absolute signal of individual molecules, separated by the number of carbon and oxygen atoms. (c) <sup>1</sup>H-NMR spectra of ambient PM1 samples collected at Gruebadet for 12 November and 24 December 2019. Specific resonances are assigned to levoglucosan (L), hydroxymethane-sulfonic acid (HMSA), methane-sulfonic acid (MSA), dimethylamine (DMA), trimethylamine (TMA) and glycerol (Gly). Unresolved mixtures of aromatic compounds and linear aliphatic chains, including possible contributions from lipids, are indicated in the spectra. The insert provides a focus on the aliphatic region of the spectra characteristic of polyols/saccharides compounds (H-C-O). Grey areas between 4.7 - 5.0 ppm and between 8 - 8.5 ppm cover the disturbance due to solvent and buffer solutions needed for the analysis.

To better understand aerosol and cloud particle nucleation in the Arctic, the FIGAERO-CIMS was used to analyze the chemical composition of aerosols, aerosol precursor gases, and cloud residuals at molecular level during NASCENT. On 12 November 2019 the instrument was set to only sample the gas phase. Therefore, to illustrate the capability of this analytical tool for aerosol phase, here we present an example from 24 December 2019, when a low-level MPC (cloud top below 2 km) was also observed with ground temperatures varying between -9° and -6°C. Figures 2.8a,b, show a comparison of the chemical composition of aerosol particles before a cloud event to aerosol particles that were activated as INPs or CCN (cloud residuals) measured during a cloud when the CVI inlet was in operation. The ~400 organic compounds identified in the particle phase by FIGAERO-CIMS are grouped based on the number of their carbon atoms and oxygen atoms, with the stacked signal of each category shown on the y-axis. To our

knowledge this is the first time that such a detailed chemical analysis is shown for Arctic cloud residuals. Numerous different molecules with up to 20 carbon atoms and 10 oxygen atoms were identified in both the total aerosol and cloud residuals. For the total aerosol, the majority of mass was contributed by compounds with 10 carbon atoms or less, and a prominent contribution of  $C_6H_{10}O_5$ , likely levoglucosan, a marker for biomass burning emissions, was observed. This can be an indicator of long range transport of pollution from wintertime solid fuel combustion on the Eurasian continent as a potential source for particle components observed here. The comparison with the cloud residual chemical composition shows a relative reduction in compounds with up to 10 carbon atoms, and more than 5 oxygen atoms for the cloud residuals. Furthermore, the cloud residuals show a relative increase of compounds with larger carbon chains and 2 oxygen atoms, potentially fatty acids, but analysis is still ongoing.

The H-NMR chemical characterization of organic aerosol in ambient PM1 filter samples at Gruebadet on 24 December 2019 shows results qualitatively comparable with those of the FIGAERO-CIMS at the Zeppelin Observatory. In particular, as highlighted in Figure 2.8c, H-NMR confirms the presence of levoglucosan associated with aromatic compounds (e.g., phenols and methoxy-phenols), further supporting the possible long-range transport of biomass burning emissions from the continents. This feature is common during the winter season (Zangrando et al., 2013; Feltracco et al., 2020). These samples are also impacted by high contributions of hydroxymethane-sulfonic acid (HMSA), a product of the atmospheric oxidation of formaldehyde and considered a tracer for anthropogenic emissions. There is no evidence for biomass burning influence in the 12 November sample, which instead has an NMR spectral fingerprint more typical of background clean and marine influenced environments, characterized by marine biogenic tracers like glycerol, methane-sulfonic acid (MSA), amines (DMA and TMA in particular) and alkylic chains, potentially attributable to lipids from marine biota. The presence of these possible fatty acid alkylic chains is evident also in the 24 December sample, as suggested also by FIGAERO-CIMS, but needs to be further investigated.

## 2.4.2 Cloud microphysical properties

Three flights into clouds were performed with HoloBalloon on 12 November 2019 (Fig. S3). Here we focus on the cloud microphysical measurements taken with HOLIMO3B on HoloBalloon and the cloud radar between 1445 and 1630 UTC (Fig. 2.9), together with the INP and CCN measurement to identify the processes responsible for ice crystal and cloud droplet formation.

During the entire flight, HOLIMO3B measured CDNCs between 5 and 15  $cm^{-3}$  and a mean diameter of  $\sim 30$   $\mu m$  (Fig. 2.9c). Drizzle drops with diameter larger than 56  $\mu m$  contributed to this large mean diameter (Fig. 2.9c,e). In comparison, continental clouds typically have higher CDNC (40-1000  $cm^{-3}$ ) and a smaller mean diameter (8  $\mu m$ ) (Lohmann et al., 2016b). Aerosol particles with dry diameters larger than 70 nm measured by an Scanning Mobility Particle Sizer (SMPS) at the Zeppelin Observatory were used as a proxy for the CCN concentration, following the method described by Koike et al. (2019). The estimated CCN concentration between 1000 and 1700 UTC was  $\sim 9$   $cm^{-3}$  (not shown) and was comparable to the CDNCs measured by HOLIMO3B. This indicates that the cloud droplet formation was limited by the CCN availability and is in accordance with previous studies showing that CDNC is sensitive to CCN concentration in aerosol-limited pristine regions (e.g., Reutter et al., 2009; Moore et al., 2013).

During the first part of the flight (1445-1545 UTC), rapidly varying mean Doppler velocities at the height of HoloBalloon were observed, even though the reflectivities remained less variable and HoloBalloon flew approximately at a constant height. This indicates a turbulent atmosphere, which is in accordance with the observed veering of the wind near the altitude of HoloBalloon (Fig. S3). This turbulence and updrafts have favored the formation of the drizzle drops observed by HOLIMO3G (Fig. 2.9c,e). During the second part of the flight (1545-1620 UTC), a fallstreak pattern is visible in the increased reflectivity measured by the cloud radar ( $\geq 10$  dBZ). As these two periods are quite distinct from each other, we refer in the following to the *turbulent period*

(1445-1545 UTC) and the *fallstreak period* (1545-1620 UTC).

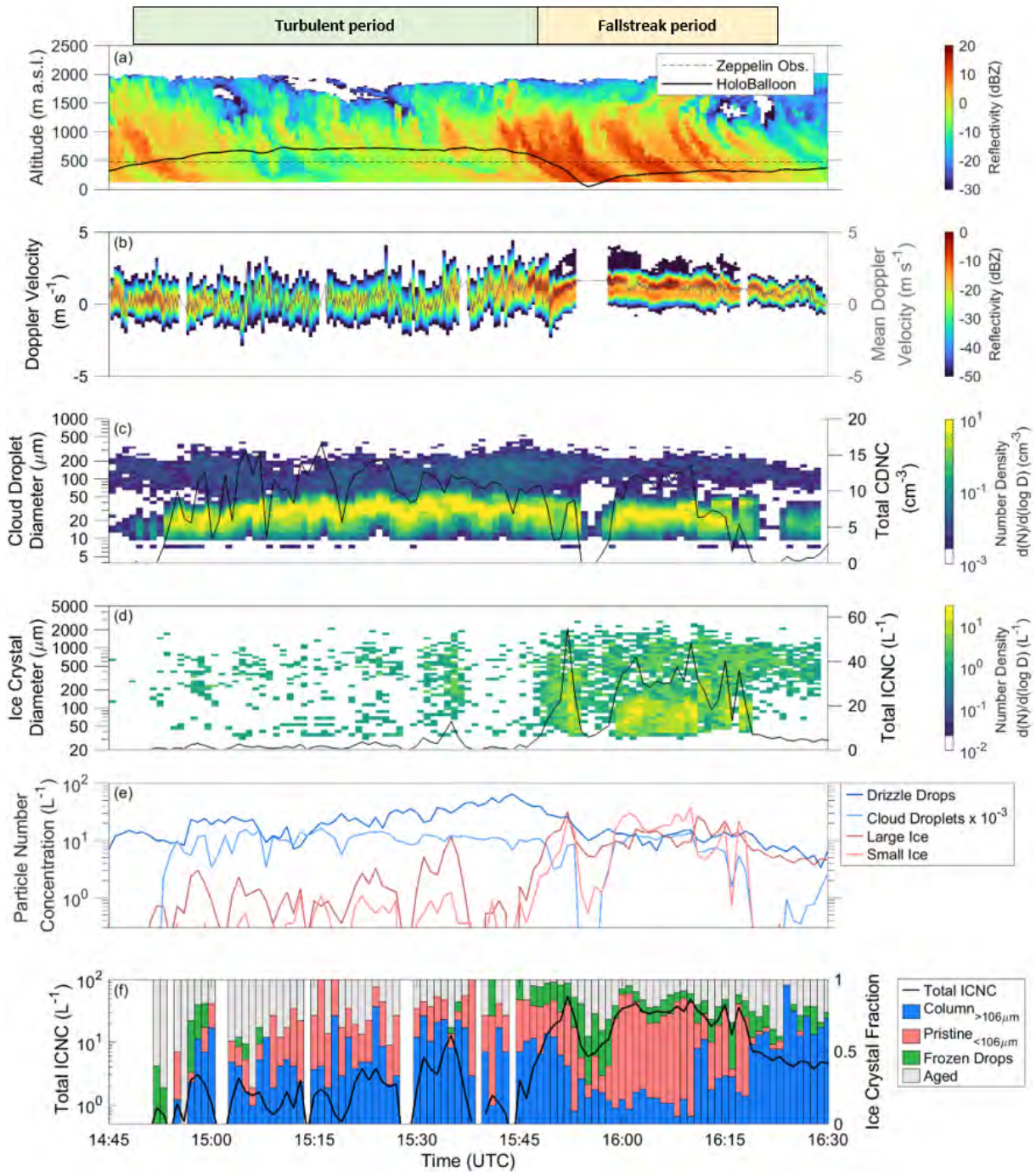


Figure 2.9: Overview of the cloud properties observed in-situ on HoloBalloon and by the cloud radar on 12 November 2019. (a) Cloud radar reflectivity, HoloBalloon path and Zeppelin altitude. (b) Doppler spectra and mean Doppler velocity at the height of the HoloBalloon path. Positive values represent a downward velocity. (c) Cloud droplet and (d) ice crystal size distributions (color) and total CDNC and ICNC (black line) measured by HOLIMO3B. (e) Cloud droplets, drizzle drops, and ICNC for crystals smaller and larger than 106  $\mu\text{m}$ . This cut-off size is defined by the bin size closest to 100  $\mu\text{m}$ . (f) Frequency of occurrence of the ice crystal habits and total ICNC. The data are averaged over 60 sec. Note that at around 1550 UTC, HoloBalloon flew out of the cloud, which explains the decrease in CDNC and ICNC measured by HOLIMO3B (c-f) and the missing reflectivity data at the HoloBalloon height (b).



We consider the fallstreak period in detail. HOLIMO3B measured an increase in total ICNC from below  $0.5 \text{ L}^{-1}$  up to  $55 \text{ L}^{-1}$  (Fig. 2.9d). Large ice crystals (diameters  $\geq 106 \mu\text{m}$ ) consisting of columns, frozen drops, and aged particles, as well as small pristine ice crystals (diameters  $\leq 106 \mu\text{m}$ ) contributed to this increase (Fig. 2.9e,f). Between 1600 - 1610 UTC, the concentration of small pristine ice crystals reached up to  $40 \text{ L}^{-1}$  and was greater than the concentration of larger ice crystals (Fig. 2.9e,f). Note that the influence from ice crystals from the ground (e.g. blowing snow) can be neglected as HoloBalloon flew up to  $\sim 700 \text{ m}$  above the surface. A representative set of (hand-labelled) pictures of ice crystals contributing to the total ICNC as shown in Figure 2.9f are displayed in Figure 2.10. Whereas the large ice crystals likely originated from higher portion of the clouds, the small pristine ice crystals must have formed close to the measurement location of HoloBalloon, as ice crystals grow rapidly in the water saturated environment. In the temperature regime of the HoloBalloon measurements (between  $-8^\circ$  and  $-1^\circ\text{C}$ ), the INPCs were below the instrument detection limit (no data in Fig. 2.6) and at cloud top temperatures ( $-13.5^\circ$  to  $-11^\circ\text{C}$ ), the INPCs were on the order of  $\sim 10^{-3} \text{ StdL}^{-1}$ . As such, primary ice nucleation due to INPs acting in the immersion mode alone can neither explain the concentration of larger ice crystals originating from close to cloud top, nor the concentration of small ice crystals formed close to the measurement location of HoloBalloon. Therefore, we deduce that SIP likely enhanced the formation of the ice crystals in higher parts of the cloud and that SIP close to the measurement location was responsible for the sudden increase in concentration of small pristine ice crystals observed.

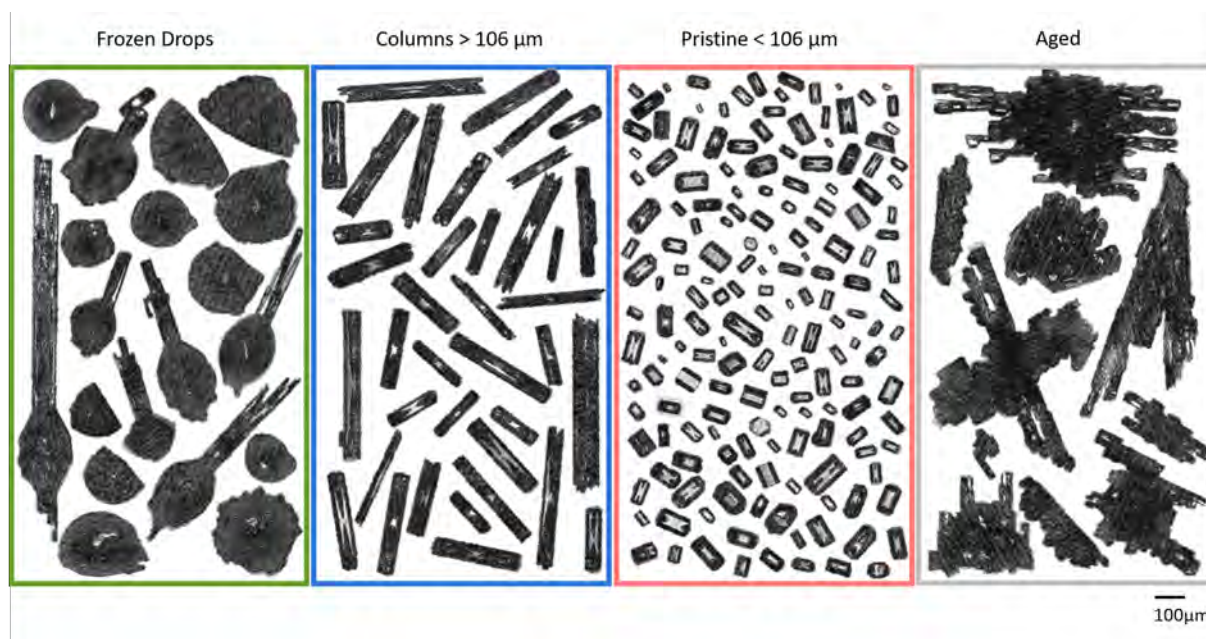


Figure 2.10: Examples of ice crystals classified as typical habits observed with HOLIMO3B. Plates and (hollow) columns with a diameter smaller than  $106 \mu\text{m}$  were classified as pristine, whereas larger columns were classified separately. Droplet 'lollipop', and drops showing evidence of freezing are classified as frozen drops. All the other ice crystals, including rimed and aggregated particles are classified as 'Aged'. The scale bar in the right panel is representative for all of the panels. The respective fractions of the typical ice crystals habits to the total ICNC are displayed in Figure 2.9f.

Our interpretation is that the primary ice was formed aloft where the cloud temperature was lower and thus more INPs were present. Then, SIP increased the ICNC near cloud top and the ice crystals grew until they were heavy enough to overcome the updrafts. As they fell, they continued to grow as column (Fig. 2.10), consistent with the ambient temperature experienced, until they reached the altitude of HoloBalloon, as indicated by the higher radar reflectivities



with decreasing altitude in the cloud (Fig. 2.9a). The columns then collided with drizzle drops, producing the observed 'ice lollipops' (Fig. 2.10) consisting of frozen drizzle drops and columns (Keppas et al., 2017). Such ice lollipops were also observed by HOLIMO3G and the Hawkeye Probe at the Zeppelin Observatory (Fig. S6). Upon collision and freezing, the drizzle drops likely created splinters through droplet shattering (e.g., Lauber et al., 2018; Korolev and Leisner, 2020). Laboratory experiments have shown that the number of ice splinters produced from a single drop freezing can reach up to 200 (Korolev and Leisner, 2020). The splinters produced during the freezing of the drizzle drops then grew to the small columns observed by HOLIMO3B. These small columns could in turn collide with drizzle drops, initiate their freezing, and the formation of additional ice splinters. We suggest that this can lead to a cascading SIP process explaining the rapid increase in concentrations of small ice crystals observed, similarly to the study by Lawson et al. (2015).

Our findings on SIP are in agreement with other studies. First, the occurrence of SIP with low INPC ( $10^{-4} \text{ L}^{-1}$  and  $0.01 \text{ L}^{-1}$ ) was already observed in a study by Lawson et al. (2015). Second, a difference of up to four orders of magnitude between the INPC and ICNC are consistent with previous observations (e.g., Ladino et al., 2017; Li et al., 2021; Wieder et al., 2022a). Finally, a recent study using remote sensing techniques showed that droplet shattering was a more efficient SIP process than the rime-splintering process at slightly supercooled temperature in Arctic MPCs (Luke et al., 2021).

Next we demonstrate how the combination of the cloud radar and in-situ measurements complement each other to evaluate the microphysical properties of the observed MPC. We start by allocating parts of the Doppler spectra signal to the different hydrometeor types using the Passive and Active Microwave radiative TRAnsfer tool (PAMTRA, Mech et al., 2020). PAMTRA simulated the cloud radar Doppler spectra based on the ice crystal and cloud droplet size distributions measured by HOLIMO3B (Fig. 2.11). The simulations were idealized, and the variety of ice crystal habits was described by only three categories (small ice, large ice, and frozen drops). More information about the PAMTRA settings is provided in the SI. Three representative time periods are compared (Fig. 2.11): (1) during the turbulent period (1525-1530 UTC) with cloud droplets, drizzle drops, and a low concentration of ice crystals, (2) during the fallstreak period (1600-1605 UTC) with frozen drops and a higher concentration of ice crystals, and (3) during the period afterwards (1625-1630 UTC) with low concentration of cloud droplets and drizzle drops.

In the PAMTRA simulations, large ice crystals were generally responsible for the higher reflectivities (up to 5 dBZ) with fall velocities between  $0\text{-}2.5 \text{ m s}^{-1}$  (Fig. 2.11e,f). This is due to the strong dependence of reflectivity on particle size (Doviak and Zrnić, 2006). Meanwhile, the measured frozen and drizzle drops were responsible for the simulated reflectivity at large fall velocities (up to  $3 \text{ m s}^{-1}$ ) (Fig. 2.11e) and for the lower reflectivity (up to -20 dBZ) with fall velocities up to  $2 \text{ m s}^{-1}$  (Fig. 2.11d-f), respectively. Finally, measured cloud droplets and smaller ice crystals (diameter  $\leq 100 \mu\text{m}$ ) were only responsible for reflectivities below -30 and -80 dBZ, respectively, and fall velocities around  $0 \text{ m s}^{-1}$ . Applying these results to the cloud radar measurements along the HoloBalloon path during the fallstreak period (Fig. 2.9b), we find that the higher reflectivities with Doppler velocities of around  $1 \text{ m s}^{-1}$  (Fig. 2.9b) were produced by large falling ice crystals, whereas observed reflectivities below -40 dBZ and fall velocities between  $2$  and  $4 \text{ m s}^{-1}$  were generated by frozen drops, as only these particles have such high fall velocities and low reflectivity (Fig. 2.9b). The reflectivity between -30 and -10 dBZ at Doppler velocities around  $0 \text{ m s}^{-1}$  indicates the presence of small ice crystals, and possibly cloud droplets when reflectivities are at the lower side (below -17 dBZ, (see e.g., Kogan et al., 2005)). Nevertheless, when looking at the PAMTRA simulations during the turbulent time periods, it can be difficult to distinguish the contributions of different hydrometeors to the Doppler spectra. Indeed, the reflectivity and fall velocity of drizzle drops and large ice crystals overlap and the drizzle drops are responsible for the highest reflectivities and fall velocities (Fig. 2.11d).

The information obtained by HOLIMO3B and the Doppler spectra can therefore be combined

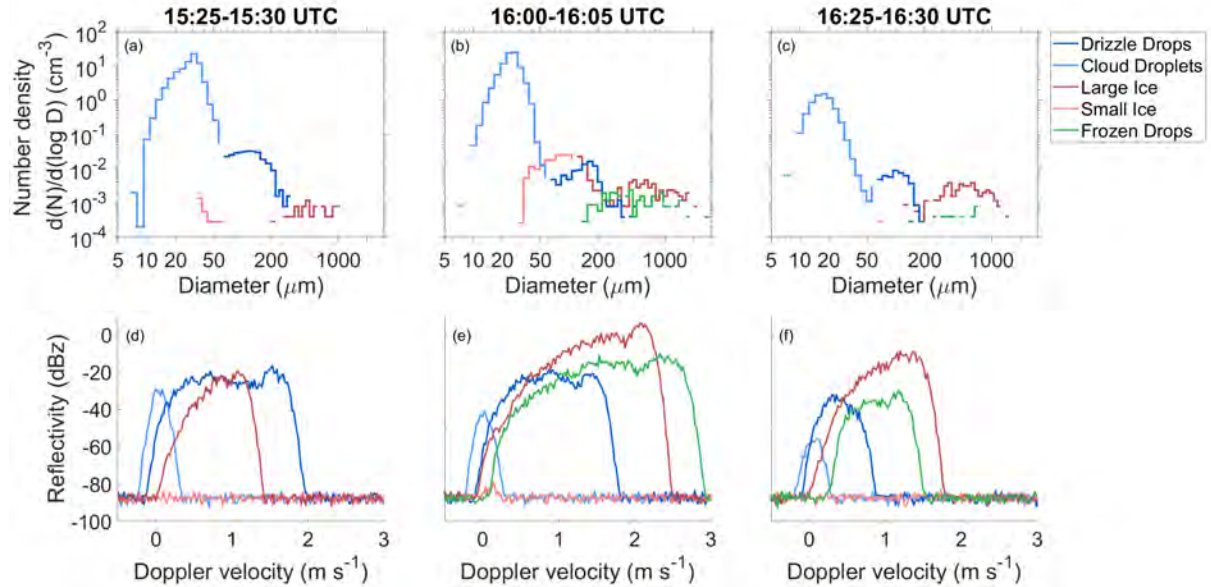


Figure 2.11: (a-c) Measured size distributions from HOLIMO3B. (d-f) Radar Doppler spectra simulated with the PAMTRA tool using the size distribution shown in a-c. The measured size distribution and simulated Doppler spectra are shown at three characteristic time periods of 5 minutes: 1525-1530 UTC (a & d), 1600-1605 UTC (b & e), and 1625-1630 UTC (c & f).

to get a better picture of the MPC. The cloud radar provides large-scale information about the entire cloud structure (including cloud top) and the presence of frozen drops and large ice crystals. HoloBalloon provides detailed information on the micrometer-scale cloud structure at one altitude in the cloud, is able to measure fluctuations in the concentration of cloud droplets and ice crystals (down to  $25 \mu\text{m}$ ), and allows the identification of ice crystal habits. The combination of both instruments is complementary and can help to better understand the microphysical processes in Arctic MPCs.

### 2.4.3 Model comparison

To understand how the representation of clouds can be ameliorated in weather and climate models, we compared the cloud properties simulated by the regional WRF model with the in-situ cloud measurements. To represent the microphysics we used the double moment scheme developed by Milbrandt and Yau (2005), which has six classes for cloud water, ice, rain, snow, graupel and hail. The CCN concentration was prescribed as  $9 \text{ cm}^{-3}$  using the observed mean CCN concentration and the INPC was prescribed based on the exponential fit of the INPC measurements on 12 November shown in Figure 2.6. The simulated meteorological conditions were validated against the radiosonde observations (Fig. S7). Further information about the model setup is given in the SI.

The data were averaged for each flight time period to compare the observed and simulated cloud properties. Additionally, to match the acquisition by HOLIMO3B, the simulated cloud droplets and drizzle/rain drops were merged into one category to obtain the total LWC and liquid droplet number concentration (LDNC). The same was done for simulated small cloud ice and larger precipitating ice crystals (snow, hail, graupel) to obtain total ice water content (IWC) and ICNC. The model correctly simulated an increase in the cloud top height from flight 1 to 3 as measured by the cloud radar (Fig. S9). Also, the cloud base height derived from the simulated hydrometeor populations is following the development indicated by ceilometer measurements (Fig. S9). Hereafter we focus on flight 3 when HOLIMO3B observed substantial SIP to assess how well the model reproduces ice production in Arctic MPCs (Fig. 2.12). Generally, the simulation is

in agreement with the observations as the LDNC and LWC are consistent with the maximum values measured by HOLIMO3B between 600 and 750 m a.s.l., albeit at altitudes between 1000 and 1500 m a.s.l.. Below the simulated cloud base ( $\sim 600$  m a.s.l.), the simulation underestimates the LDNC and LWC. This may be the reason for the sharper decrease in the simulated ICNC and IWC than in the observed ones below 300 m a.s.l.. Regardless, the simulation reproduces the maximum concentrations of ICNC and IWC observed by HOLIMO3B during flight 3, but the principle constituent of the simulated ICNC and IWC is graupel, which was not observed by HOLIMO3B (see Figs. 2.9f and 2.10). The ability for the simulation to reproduce the observed ICNC is surprising considering that the prescribed INPC at cloud top ( $\sim 10^{-3}$  L $^{-1}$ ) is approximately four orders of magnitude lower than the observed and simulated ICNC. The Milbrandt and Yau scheme (Milbrandt and Yau, 2005) includes SIP via the Hallett-Mossop (HM) process, which could potentially improve the models ability to accurately predict the ICNC, especially as a significant fraction of the cloud falls within the temperature range relevant for the HM process (Fig. 2.12c,d). To determine if the HM process is responsible for the realistic ICNC simulated, we conducted the simulation again without the HM process activated. The ICNC decreases above  $\sim 800$  m when the HM process is deactivated (Fig. 2.12). However, below this height, the model still simulates ICNCs that exceed the maximum ICNC when the HM process is active. This indicates that the microphysics scheme is producing ice independently of HM being active in the simulations. This may partly be due to the Milbrandt and Yau scheme lacking a sink term for INPC, which has been recommended to prevent models from nucleating ice continuously (Kärcher and Marcolli, 2021). Regardless, the production of graupel by the model when none was actually observed, indicates that the simulations fail to accurately represent the formation and evolution of ice in Arctic MPCs.

To conclude, the simulation is able to qualitatively represent the structure of the cloud, including the cloud top and base heights when the correct CCN and INP concentrations are prescribed. It also represents the realistic ICNC during flight 3 but for the wrong reasons. This indicates that the Milbrandt and Yau scheme has inconsistencies in the formation of ice hydrometeors and in particular, graupel, in the presence of very low CCN and INP concentrations representative of the Arctic. Future work will utilize the in-situ aerosol and cloud microphysical measurements as well as the remote sensing observations to address this inconsistency and develop and validate parametrizations for the SIP observed.

## 2.5 Summary and Future Work

The Ny-Ålesund Aerosol and Cloud Experiment (NASCENT) was initiated to improve our understanding on how aerosols, clouds, and their interactions influence the Arctic climate. A comprehensive set of cloud, aerosol, and meteorological observations was obtained over the course of one year, which included detailed in-situ and remote sensing techniques on ground-based and airborne platforms. Regarding the atmospheric seasonality, the mean temperature between December 2019 and April 2020 was substantially colder than the climatology (up to 6°C) due to a strong polar vortex, whereas the summer 2020 was slightly warmer than usual. The wind speed and direction was strongly influenced by the surrounding topography as found in previous studies. Aerosol particles, such as BC particles, followed the typical aerosol mass cycle found on Svalbard, with maximum concentrations during winter and spring. MPCs were the most abundant low cloud type during NASCENT. This high frequency highlights their importance for the Arctic climate.

We present first highlights from NASCENT by showing a detailed case study and discuss how in-situ observations of aerosols and clouds, together with remote sensing instrumentation and modelling can be combined to better understand the aerosol and cloud microphysical processes related to Arctic MPCs. The cloud residuals measured by the CVI inlet were in good temporal agreement with measurements taken by two cloud probes at the Zeppelin Observatory. The

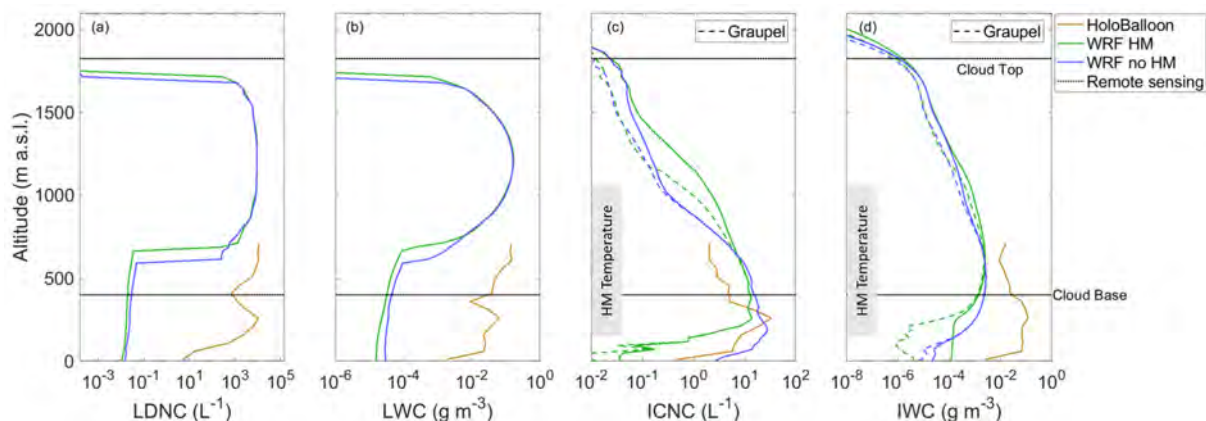


Figure 2.12: The averaged vertical profiles during flight 3 on 12 November 2019 observed by HOLONIMO3B and simulated by WRF. (a) LDNC, (b) LWC, (c) ICNC & (d) IWC. The contribution of graupel to the ICNC and IWC are shown with the colored dashed profile line in (c) and (d). The data from HOLONIMO3B are averaged over 50 m altitude bins and the WRF data over every model layer. The average cloud base and cloud top measured by the remote sensing instrumentation (ceilometer and cloud radar, respectively) are represented by the black dotted horizontal lines and the HM temperature range ( $-8^{\circ}$  to  $-3^{\circ}\text{C}$ ) is highlighted in (c) and (d).

measurements also revealed clear differences in molecular composition between ambient aerosol particles and those particles that were involved in cloud formation and evidences were found that biological particles acted as INP at warm temperatures. In future work, our dataset will be used to further examine the composition and physical properties of cloud residuals and ambient aerosols and their role and fate during cloud formation. Furthermore, a parametrization for estimating the INPC in the Arctic is being developed (Li et al., 2022).

Using aerosol in-situ measurements and vertical cloud profiling with the tethered balloon system HoloBalloon, we found that the cloud droplet formation was limited by the available CCN concentration. Regarding the cold cloud processes, we showed that INPC could not explain the measured ICNC. Instead, frozen drops, followed by an increase in small pristine ice crystals were observed and provide evidences for the occurrence of SIP via droplet shattering. Further measurements of the HoloBalloon system are being analyzed together with remote sensing observations to constrain the required conditions for different SIP processes in Arctic MPCs.

First modeling results with the WRF model have shown that the model is able to simulate the cloud structure and simulates a representative ICNC probably for the wrong reasons. In future work, more SIP parametrizations will be tested and compared to the measurements with HoloBalloon to ameliorate the representation of clouds in weather and climate models and to understand how they influence the radiative fluxes in the Arctic climate.

The NASCENT study has acquired a unique and holistic set of observations that will contribute to improve our understanding of aerosol and cloud processes in the Arctic. Together with further in-depth analysis and modelling studies, this work will help to clarify their role in the observed Arctic Amplification and the Arctic climate system in general.

## Acknowledgment

This project has received funding from the European Union’s Horizon 2020 research and innovation programme under grant agreement No 821205 (FORCeS), from the Swiss Polar Institute (Exploratory Grants 2018), and from the Swiss National Science Foundation (SNSF) (grant no. 200021\_175824). We gratefully acknowledge the funding by the European Research Council (ERC) (grant no. StG 758005) and the Deutsche Forschungsgemeinschaft (DFG, German Research Foundation) – Project-ID 268020496 – TRR 172, within the Transregional Collaborative Research Center “ArctiC Amplification: Climate Relevant Atmospheric and SurfaCe Processes, and Feedback Mechanisms (AC)<sup>3</sup>”. We are thankful for funding support from Knut and Alice Wallenberg (KAW) foundation financed projects Arctic Climate Across Scales (ACAS, project no. 2016.0024) and WAF project CLOUDFORM, grant no. 2017.0165, Swedish environmental protection agency (Naturvårdsverket), the Swedish Research Council (Vetenskapsrådet starting grant, project no. 2018-05045) and FORMAS agency funded project "Interplay between water vapor, clouds and aerosols in the Arctic". This project was supported by the Environment Research and Technology Development Fund (JPMEERF20202003) of the Environmental Restoration and Conservation Agency of Japan, and the Ministry of Education, Culture, Sports, Science, and Technology (MEXT) in Japan (ArCS II Project, JPMXD1420318865) and JSPS KAKENHI (grant numbers JP18H03745, JP18KK0292, JP19K14802, JP19H01972). This project was supported by the Korea Polar Research Institute (PE21010). We gratefully acknowledge funding from an access grant provided by the Research Council of Norway, project number 291644, Svalbard Integrated Arctic Earth Observing System – Knowledge Centre, operational phase. We thank Rafael Tazima (Brazil) for helping in designing our NASCENT logo of a polar bear studying the “nascency” of an Arctic cloud droplet. We thank Davide Ori for his precious help regarding the PAMTRA simulations. We owe great thanks to all technicians and helpers involved in the field work associated with NASCENT, particularly the AWIPEV and Norwegian Polar Institute Sverdrup stations staff. Finally, we thank two anonymous reviewers for their constructive and helpful feedback on the manuscript, which strengthened the paper.

## Data availability

The data and meta-data of NASCENT campaign will be available on the Bolin Centre Data base (<https://bolin.su.se/data/>) using the keyword “NASCENT”. Data from AWIPEV is available in PANGAEA ([www.pangaea.de](http://www.pangaea.de)). The Cloudnet dataset is available in the Cloudnet data portal (<https://cloudnet.fmi.fi/>).

Table 2.1: Retrieved variables at the five measurement locations. The black crosses show long-term measurements and the measurements performed only during NASCENT are represented with the symbol 'N'. Parameters that were in addition measured behind the ground-based Counterflow Virtual Impactor (CVI) inlet are marked by an asterisk (\*).

	<i>Measured quantities</i>	<i>Zeppelin Obs.</i>	<i>HoloBalloon</i>	<i>Swiss Site</i>	<i>Gruvebadet</i>	<i>CCT</i>	<i>AWIPEV</i>
Meteorology	Wind vector	N	N	N		X	X
	Temperature	X	N	N	X	X	X
	RH	X		N	X	X	X
	Precipitation		N	N	X	X	X
	Vertical profiles of T, p, RH						X
	Vertical profiles wind vector					X	X
	Cloud	Phase-resolved particle number size distribution	N	N			
	IWC	N	N				X
	LWC or LWP	N	N				X
	Ice crystal habits	N	N				
	Base & top height		N				X
	Radar reflectivity factor						X
Aerosol	Particle size distribution	X*		N	X		
	CCN properties	X*		N			
	INP concentration	X		N	X		
	Chemical composition	X/N*			N		
	Total particle concentration	X*			N		
	Particle size, shape, fluorescence	N*		N			
	Black carbon Single-particle analysis	X/N* X*				X	
Radiation	Broadband shortwave & longwave	X	N			X	X

## Chapter 3

# Conditions favorable for secondary ice production in Arctic mixed-phase clouds

J. T. Pasquier (1), J. Henneberger (1), F. Ramelli (1), A. Lauber (1), R. O. David (2), J. Wieder (1), T. Carlsen (2), R. Gierens (3), Marion Maturilli (4), and U. Lohmann (1)

(1) Department of Environmental System Sciences, Institute for Atmospheric and Climate Science, ETH Zurich, Zurich, Switzerland

(2) Department of Geosciences, University of Oslo, Norway

(3) Institute for Geophysics and Meteorology, University of Cologne, Cologne, Germany

(4) Alfred Wegener Institute, Helmholtz Centre for Polar and Marine Research (AWI), Potsdam, Germany

*This work is currently in review in Atmospheric Chemistry and Physics.*

DOI: <https://doi.org/10.5194/acp-2022-314>

---

### Abstract

The Arctic is very susceptible to climate change and thus warming much faster than the rest of the world. Clouds influence terrestrial and solar radiative fluxes, and thereby impact the amplified Arctic warming. The partitioning of thermodynamic phases (i.e. ice crystals and water droplets) within mixed-phase clouds (MPCs) especially influences their radiative properties. However, the processes responsible for ice crystal formation remain only partially characterized. In particular, so-called secondary ice production (SIP) processes, which create supplementary ice crystals from primary ice crystals and the environmental conditions that they occur in, are poorly understood. The microphysical properties of Arctic MPCs were measured during the Ny-Ålesund AeroSol Cloud Experiment (NASCENT) campaign to obtain a better understanding of the atmospheric conditions favorable for the occurrence of SIP processes. To this aim, the in-situ cloud microphysical properties retrieved by a holographic cloud imager mounted on a tethered balloon system were complemented by ground-based remote sensing and ice nucleating particle measurements. During six days investigated in this study, SIP occurred during 40% of the in-cloud measurements and high SIP events with number concentrations larger than  $10 \text{ L}^{-1}$  of small pristine ice crystals in 3.5% of the in-cloud measurements. This demonstrates the role of SIP for Arctic MPCs. The highest concentrations of small pristine ice crystals were produced at temperatures between  $-3 \text{ }^{\circ}\text{C}$  and  $-5 \text{ }^{\circ}\text{C}$  and were related to the occurrence of drizzle drops freezing

upon collision with ice crystals. This suggests that a large fraction of ice crystals in Arctic MPCs is produced via the droplet shattering mechanism. From evaluating the ice crystal images, we could identify ice-ice collision as a second SIP mechanism that dominated when fragile ice crystals were observed. Moreover, SIP occurred over a large temperature range and was observed in up to 95% of the measurements down to  $-24\text{ }^{\circ}\text{C}$  due to the occurrence of ice-ice collisions. This emphasizes the importance of SIP at temperatures below  $-8\text{ }^{\circ}\text{C}$ , which are currently not accounted for in most numerical weather models.

## Introduction

Clouds influence the radiation budget in two competing ways. On the one hand, they scatter shortwave radiation back to space and thereby cool the surface. On the other hand, they absorb and re-emit longwave radiation and thereby warm the surface. The Arctic is experiencing an amplified warming (Meredith et al., 2019), which is influenced by several feedback processes associated with temperature, water vapour, and clouds (Goosse et al., 2018). The influence of clouds on the radiation budget in the Arctic is especially complex and uncertain in because of the strongly varying reflection from the surface below (sea ice or water) or the lack of solar radiation during polar night (e.g., Goosse et al., 2018). In addition, the phase partitioning and concentration of the cloud particles determine the exact radiative properties of the mixed-phase clouds (MPCs) consisting of water vapor, cloud droplets, and ice crystals (Sun and Shine, 1994). Because the cloud particle concentration and phase partitioning strongly influence the radiative properties of MPCs, a thorough understanding of the processes that determine the formation and transformation of cloud particles is required.

At temperatures below  $-38\text{ }^{\circ}\text{C}$ , cloud droplets freeze homogeneously, whereas at temperatures between  $-38\text{ }^{\circ}\text{C}$  and  $0\text{ }^{\circ}\text{C}$ , primary ice crystals form on ice nucleating particles (INPs). However, many observations have shown that the ice crystal number concentration (ICNC) in MPCs is frequently several orders of magnitude higher than the measured INP concentration (INPC) (e.g., Hobbs and Rangno, 1985, 1998; Ladino et al., 2017; Korolev et al., 2020). This discrepancy can be explained by additional ice crystals falling from a seeder cloud aloft (Proske et al., 2021), by the influence of surface processes such as blowing snow (e.g. Beck et al., 2018), or by the formation of secondary ice crystals from the existing ice crystals (e.g., Hallett and Mossop, 1974; Takahashi et al., 1995; Field et al., 2017; Korolev and Leisner, 2020). This last process, known as secondary ice production (SIP), is thought to play a critical role in the formation of ice crystals in supercooled clouds (e.g., Korolev et al., 2020; Korolev and Leisner, 2020).

Several SIP mechanisms have been proposed over the past decades: droplet shattering during freezing, rime-splintering during riming, fragmentation during ice-ice collision, and fragmentation during sublimation (e.g. Field et al., 2017; Korolev and Leisner, 2020). Droplet shattering is defined as the ejection of secondary ice crystals caused by cracking, fragmentation, bubble bursting or jetting, which can occur due to pressure build-up during freezing of droplets (e.g., Mason and Maybank, 1960; Takahashi and Yamashita, 1970; Lauber et al., 2018; Keinert et al., 2020). The rime-splintering or Hallett-Mossop process (Hallett and Mossop, 1974; Mossop, 1978) refers to the production of secondary ice during riming and is expected to occur when cloud droplets freeze upon collision with large rimed ice particles (e.g., Mossop, 1978, 1985; Field et al., 2017; Korolev and Leisner, 2020). Fragmentation during collision of several ice particles can lead to their fragmentation, which creates secondary ice crystals (Vardiman, 1978; Takahashi et al., 1995). Finally, fragmentation during ice crystal sublimation in unsaturated regions can create secondary ice crystals, but it requires the re-entering of the fragments back into saturated cloud regions, otherwise the complete sublimation of the fragment is likely (Dong et al., 1994; Bacon et al., 1998).

The environmental conditions favorable for SIP were mostly assessed in laboratory studies (see Korolev and Leisner, 2020, for an overview of laboratory studies on SIP). Temperature,



cloud droplet concentrations and sizes, and ice crystal sizes and habits are particularly relevant for the occurrence of SIP (e.g., Korolev and Leisner, 2020). The temperature range between  $-3\text{ }^{\circ}\text{C}$  and  $-8\text{ }^{\circ}\text{C}$  was suggested to be the most favorable for the occurrence of rime-splintering (Hallett and Mossop, 1974; Mossop and Hallett, 1974), whereas the maximum rate of fragments produced by droplet shattering or by ice-ice collision was observed at around  $-15\text{ }^{\circ}\text{C}$  in laboratory studies (Takahashi and Yamashita, 1970; Takahashi et al., 1995; Lauber et al., 2018). However, evidence for droplet shattering has been observed over a much wider temperature range, from  $-20\text{ }^{\circ}\text{C}$  up to  $-0.5\text{ }^{\circ}\text{C}$  during field observations of natural MPCs (Korolev et al., 2020; Lauber et al., 2021; Pasquier et al., 2021) and in laboratory experiments (Keinert et al., 2020). Cloud droplets are needed for the rime-splintering and the droplet shattering processes. Although droplets smaller than  $12\text{ }\mu\text{m}$  and larger than  $24\text{ }\mu\text{m}$  are necessary for the rime-splintering process (e.g., Mossop, 1978, 1985; Korolev and Leisner, 2020), the probability for droplet shattering occurrence increases with increasing droplet size (Lauber et al., 2018; Keinert et al., 2020). The size and concentration of the droplets is in turn influenced by aerosol particles acting as cloud condensation nuclei (CCN), by updrafts, by the general cloud dynamics, and by the cloud lifetime (Lohmann et al., 2016b). The ice crystal number concentrations and the ice crystal shapes and sizes are also relevant for SIP. In particular, large rimed ice crystals were found to increase the rate of splinters ejected during rime-splintering (Hallett and Mossop, 1974) and ice-ice collision (Vardiman, 1978).

However, there are large inconsistencies and many gaps in current knowledge of the physical mechanisms and environmental conditions favourable for SIP due to the scarcity of laboratory and field measurements (Korolev and Leisner, 2020). In addition, direct measurements of SIP processes in-cloud are challenging as the secondary fragments and splinters of a few micrometers or less are typically below the resolution limit of cloud measurement probes and the probability of observing a cloud particle when it is involved in SIP is infinitesimally small. Furthermore, the presence of an INP in ice particles can only be determined on a crystal by crystal basis, which requires that each ice crystal is sampled and analyzed individually for the presence of an INP (Hoffer and Braham, 1962; Mertes et al., 2007; Worringen et al., 2015; Mignani et al., 2019). However, when the concentration of small ice crystals exceeds that of ambient INPs, SIP processes must have contributed to the ICNC. As such, several studies compare INPC with total ICNC to infer the occurrence of SIP (e.g., Ladino et al., 2017; Li et al., 2021; Wieder et al., 2022a). The cloud microphysical properties can additionally be used to identify the mechanism potentially responsible for SIP. For example, rimed particles together with a sufficient concentration of cloud droplets (with diameter below  $12\text{ }\mu\text{m}$  and above  $24\text{ }\mu\text{m}$ ) at temperatures between  $-8\text{ }^{\circ}\text{C}$  and  $-3\text{ }^{\circ}\text{C}$  are an indicator for the occurrence of the rime-splintering process (e.g., Lloyd et al., 2015). Meanwhile, drizzle drops and/or frozen drops can be indicators for the occurrence of droplet shattering (e.g., Lawson et al., 2017), and large rimed particles or broken ice crystals at relatively low temperatures may be indicators for ice-ice collisions.

Even if SIP parametrisations were used on case studies for the ice-ice collision and droplet shattering mechanisms (e.g., Sotiropoulou et al., 2020; Dedekind et al., 2021; Georgakaki et al., 2022), only the rime-splintering process is widely used in numerical weather and climate models. However, an accurate description of SIP processes and of the environmental conditions favorable for SIP is needed to correctly represent the phase partitioning within MPCs to estimate their radiative properties in the Arctic (Young et al., 2019).

The present study aims to identify conditions favorable for SIP in low-level Arctic MPCs using a holographic imager mounted on the tethered balloon system HoloBalloon (Ramelli et al., 2020), together with ground-based INP and remote sensing measurements. The results presented originate from six days of measurement in MPCs collected during the Ny-Ålesund AeroSol Cloud Experiment (NASCENT) campaign (Pasquier et al., 2021) in Ny-Ålesund, Svalbard. First, the main instrumentation and the methodology applied for SIP identification are described in Section 3.1. Second, we present the meteorology and the occurrence of SIP during six measurement days

in Section 3.2. Then, the environmental conditions associated with the SIP occurrence are then examined in Section 3.3. Lastly, the final remarks and recommendations for future work are given in Section 3.3.2.

## 3.1 Methods

### 3.1.1 Measurement location

The data presented in this paper was collected during the NASCENT campaign, which took place in Ny-Ålesund, Svalbard, (78.9° N, 11.9° E, Fig. 3.1a) from September 2019 to August 2020 with the goal to enhance the existing knowledge about aerosols and clouds in the Arctic climate, and their interactions throughout the year. A description of the campaign and the main instrumentation is given in Pasquier et al. (2021). Ny-Ålesund is situated on the south side of Kongsfjorden and on the northern side of a mountain range, with Mt. Zeppelin as the closest mountain 2.5 km southeastward of the settlement (Fig. 3.1b). The surface wind is strongly influenced by the topography (Fig. 3.1b) and is typically channelled along Kongsfjorden (Beine et al., 2001; Maturilli et al., 2013; Maturilli and Kayser, 2017; Pasquier et al., 2021).

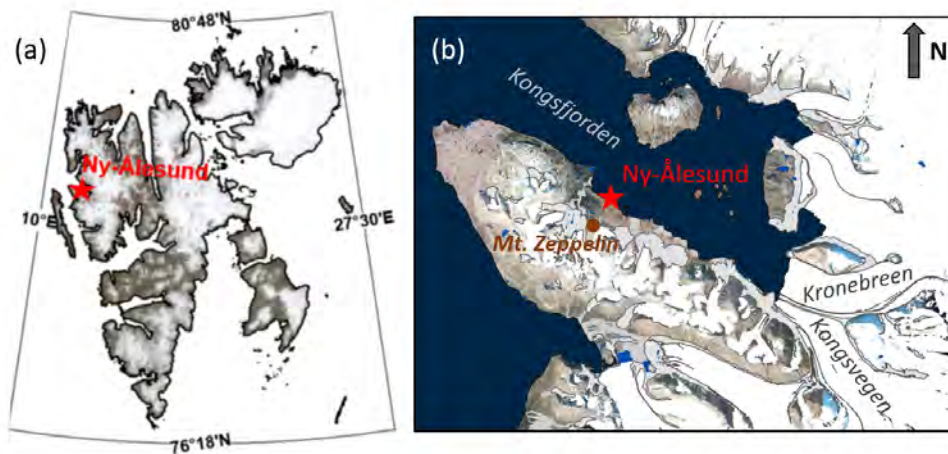


Figure 3.1: (a) Map of Svalbard with the location of Ny-Ålesund marked with the red star. (b) Map of the peninsula close to Ny-Ålesund. Ny-Ålesund, the Kronebreen and Kongsvegen glaciers, the fjord Kongsfjorden, and the Mt. Zeppelin mountain are labelled. (Topographical data from Norwegian Polar Institute, 2014).

### 3.1.2 Instrument setup

The tethered balloon system HoloBalloon (Ramelli et al., 2020) was used to perform in-situ cloud microphysical measurements during October - November 2019 and March - April 2020. HoloBalloon consists of a cloud measurement platform hanging 12 m below a helikite. The main instrument on the measuring platform is the HOLographic cloud Imager for Microscopic Objects (HOLIMO). HOLIMO images cloud particles in the size range from small cloud droplets (6  $\mu\text{m}$ ) to precipitation-sized particles (2 mm) in a three-dimensional sample volume to obtain information about the phase-resolved particle size distribution and particle habits (Henneberger et al., 2013; Beck et al., 2017; Ramelli et al., 2020). The classification of cloud droplets and ice crystals is performed based on their shape using a convolutional neural network trained and fine-tuned on cloud particles from holographic imagers (Touloupas et al., 2020; Lauber, 2020). The smallest detectable ice crystals are 25  $\mu\text{m}$  and all particles below this threshold are automatically classified as cloud droplets. Furthermore, ice crystals with a rather circular shape in the 2D image are

misclassified as cloud droplets. All ice crystals were manually classified into habits based on their 2D shape to plates, columns, frozen drops, recirculation particles (see Section 3.2.2 for details), and aged particles that comprise rimed, aggregated, and irregular ice crystals. In addition, cloud droplets and artefacts wrongly classified as ice crystals by the convolutional neural network were manually reclassified. Therefore, the uncertainty in the concentration of ice particles can be estimated with  $\pm 5\%$  for ice crystals smaller than  $100\ \mu\text{m}$  and  $\pm 15\%$  for ice crystals larger than about  $100\ \mu\text{m}$  (Beck, 2017). For cloud droplets, the uncertainty is estimated to be  $\pm 6\%$  as determined for the classification with the convolutional neural network in Touloupas et al. (2020). The sampling volume of HOLIMO is about  $16\text{--}20\ \text{cm}^3$  per frame, and approximately 4–6 frames were taken per second, which gives a volume of 3 L to 60 L for the averages over 30 s to 5 min used in this study. Thus, the limit of detection of HOLIMO, corresponding to one cloud particle measured in the time average, amounts to  $\sim 0.3\ \text{L}^{-1}$  for measurements averaged over 30 seconds. Note that using a tethered balloon system such as HoloBalloon for cloud microphysical measurements has the advantage that the influence from ice crystals lifted from the ground (e.g., blowing snow, Beck et al., 2018) can be neglected due to the distance of the measurements from the surface. In addition, thanks to the low true air speed of HOLIMO on the tethered balloon system and the adequate tower tips, the shattering of ice crystals in the sample volume is minimized.

Ambient aerosol was sampled through a heated inlet mounted on top of an observatory container located next to the launching location of HoloBalloon (Pasquier et al., 2021). Downstream the inlet, a high flow-rate impinger (Coriolis<sup>®</sup>  $\mu$ , Bertin Instruments, France) operating at  $300\ \text{L}\ \text{min}^{-1}$  collected ambient aerosol particles with aerodynamic diameter of  $0.5\ \mu\text{m}$  and larger into pure water. For one sample, the impinger collected aerosol particles for one hour, probing a volume of  $18\ \text{m}^3$ . Directly after collection, each sample was analysed for INPC via the offline technique DRoplet Ice Nuclei Counter Zurich (DRINCZ, David et al., 2019a), which measured INPC at sub-freezing temperatures between approximately  $-3\ ^\circ\text{C}$  and  $-20\ ^\circ\text{C}$ . INPCs were calculated according to Vali (1971), corrected for the sampling water’s background, converted to concentration in air, and their uncertainties were calculated applying Gaussian error propagation. Further details of the processing are presented in Wieder et al. (2022c) and Li et al. (2022). The lower INPC detection limit amounts to  $1.4 \cdot 10^{-4}\ \text{L}^{-1}$  and the relative measurement uncertainty is on average given by a factor of two.

The in-situ measurements were complemented by remote sensing instruments installed at the French–German Arctic Research Base AWIPEV. In particular, the 94 GHz cloud radar of University of Cologne (JOYRAD-94, Kuchler et al., 2017) was used for analyzing the whole cloud structure, the ceilometer (Vaisala-CL51, Maturilli and Ebell, 2018) was utilized to determine the cloud base height, and the wind lidar (Windcube200) enabled the continuous characterisation of wind direction and speed in the lower troposphere. Meteorological surface measurements were continuously available from the AWIPEV observation site (Maturilli et al., 2013, 2015) and the vertical atmospheric structure was determined by daily and additional radiosondes (Maturilli and Kayser, 2017) during specific measurement periods.

### 3.1.3 SIP identification

We use a specific method to identify cloud regions where SIP was recently occurring from in-situ measurements, using the concentration of small pristine ice crystals (diameters  $< 100\ \mu\text{m}$ ) following the approach introduced by Korolev et al. (2020). This approach is based on the fact that if SIP occurs in a supersaturated environment, the newly formed ice fragments or splinters rapidly grow by water vapor diffusion into detectable faceted ice crystal habits representative of the environment in which they grow in (e.g. Nakaya, 1954; Libbrecht, 2005). With time, the ice crystal habit can lose its spatial correlation with its environment of origin due to turbulent diffusion, horizontal and/or vertical advection. Korolev et al. (2020) estimated the time for which a secondary ice particle remains associated with its environment of origin to be 60–120 s, which

allows a hexagonal plate or column to grow to a width or length between 50  $\mu\text{m}$  and 150  $\mu\text{m}$  at water saturation, depending on its aspect ratio and the environmental temperature. Following this method, we use the occurrence of pristine ice crystals with a major axis between 25  $\mu\text{m}$  and 106  $\mu\text{m}$  as an indicator for SIP regions. The major axis is defined as the major axis of an ellipse that encompasses the detected pixels of the particle. This specific cut-off size was chosen as it is the bin size of the size distribution used in the processing of the data closest to 100  $\mu\text{m}$ , thus lying in between 50  $\mu\text{m}$  and 150  $\mu\text{m}$ . Examples of pristine ice crystals smaller than 106  $\mu\text{m}$ , used as indicators for SIP regions, are shown in Figure 3.2 and contrasted with non-pristine smaller than 106  $\mu\text{m}$  and pristine ice crystals larger than 106  $\mu\text{m}$ . Non-pristine crystals cannot have formed from vapor deposition growth, and could originate from breakups during impact with the instrument payload or from rime falling from the tethered balloon. Such particles were therefore excluded from the SIP analysis.

The identified SIP regions were further classified into three SIP classes, namely, low SIP regions ( $\text{SIP}_{\text{low}}$ ), moderate SIP regions ( $\text{SIP}_{\text{mod}}$ ), and high SIP regions ( $\text{SIP}_{\text{high}}$ ) using the number concentration of pristine ice crystals with diameters  $< 106 \mu\text{m}$  ( $\text{ICNC}_{\text{pr}<106 \mu\text{m}}$ ) as follows:

- (1)  $\text{SIP}_{\text{low}}$ :  $0.3 \text{ L}^{-1} \leq \text{ICNC}_{\text{pr}<106 \mu\text{m}} < 1 \text{ L}^{-1}$ ,
- (2)  $\text{SIP}_{\text{mod}}$ :  $1 \text{ L}^{-1} \leq \text{ICNC}_{\text{pr}<106 \mu\text{m}} \leq 10 \text{ L}^{-1}$ ,
- (3)  $\text{SIP}_{\text{high}}$ :  $\text{ICNC}_{\text{pr}<106 \mu\text{m}} \geq 10 \text{ L}^{-1}$ .

In addition,  $\text{SIP}_{\text{all}}$  represents the three SIP classes combined and  $\text{SIP}_{\text{no}}$  refers to  $\text{ICNC}_{\text{pr}<106 \mu\text{m}} < 0.3 \text{ L}^{-1}$ , with  $0.3 \text{ L}^{-1}$  being the lower limit of detection of HOLIMO for measurements averaged over 30 s. This means that if no small pristine ice crystals is measured, the actual  $\text{ICNC}_{\text{pr}<106 \mu\text{m}}$  is below  $0.3 \text{ L}^{-1}$  but not necessarily  $0 \text{ L}^{-1}$ . This signifies that all the  $\text{ICNC}_{\text{pr}<106 \mu\text{m}}$  smaller than  $0.3 \text{ L}^{-1}$  are not taken into account in the analysis of SIP in this study. Note that the contribution from primary ice nucleation in the remote Arctic region around Ny-Ålesund is expected to be lower than this  $0.3 \text{ L}^{-1}$  at temperatures above  $-20 \text{ }^\circ\text{C}$  (e.g., Tobo et al., 2020; Rinaldi et al., 2021; Li et al., 2022).

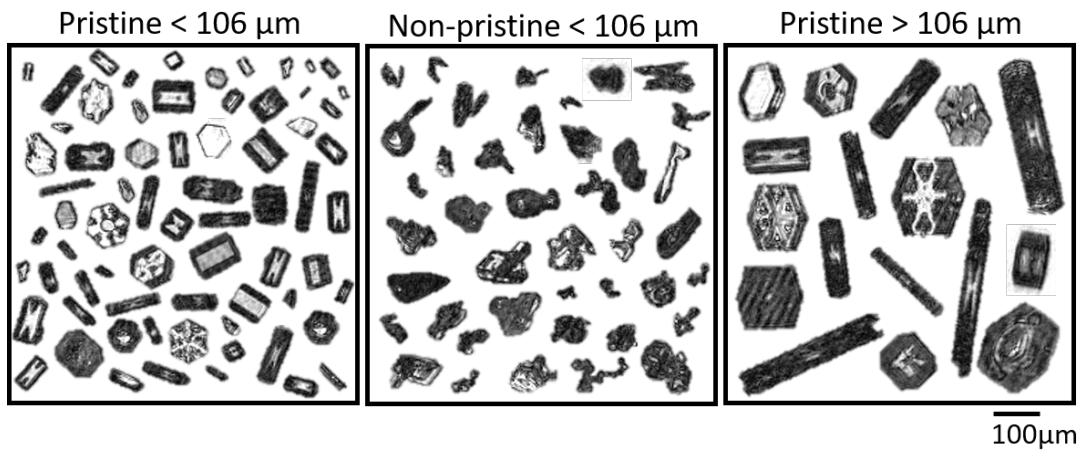


Figure 3.2: Examples of ice crystals observed with HOLIMO classified as pristine with diameters  $< 106 \mu\text{m}$ , non-pristine ice crystals with diameters  $< 106 \mu\text{m}$ , and pristine ice crystals with diameters  $> 106 \mu\text{m}$ . The presence of pristine ice crystals with diameter  $< 106 \mu\text{m}$  was used for identification of SIP. The scale bar applies to all panels.

To ensure that the measurements were conducted in-cloud, only regions where the relative humidity with respect to ice derived from the interpolated radiosonde measurements is higher than 95% or the liquid water content measured by HOLIMO was larger than  $0.005 \text{ g m}^{-3}$  are taken into account. Both criteria are used disjointly because in some cases the cloud may only be saturated with respect to ice, and in other cases the relative humidity measured by the radiosonde closest in time may not be capturing local areas of saturation.

### 3.1.4 Determination of INP concentrations

The INPC derived from the DRINCZ measurements on the ground is used to estimate the INPC at the cloud top ( $\text{INPC}_{\text{CT}}$ ) and at the HoloBalloon measurement altitude ( $\text{INPC}_{\text{HB}}$ ). As the INPC is a function of the nucleation temperature (increasing exponentially with decreasing temperature), we use the temperatures at cloud top and at the measurement location of HoloBalloon to estimate  $\text{INPC}_{\text{CT}}$  and  $\text{INPC}_{\text{HB}}$ . These temperatures are derived from the linearly interpolated radiosonde temperature profiles together with the highest cloud top altitude retrieved by the cloud radar on each day and the measurement altitude of HoloBalloon (see Section 3.3.2 in the Appendix for details).  $\text{INPC}_{\text{CT}}$  represents the cloud’s highest INPC estimate as the lowest cloud temperatures are generally found at cloud top.  $\text{INPC}_{\text{CT}}$  is therefore representative for the maximum ICNC that could have formed via primary nucleation from INPs.  $\text{INPC}_{\text{HB}}$  is representative for the ICNC that could have formed by primary nucleation on INPs at the measurement location and can be directly compared to  $\text{ICNC}_{\text{pr}<106\mu\text{m}}$  because the method employed assumes that the ice crystals smaller  $106\ \mu\text{m}$  have formed close to HoloBalloon’s location.

Uncertainties arise from using INP measurements taken at the surface to estimate the in-cloud INPC. For well-mixed boundary layers, in which the aerosol particle concentrations are constant between the surface and cloud base, the INPC at the ground and in the cloud should be comparable (neglecting INP depletion by scavenging and INP entrainment at cloud top). However, in decoupled cloud cases, when a shear layer and/or a large potential temperature increase is observed below the cloud base, the INPC in the cloud could be different than the one observed at the ground. In the cases presented in this study, the layers from cloud base to the surface were generally well-mixed and no strong decoupling case was observed (Fig. 3.13). In addition, Pasquier et al. (2021) compared the INPC measured at the observatory container at sea level on 12 November 2019 and the INPC averaged over several days at the mountaintop Zeppelin Observatory located 2 km southwestward at 475 m a.s.l. (Fig. 3.1b) and found that the INPC were in agreement within a factor of 5 at the two location despite the different measurement method and time averages used.

## 3.2 SIP occurrence during six days of MPC measurements in Arctic MPCs

### 3.2.1 Overview of the six days with MPCs

The microphysical properties of the MPCs were identified with HOLIMO on five consecutive days from 8 to 12 November 2019 and on 1 April 2020. The total cloud droplet number concentrations (CDNC) measured by HOLIMO reached up to  $30\ \text{cm}^{-3}$  and drizzle drops (defined with diameter larger than  $64\ \mu\text{m}$ ) were observed during four measurement flights (Fig. 3.3d). This CDNC is considerably lower than for comparable continental clouds, which typically have CDNCs of up to  $1000\ \text{cm}^{-3}$  (Lohmann et al., 2016b), but is representative for the pristine Arctic environment where limited CCN availability results in low CDNCs, as discussed in e.g., Lance et al. (2011) and Koike et al. (2019). Generally,  $\text{ICNC}_{\text{pr}<106\ \mu\text{m}}$  is orders of magnitude larger than  $\text{INPC}_{\text{HB}}$  and ICNC is orders of magnitude larger than  $\text{INPC}_{\text{CT}}$ , except on 10 November 2019 (Fig. 3.3e). This indicates that primary ice nucleation via INPs cannot be solely responsible for the observed ICNC, and suggests that SIP processes contributed to the ICNC.

On 8 November 2019, an occluded front moved over Ny-Ålesund, producing strong south-westerly large-scale winds (up to  $20\ \text{m s}^{-1}$  at 2000 m a.s.l.) and about 12 mm of accumulated precipitation (not shown). As the front passed, the low-level cloud field was overrun by a deep cloud layer that extended to cloud top temperatures below  $-38\ ^\circ\text{C}$  at an altitude of 5000 m a.s.l. At these temperatures, any cloud droplet would freeze independently of INPs via homogeneous freezing. On 9 November 2019, the sea level pressure dropped by about 7 hPa and the surface wind speed increased from 2 to  $8\ \text{m s}^{-1}$  as another low pressure system passed over

Ny-Ålesund (Fig. 3.3a,b). During the flights performed on 8 and 9 November 2019, HoloBalloon measured mostly in subsaturated regions below cloud, where the cloud droplets and ice crystals were evaporating and sublimating, respectively, as also indicated by the relative humidity below 100% below  $\sim 700$  m observed by the radiosondes (Fig. 3.4). Evidence of ice crystal sublimation can be deduced from the rounded edges of the ice crystals and the thin filaments connecting parts of the crystals to their main body (Fig. 3.5a). It is evident that such ice crystals could easily break up in two or more particles depending on their original shape, thereby creating secondary ice crystals. However, unless these fragments were reintroduced into regions with ice (super)saturation by updrafts, they will sublimate completely.

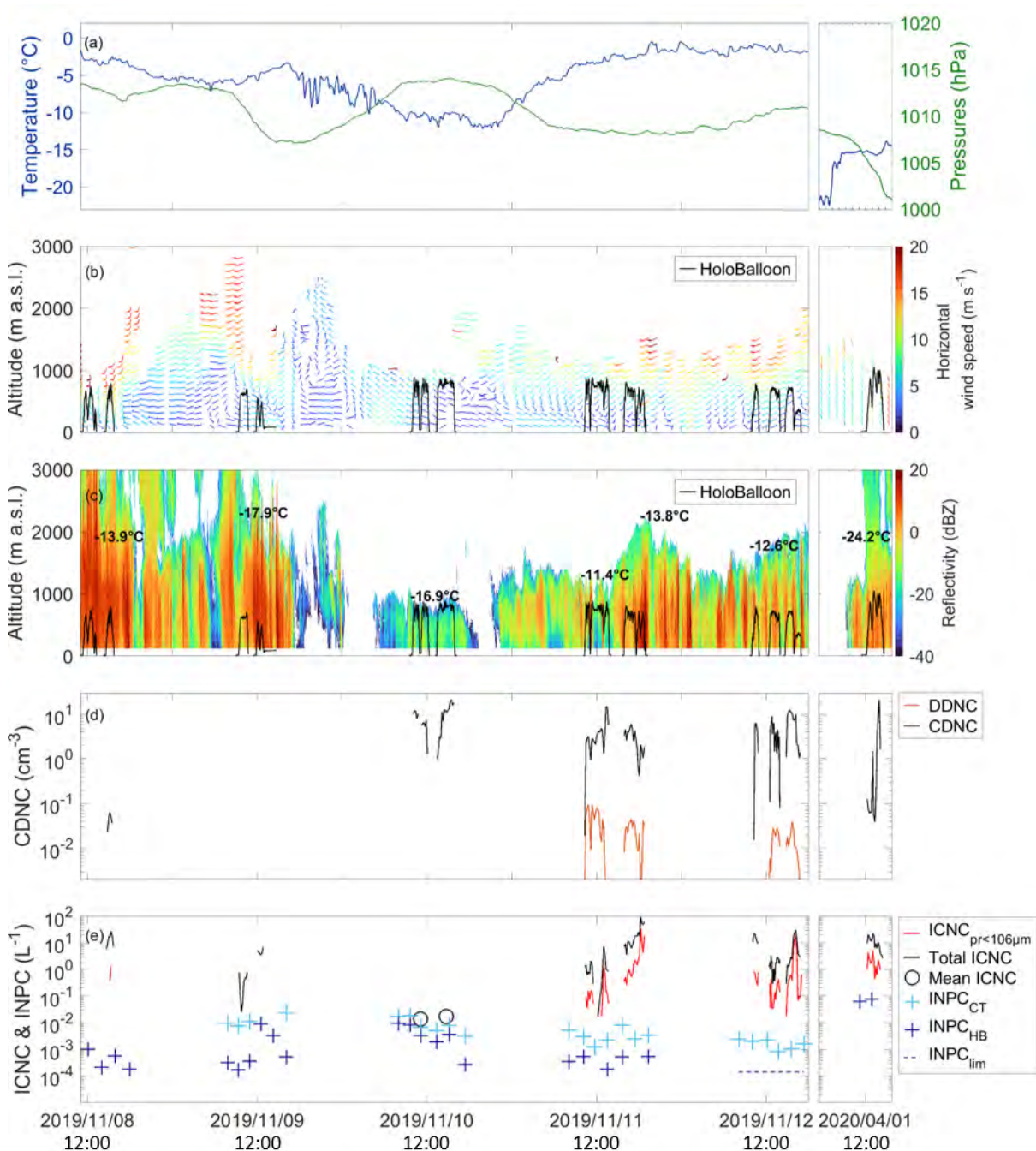




Figure 3.3: (a) Ambient temperature and pressure measured from the weather mast two meters above ground at the AWIPEV Observatory. (b) Horizontal wind speed measured with the wind lidar averaged over 1h30 (wind barbs) and HoloBalloon measurement height (black line). (c) Cloud radar reflectivity (color), HoloBalloon measurement height (black line), and cloud top temperatures from radiosonde launches measured during the six-day measurement period. On 8 November 2019 and 1 April 2020 the temperature is shown at an altitude of 1800 m a.s.l. because the cloud top is higher than 3000 m a.s.l.. (d) Total CDNC (black) and drizzle drops number concentration (DDNC) (orange) averaged over 5 min. The uncertainty in the concentration of cloud and drizzle is estimated to be  $\pm 6\%$ . (e) Total ICNC (black line) and  $\text{ICNC}_{\text{pr}<106 \mu\text{m}}$  (red line) averaged over 5 min,  $\text{INPC}_{\text{CT}}$  (light blue crosses) and  $\text{INPC}_{\text{HB}}$  (dark blue crosses). For 10 November 2019, the ICNCs averaged over each flight are shown with black circles because the ICNC are too low to display a time series. On 12 November 2019, the  $\text{INPC}_{\text{HB}}$  were below the limit of detection of the INP instrumentation, therefore the limit of detection ( $1.4 \cdot 10^{-4} \text{ L}^{-1}$ ) is displayed instead ( $\text{INPC}_{\text{lim}}$ , dark blue dashed line). The uncertainty for the concentration of ice particles smaller than  $100 \mu\text{m}$  is estimated to  $\pm 5\%$  and to  $\pm 15\%$  for ice crystals larger than  $100 \mu\text{m}$ . The uncertainty for the INPC amounts to a factor of two. On 8 November 2019 and 1 April 2020, no  $\text{INPC}_{\text{CT}}$  can be provided as the cloud top temperatures were below the observable nucleation temperatures of our INP instrumentation. All data are shown from 11:00 UTC on 8 November to 18:00 UTC on 12 November 2019 and on 1 April 2020 from 05:00 to 16:00 UTC. Note that the ticks are at 12:00 UTC for each day.

On 8 and 9 November 2019, updrafts estimated from the remote sensing observation at the HoloBalloon location (see Appendix 3.3.2 for the methods) reached up to  $2.5 \text{ m s}^{-1}$  and  $1 \text{ m s}^{-1}$ , respectively. These moderate updrafts could have lifted some fragments back into ice supersaturated regions, where they could have grown again and increased the ICNC. Otherwise, if the ice crystals sublimated completely, the remaining INPs could have re-entered the cloud and formed new ice crystals (e.g., Solomon et al., 2015; Possner et al., 2017; Fu et al., 2019). Although this could act as a pathway to enhance ICNCs, the resulting ice formation mechanism would be primary ice crystal nucleation and not SIP.

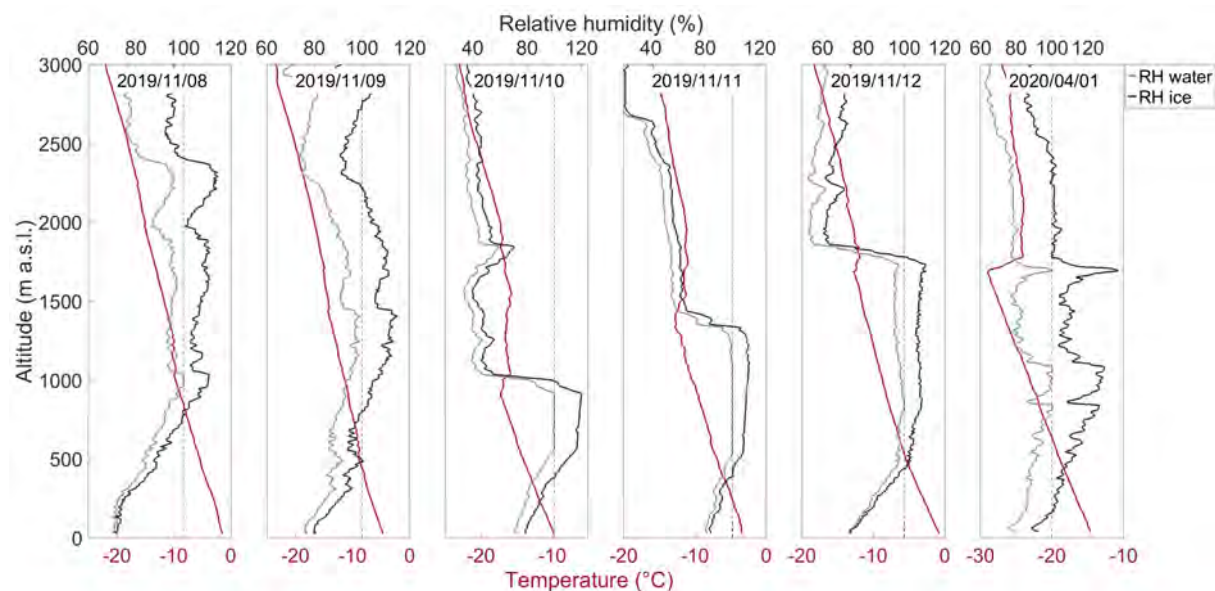


Figure 3.4: Temperature (red) and relative humidity (RH) with respect to water (bright grey) and ice (dark grey) measured by the radiosonde launched at 11:00 UTC on 8 to 12 November 2019 and at 17:00 UTC on 1 April 2020. The 100% RH line is shown with the broken black line.

After the low pressure system moved eastward of Ny-Ålesund on 10 November 2019, the

flow became northwesterly and advected cold air towards Ny-Ålesund. This cold northwesterly flow pushed under the warmer air that was present in the fjord valley before, and by that acted like a cold front lifting the air and causing the formation of a shallow and very lightly precipitating stratocumulus cloud deck. Consistently, the temperature at the surface dropped from approximately  $-3\text{ }^{\circ}\text{C}$  to  $-10\text{ }^{\circ}\text{C}$  within a few hours (Fig. 3.3a). Two measurement flights were conducted on 10 November 2019 and HoloBalloon was able to penetrate through the cloud deck with cloud top temperature of  $-17\text{ }^{\circ}\text{C}$  (Figs. 3.3c and 3.4). The CDNCs measured by HOLIMO were about  $20\text{--}30\text{ cm}^{-3}$  (Fig. 3.3d). A few dendrite-like ice crystals were measured by HOLIMO during both flights (Fig. 3.5b) and the ICNC averaged over the entire flight period amounted to  $1.4 \cdot 10^{-2}\text{ L}^{-1}$  (Fig. 3.3e). No pristine ice crystals smaller than  $106\text{ }\mu\text{m}$  were measured and the mean ICNC lies in the daily variability of the  $\text{INPC}_{\text{CT}}$  observed (Fig. 3.3e). Thus, we conclude that the ice crystals formed by primary nucleation on INPs and that no SIP process substantially increased the ICNCs on this day. Therefore, the INP availability determined the ice crystal formation. This shows the ability of INPs to control ice crystal formation in remote pristine areas like the Arctic in case of shallow clouds and weak dynamics.

On 11 and 12 November 2019, the weather in Ny-Ålesund was influenced by the passage of a warm front embedded with several precipitation showers. In these two days, the MPC evolved from a  $\text{SIP}_{\text{low}}$  state with  $\text{ICNC}_{\text{pr}<106\text{ }\mu\text{m}}$  below  $1\text{ L}^{-1}$  to a  $\text{SIP}_{\text{high}}$  state with  $\text{ICNC}_{\text{pr}<106\text{ }\mu\text{m}}$  greater than  $50\text{ L}^{-1}$ . As this is about 5 orders of magnitude higher than the estimated  $\text{INPC}_{\text{HB}}$ , we propose that SIP mechanisms were responsible for the sudden increase in  $\text{ICNC}_{\text{pr}<106\text{ }\mu\text{m}}$  and examine the contribution from the likely active SIP processes in detail in Section 3.2.2.

On 1 April 2020, a warm front passed over Ny-Ålesund and produced a cirrostratus cloud at 8000 m. This cirrostratus deepened to an altostratus deck that acted as a *seeder* cloud that precipitated into the low-level mixed-phase *feeder* cloud below, thereby enhancing the ICNC in the low-level MPC measured by HoloBalloon. However, the  $\text{INPC}_{\text{HB}}$  was up to 1 to 2 orders of magnitude smaller than the  $\text{ICNC}_{\text{pr}<106\text{ }\mu\text{m}}$ , which indicates that some SIP processes were likely active in the low-level MPC. The microphysical properties of the low-level mixed-phase feeder cloud are discussed in Section 3.2.3.

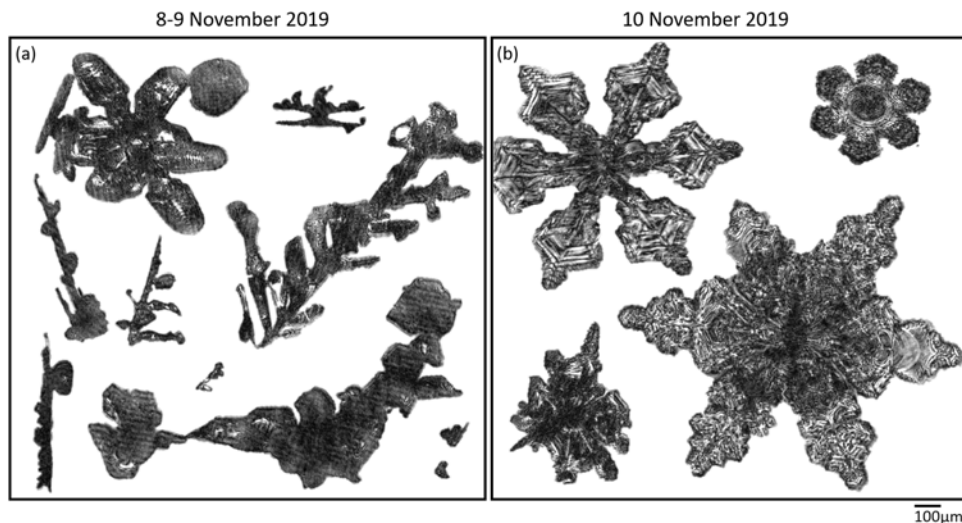


Figure 3.5: Representative examples of ice crystals observed with HOLIMO during the flights on (a) 8 and 9 November 2019 and (b) 10 November 2019. The scale bar applies to both panels.

### 3.2.2 High SIP event on 11 November 2019

On 11 November 2019, a precipitating low-level MPC was observed with a cloud base around 700 m a.s.l. and cloud top rising from about 1000 m a.s.l. to 2200 m a.s.l. (Fig. 3.6a). The surface temperature increased from  $-3.1\text{ }^{\circ}\text{C}$  to  $-0.3\text{ }^{\circ}\text{C}$  between 11:00 UTC and 20:00 UTC (Fig. 3.3a),



whereas the cloud top temperature decreased from  $-11^{\circ}\text{C}$  to  $-13.5^{\circ}\text{C}$  as the cloud top height increased. The cloud radar observed regions of enhanced reflectivity, indicative of the presence of large ice crystals (Fig. 3.6a). Two flights were performed at 10:15–13:40 UTC and 15:50–19:00 UTC into the MPC with HoloBalloon (Fig. 3.6a). The measured cloud droplet size distribution peaked at around  $50\ \mu\text{m}$  and drizzle drops were observed, except for a short period between 13:15 and 13:45 UTC when the CDNC spectra peaked at smaller sizes (Fig. 3.6b).

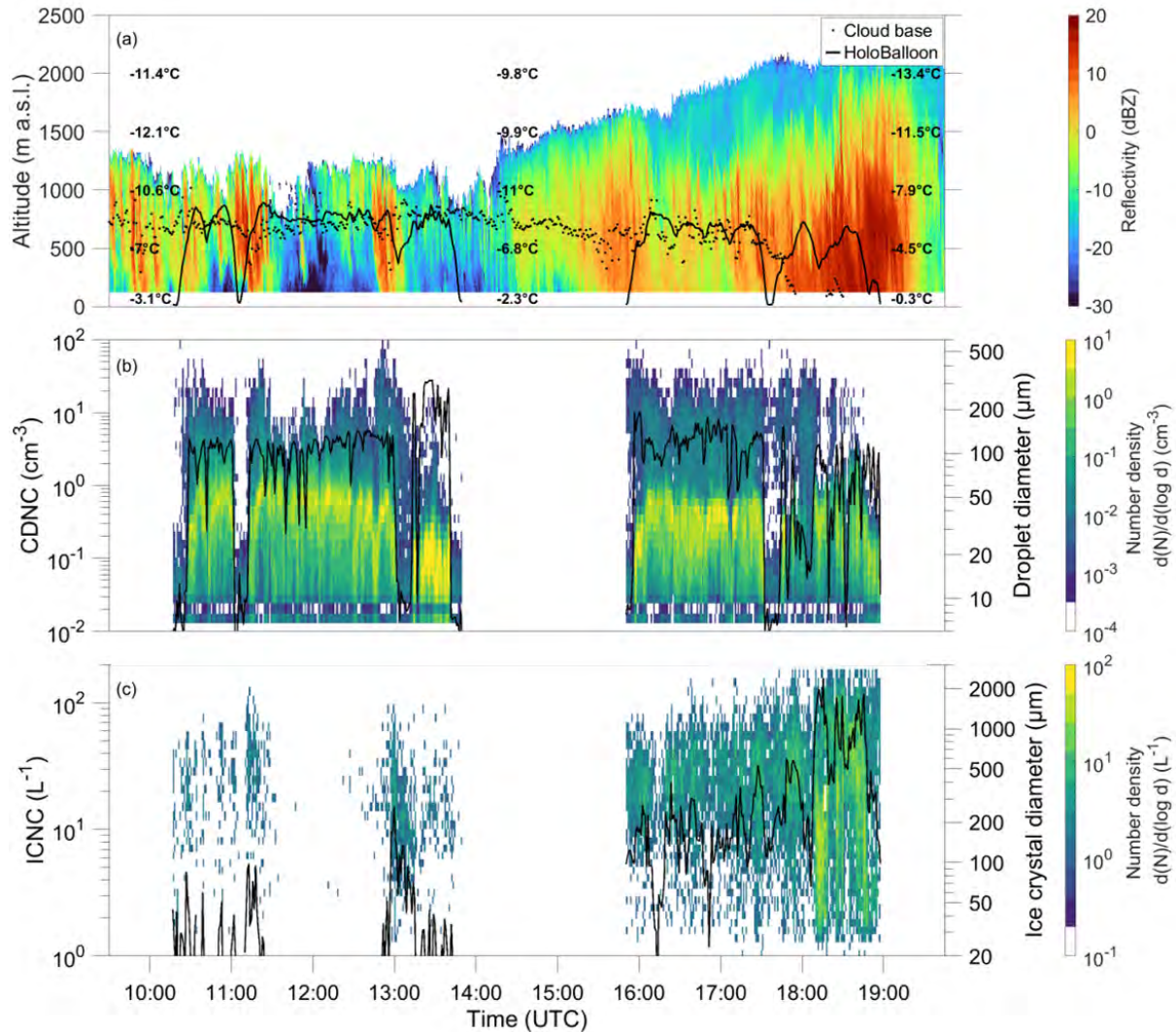


Figure 3.6: Overview of the cloud properties on 11 November 2019. (a) Cloud radar reflectivity (color), HoloBalloon measurement height (black line), cloud base height measured by the ceilometer (black dots), and temperatures at the corresponding altitudes measured by the radiosonde at 11:00 UTC, 14:00 UTC, and 20:00 UTC. Note that the lowering of the cloud base to the surface detected by the ceilometer after 17:30 UTC is caused by precipitation. (b) Cloud droplet size distributions (color shading) and total CDNC (black line). The uncertainty in the concentration of cloud and drizzle is estimated to be  $\pm 6\%$ . (c) Ice crystal size distributions (color shading) and total ICNC (black line) measured by HOLIMO averaged over 1 min. The uncertainty for the concentration of ice particles smaller than  $106\ \mu\text{m}$  is estimated to  $\pm 5\%$  and for the concentration of larger ice crystals to  $\pm 15\%$ .

The measured cloud evolved from low total ICNC ranging between  $0.3$  and  $10\ \text{L}^{-1}$  and  $\text{ICNC}_{\text{pr}<106\ \mu\text{m}}$  below  $1\ \text{L}^{-1}$  during the first flight (10:15–13:40 UTC), to a region with total ICNC ranging mostly between  $5$  and  $20\ \text{L}^{-1}$  and  $\text{ICNC}_{\text{pr}<106\ \mu\text{m}}$  between  $1$ – $3\ \text{L}^{-1}$  (contributing about 3–30% to total ICNC) (15:50–18:10 UTC) and finally to a region with ICNC up to  $150$

$L^{-1}$ , out of which up to  $90 L^{-1}$  (60%) were  $ICNC_{pr<106 \mu m}$  (18:10-18:45 UTC) (Figs. 3.6c and 3.7b,c). This last period (18:10-18:45 UTC) is marked by several peaks in ICNC above  $100 L^{-1}$  and  $ICNC_{pr<106 \mu m}$  above  $10 L^{-1}$  (Figs. 3.6c and 3.7b). On this day, the  $INPC_{CT}$  varied between  $1 \cdot 10^{-3}$  and  $9 \cdot 10^{-3} L^{-1}$  and the  $INPC_{HB}$  between  $1 \cdot 10^{-4}$  and  $4 \cdot 10^{-4} L^{-1}$  (Fig. 3.3e), thus four to five orders of magnitude lower than the ICNC and  $ICNC_{pr<106 \mu m}$ . No increase in INPC is observed during the course of the day. Hence, nucleation on INPs cannot explain the measured peaks in  $ICNC_{pr<106 \mu m}$  at 18:10 UTC onwards. Therefore, we assign the increases to local SIP processes.

Locally formed ice crystals smaller than  $106 \mu m$  were mostly elongated columns with a large aspect ratio between 3 and 9 (Fig. 3.7a). These habits are consistent with the environmental temperature ( $-4.5 \text{ }^\circ C$ ) at their measurement location. The high aspect ratio of the columns indicates that the cloud layer had a relatively high water supersaturation (Nakaya, 1954; Libbrecht, 2005). Note that columns with a maximum length larger than  $106 \mu m$  were observed (see Fig. 3.7a) but not accounted for in the  $ICNC_{pr<106 \mu m}$ .

Ice crystal habits help to understand which SIP processes contributed to the increase in  $ICNC_{pr<106 \mu m}$ . Ice crystals observed during SIP periods were frozen drops, aged particles, and recirculated particles (Fig. 3.7a), which are a mix of columnar and plate-like crystals due to the crystals growing in different temperature regimes (Korolev et al., 2020; Pasquier et al., 2022a). The observation of frozen drops during SIP periods suggests that the droplet shattering process produced splinters during the freezing of drizzle drops (e.g., Lauber et al., 2018; Korolev and Leisner, 2020). In particular, the ratios of frozen drops to total ICNC were especially large (0.6) at 18:05-18:10 UTC just before the first and largest peak in  $ICNC_{pr<106 \mu m}$  (Fig. 3.7c). Coincidentally, some observed frozen drops were identified on HOLIMO images to have accreted with small columns, suggesting that the collision of drizzle drops with ice crystals initiated their freezing.

A likely explanation for this first  $ICNC_{pr<106 \mu m}$  peak is therefore that the droplet shattering mechanism caused the formation of splinters which grew to small pristine columns. Then these small columns could collide with further drizzle drops, thereby initiating their freezing and the formation of additional ice splinters. This could have led to a cascading SIP process via a positive feedback loop that can explain the rapid increase in  $ICNC_{pr<106 \mu m}$ , as already proposed by Lawson et al. (2015). The fraction of frozen drops is lower after this peak in  $ICNC_{pr<106 \mu m}$  at 18:10 UTC (Fig. 3.7c) and the concentration of large drops decreased after this peak as well (Fig. 3.6b), indicating that the drizzle drops froze and precipitated out of the cloud. Thus, we propose that droplet shattering was largely contributing to the peak of  $ICNC_{pr<106 \mu m}$  ( $90 L^{-1}$ ) at 18:10 UTC.

Between 18:20 and 18:55 UTC, droplet shattering plays likely a lesser role. Instead, SIP by ice-ice collision seem to dominate after recirculation particles appear to concentration up to  $10 L^{-1}$  after 18:15 UTC (Fig. 3.7b,c). As these particles contained fragile branches, their collision and subsequent break-up could create additional ice crystals. Indeed, particles resembling broken branches were observed (highlighted with the dark brown box in Figure 3.7a). The fraction of recirculation particles to ICNC is especially large between 18:20 and 18:45 UTC. Therefore, we suggest that the ice-ice collision break-up contributed to the peaks in  $ICNC_{pr<106 \mu m}$  observed during this period together with droplet shattering.

The temperature was in the range of the rime-splintering process, however the CDNC was between  $0.1$  and  $3 \text{ cm}^{-3}$  between 18:10 and 18:45 UTC (Fig. 3.6b), and the concentration of cloud droplets smaller than  $12 \mu m$  required for the rime-splintering process (Mossop, 1978, 1985) was between  $0.01$  and  $0.2 \text{ cm}^{-3}$ . Thus, the probability of collision of rimed particles with droplets at these small concentrations is likely too low to have any important effect on the rime-splintering process. Earlier on this day, the aged/rimed particles were the most frequent ice crystal observed (Figure 3.7c) and the CDNCs (Fig. 3.6b) were larger, without a significant increase of the  $ICNC_{pr<106 \mu m}$ . Therefore, the rime-splintering process probably did not contribute significantly to the increase in  $ICNC_{pr<106 \mu m}$ .

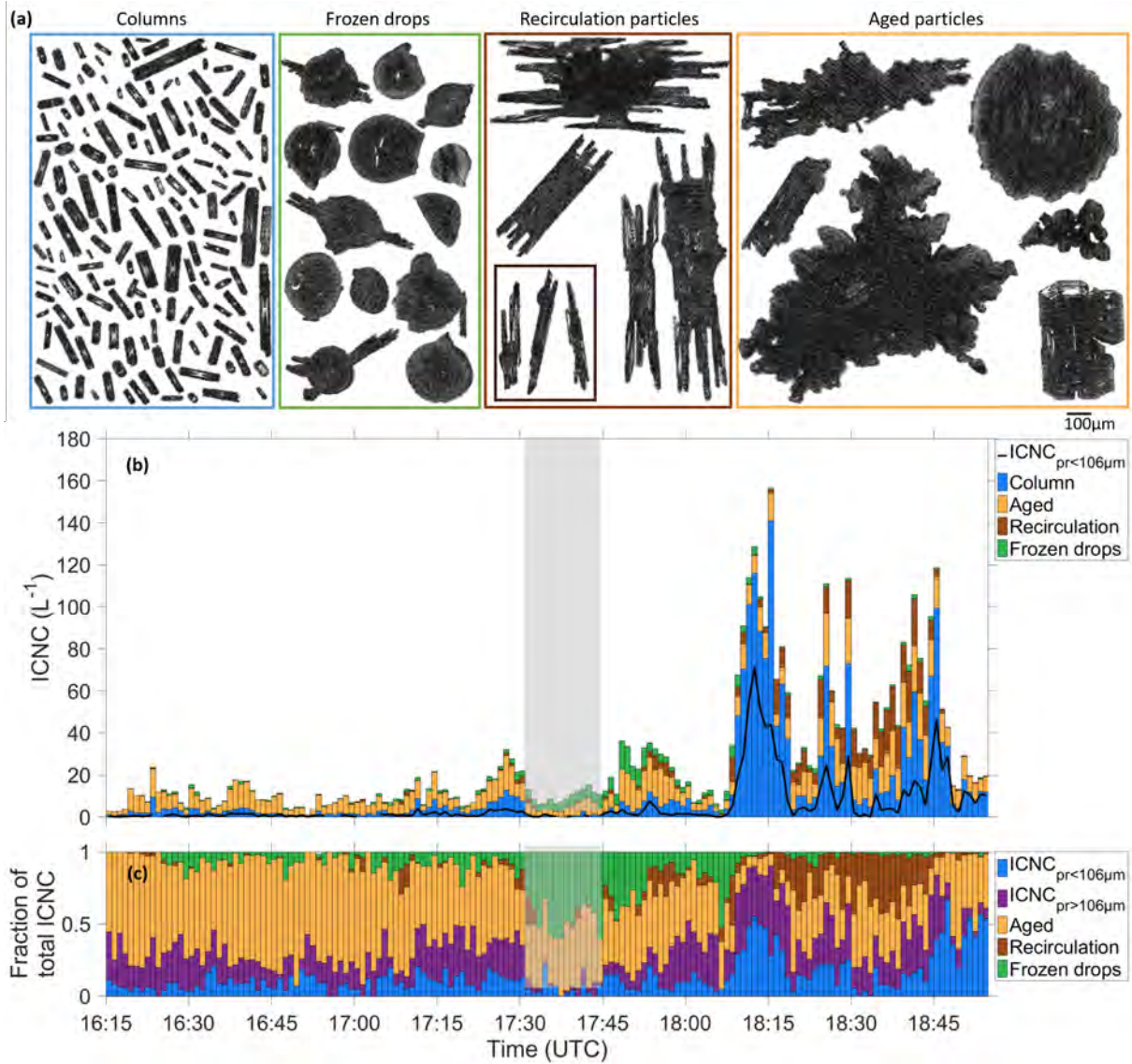


Figure 3.7: (a) Representative examples of ice crystals classified in typical habits observed with HOLIMO between 18:00 UTC and 19:00 UTC on 11 November 2019. The scale bar applies to all panels. (b) Concentrations of ice crystals classified into habits and  $\text{ICNC}_{\text{pr}<106\mu\text{m}}$  (black line). (c) Fraction of  $\text{ICNC}_{\text{pr}<106\mu\text{m}}$ , pristine ice crystals with diameter  $> 106 \mu\text{m}$  ( $\text{ICNC}_{\text{pr}>106\mu\text{m}}$ ), aged ice crystals, recirculation particles, and frozen drops concentrations to ICNC. The shaded area shows when HoloBalloon flew out of the cloud. The measurements are averaged over 1 min. The uncertainty for the concentration of ice particles smaller than  $106 \mu\text{m}$  is estimated to  $\pm 5\%$  and for the concentration of ice larger crystals to  $\pm 15\%$ .

In conclusion, we propose that droplet shattering was mainly responsible for the high peak in  $\text{ICNC}_{\text{pr}<106 \mu\text{m}}$  at 18:10-18:15 UTC and ice-ice collisions, in particular between recirculation particles, contributed to the peaks in  $\text{ICNC}_{\text{pr}<106 \mu\text{m}}$  between 18:20-18:55 together with droplet shattering. A comparable  $\text{SIP}_{\text{high}}$  event with  $\text{ICNC}_{\text{pr}<106 \mu\text{m}}$  up to  $55 \text{ L}^{-1}$  was observed on 12 November 2019. On this day, columns having formed in higher part of the cloud collided with drizzle drops during sedimentation, thereby initiating their freezing and splinters production via the droplet shattering mechanism as described in Pasquier et al. (2021).



### 3.2.3 Seeder-feeder event on 1 April 2020

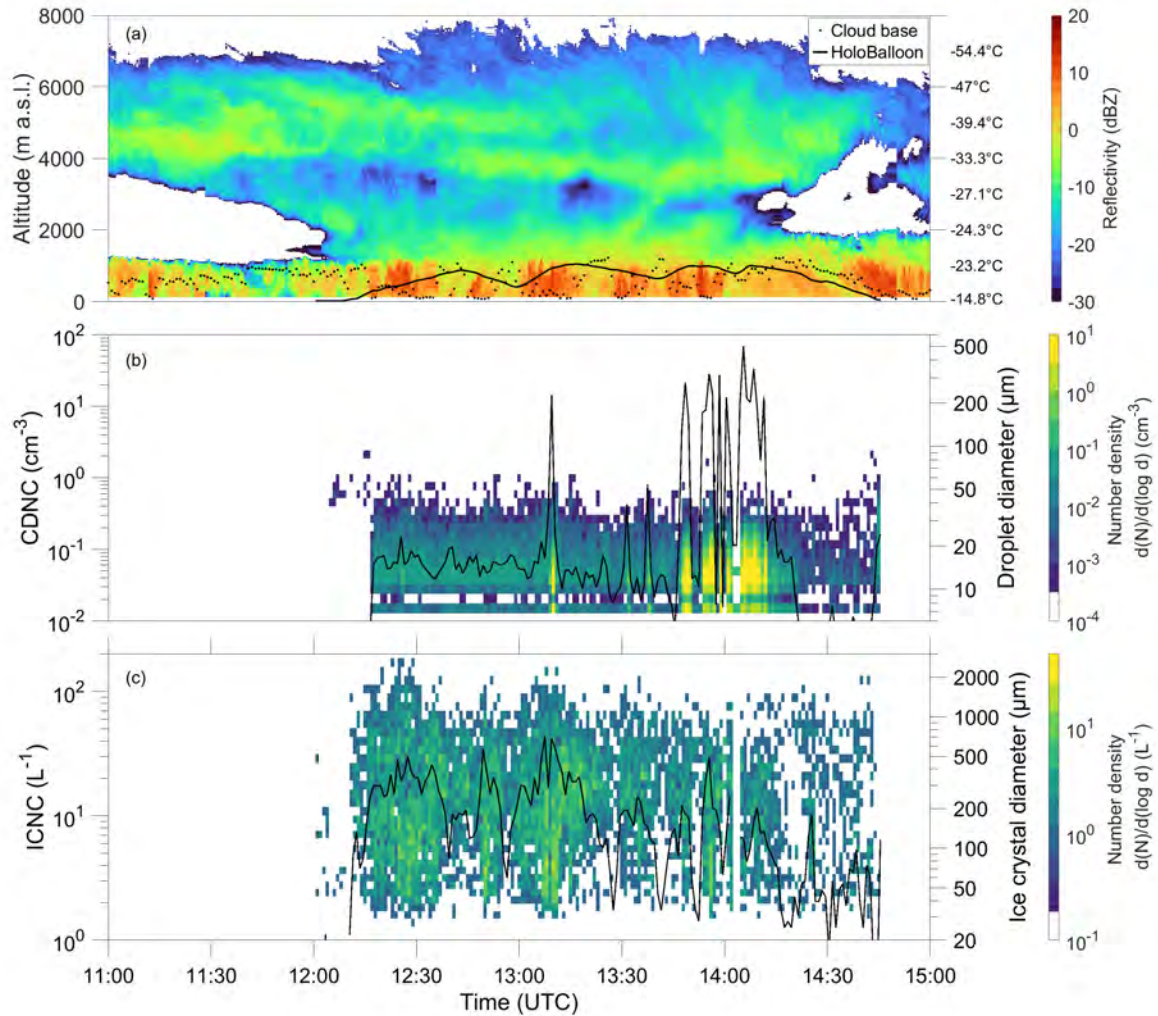


Figure 3.8: Overview of the cloud properties on 1 April 2020. (a) Cloud radar reflectivity (color), HoloBalloon measurement height (black line), cloud base height measured by the ceilometer (black dots), and temperatures at the corresponding altitudes measured by the radiosounding at 17:00 UTC. (b) Cloud droplet size distributions (color shading) and total CDNC (black line). The uncertainty in the concentration of cloud and drizzle is estimated to be  $\pm 6\%$ . (c) Ice crystal size distributions (color shading) and total ICNC (black line) measured by HOLIMO averaged over 1 min. The uncertainty for the concentration of ice particles smaller than 106  $\mu\text{m}$  is estimated to  $\pm 5\%$  and for the concentration of larger ice crystals to  $\pm 15\%$ .

On 1 April 2020, a warm front passed over Ny-Ålesund and caused the observed temperature increase of 7 °C in less than 2 hours, the pressure drop from 1009 hPa to 994 hPa, the wind direction change from southeasterly to northwesterly and the increase in wind speed at the surface (Fig. 3.3a,b). Warm air overrunning produced a thickening cirrus cloud, which initially formed at 7000 m and then continued to deepen into an altostratus cloud (Fig. 3.8a). The temperature above  $\sim 4500$  m a.s.l. was below  $-38$  °C and thus, the ice crystals formed by homogeneous and/or heterogeneous nucleation in the cirrus/altostratus cloud. The radar reflectivity signal indicates that ice crystals were sedimenting to about 3000 m a.s.l., where a region of lower reflectivity suggests their partial sublimation (Fig. 3.8a). This is in agreement with the relative humidity

with respect to ice below 100% measured by the radiosonde above 2500 m a.s.l. (Fig. 3.4). A low-level cloud formed at around 09:00 UTC with cloud top height rising from 1000 to 1500 m a.s.l. during the day. This cloud is characterized by regions of higher reflectivity, indicating the presence of larger ice crystals. Additionally, an increase in reflectivity is visible between 1500 m and 2000 m a.s.l. from 12:00 to 14:00 UTC shows that the layer is saturated with respect to ice, allowing the ice particles to grow, and suggests the presence of an embedded supercooled liquid layer. This layer can also be seen in the cloud base measured by the ceilometer when the signal is not attenuated by precipitation.

The CDNCs measured by HOLIMO was generally below  $1 \text{ cm}^{-3}$  except at 13:10 UTC or between 13:45 and 14:15 UTC, when increases in CDNC were observed (Fig. 3.8b). These comparatively large CDNCs ( $> 10 \text{ cm}^{-3}$ ) are observed when HoloBalloon was in the transition region from low to high radar reflectivity (i.e. in the embedded supercooled liquid layer). It suggests that in this region water saturation was sustained and promoted the formation and growth of cloud droplets, while below, the environment was subsaturated with respect to water and the cloud droplets were evaporating.

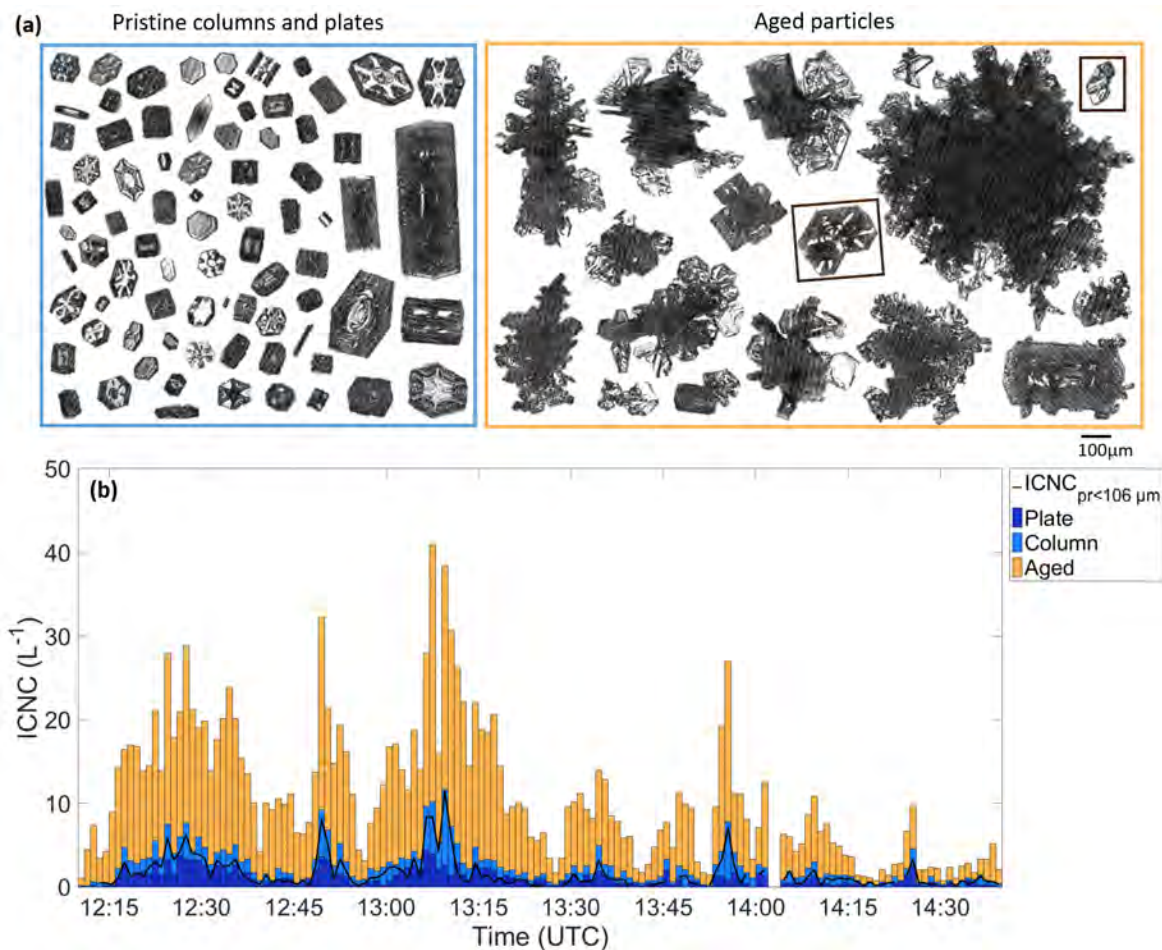


Figure 3.9: (a) Representative examples of ice crystals classified in typical habits observed with HOLIMO on 1 April 2020. Ice crystals with indication of broken features are highlighted with blue frames. The scale bar is representative for both panels. (b) The concentration of the ice crystals by habit and  $\text{ICNC}_{\text{pr}<106\mu\text{m}}$  (black line) between 12:20 UTC and 14:40 UTC (bottom) on 1 April 2020 are shown. The uncertainty for the concentration of ice particles smaller than  $100 \mu\text{m}$  is estimated to  $\pm 5\%$  and for the concentration of larger ice crystals to  $\pm 15\%$ .

In the low-level cloud, the ICNC amounted up to  $55 \text{ L}^{-1}$  because of the contribution from crystals sedimenting from the seeder cloud (Fig. 3.8). The ice crystal habits were composed of

pristine plates and columns together with aged particles (Fig. 3.9a). The large aged ice crystals likely originated from the seeder cloud aloft and experienced collisions with cloud particles during their sedimentation. In contrast, the small columns and plates observed (Fig. 3.9a) must have formed close to the measurement location due to their small size and pristine nature. At temperatures below  $-22^{\circ}\text{C}$  as experienced above 600 m, supersaturation relative to ice determines whether ice crystals grow to plates or columns (Nakaya, 1954). The columns therefore originated from regions with higher supersaturation (likely in the embedded supercooled liquid layer) and plates from region of lower supersaturation with respect to ice. Indeed, peaks in the concentrations of columns at 13:10 and 14:00 UTC (Fig. 3.9b) coincide with the increases in CDNC (Fig. 3.8b).

As the  $\text{INPC}_{\text{HB}}$  ( $8 \cdot 10^{-2} \text{ L}^{-1}$ ) was two to three orders of magnitude lower than the  $\text{ICNC}_{\text{pr}<106 \mu\text{m}}$  ( $15 \text{ L}^{-1}$ ) (Fig. 3.3c), SIP processes were active. Again, we use the ice crystal habits together with the environmental conditions prevailing in this cloud to evaluate the likely SIP processes contributing to  $\text{ICNC}_{\text{pr}<106 \mu\text{m}}$ . Rimed particles were observed and the concentration of small droplets may have been sufficient in some regions of the low-level cloud (13:10 UTC and 13:45-14:15 UTC) to trigger the rime-splintering mechanism. However, the observed temperature ( $-24^{\circ}$  to  $-18^{\circ}\text{C}$ ) was far below the temperature range of rime splintering ( $-8^{\circ}\text{C}$  to  $-3^{\circ}\text{C}$ ). Furthermore, no large droplets necessary for the droplet shattering process were observed. Therefore, the rime-splintering and the droplet shattering processes are unlikely to have played a significant role as SIP mechanisms in the observed cloud. On the contrary, some ice crystals showed broken features, as highlighted by the blue frames in Figure 3.9a. As the ICNCs were large (up to  $55 \text{ L}^{-1}$ ) collisions between ice crystals have likely occurred. In addition, ice-ice collisions is believed to be most efficient at colder temperature (Takahashi et al., 1995) such as observed on this day. Therefore, we deduce that the ice-ice collisions were again the most likely active SIP mechanism in the low-level feeder cloud.

### 3.3 Environmental conditions favorable for SIP

During the six days of observations performed with HoloBalloon during the NASCENT campaign, 2252 measurements of 30 s intervals were taken in-cloud, corresponding to a total of 18.7 hours and a volume of 6425 L. Out of these measurements,  $\text{SIP}_{\text{all}}$  (representing all measurements with  $\text{ICNC}_{\text{pr}<106 \mu\text{m}} > 0.3 \text{ L}^{-1}$ ) was present during 40% of the measurements. When dividing by the intensity of the SIP,  $\text{SIP}_{\text{low}}$ ,  $\text{SIP}_{\text{mod}}$  and  $\text{SIP}_{\text{high}}$  occurred 20.5%, 16%, and 3.5% of the time, respectively (Fig. 3.10).

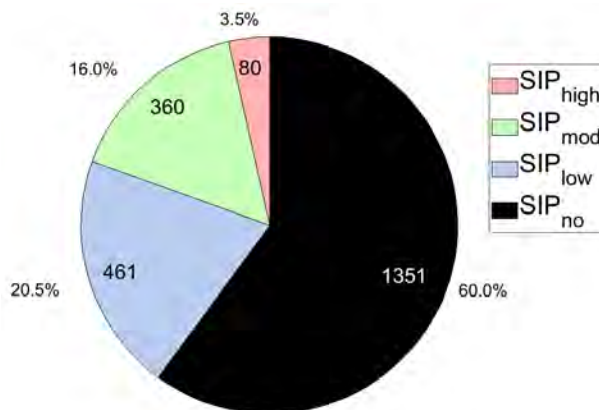


Figure 3.10: Frequency of occurrence of  $\text{SIP}_{\text{no}}$  ( $\text{ICNC}_{\text{pr}<106 \mu\text{m}} < 0.3 \text{ L}^{-1}$ ),  $\text{SIP}_{\text{low}}$  ( $0.3 \text{ L}^{-1} < \text{ICNC}_{\text{pr}<106 \mu\text{m}} < 1 \text{ L}^{-1}$ ),  $\text{SIP}_{\text{mod}}$  ( $1 \text{ L}^{-1} < \text{ICNC}_{\text{pr}<106 \mu\text{m}} < 10 \text{ L}^{-1}$ ), and  $\text{SIP}_{\text{high}}$  ( $10 \text{ L}^{-1} < \text{ICNC}_{\text{pr}<106 \mu\text{m}}$ ). The numbers refer to the number of 30 s intervals observed within each SIP class.

As described in Section 3, several environmental conditions (e.g., cloud droplet concentration and size, ice crystal size and habit, and temperature) influence the occurrence of SIP. Using the assumption that pristine ice crystals smaller than 106  $\mu\text{m}$  are associated with their environment of origin, we can relate SIP to the environmental conditions prevailing at the measurement location. The role of the different hydrometeor types and temperatures for the occurrence of SIP observed on the six days of measurements in MPCs is discussed below.

### 3.3.1 Role of the hydrometeor types for SIP

The comparison between  $\text{ICNC}_{\text{pr}<106\ \mu\text{m}}$  representative of SIP and the concentrations of cloud droplets (diameter  $< 64\ \mu\text{m}$ ), drizzle drops (diameter  $> 64\ \mu\text{m}$ ), frozen drops, and ice crystals help to understand their relationship to SIP. The analysis of the influence of ice crystals on SIP is delicate because it is possible that the larger ice crystals are secondary ice crystals having grown to larger sizes than the threshold used (106  $\mu\text{m}$ ). To overcome this issue, we discuss only the connection between SIP and ice crystals larger than 327  $\mu\text{m}$ , and refer to these as snow crystals. Snow crystals seem to follow the same trend as  $\text{ICNC}_{\text{pr}<106\ \mu\text{m}}$  (Fig. 3.11a,d) and the correlation coefficient between the concentrations of snow crystals and  $\text{ICNC}_{\text{pr}<106\ \mu\text{m}}$  amounts to 0.4. This demonstrates the obvious connection between snow crystals and SIP, i.e. primary ice is needed in order for SIP to be initiated. On the contrary, no obvious connection between  $\text{ICNC}_{\text{pr}<106\ \mu\text{m}}$  and cloud droplet is observed (correlation coefficient of 0.01). Indeed, the highest CDNCs prevail on 10 November 2019, when no evidence for SIP is observed and the CDNCs are mostly below 5  $\text{cm}^{-3}$  during the prevalence of  $\text{SIP}_{\text{mod}}$  and  $\text{SIP}_{\text{high}}$  events on 11 and 12 November 2019 (Fig. 3.11a,b). Drizzle drops are always observed during SIP occurrence, except on 1 April 2020, when only snow crystals are observed (Fig. 3.11a,b,d). This suggests that on 1 April 2020, the presence of snow crystals alone was sufficient for the occurrence of SIP, likely via the ice-ice collision process as discussed in Section 3.2.3. During the first flight on 11 November 2019, the highest drizzle drop number concentrations (up to 20  $\text{L}^{-1}$ ) were measured, but no SIP was observed. The reason is likely that there were not enough snow crystals colliding with the drizzle drops, thereby not initiating their freezing causing a lack of SIP via the droplet shattering process. In fact, no frozen drops were observed on this day. This indicates that freezing of drizzle drops via immersion or contact freezing with an INP is not sufficient to trigger droplet shattering at the temperature experienced ( $-8^\circ\text{C}$  to  $-2^\circ\text{C}$ ), but the presence of snow crystals is needed to initiate their freezing. Indeed, frozen drops are observed during 41.5% of  $\text{SIP}_{\text{all}}$  and 87.5% of the  $\text{SIP}_{\text{high}}$  events (Table 3.1).

To quantify the importance of different hydrometeor types for SIP, we calculate an occurrence enhancement factor (OEF) relative to  $\text{SIP}_{\text{no}}$  for all the SIP classes and for the hydrometeor types: cloud droplets, drizzle drops, frozen drops, and snow crystals. First, the frequency of occurrence of a hydrometeor type during each SIP class ( $F_{\text{SIP}_{\text{class}}}$ ) and the frequency of occurrence of a hydrometeor type during when no SIP is observed ( $F_{\text{SIP}_{\text{no}}}$ ) were calculated. Then, the OEF for every hydrometeor type and SIP class ( $\text{OEF}_{\text{SIP}_{\text{class}}}$ ) was derived as follows:

$$\text{OEF}_{\text{SIP}_{\text{class}}} = \frac{F_{\text{SIP}_{\text{class}}}}{F_{\text{SIP}_{\text{no}}}} \quad (3.1)$$

An OEF greater than unity signifies that the hydrometeor type is more frequently present during SIP than during  $\text{SIP}_{\text{no}}$  and thus hints at a possible connection between the hydrometeor type and the occurrence of SIP.



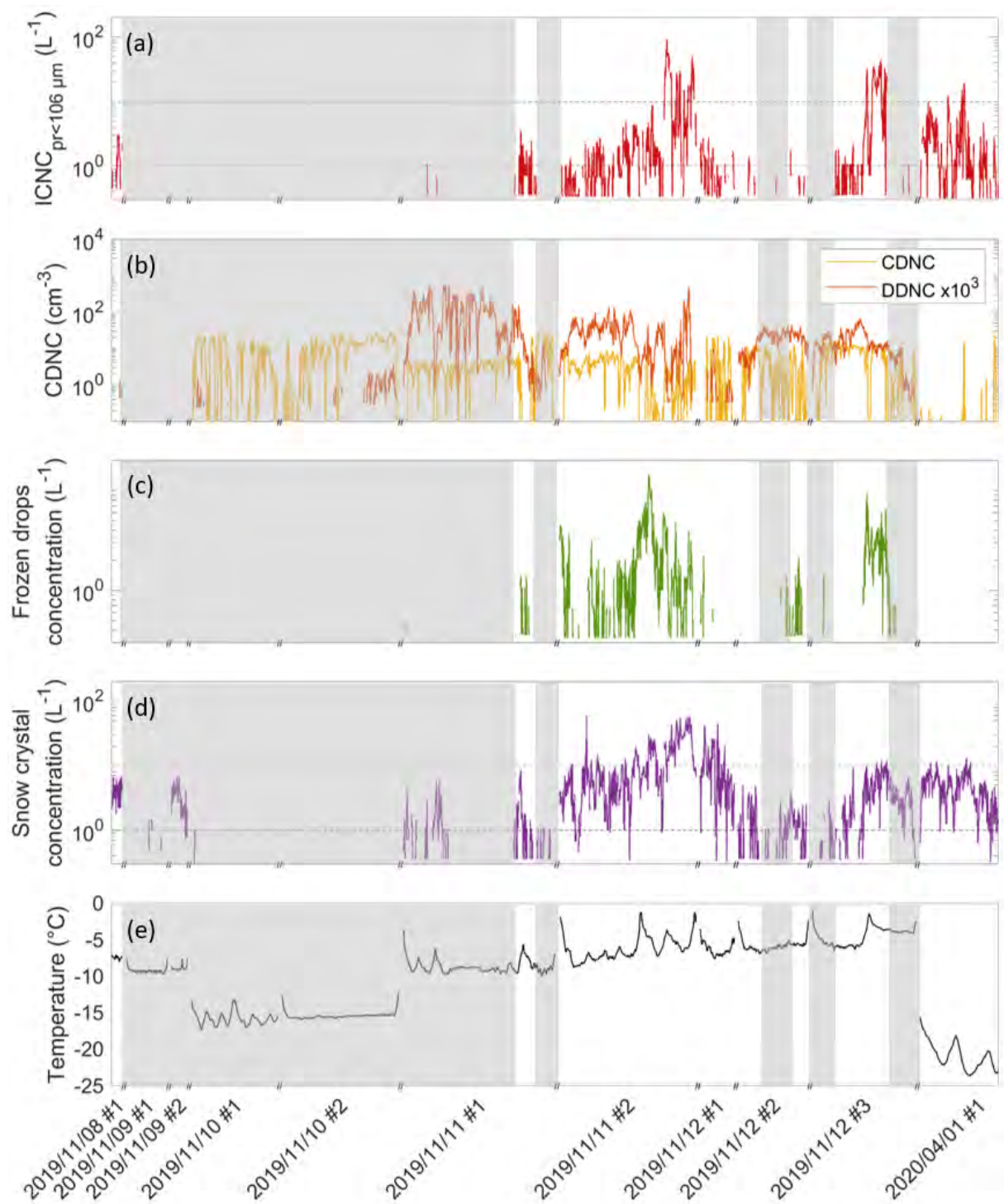


Figure 3.11: (a)  $\text{ICNC}_{\text{pr}<106 \mu\text{m}}$ , (b) CDNC and drizzle drop number concentrations (DDNC), (c) frozen drop number concentrations, and (d) snow crystals number concentrations retrieved with HOLIMO averaged over 30 s. The uncertainty for the concentration of cloud droplets is estimated to  $\pm 6\%$ , for the concentration of ice particles smaller than  $100 \mu\text{m}$  to  $\pm 5\%$  and for the concentration of snow crystals and frozen drops to  $\pm 15\%$ . (e) Temperature derived from the radiosondes at the HoloBalloon location. The breaks on the time axis separate measurement flights. The black dashed lines in panel (a) and (c) denote the  $\text{SIP}_{\text{mod}}$  ( $1 \text{ L}^{-1}$ ) and  $\text{SIP}_{\text{high}}$  ( $10 \text{ L}^{-1}$ ) limits. The white regions show the occurrence of SIP, whereas the grey shaded regions show no SIP.

During the presence of snow crystals, the frequency of occurrence of  $\text{SIP}_{\text{all}}$  compared to  $\text{SIP}_{\text{no}}$

is enhanced by a factor of 2.7, and  $SIP_{high}$  by a factor of 2.9 (Table 3.1). This further demonstrates that the production of ice crystals prior to SIP is required. The influence of a high concentration of cloud droplets on SIP was identified by using a threshold of  $CDNC > 5 \text{ cm}^{-3}$ , which represents the mean  $CDNC$  over the six measurement days. The OEF of cloud droplets is below 1 for all SIP classes except  $SIP_{high}$ , for which it is slightly increased to 1.33 (Table 3.1). This signifies that the occurrence of SIP is reduced compared to  $SIP_{no}$  when the concentration of cloud droplets was higher than  $5 \text{ cm}^{-3}$  and indicates that concentrations of cloud droplets exceeding  $5 \text{ cm}^{-3}$  were not necessary for SIP occurrence in the measurements presented. In contrast, the occurrences of all SIP classes are enhanced when drizzle drops are present, suggesting an influence of the droplet shattering mechanism. Finally, the occurrence of SIP is enhanced by a factor between 3 and 10 compared to  $SIP_{no}$  when frozen drops are observed (Table 3.1). This large enhancement is also consistent with a dominant role of the droplet shattering mechanism, especially for  $SIP_{mod}$  and  $SIP_{high}$ .

Previous studies have linked the presence of drizzle drops to the occurrence of SIP in tropical and midlatitude convective clouds (e.g., Lawson et al., 2015, 2017; Keppas et al., 2017). In convective clouds with a warm cloud base, the formation of drizzle drops occurs by collision-coalescence in updraft cores that extend over a large portion of the troposphere (Lawson et al., 2017). In other cases, the drizzle drops responsible for the initiation of droplet shattering close to the melting layer were suggested to originate from melted ice crystals recirculating through the melting layer within updrafts (Korolev et al., 2020; Lauber et al., 2021). Here, we propose that the formation of large drizzle drops, which are related to SIP, is determined by the low  $CCN$  concentration prevailing in the clean Arctic environment, together with the sufficiently high updraft speeds as observed in cloud containing drizzle drops during NASCENT. A connection between drizzle drops and ice crystal formation was already proposed by Rangno and Hobbs (2001) and Lance et al. (2011). However, they did not relate the formation of the ice crystals to SIP via the droplet shattering mechanisms.

In summary, no connection was found between the concentration of cloud droplets exceeding  $5 \text{ cm}^{-3}$  and SIP. On the contrary, a strong relationship exists between drizzle drops and SIP, with the prerequisite that sufficient snow crystals are present to initiate their freezing upon collision and activate the droplet shattering process. Moreover, snow crystals can be sufficient for triggering SIP via ice-ice collisions.

Table 3.1: Frequency of occurrence and OEF of the hydrometeor types cloud droplets (with concentrations larger than  $5 \text{ cm}^{-3}$ ), drizzle drops, frozen drops, and snow crystals during all measurements ( $N_{all}$ ),  $SIP_{all}$ ,  $SIP_{low}$ ,  $SIP_{mod}$ , and  $SIP_{high}$ . Bold font signifies OEF values larger than 1, i.e. enhancements.

		$N_{all}$	$SIP_{no}$	$SIP_{all}$	$SIP_{low}$	$SIP_{mod}$	$SIP_{high}$
Cloud droplets	F (%)	32.5	35.5	28	28.5	22.5	47.5
	OEF			0.78	0.8	0.63	<b>1.33</b>
Drizzle drops	F (%)	58.5	53.5	65.5	69.5	56.5	85
	OEF			<b>1.22</b>	<b>1.3</b>	<b>1.05</b>	<b>1.59</b>
Frozen drops	F (%)	22	8.5	41.5	32	77.5	87.5
	OEF			<b>4.95</b>	<b>3.78</b>	<b>9.2</b>	<b>10.37</b>
Snow crystals	F (%)	58	35	93	87	99	100
	OEF			<b>2.7</b>	<b>2.5</b>	<b>2.8</b>	<b>2.9</b>

### 3.3.2 Temperature

During the six days of MPC observations, measurements covered temperatures between  $-24 \text{ }^\circ\text{C}$  and  $-1 \text{ }^\circ\text{C}$ , albeit with very few measurements between  $-14 \text{ }^\circ\text{C}$  and  $-10 \text{ }^\circ\text{C}$  (Fig. 3.12c,d). Between  $-8 \text{ }^\circ\text{C}$  and  $-2 \text{ }^\circ\text{C}$ , evidence of SIP was observed between 55% and 75% of the time (Fig. 3.12c).

Meanwhile, at temperatures below  $-18\text{ }^{\circ}\text{C}$ , evidence of SIP was almost always observed, with 96% of the measurements involving SIP (Fig. 3.12c). However, the measurements obtained at these low temperatures originate solely from 1 April 2020 (Fig. 3.12d) and are related to the ice-ice collision process, as discussed in Section 3.2.3. It should also be noted that the large number of measurements without SIP at  $-16\text{ }^{\circ}\text{C}$  occurred during the cloud case on 10 November 2019 (Fig. 3.12d), when ice formation was limited by the INPC, as discussed in Section 3.2.1 (see also the temperature evolution during the flights in Figure 3.11e).

In addition to the frequency of occurrence of SIP, the number of secondary ice crystals produced determine the impact of SIP. The distribution of the fraction of  $\text{ICNC}_{\text{pr}<106\text{ }\mu\text{m}}$  to total ICNC as a function of temperature and  $\text{ICNC}_{\text{pr}<106\text{ }\mu\text{m}}$  (Fig. 3.12b) gives information on the number of ice crystals produced by SIP at each temperature. The highest  $\text{ICNC}_{\text{pr}<106\text{ }\mu\text{m}}$  were observed at temperatures between  $-7\text{ }^{\circ}\text{C}$  and  $-2\text{ }^{\circ}\text{C}$ , with concentrations exceeding  $50\text{ L}^{-1}$  (i.e., in the  $\text{SIP}_{\text{high}}$  class) between  $-5\text{ }^{\circ}\text{C}$  and  $-3\text{ }^{\circ}\text{C}$  (Fig. 3.12b). Measurements performed on 11 and 12 November 2019 are responsible for this  $\text{SIP}_{\text{high}}$  event (Fig. 3.12d) and are mainly caused by the droplet shattering and the ice-ice collision processes (as discussed in Section 3.2.2 and Pasquier et al. (2021)). Moderate to high  $\text{ICNC}_{\text{pr}<106\text{ }\mu\text{m}}$  ( $\text{SIP}_{\text{mod}}$  and  $\text{SIP}_{\text{high}}$  classes) were also observed at temperatures between  $-24\text{ }^{\circ}\text{C}$  and  $-16\text{ }^{\circ}\text{C}$  on 1 April 2020 (Fig. 3.12b,d). Note that the warmer temperature range ( $-7\text{ }^{\circ}\text{C}$  and  $-2\text{ }^{\circ}\text{C}$ ) overlaps with the rime-splintering process. However, since the other criteria for the rime-splintering process (i.e., rimed ice crystals and a sufficient concentrations of cloud droplets with diameters smaller than  $12\text{ }\mu\text{m}$ ) were not met during the measurements with SIP, the contribution of the rime-splintering process is assumed to be negligible.

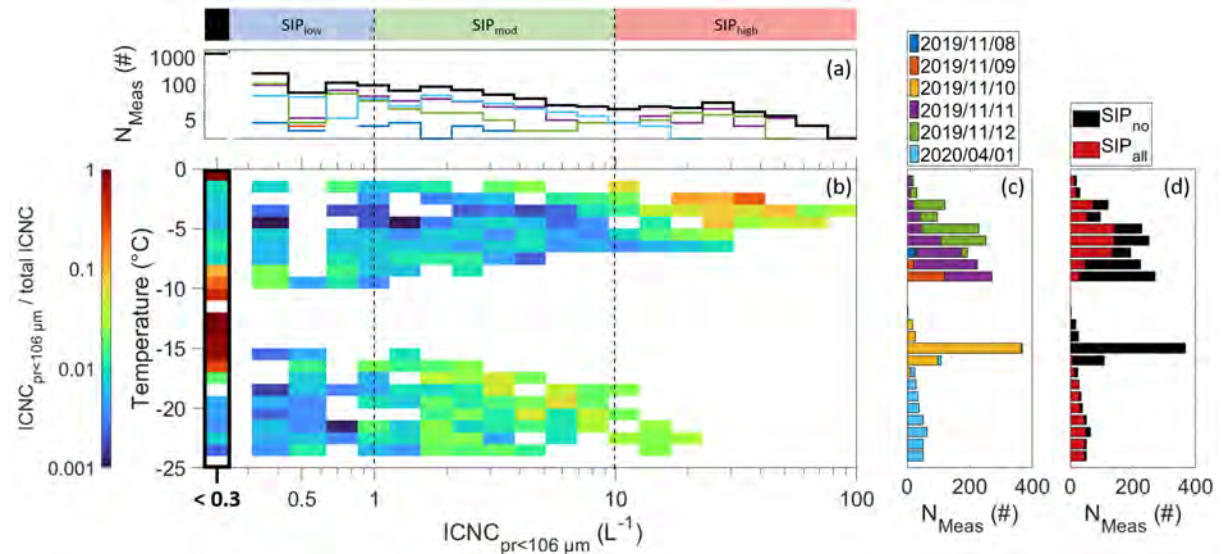


Figure 3.12: (a) Number of measurements for each  $\text{ICNC}_{\text{pr}<106\text{ }\mu\text{m}}$  bin (note the log scale) for each day of measurements (color lines) and all measurements (black line). The  $\text{ICNC}_{\text{pr}<106\text{ }\mu\text{m}}$  regions defined as  $\text{SIP}_{\text{low}}$ ,  $\text{SIP}_{\text{mod}}$ ,  $\text{SIP}_{\text{high}}$  are shown on top and  $\text{SIP}_{\text{no}}$  is represented with a black box. (b)  $\text{ICNC}_{\text{pr}<106\text{ }\mu\text{m}}$  fraction from total ICNC for each temperature bin of  $1\text{ }^{\circ}\text{C}$  (color shading) and  $\text{ICNC}_{\text{pr}<106\text{ }\mu\text{m}}$  bin. The frequency of  $\text{ICNC}_{\text{pr}<106\text{ }\mu\text{m}} < 0.3\text{ L}^{-1}$  to ICNC ( $\text{SIP}_{\text{no}}$  class conditions) is highlighted by the thick black frame. A concentration of  $0.3\text{ L}^{-1}$  was used for the calculation of  $\text{ICNC}_{\text{pr}<106\text{ }\mu\text{m}}$  to total ICNC when no ice crystal was measured in the 30 s interval. (c) Number of measurements ( $N_{\text{meas}}$ ) per temperature bin ( $1\text{ }^{\circ}\text{C}$ ) for measurements with SIP (red bars), and for measurements with  $\text{SIP}_{\text{no}}$  (black bars). (d) Number of measurements ( $N_{\text{meas}}$ ) per temperature bin for each day of measurements (colored lines). The data were averaged over 30 s for the analysis.

The concentrations of small ice crystals are higher (Fig. 3.12b), but the proportion of measurements with SIP occurrence (Fig. 3.12c) was lower on 11 and 12 November 2019 between

-7 °C and -2 °C, compared to measurements obtained on 1 April 2020 between -24 °C and -18 °C. Thus, the droplet shattering processes found to be active at the warmer temperatures on 11 and 12 November seems to be less frequently active but to create more splinters than the ice-ice collision process found to be active at the colder temperatures on 1 April 2020. This would be in agreement with laboratory studies showing that a large number of splinters ( $>10$ ) can be produced from the freezing of a single drop (Lauber et al., 2018; Korolev and Leisner, 2020) Note however that one measurement flight at lower temperature is not sufficient to draw a conclusive statement about the number splinters produced at these temperatures.

To conclude, SIP occurred over the entire temperature range where measurements were performed, with the highest concentrations of ice crystals smaller than 106  $\mu\text{m}$  ( $>50 \text{ L}^{-1}$ ) observed between -3° and -5 °C caused mainly by the droplet shattering process and the highest percentage of the measurements with SIP between -18° and -24 °C caused by the ice-ice collision mechanism. This denotes the importance of the droplet shattering and ice-ice collision mechanisms over a large temperature range and highlights the necessity to include these processes over a larger temperature range in numerical weather and climate models.

## Conclusion

In this paper, the microphysical properties of Arctic MPCs measured during the NASCENT campaign with the tethered balloon system HoloBalloon during five consecutive days from 8 to 12 November 2019 and on 1 April 2020, together with ground-based INP and remote sensing measurements as well as radiosonde profiling are discussed. An emphasis is placed on the formation of ice crystals, especially on the occurrence of SIP, and on the environmental conditions favorable for SIP. We used the concentration of small pristine ice crystals ( $\text{ICNC}_{\text{pr}<106 \mu\text{m}}$ ) to identify SIP occurring in the 60 to 120 s preceding the measurements. The key findings are summarized as follows:

- SIP regions were identified in 40% of the in-cloud measurements. In one probed MPC on 10 November 2019, ice crystal formation was limited by the concentration of aerosols acting as INPs at -17 °C. In two other MPCs on 11 and 12 November 2019, the  $\text{ICNC}_{\text{pr}<106 \mu\text{m}}$  suddenly increased from below 1  $\text{L}^{-1}$  ( $\text{SIP}_{\text{low}}$ ) to more than 50  $\text{L}^{-1}$  ( $\text{SIP}_{\text{high}}$ ) due to the droplet shattering mechanism, which most likely generated a positive SIP feedback loop by creating splinters causing the freezing of additional droplets, creating splinters again. Finally, in two MPCs on 11 November 2019 and on 1 April 2020, the ice-ice collision mechanism was proposed to be responsible for moderate to high SIP ( $\text{ICNC}_{\text{pr}<106 \mu\text{m}}$  up to 15  $\text{L}^{-1}$ ).

- Drizzle drops were found to be favorable for the occurrence of SIP, as the frequency of SIP was enhanced in the presence of drizzle drops. Moreover, the frequency of occurrence of frozen drops was enhanced by a factor of 5 during SIP events (Table 3.1), whereby frozen drops were measured in 87.5% of the  $\text{SIP}_{\text{high}}$  observations. Thus, freezing of drizzle drops was strongly favorable for SIP, which indicates a large contribution from the droplet shattering mechanism. We relate the presence of drizzle drops itself to the strong updrafts and low CCN concentrations observed in the clean Arctic environment.

- SIP cloud regions were observed over a large temperature range (-24 °C to -1 °C). The highest concentrations of secondary ice crystals were measured between -5 °C and -3 °C ( $>50 \text{ L}^{-1}$ , Fig. 3.12b) and related mainly to the droplet shattering mechanism (Section 3.2.2), while the highest proportion of the measurements showed the occurrence of SIP between -24 °C and -18 °C (up to 95%, Fig. 3.12c) in one MPC related to the ice-ice collision mechanism (Section 3.2.3). This emphasizes the need to include SIP parametrizations for this two processes over a large temperatures range in numerical weather prediction models, which generally only include

a parametrization for the rime-splintering process active at temperatures between  $-8\text{ }^{\circ}\text{C}$  and  $-3\text{ }^{\circ}\text{C}$ .

Overall, this study observed a large variety of microphysical properties of Arctic MPCs during the six days of measurements including two SIP mechanisms and the conditions favorable for these SIP mechanisms were discussed. However, further field and laboratory studies are required to better constrain the environmental conditions favorable for SIP in order to develop robust SIP parametrizations for numerical weather prediction models. In particular, field studies should characterize in-cloud INPC up to high sub-freezing temperatures ( $>10\text{ }^{\circ}\text{C}$ ) to accurately constrain the SIP rate. Furthermore, we especially recommend to include the presence of drizzle drops and their collision frequency with ice to estimate the contribution from the droplet shattering mechanism, which was shown to play an important role for ice crystal formation in the observed Arctic MPC. Finally, we propose to extend the SIP parametrizations to all sub-freezing temperatures, as SIP was observed down to  $-24\text{ }^{\circ}\text{C}$  in one sampled Arctic MPC.

## Data and colde availability

The cloud microphysical and aerosol datasets as well as the scripts to reproduce the figures will be available on Zenodo (<https://zenodo.org/>). Radiosonde and surface weather data are available in PANGAEA (<https://www.pangaea.de/>) (Maturilli, 2020f,a,e,b).

## Author contribution

JTP analyzed the cloud observational data and prepared the figures of the paper. FR, JH, ROD, AL, JW, and UL helped in analyzing and interpreting the observational data. JTP, JW, ROD, TC, JH performed the HoloBalloon measurements. JW performed the INP measurements. RG processed the remote sensing data and helped in interpreting the remote sensing observations. MM was responsible for the radiosonde launches during the NASCENT campaign. JTP prepared the manuscript with contributions from all authors.

## Acknowledgements

This project has received funding from the European Union’s Horizon 2020 research and innovation programme under grant agreement No 821205 (FORCeS), from the Swiss Polar Institute (Exploratory Grants 2018), and from the Swiss National Science Foundation (SNSF) (grant no. 200021\_175824). RG and MM gratefully acknowledge the funding by the Deutsche Forschungsgemeinschaft (DFG, German Research Foundation) – Project-ID 268020496 – TRR 172, within the Transregional Collaborative Research Center “ArctiC Amplification: Climate Relevant Atmospheric and SurfaCe Processes, and Feedback Mechanisms (AC)3”. ROD and TC gratefully acknowledge the funding by the European Research Council (ERC) through Grant StG758005. We thank Prof. Alexei Korolev for the fruitful scientific discussions. We thank Michael Roesch for his help in the installation of the setup for the campaign. We would also like to particularly thank Roland Neuber and Paul Zieger for their support and advice during the organisation of the campaign. We thank all those involved in the field work associated with NASCENT, particularly the AWIPEV and Norwegian Polar Institute Sverdrup stations staff.



## Auxiliary parameters

### Potential temperature and wind profile

The potential temperature and wind profiles observed from the radiosondes on the six days of measurements suggest well-mixed boundary layers and no strongly decoupled cloud is observed.

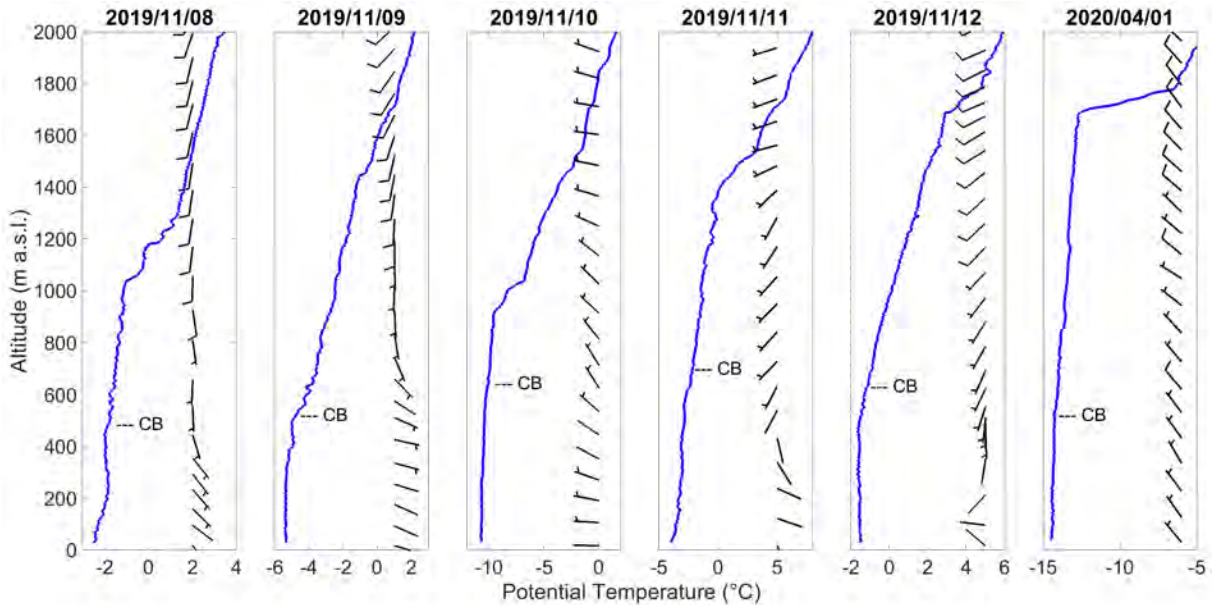


Figure 3.13: Potential temperature and wind speed and direction measured by the radiosonde launched at 11:00 UTC or 17:00 UTC on the six days of measurements. The mean cloud base (CB) measured with the ceilometer is labeled.

### Cloud top and HoloBalloon temperature and relative humidity determination from radiosonde measurements

The temperature profile from the radiosondes was used to determine the ambient temperature at HoloBalloon's measurement location and the cloud top temperature. If several radiosondes were launched during a day, the temperature profile between two launches was linearly interpolated from the two closest profiles. If only the daily radiosonde was launched, the temperature profile was used for the whole day. The same method was applied for the relative humidity. The cloud top altitude was determined from the first altitude where the cloud radar does not measure the reflectivity and a running mean over 5 minutes was used to smooth high temporal variability in cloud top height. From this altitude the temperature at cloud top was derived.

### Updraft wind speed estimate

As the Doppler velocity is the sum of the fall velocity of cloud particles and updraft/downdraft, the largest Doppler velocities within a measured Doppler spectrum can be used as approximation for the updraft velocities experienced by the smallest cloud particles (Shupe et al., 2008b). We use a similar approach as in Ramelli et al. (2021b) to estimate the updraft velocity from the maximum Doppler velocity derived from the Doppler spectra as shown in Figure 3.14. First, a running mean was used to smooth the Doppler spectra. If the difference between  $Z_{\max}$  and  $Z_{\min}$  exceeded 20 dBZ, the maximum Doppler velocity  $v_{\max}$  was derived as follows:

$$v_{\max} = \text{maximal Doppler velocity where } Z \geq (Z_{\min} + 0.2 * (Z_{\max} - Z_{\min})) \quad (3.2)$$

where  $Z_{\max}$  and  $Z_{\min}$  are the maximum and minimum radar reflectivity. If the difference between  $Z_{\max}$  and  $Z_{\min}$  was lower than 20 dBZ,  $v_{\max}$  was derived at -47 dBZ to avoid the selection of noise in Doppler spectra with low amplitude. The threshold of -47 dBZ was chosen because it is the lowest reflectivity that was typically above the noise level. A positive (negative) Doppler velocity indicates downdraft (updraft). Note that in the absence of small cloud particles, the updraft may be strongly underestimated by this method.

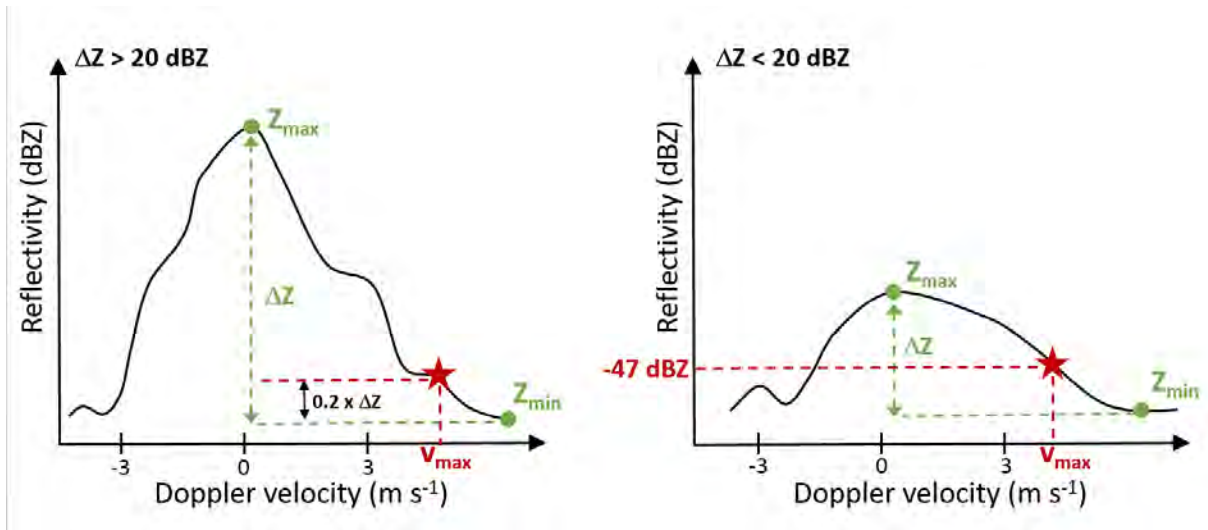


Figure 3.14: Schematic of the derivation of the maximum Doppler velocity  $v_{\max}$  (red star) from the Doppler spectra.  $Z_{\min}$  and  $Z_{\max}$  (green dots) are the minimum and maximum radar reflectivity (see the text for more details).



## Chapter 4

# Understanding the history of complex ice crystal habits deduced from a holographic imager

J. T. Pasquier (1), J. Henneberger (1), A. Korolev (2), F. Ramelli (1), J. Wieder (1), A. Lauber (1), R. O. David (3), T. Carlsen (3), G. Li (1), R. Gierens (4), M. Maturilli (5), U. Lohmann (1)

(1) Department of Environmental System Sciences, Institute for Atmospheric and Climate Science, ETH Zurich, Zurich, Switzerland

(2) Environment and Climate Change Canada, Toronto, Canada

(3) Department of Geosciences, University of Oslo, Norway

(4) Institute for Geophysics and Meteorology, University of Cologne, Cologne, Germany

(5) Alfred Wegener Institute, Helmholtz Centre for Polar and Marine Research (AWI), Potsdam, Germany

*This manuscript is in preparation to be submitted to Geophysical Research Letters.*

---

### Abstract

The sizes and shapes of the ice crystals influence the radiative properties of the clouds, as well as precipitation initiation and aerosol scavenging. Although the formation of ice crystals has been investigated since decades (e.g., Nakaya, 1954; Libbrecht, 2005), their growth mechanisms remain only partially characterised (Libbrecht, 2017). Here, we present the growth processes of two types of complex ice crystal habits observed in Arctic mixed-phase clouds during the Ny-Ålesund AeroSol Cloud Experiment (NASCENT) campaign. First, so-called recirculation particles show evidences for successive growth in the column and plate temperature regimes. These ice crystals originated from a column growing regions of the cloud between  $-10^{\circ}\text{C}$  and  $-3^{\circ}\text{C}$ , were then lifted up or down in parts of the clouds where the temperature was below  $-10^{\circ}\text{C}$  or above  $-3^{\circ}\text{C}$  where they grew in the plate regime, before being brought back to the same environmental conditions where they had formed originally. Second, aged-rimmed plates and columns were observed, exhibiting faceted protuberances that were growing from rime on their surface. Despite their complexity, the shapes of these ice crystals enable us to infer their growth history and provides information about the environmental conditions prevailing in the clouds, such as temperature, supersaturation and/or changing updraft velocities.

## Plain Language Summary

Snowflakes have a wide variety of shapes and sizes and not two of them look exactly the same. The reason for this infinite number of shapes is that the environmental temperature and relative humidity prevailing during the snowflake's formation determine their exact aspects. As every snowflake is exposed to slightly different environmental conditions during its growth, every snowflake is different. The shape of snowflakes provides therefore information about the environmental conditions to which they were exposed during their growth. However, with increasing shape complexity, the exact determination of the environmental conditions prevailing during the snowflake's formation is difficult. During a measurement campaign in the Arctic, we measured two types of snowflakes with particularly complex shapes and were able to relate them to the environmental conditions in which they grew in with precision. We could establish that some snowflakes were recirculating to higher or lower parts of the clouds and that other snowflakes had collided with cloud droplets only at the early stage of their growth.

### 4.1 Introduction

Clouds produce snowflakes of a fascinating diversity of shapes and patterns, and not two single ice crystals are identical. The shape of ice crystals influence the radiative properties of clouds (e.g., Järvinen et al., 2018) as ice crystal habits influence their scattering properties (Wyser, 1999). Ice crystals with larger surface roughness cause additional shortwave cooling (Yi et al., 2013; Järvinen et al., 2018). In addition, the shapes and sizes of ice crystals determine their fall velocities. This, in turn, impacts their collision rates with other cloud particles and hence precipitation formation as well as the cloud lifetime, which is of high importance for the radiative budget (Morrison et al., 2011). The shape and fall velocity of the ice crystals also affect their collision rate with aerosol particles and thus the scavenging rate which influences the aerosol concentrations and clouds, and their respective radiative forcings (Croft et al., 2009). However, despite the extensive research performed since more than 75 years (e.g., Nakaya, 1954; Korolev et al., 1999; Libbrecht, 2005, 2017), the ice crystals growth mechanisms remain only partly understood and characterized (Libbrecht, 2017).

Ice crystals grow by water vapour diffusion to pristine columns or plates. Meanwhile, the shape of hexagonal ice crystals depends on the experienced temperature and water vapour supersaturation with respect to ice (Nakaya, 1954; Libbrecht, 2005). If the nucleation barrier for the basal face of the ice crystal is lower, it grows faster and the ice crystals develop into plates (Libbrecht, 2005). On the contrary, if the nucleation barrier for the prism face is lower, they develop into columns (Libbrecht, 2005). Nakaya (1954), who was the first to investigate ice crystal shapes using precipitating snowflakes as well as synthetically grown ice crystals, summarised his observations into a so-called *snow crystal morphology diagram* or *Nakaya diagram* (Nakaya, 1954). This diagram shows that the ice crystal's growth is plate-like at temperatures above about  $-3^{\circ}\text{C}$ , columnar between  $-3^{\circ}\text{C}$  and  $-10^{\circ}\text{C}$ , and plate like again at colder temperatures. Furthermore, the structures of the ice crystals get more complicated with increasing supersaturation and develop to e.g., needles, sheaths (hollow columns or bullets), dendrites or rosettes (Bailey and Hallett, 2009; Pruppacher and Klett, 2010; Knight, 2012). In addition to growth by diffusion, ice crystals can grow by aggregation of several ice crystals or by riming of cloud droplets on their surface, and thereby loose their pristine plate or column shapes.

The appearance of ice crystals thus gives information about their history within clouds. In particular, it indicates the mechanism involved in ice crystal growth (diffusional growth or growth by accretion). Moreover, if ice crystal have a pristine shape, the temperature and supersaturation experienced during the growth by diffusion can be deduced, and the time of formation can be approximated from the size of the ice crystal. On the contrary, little can be determined from ice crystals with complex shapes having grown by accretion, except for the presence of cloud

droplets and/or other ice crystals within the cloud.

This work builds on previous studies that investigated the growth history of ice crystals using their shapes and extends the analysis to two types of ice particles with complex habits. To this aim, we use images obtained with a holographic imager mounted on a tethered balloon system (Ramelli et al., 2020) in Arctic mixed-phase clouds, together with temperature measurements obtained from radiosondes and cloud radar retrieval obtained during the Ny-Ålesund AeroSol Cloud Experiment (NASCENT) campaign (Pasquier et al., 2021).

## 4.2 Methods

The data presented in this paper was collected in Ny-Ålesund, Svalbard (78.9°N, 11.9°E), during the NASCENT campaign (Pasquier et al., 2021). The main instrument used was the HOLOGraphic cloud Imager for Microscopic Objects (HOLIMO) that was mounted on the tethered balloon system HoloBalloon (Ramelli et al., 2020). HOLIMO uses in-line holography to image cloud particles in the size range from small cloud droplets (6  $\mu\text{m}$ ) to large precipitating ice particles (2 mm) in a three-dimensional sample volume of approximately 15  $\text{cm}^3$  (Henneberger et al., 2013; Beck et al., 2017; Ramelli et al., 2020). Ice crystals of sizes down to 25  $\mu\text{m}$  are captured and the pictures are used to classify their habits manually based on their shape.

The in-situ holographic measurements were complemented by ground-based remote sensing instruments installed at the French–German Arctic Research Base (AWIPEV). In particular, the 94 GHz cloud radar of University of Cologne (JOYRAD-94, Küchler et al., 2017) and the ceilometer (Maturilli and Ebell, 2018, Vaisaila-CL51,) were used to acquire continuous information on the vertical structure of the clouds. In addition, radiosondes were launched (Maturilli and Kayser, 2017) to obtain information about the vertical distribution of wind, temperature, and humidity in the atmosphere.

## 4.3 Results

A large variety of ice crystal sizes and shapes were identified with HOLIMO during the NASCENT campaign. In particular, the typical ice crystal habits as defined in the snow crystal morphology diagram were identified (Fig. 4.1). First, columns with lengths ranging from a few micrometers to almost 1 cm and with varying aspect ratios ( $\sim 1$  to  $\geq 12$ ). Some observed columns are bright in their centre, indicating that they are hollow columns. Second, plates of varying size, thickness, and pattern were observed (Fig. 4.1). Third, a few dendrite-like ice crystals were observed, indicating a high supersaturation in the measured clouds. In addition to these pristine ice crystal habits, many aged ice crystals with signs of aggregation and/or riming were observed. For these ice crystals, it is impossible to determine with certainty their original ice crystal habit (column, plate, dendrite).

In addition, two particular ice crystal habits having complex structures but still providing information about their origin and growth history were observed. First, particles growing successively in different temperature regimes, which is evidence for their recirculation within the clouds, are named *recirculation particles*. Second, particles with faceted protuberances originating from growing rime are defined as *aged-rimed particles*. We will explain the growth processes of these two ice crystal types in the following sections.

### 4.3.1 Observation of recirculation particles

On 11 November 2019, a stratocumulus with cloud top height increasing from 1700 m to 2200 m a.s.l. was observed over Ny-Ålesund (Fig. 4.2). The temperature retrieved from the radiosonde was  $-3^\circ\text{C}$  at 300 m a.s.l.,  $-10^\circ\text{C}$  at 1300 m a.s.l., and  $-14^\circ\text{C}$  at cloud top at 2200 m a.s.l. The Doppler velocity, which consists of the sum of the updraft and fall velocities of cloud particles,

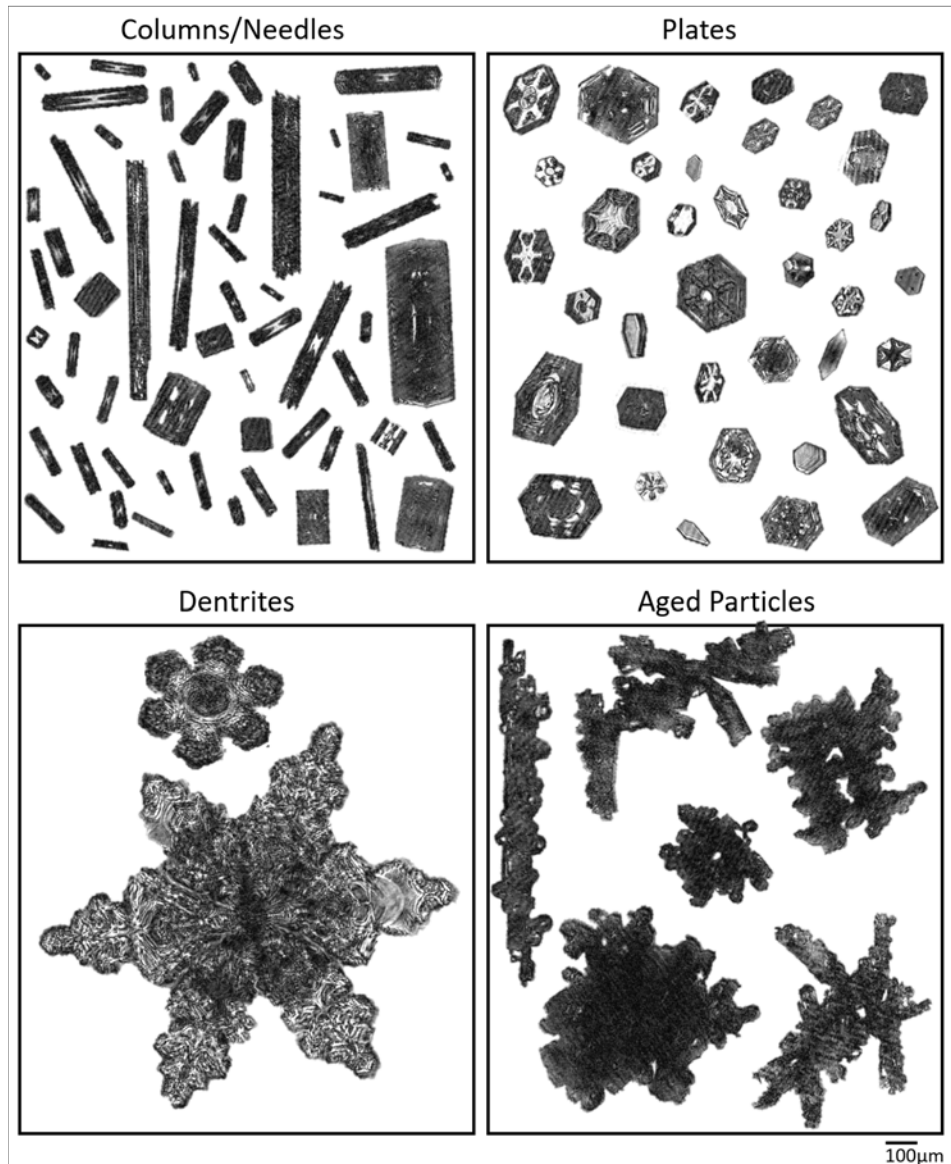


Figure 4.1: Examples of ice crystals observed with HOLIMO and classified manually as columns, plates, dendrites, and aged particles. The scale bar at the bottom right applies for all panels.

indicates a turbulent cloud structure and rapidly changing updraft/downdraft velocities within the cloud. A flight was performed with HoloBalloon into the cloud deck at temperature between  $-3^{\circ}\text{C}$  and  $-10^{\circ}\text{C}$  (Fig. 4.2), which is the temperature regime where columnar growth is expected (Nakaya, 1954; Libbrecht, 2005). Correspondingly, many columnar crystals together with aged ice crystals showing signs of aggregation and riming were observed during this flight (not shown). However, particles with columnar and plate-like shapes were also formed in this cloud (Fig. 4.3 right). This signifies that these ice particles have experienced growth both in columnar and plate growth environments. As the ice crystal grew into plates or columns depending on the temperature, which decreased with altitude, these ice crystals were growing at different altitudes within the cloud. Indeed, we suggest that the particles started to grow as columns between  $-10^{\circ}\text{C}$  and  $-3^{\circ}\text{C}$  between 300 m a.s.l. 1300 m a.s.l. (Fig. 4.3). Then, they were transported upward (above  $\sim 1300$  m a.s.l.) to colder ( $\leq -10^{\circ}\text{C}$ ) or downward (below  $\sim 300$  m a.s.l.) to warmer ( $\geq -3^{\circ}\text{C}$ ) regions of the cloud, grew in plate growth conditions, and developed into capped columns (Fig. 4.3). The crystals were then transported back to the columnar growth environment

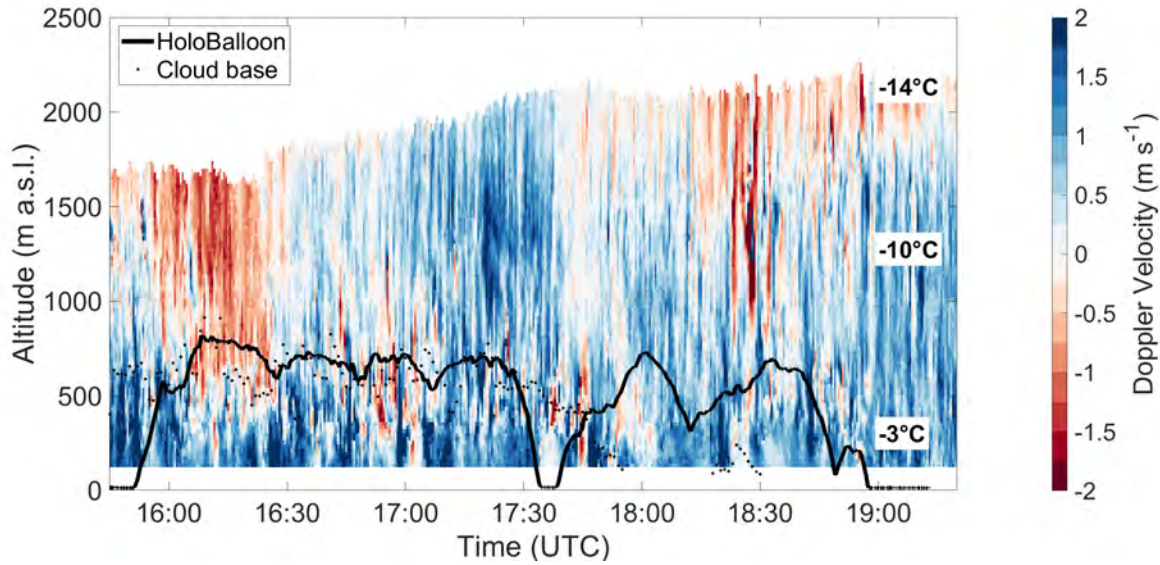


Figure 4.2: Doppler velocity (colour), HoloBalloon path (black line) and cloud base height measured by the ceilometer (black dots) on 11 November 2019. The cloud top temperature as well as the altitudes where  $-3^{\circ}\text{C}$  and  $-10^{\circ}\text{C}$  were measured by the radiosondes launched at 20:00 UTC are indicated.

(between  $-10^{\circ}\text{C}$  and  $-3^{\circ}\text{C}$ ) and developed columns that grow out of their plate corners (Fig. 4.3). The columns preferentially grow at the corners of the plate where the supersaturation is highest. Such recirculation particles give insight on the cloud's properties, which can be very helpful in the

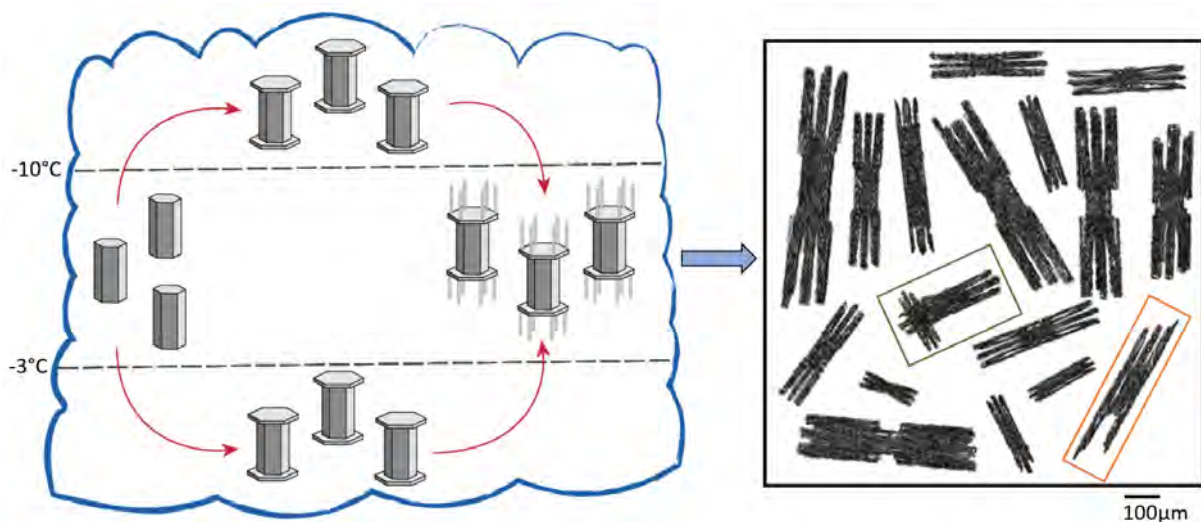


Figure 4.3: Schematic of the growth of recirculation particles within clouds. See text for detailed description. Examples of recirculation particles observed with HOLIMO. An example of two aggregated recirculation particles is highlighted with the green frame, and of a recirculation particle with a missing column is highlighted with the orange frame.

absence of collocated cloud radar and radiosonde measurements. First, the temperature at the measurement location must range between  $-3^{\circ}$  and  $-10^{\circ}\text{C}$ , and the cloud top temperature below  $-10^{\circ}\text{C}$  or cloud base temperature above  $-3^{\circ}\text{C}$ . Second, changing updraft velocities must have been prevailing, enabling the lifting of the ice particles within the cloud. Third, the recirculation particles observed show no sign of riming (Fig. 4.3). Despite their recirculation within the cloud, the ice crystals were thus not colliding with cloud droplets. This suggests a low liquid water

content within the observed cloud. Indeed the mean liquid water content observed with HOLIMO amounted to  $0.07 \text{ g m}^{-3}$ . In addition, observed droplets were large (mean droplet diameter  $31 \mu\text{m}$ ) making riming less likely.

Some recirculation particles were aggregated (see the particle highlighted with the green frame in Figure 4.3) and some particles had one or more columns growing from the plates missing (see the particle highlighted with the orange frame in Figure 4.3). This suggests that some branches broke off from the recirculation particles upon collision and created secondary ice particles. As the outer columns of the recirculation particles seem to be rather fragile, these particles could be favorable for the initiation of secondary ice production (Pasquier et al., 2022b).

### 4.3.2 Observation of aged-rimed particles

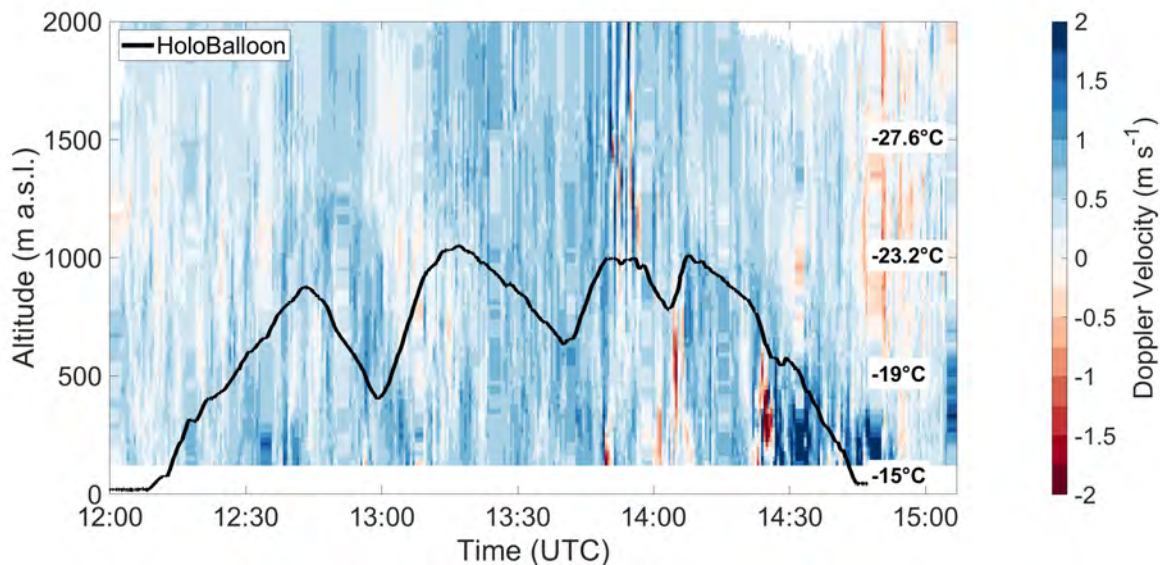


Figure 4.4: Doppler velocity (colour) and HoloBalloon path (black line) on 1 April 2020. The temperature is indicated every 500 m in altitude as measured by the radiosondes launched at 17:00 UTC. Note that the cloud base measured by the ceilometer is not shown because its detection was obstructed by snowfall and blowing snow.

Other ice crystals observed on 11 November 2019 with HOLIMO were aged-rimed columns. These particles have particular faceted protuberances that grew in the columnar growth regime, similar to the original column (Fig. 4.5 top). Ice crystal showing similar, but plate-like, faceted protuberances growing on plates were observed on 1 April 2020 (Fig. 4.5 bottom). On this day, the temperature in the cloud measured with HoloBalloon varied between  $-15^\circ\text{C}$  to  $-23.5^\circ\text{C}$  (Fig. 4.4), hence in the plate growth regime with low supersaturation with respect to ice (Nakaya, 1954). The Doppler velocities measured by the cloud radar show less variation except at around 14:30 UTC (Fig. 4.4), therefore the updraft/downdraft velocities seem to be more constant than on 11 November 2019 (Fig. 4.2). The formation of aged-rimed ice crystals occurs as follows (see also Figure 4.5): first cloud droplets rime on the columnar or plate-like ice crystal and freeze. The frozen protuberances then grow on the basal face (plate growth regime) or prism face (columnar growth regime) depending on the temperature and supersaturation experienced. Note that the orientation of the growing protuberance in the basal or prism face remains identical to that of the original ice crystal. This creates faceted protuberances observed on aged-rimed particles, in comparison to the smaller round protuberances observed on freshly rimed ice crystals. For aged-rimed plates this produces rectangular-like protuberance are obtained because the columns are observed from the side on the 2D holographic images. The presence of aged-rimed without



fresh rime suggests that the ice crystal originates from a region with a higher liquid water content than at the measurement location. In addition, several aged-rimed plates showed evidence of breaking, as for example the particle highlighted with the orange frame in Figure 4.5. The fragility of the aged-rimed particles could augment their chance of breaking upon collision with other ice crystals. Therefore they could favor secondary ice production via the ice-ice collision process.

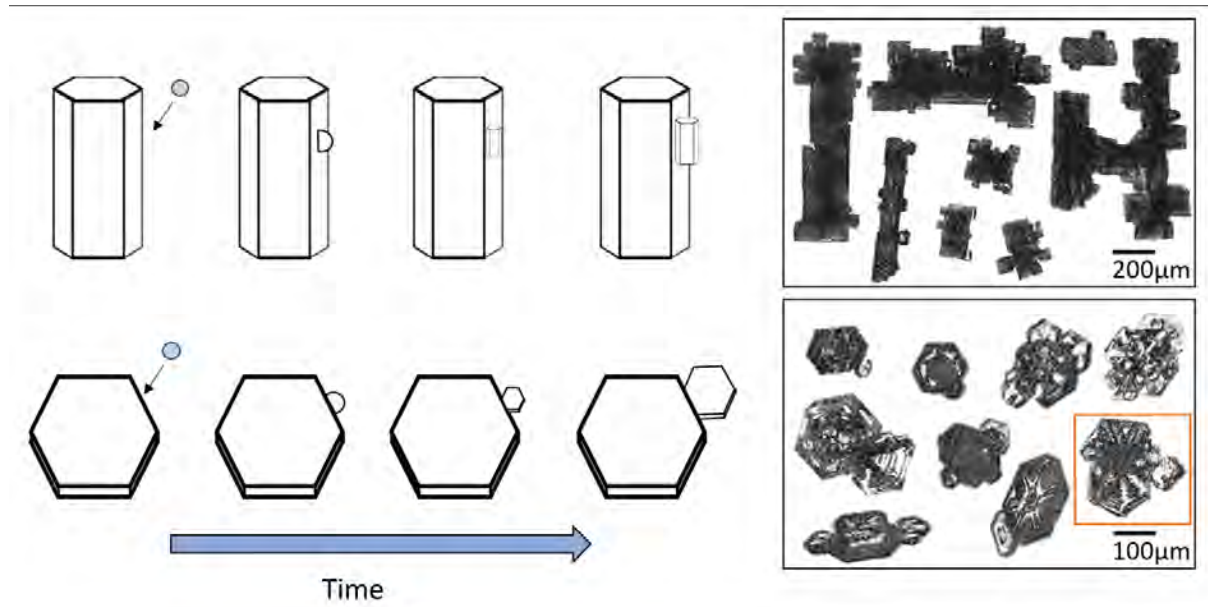


Figure 4.5: Growth of columns and plates after a droplet collided, rimed, and grew in the columnar or plate regime. These ice crystals are referred to as aged-rimed and examples of such ice crystals measured with HOLIMO are shown in the black frames on the right. An aged-rimed plate showing signs of breaking is highlighted with an orange frame.

## 4.4 Summary

The growth of ice crystals to typical habits has been investigated since decades (i.e., Nakaya, 1954; Libbrecht, 2005) and is important for cloud radiative properties, for precipitation formation, and scavenging processes. The habits of pristine ice crystals can be used to identify their growth history within clouds, but determining the history of complex ice crystals having grown for long enough in clouds and experienced aggregation or riming is generally almost impossible. Here, we present two types of complex ice crystal habits observed in Arctic mixed-phase clouds during the NASCENT campaign that reveal their growth history despite their complex shapes.

First, the so-called recirculation particles were growing successively in the column and plate growth regimes and thus exhibited a special ice crystal shape similar to a capped-column with columns growing out of the corner of their plates (Fig. 4.3). Because the plate and column growth regimes depend on temperature, we could determine that these ice crystals were recirculating in the upper or lower parts of the clouds where the temperature was below  $-10^{\circ}\text{C}$  or above  $-3^{\circ}\text{C}$  respectively, before being brought back to the same environmental conditions in which they originally formed between  $-10^{\circ}\text{C}$  and  $-3^{\circ}\text{C}$ . Second, aged-rimed plates and columns exhibiting faceted protuberances were observed, indicative of rime at former stages of their growth process. After the rime froze on the surface of the plates and columns, it grew as a faceted protuberance with the same habit and along the same axis as the original ice crystal.

The aged-rimed ice crystals look similar to aggregated particles, but their angular shape



originate from riming at an earlier stage of the growth process, and not from aggregation with other ice crystals. Furthermore, the observations of broken ice crystals suggest that both the outer columns of recirculation particles as well as the protuberances of aged-rimed plates are fragile and break easily upon collision (Pasquier et al., 2022b). These ice crystals are therefore likely to favour secondary ice production via the ice-ice collision process. Finally, the observation of recirculation particles enables the determination of the cloud’s temperature profile and of changing updraft velocities within the cloud, whereas the observation of aged-rime particles allow to identify that regions of the clouds were characterised by larger liquid water content.

## Acknowledgments

This project has received funding from the European Union’s Horizon 2020 research and innovation programme under grant agreement No 821205 (FORCeS), from the Swiss Polar Institute (Exploratory Grants 2018), and from the Swiss National Science Foundation (SNSF) (grant no. 200021\_175824). We gratefully acknowledge the funding by the Deutsche Forschungsgemeinschaft (DFG, German Research Foundation) – Project-ID 268020496 – TRR 172, within the Transregional Collaborative Research Center “ArctiC Amplification: Climate Relevant Atmospheric and SurfaCe Processes, and Feedback Mechanisms (AC)3”. We would also like to particularly thank Roland Neuber and Paul Zieger for their support and advice during the organisation of the campaign. We thank all those involved in the field work associated with NASCENT, particularly the AWIPEV and Norwegian Polar Institute Sverdrup stations staff.

## Chapter 5

# Collocated in-situ measurements of radiation and cloud microphysical properties in Arctic mixed-phase clouds with the tethered balloon system HoloBalloon

J. T. Pasquier (1), T. Carlsen (2), A. Iraqi (1), J. Wieder (1), G. Li (1), R. O. David (2), F. Ramelli (1), U. Lohmann (1), and J. Henneberger (1)

(1) Department of Environmental System Sciences, Institute for Atmospheric and Climate Science, ETH Zurich, Zurich, Switzerland

(2) Department of Geosciences, University of Oslo, Oslo, Norway

---

### Abstract

The Arctic is warming two to three times faster than the rest of the world and clouds play an important role in the radiation budget of this remote region. The particle sizes and number concentration in clouds influences their radiative properties. The insufficient description of thermodynamical phase distribution is partly responsible for the large uncertainties related to cloud radiative feedback in the Arctic. Despite the importance to assess the impact of the microphysical properties of clouds on their radiative fluxes, collocated in-situ microphysical and radiative properties of clouds have rarely been performed in Arctic mixed-phase clouds. In this study, we successfully use for the first time radiation sensors mounted on the measurement platform of the tethered balloon system HoloBalloon to complement the cloud microphysical observations. The in-situ microphysical and radiative properties are discussed for two case studies. A longwave cooling at cloud top of a shallow stratocumulus mixed-phase cloud was measured during the first case study. During the second case study, vertical profiles in a low-level feeder clouds revealed that the ice crystal number concentrations determined the radiative properties of this optically thin feeder cloud. We demonstrate the great potential of the combined microphysical and radiation measurements on the tethered balloon platform HoloBalloon and identified possibilities to improve the data quality for future measurements.

## 5.1 Introduction

Clouds play an important role in the Earth’s radiation budget as they influence the surface radiation budget in two competing ways: they cool the surface by scattering solar radiation (spectral range 300 nm to 3000 nm) back to space, and warm the surface by emitting longwave radiation (spectral range 6000 nm to 20’000 nm) (Shupe and Intrieri, 2004; Nomokonova et al., 2019; Ebell et al., 2020). Clouds play an important role in the faster warming of the Arctic, a phenomenon called Arctic Amplification (e.g., Bennartz et al., 2013). The processes and feedbacks connected with clouds in the Arctic are complex. The role of clouds in the Arctic’s shortwave radiation budget is complicated because of the high surface albedo of the underlying sea ice, the lack of solar radiation in the winter months, and the large solar zenith angle in the summer (e.g., Shupe and Intrieri, 2004). The role of cloud in the Arctic is also particularly important for the longwave radiation budget (e.g., Park et al., 2015; Dahlke and Maturilli, 2017) because the atmosphere is drier in the Arctic than at lower altitudes. Therefore more clear-sky emissions are generated in the absence of clouds. In addition, the cloud microphysical properties (i.e. the cloud thermodynamic phase) influence the radiation budget in both spectral ranges (e.g., Shupe and Intrieri, 2004; Dong et al., 2010; Sedlar et al., 2012). Thus, mixed-phase clouds (MPCs) consisting of water vapor, cloud droplets, and ice crystals play a particularly important role in the Arctic climate. The cloud optical depth, corresponding to the extinction coefficient integrated over the thickness of the cloud, especially influence its radiation properties. The extinction coefficient is related to the square of the particle radius and the particle number. Liquid cloud have a larger extinction coefficient because cloud droplets are smaller and more numerous than ice crystals for a given cloud water path. Therefore, the optical depth of a liquid cloud is larger than the one of an ice cloud. This combined with the difference in scattering properties between spherical water droplets and nonspherical ice crystals (e.g. Järvinen et al., 2018), causes a higher albedo for liquid clouds than for corresponding ice clouds. Therefore, the surface shortwave cooling effect of liquid cloud is larger. Additionally, liquid water clouds have the strongest impact on the longwave radiative fluxes because of their larger optical depth, which increase their emissivity. Radiative cooling occurs at cloud top of MPCs. This cooling is enhanced by the frequently measured cloud top supercooled liquid water layer in Arctic MPCs (e.g., Pinto, 1998; Jiang et al., 2000; Shupe and Intrieri, 2004). However, MPCs have a net longwave warming effect at the surface because the cloud base is warmer than the cloud top (e.g. Zuidema et al., 2005a; Shupe and Intrieri, 2004).

It was found from combined remote sensing and modelling studies that the cloud radiative forcing shows a distinct seasonality in the Arctic. Clouds induce a surface warming during most of the year and a short period of surface cooling in the summer, when the shortwave cooling outweighs the longwave warming effect (Shupe and Intrieri, 2004; Dong et al., 2010; Ebell et al., 2020).

The radiative effect of clouds in the Arctic have mostly been studied using radiation measurements at the surface, combined with observations of cloud properties from remote sensing (e.g., Dong et al., 2010; Ebell et al., 2020), but also from aircraft measurements (Albrecht et al., 1985; Zuidema et al., 2005a; Wendisch et al., 2019), and modelling (e.g., Stapf et al., 2020). Radiative fluxes were less frequently measured with balloon-borne measurements, often together with turbulence and humidity fluxes (Duda et al., 1991b; Dexheimer et al., 2019; Egerer et al., 2021). In this work an innovative approach is introduced. We use collocated broadband radiation measurements and phase-resolved microphysical cloud properties measured with the tethered balloon platform HoloBalloon in the Arctic to discuss the effect of the cloud microphysical processes on the radiation budget of the observed clouds. The measurements were conducted in the framework of the Ny-Ålesund Aerosol Cloud Experiment (NASCENT) in Ny-Ålesund (78.9° N, 11.9° E), Svalbard, during October-November 2019 and March-April 2020. First, the main instrumentation, and the specification of the newly installed radiation sensors are described in Section 5.2. Second, two case studies are presented to discuss the longwave and shortwave radiative and microphysical properties of the measured MPCs (Section 5.3). Finally, the results are summarized

and suggestions for improving the data quality for future measurements are given in Section 5.4.

## 5.2 Methods

### 5.2.1 Main instrumentation

The data used in this study was collected during the NASCENT campaign, which took place in Ny-Ålesund from September 2019 to August 2020 (Pasquier et al., 2021).

The remote sensing instruments installed at the French–German Arctic Research Base AWIPEV were utilized. In this study, the 94 GHz cloud radar of University of Cologne (JOYRAD-94, K uchler et al., 2017), and the ceilometer (Vaisaila-CL51, Maturilli and Ebell, 2018) were used. Additionally, we used meteorological and radiation surface measurements sampled continuously at the Baseline Surface Radiation Network (BSRN) measurement field (Maturilli, 2020c) and daily radiosondes (Maturilli and Kayser, 2017).

The tethered balloon system HoloBalloon (Ramelli et al., 2020) measured in-situ cloud microphysical and radiation properties in October - November 2019 and March - April 2020. The instrument platform was hanging 12 m below the tethered balloon. Phase-resolved particle size distribution and particle habits were measured with the HOLOGraphic cloud Imager for Microscopic Objects (HOLIMO3B).

### 5.2.2 Radiation measurements

#### 5.2.2.1 Sensors specifications

The shortwave and longwave radiative fluxes were measured by up- and downward looking pyranometers and pyrgeometers (SP-510-SS; SP-610-SS; SL-510-SS; SL-610-SS, Apogee Instruments Inc., Utah, USA). The sensors were installed on the backward side of HOLIMO3B (see Fig.A.4 in the Appendix). They were mounted on plates 7 cm from the main case, to avoid unwanted influence from the box.

The SP-510 pyranometer uses a diffuser and a blackbody detector to measure direct incoming shortwave radiation, whereas the downward looking SP-610 pyranometer consists of a quartz window with a blackbody detector to measure reflected shortwave radiation. The SL-510 and SL-610 pyrgeometers both consists of a thermopile detector, a silicon filter with a diamond-like carbon coating, and a thermistor to detect the temperature of the measurements. Additionally, all sensors have internal heaters to allow for sensor heating under conditions of dew or frost deposition, or during precipitation events. The pyrgeometers and the downward-looking pyranometer have a field of view of 150° and the upward-looking pyranometer has a field of view of 180°.

The SP-510 and SP-610 pyranometers have sensor-specific calibration factors that were established during calibration by the manufacturer. The measured voltage signal  $S_D$  (in mV) must be multiplied by this specific calibration factor  $k_1^{\uparrow\downarrow}$  ( $\text{W m}^{-2} \text{mV}^{-1}$ ) to obtain the downward and upward (reflected) shortwave radiation  $F_{SW}^{\uparrow\downarrow}$  in  $\text{W m}^{-2}$ :

$$F_{SW_{HoloBalloon}}^{\uparrow\downarrow} = k_1^{\uparrow\downarrow} S_D^{\uparrow\downarrow} \quad (5.1)$$

The detector output from the pyrgeometers follows the Stefan-Boltzmann law ( $\sigma T^4$ ). The longwave radiation is calculated from the radiation balance measurement and from the detector temperature measurement. For this, a modified form of the Stefan-Boltzmann law is used:

$$F_{LW_{HoloBalloon}}^{\uparrow\downarrow} = k_2^{\uparrow\downarrow} S_D^{\uparrow\downarrow} + \sigma k_3^{\uparrow\downarrow} T^4 \quad (5.2)$$

where  $F_{LW_{HoloBalloon}}^{\uparrow\downarrow}$  are the upward and downward longwave radiation ( $\text{W m}^{-2}$ ),  $S_D^{\uparrow\downarrow}$  is the millivolt signal from the detector,  $T$  is the temperature measured with the thermistor (K),  $\sigma$  is the Stefan-Boltzmann constant ( $5.67 \times 10^{-8} \text{W m}^{-2} \text{K}^{-4}$ ), and  $k_2^{\uparrow\downarrow}$  and  $k_3^{\uparrow\downarrow}$  are the sensor-specific calibration coefficients ( $\text{W m}^{-2} \text{mV}^{-1}$ ).

### 5.2.2.2 Comparison with BSRN radiation measurements

During the NASCENT campaign, the shortwave and longwave measurements of the sensors mounted on HOLIMO3B were compared with broadband radiation measurements retrieved from the BSRN site installed at Ny-Ålesund (Maturilli, 2020c). To this aim, HOLIMO3B was placed on the ground on a cloud-free day (Fig. 5.1) and horizontally aligned.



Figure 5.1: Picture of HOLIMO3B located on the ground during the comparison with the BSRN measurements.

The  $F_{SW_{HoloBalloon}}^{\downarrow}$  and  $F_{LW_{HoloBalloon}}^{\downarrow}$  measurements have a mean positive offset of  $20.9 \pm 1.25 \text{ W m}^{-2}$  and  $14.1 \pm 4 \text{ W m}^{-2}$ , respectively, compared to the downward radiation measured at the BSRN site ( $F_{SW_{BSRN}}^{\downarrow}$  and  $F_{LW_{BSRN}}^{\downarrow}$ ) (Fig. 5.2). After comparison of the downward radiation, HOLIMO3B was turned upside-down, for a comparison of the downward-looking sensors with the BSRN measurements. The longwave measurements of the downward-looking show a mean positive offset of  $18.1 \pm 4 \text{ W m}^{-2}$  compared to  $F_{LW_{BSRN}}^{\downarrow}$  (not shown). The measurements of the downward-looking shortwave sensor cannot be compared to the BSRN measurements as this sensor is designed to measure solely reflected solar radiation, and not direct solar radiation. Possible reasons for the observed offsets of about 10% could be the position of HOLIMO3B on the ground compared to the BSRN measurements located at 2 m above ground or the distance of about 200 m between HOLIMO3B and the BSRN field. Moreover, the specification of the sensors on HOLIMO3B are different from the sensors on the BSRN field. The field of view of SL-pyrgeometers is  $150^\circ$ , whereas the pyrgeometers on the BSRN field have a field of view of  $180^\circ$ . The upward-looking pyrgeometer (pyranometer) on the BSRN field measures at a spectral range between 4 - 50  $\mu\text{m}$  (200 - 3600 nm), whereas the pyrgeometers (pyranometers) on HOLIMO3B measure between 5 - 30  $\mu\text{m}$  (385 - 2105 nm). Additionally, the solar zenith angle was larger than  $75^\circ$  during the entire period of the comparison. The sensors on HOLIMO3B were calibrated for smaller solar zenith angles. Higher uncertainty in the measurements can arise from higher solar zenith angles. Finally, while BSRN radiation sensors are primary standard instruments correcting for the dependence on the environmental temperature and for temperature artifacts in the sensor's construction (Beaubien et al., 1998), the sensors installed on HOLIMO3B have larger uncertainties related to the temperature gradient in the instrument that can amount up to  $\pm 25 \text{ W m}^{-2}$  during field measurements (Eugster Werner, personal communication). For future field campaigns, we recommend to use radiation sensors with lower instrumental uncertainties. A comparison with

measurements from a BSRN field should be performed again, but in controlled conditions, e.g. with HOLIMO3B installed horizontally directly next to the BSRN field 2 m above the ground at small solar zenith angles, as well as during night conditions. We do not correct for this offset in the rest of this study, as the reason for the offset are not clear. One should keep in mind that uncertainty of  $\sim 10\%$  exist on the absolute values. However, the offset should cancel while looking at net fluxes or albedo.

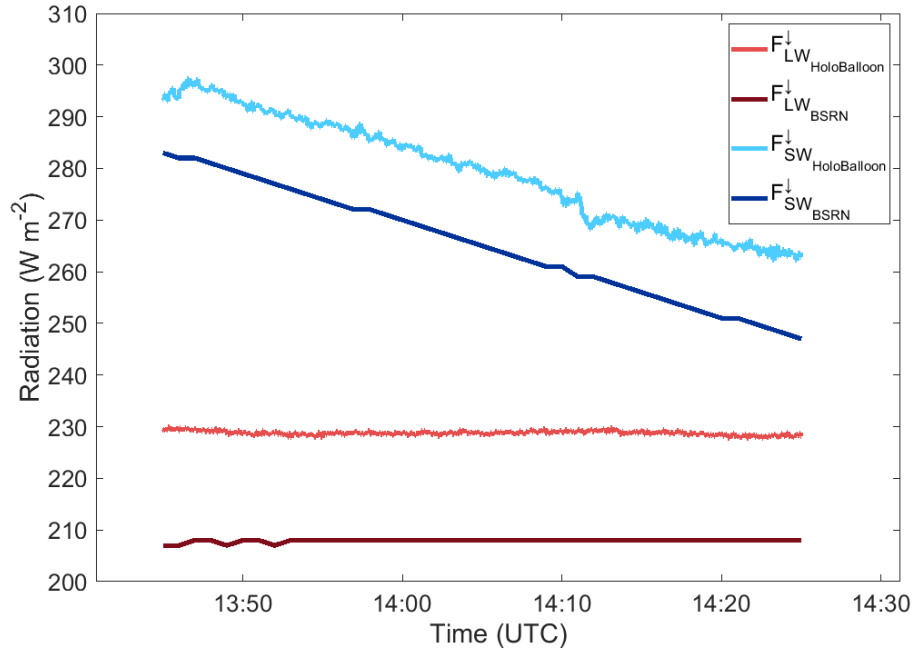


Figure 5.2: Comparison of radiation sensors (upward-looking configuration) with downward radiation measured by the BSRN station.

### 5.2.2.3 Measurement corrections

The pyrgeometer and pyranometer measurements are only reliable when the sensors are approximately horizontally leveled. Therefore, measurements are neglected when the pitch or roll experienced by the measurement platform hanging 12 m below HoloBalloon were larger than  $15^\circ$ .

Radiation sensors need to adapt for changes in the incident irradiance. For precise measurements of broadband irradiance, a high temporal resolution is needed as changes in irradiance can occur more rapidly than the response time of the sensors (Ehrlich and Wendisch, 2015). This is especially important when performing vertical profiles at cloud top, as the irradiance is expected to change rapidly. The sensors used have a response time of 0.5 sec, which is faster than most of the broadband radiation sensors and is assumed to be sufficient to resolve fast changes in irradiance. In future studies, the method introduced by Ehrlich and Wendisch (2015) using Fourier transform could be applied to the radiation measurements performed on HoloBalloon to further enhance the temporal resolution of the measurements.

## 5.3 Results & Discussion

Ny-Ålesund is located at  $78.9^\circ$  N,  $11.9^\circ$  E and the sun does not set between April and beginning of September, and does not rise between October and March. There is therefore a lack of direct solar radiation in the winter months. We present in this section two case studies of combined in-situ microphysical and radiative properties, on 10 November 2019 (no direct sunlight) and on 1 April 2020 (direct sunlight).

### 5.3.1 Longwave radiative cooling at cloud top

On 10 November 2019, a shallow stratocumulus cloud was observed over Ny-Ålesund. Two flights were performed through the entire cloud layer with HoloBalloon (Fig. 5.3). The cloud consisted mostly of cloud droplets and only few ice crystals were measured (see Section 3.2.1 for detailed description). No direct shortwave radiation was reaching the cloud, as the sun was below the horizon (with a highest altitude of  $-6^\circ$ ). Therefore, only the longwave radiation measurements is discussed. The 5-min averages of the net longwave radiative fluxes ( $F_{LWnet}$ ) were calculated along the path of HoloBalloon and at the surface using the BSRN measurements with:

$$F_{LW}^{net} = F_{LW}^{\downarrow} - F_{LW}^{\uparrow} \quad (5.3)$$

A negative (positive)  $F_{LW}^{net}$  indicates a net cooling (warming). The net longwave radiative flux measured on HoloBalloon ( $F_{LW}^{net}_{HoloBalloon}$ ) was increasing when HoloBalloon was flying closer to the top of the cloud, dominated by a longwave radiative cooling at cloud top (Fig. 5.3). When HoloBalloon penetrated deeper in the cloud starting from 15:00 UTC,  $F_{LW}^{net}_{HoloBalloon}$  rapidly decreased in magnitude. The longwave cooling at cloud top varied between  $65 \text{ W m}^{-2}$  and  $75 \text{ W m}^{-2}$  (Fig. 5.3). The radiative cooling rate (RHR) was calculated with:

$$RHR(z) = \frac{g}{C_p} \left( \frac{\Delta F_{LW}^{net}}{\Delta p} \right) (z) \quad (5.4)$$

A cooling rate of  $1.5 \text{ K hr}^{-1}$  was found at cloud top. Despite this cooling at cloud top, the cloud had a warming effect at the surface. This can be seen on the decrease in magnitude of the net longwave radiative flux measured at the surface ( $F_{LW}^{net}_{LWBSRN}$ ) when the cloud was present on Figure 5.3. The lower  $F_{LW}^{net}_{LWBSRN}$  when the cloud is present, indicates that less net longwave radiation is emitted to space and more back to the surface, thus warming the surface.

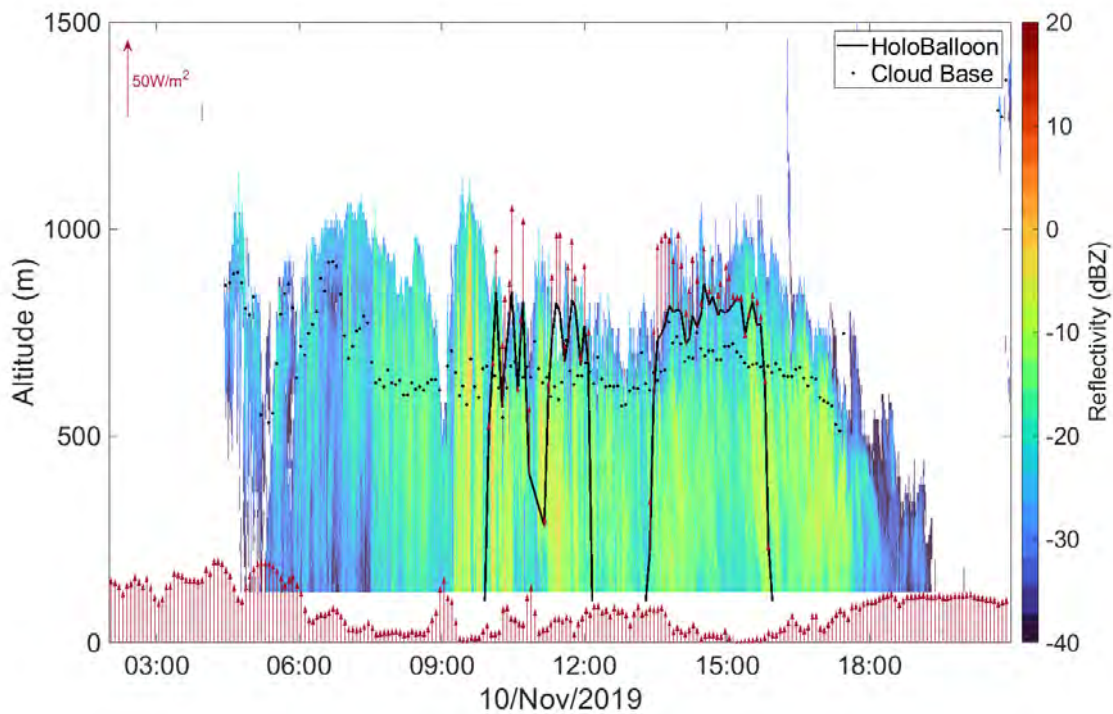


Figure 5.3: Longwave radiative fluxes (red arrows) along HoloBalloon path (black line) and at the BSRN station at the surface (at the bottom). The shading shows the reflectivity measured by the cloud radar and the black dots the cloud base measured by the ceilometer.



The cloud thickness was calculated from cloud base measured by the ceilometer and cloud top detected by the cloud radar.  $F_{LW_{BSRN}}^{net}$  at the surface was inversely proportional to the cloud thickness (Pearson's correlation coefficient of -0.8, Fig. 5.4).

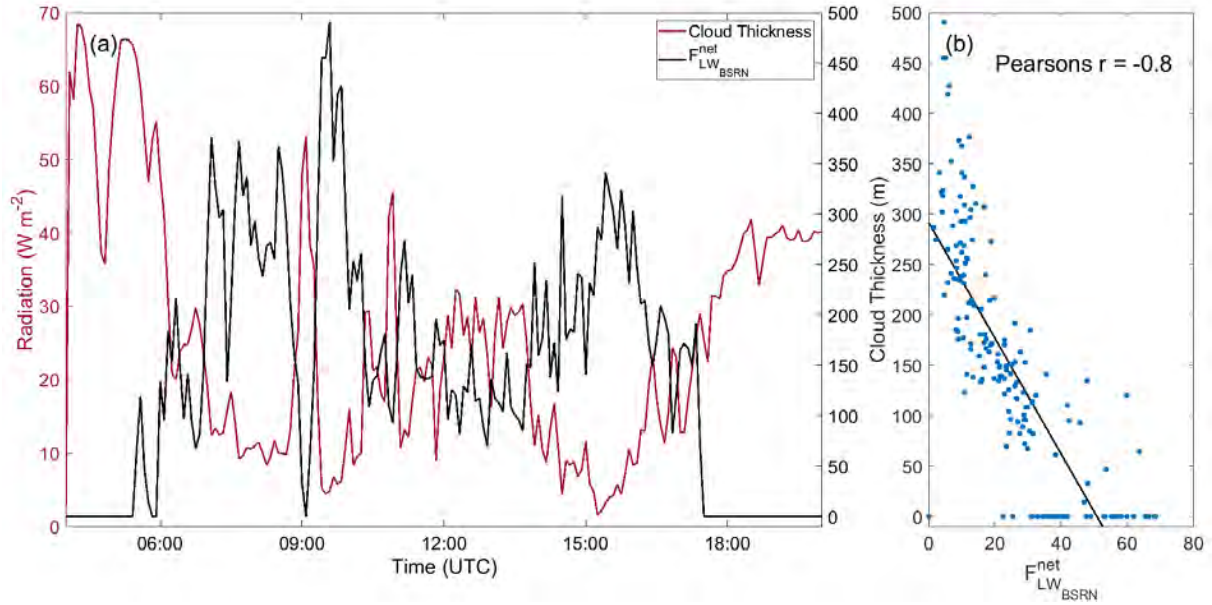


Figure 5.4: (a) Cloud thickness and the  $F_{LW_{BSRN}}^{net}$  on 10 November 2019. (b) Cloud thickness vs.  $F_{LW_{BSRN}}^{net}$ . The Pearson's correlation and the linear fit over the data is shown.

### 5.3.2 Influence of ice crystal concentration on shortwave radiation

On 1 April 2020, the sun was above the horizon from 03:17 UTC to 19:20 UTC, with a minimum zenith angle of  $74.1^\circ$  at 11:16 UTC. A seeder-feeder cloud event was observed above Ny-Ålesund and one flight was performed with HoloBalloon into the feeder cloud (Fig. 5.5a). The microphysical properties of the feeder cloud are described in detail in Chapter 3.2.2. Note that mountains located around Ny-Ålesund block direct sunlight up to  $\sim 10^\circ$  above the horizon (solar zenith angle above  $80^\circ$ ) in the southward direction.

The downward shortwave radiation measurements at the BSRN site showed an increase in the total incoming shortwave downward radiation ( $F_{SW_{BSRN}}^\downarrow$ ) at the surface straight after sunrise (Fig. 5.5). The direct shortwave radiation ( $F_{SW_{BSRN,dir}}^\downarrow$ ) began to fluctuate as soon as the seeder cloud aloft first appeared in the reflectivity signal and completely disappeared as soon as the lower optically thicker feeder cloud formed. The diffuse shortwave component ( $F_{SW_{BSRN,diff}}^\downarrow$ ) showed a steady increase until the appearance of the lower cloud, and then exhibited more fluctuation and decreased after solar noon. The trend in  $F_{SW_{HoloBalloon}}^\uparrow$  and  $F_{SW_{HoloBalloon}}^\downarrow$  measured in cloud with HoloBalloon had a comparable trend as the radiation at the surface, but lower values were observed on HoloBalloon (Fig. 5.5). The reason is probably that the snow-covered surface reflected shortwave radiation from the sun shining just above the horizon, which was re-reflected back by the cloud, and thus increased the shortwave radiation at the surface. Additionally, the scattering of the shortwave radiation in cloud attenuated the diffuse radiation more than below cloud.

The comparison of the cloud microphysical properties with the shortwave radiation on 1 April 2020 (Fig. 5.6) is discussed in the following. To this aim, the shortwave albedo at flight altitude ( $albedo_{HoloBalloon}$ ) was calculated from the outgoing and incoming shortwave radiation using:

$$albedo_{HoloBalloon} = \frac{F_{SW_{HoloBalloon}}^\uparrow}{F_{SW_{HoloBalloon}}^\downarrow} \quad (5.5)$$

The  $\text{albedo}_{\text{HoloBalloon}}$  was calculated along the path of HoloBalloon using 5-min averages and is displayed in Figure 5.6. It was varying between 0.86 and 0.98. The cloud droplet number concentration (CDNC) was generally lower than  $1 \text{ cm}^{-3}$ , with some regions of enhanced CDNC up to  $70 \text{ cm}^{-3}$  towards the end of the flight. The ice crystal number concentration (ICNC) in comparison was relatively large and reached up to  $40 \text{ L}^{-1}$ . Small ice crystals ( $\text{ICNC}_{<106 \mu\text{m}}$ ) contributed noticeably to the total ICNC. Note that here all small ice crystals were taken into account and not solely the pristine faceted ice crystals as discussed in Chapter 3 because all small ice crystals are influencing the shortwave radiation.

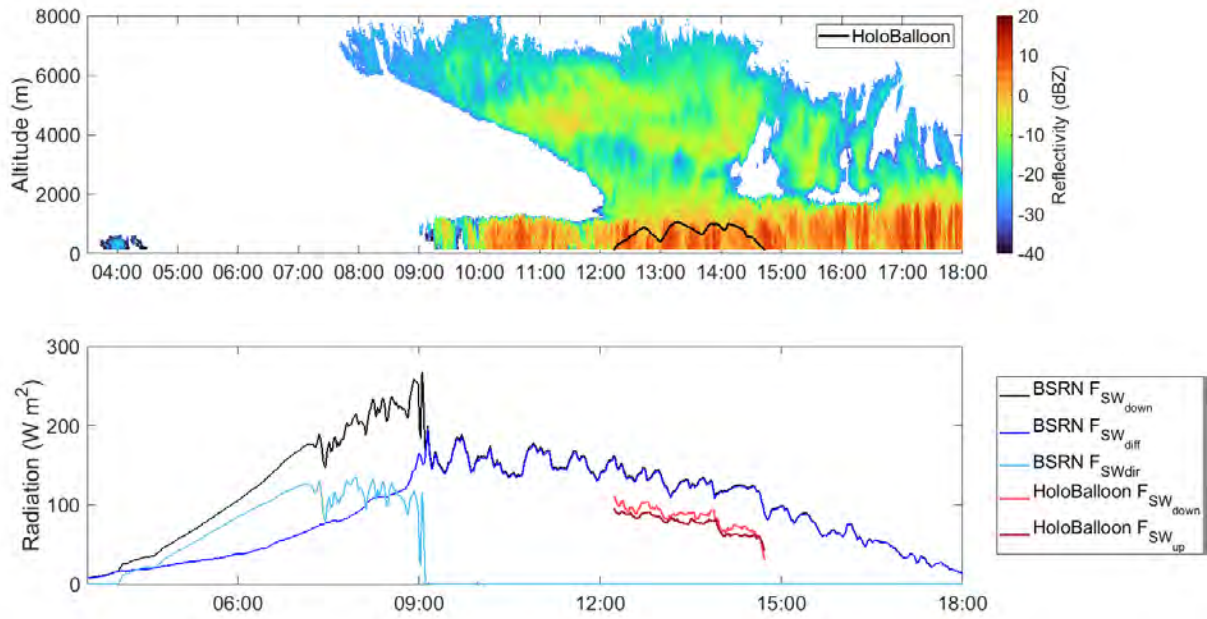


Figure 5.5: (a) HoloBalloon path (black line) and reflectivity measured by the cloud radar. (b) Total  $F_{\text{SW BSRN}}^{\downarrow}$ ,  $F_{\text{SW BSRN,diff}}^{\downarrow}$ , and  $F_{\text{SW BSRN,dir}}^{\downarrow}$  measured at the BSRN field, and  $F_{\text{SW HoloBalloon}}^{\uparrow}$  and  $F_{\text{SW HoloBalloon}}^{\downarrow}$ . The downward shortwave consists of the direct and diffuse shortwave radiation. The normal component of the direct shortwave radiation was corrected with the solar zenith angle to obtain its effective component to the total downward shortwave radiation.

The region with the  $\text{albedo}_{\text{HoloBalloon}}$  was larger than 0.91 (median  $\text{albedo}_{\text{HoloBalloon}}$ ) are highlighted in grey in Fig. 5.6. The  $\text{albedo}_{\text{HoloBalloon}}$  did not seem to be dominantly influenced by the fluctuation in CDNC, or to depend directly on altitude (e.g., on distance from cloud top). Rather, the increase in  $\text{albedo}_{\text{HoloBalloon}}$  and the increase in ICNC were coinciding (Fig. 5.6). These regions were also regions of enhanced reflectivity (Fig. 5.6a). The higher influence from the ice crystals than from the cloud droplets can be understood by looking at their respective extinction coefficients (Figure 5.6c). The extinction coefficients were obtained from the sum of the particles area per volume and correspond to the local optical thickness of the cloud. Until 13:45 UTC, the CDNC was too low to compensate for the larger area of the ice crystals. Therefore the ice crystals had a larger extinction coefficient and were determining the optical thickness of the cloud. After 13:45 UTC, the CDNC increased in some regions and had a larger extinction coefficient than the ice. These peaks in CDNC and water extinction coefficient affect the  $\text{albedo}_{\text{HoloBalloon}}$ . The increase in  $\text{albedo}_{\text{HoloBalloon}}$  is less than could be expected by the high peak of the water extinction coefficient, but a correlation exists between the water extinction coefficient and the  $\text{albedo}_{\text{HoloBalloon}}$  (Pearson's correlation coefficient of 0.78) between 14:00 UTC and 14:10 UTC. A possible reason for the smaller increase in  $\text{albedo}_{\text{HoloBalloon}}$  could be that  $F_{\text{SW HoloBalloon}}^{\uparrow}$  and  $F_{\text{SW HoloBalloon}}^{\downarrow}$  both decreased before the peak of the water extinction coefficient, shortly before 14:00 UTC (Figure 5.6e). As the absolute  $F_{\text{SW HoloBalloon}}^{\uparrow\downarrow}$  values are

lower, an identical difference would result in a smaller albedo. The reason for the decrease of  $F_{SW_{HoloBalloon}}^{\uparrow\downarrow}$  could be that the thickness of the seeder cloud increased and less solar radiation reached the feeder cloud, or that the terrain blocked some of the solar radiation. The ice and water extinction coefficients together determined the in-cloud albedo.

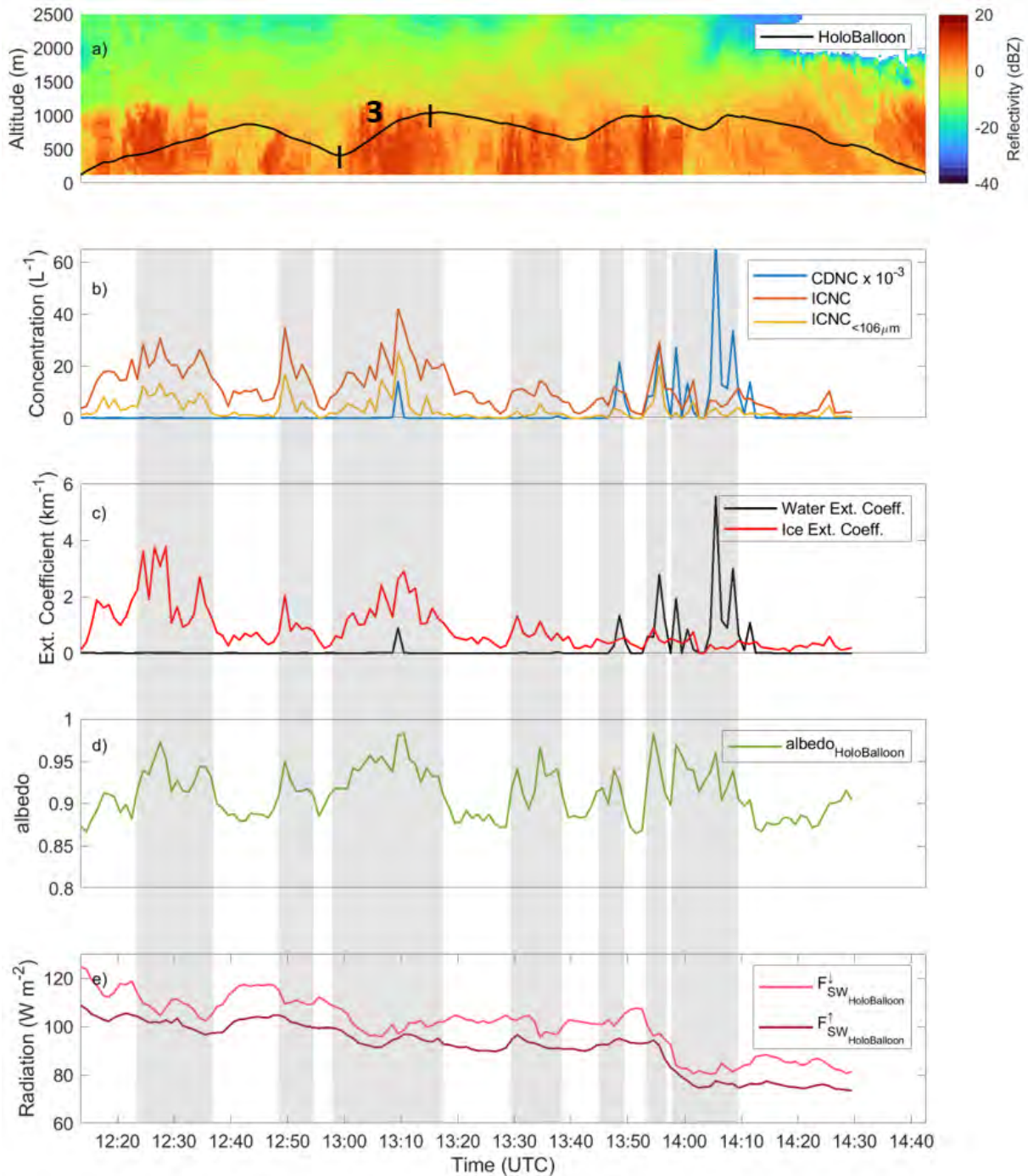


Figure 5.6: (a) HoloBalloon path (black line) and reflectivity measured by the cloud radar. (b) CDNC, ICNC and ICNC $_{<106 \mu m}$  measured by HOLIMO3B. (c) Ice and water extinction coefficient ( $m^{-1}$ ). (d) SW ratio calculated from the  $F_{SW_{HoloBalloon}}^{\uparrow}$  and  $F_{SW_{HoloBalloon}}^{\downarrow}$  measured on HoloBalloon. (e)  $F_{SW_{HoloBalloon}}^{\uparrow}$  and  $F_{SW_{HoloBalloon}}^{\downarrow}$ . The grey shading highlight regions where the  $albedo_{HoloBalloon}$  is higher than 0.9 and profile 3 is labelled. The data were averaged for 60 sec.

A closer look at the profile 3 (as labelled between the two black vertical lines in Figure 5.6a)



gives further insight into the connection between the cloud microphysical and radiative properties. The region of largest  $\text{albedo}_{\text{HoloBalloon}}$  was located at 800 m a.s.l., together with the region of enhanced ICNC. At 950 m a.s.l., a smaller increase in  $\text{albedo}_{\text{HoloBalloon}}$  was observed simultaneously with an increase in CDNC and ICNC. A strong correlation was found between  $\text{albedo}_{\text{HoloBalloon}}$  and the ICNC for this profile 3 (pearson's correlation coefficient of 0.87). Accordingly a strong correlation is found with the ice extinction coefficient too (pearson's correlation coefficient of 0.87 as well) whereas no correlation is found with the water extinction coefficient. As explained above, the observed cloud was optically thin because of the low CDNC ( $\sim 1 \text{ cm}^{-3}$ ). Therefore, the shortwave reflection by the measured cloud was low and shortwave radiation was transmitted through the cloud. When HoloBalloon entered a more dense region of the cloud with higher ICNC (and higher extinction coefficient), more scattering of the light occurred. In these regions, the diffuse shortwave radiation became nearly isotropic ( $F_{\text{SW}_{\text{HoloBalloon}}}^{\downarrow}$  and  $F_{\text{SW}_{\text{HoloBalloon}}}^{\uparrow}$  more similar), and the  $\text{albedo}_{\text{HoloBalloon}}$  was approaching unity.

It is beyond the scope of this chapter to assess the exact causes for the inhomogeneities in the CDNC and ICNC in the feeder cloud. A detailed description of the cloud microphysical measurements is given in Chapter 3. Possible mechanisms could be increased updrafts leading to higher supersaturations and growth of cloud droplets, or secondary ice production increasing the ICNC of small ice crystals. This increase in (small) ICNC or CDNC increases the total extinction coefficient of the cloud, increasing the optical thickness of the otherwise optically thin cloud, and therefore impacting the cloud radiative properties. It may be that the occurrence of secondary ice production increasing the small ICNC changes the radiative properties of the cloud when the CDNC is low.

The theoretical LW Stefan-Boltzmann radiation (LW-SB) was calculated with the Stefan-Boltzmann law using the temperature profile measured by the radiosonde launched at 17:00 UTC. The  $F_{\text{LW}_{\text{HoloBalloon}}}^{\uparrow}$  and  $F_{\text{LW}_{\text{HoloBalloon}}}^{\downarrow}$  measured during profile 3 show a similar decrease with altitude than the calculated  $F_{\text{LW}_{\text{SB}}}^{\uparrow}$ , but an offset of about  $20 \text{ W m}^{-2}$  compared to the calculated  $F_{\text{LW}_{\text{SB}}}^{\uparrow}$ . The offset is likely caused by the lower emissivity of the cloud compared to the assumed emissivity of 1 in the Stefan-Boltzmann calculation.

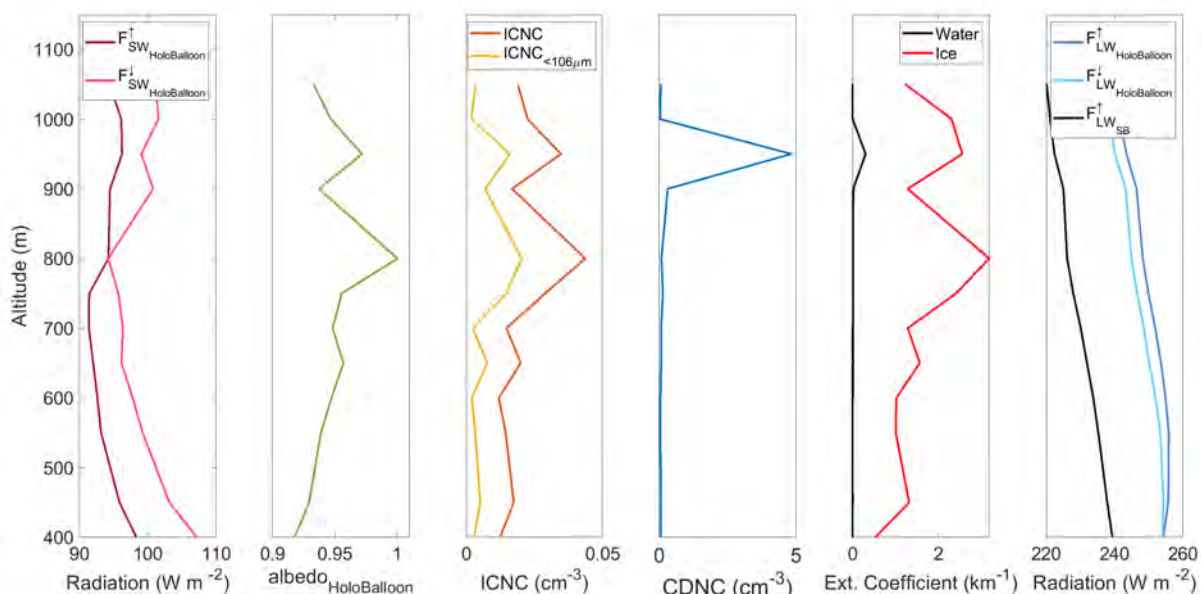


Figure 5.7: Measured cloud and radiative properties during profile 3. The data were averaged over 50 m.

## 5.4 Conclusion

The capability to perform collocated in-situ radiative and microphysical cloud properties measurements with HoloBalloon was shown in this study. To this aim, upward and downward looking pyrgeometers and pyranometers measuring longwave and shortwave radiation were mounted on HOLIMO3B hanging 12 m below the tethered balloon system HoloBalloon. The measurements of the installed radiation sensors were compared with the standard radiation measurements performed at the BSRN field. A positive offset of 14 to 20 W m<sup>-2</sup> was observed for the longwave pyrgeometers and for the shortwave downward measuring pyranometers.

The radiation measurements performed during one autumn (no sunlight) and one spring (sunlight) days in Ny-Ålesund were discussed. On 10 November 2019, measurements were performed through a shallow stratocumulus cloud, consisting mostly of cloud droplets and only of few ice crystals. Longwave cooling was observed at cloud top, but the cloud had a net longwave warming effect at the surface that was inversely proportional to the cloud's thickness.

On 1 April 2020, a seeder-feeder cloud event occurred over Ny-Ålesund and HoloBalloon performed one flight into the feeder cloud. The measured CDNC was low during the first part of the flight ( $\sim 1 \text{ cm}^{-3}$ ) in the feeder cloud. Therefore, the optical thickness of the cloud was small, resulting in a low amount of reflected shortwave radiation, and the shortwave radiation was mainly transmitted through the cloud. In this case, the extinction coefficient of ice mostly increased the optical depth of the cloud. When higher ICNC were prevailing, the diffuse shortwave radiation became nearly isotropic and the  $F_{SW\text{HoloBalloon}}^{\downarrow}$  equaled  $F_{SW\text{HoloBalloon}}^{\uparrow}$  and the  $\text{albedo}_{\text{HoloBalloon}}$  became close to unity. The importance of the ICNC in such optically thin clouds with low CDNC indicates that ice crystal formation, for example via secondary ice production, can change the radiative properties of the optically thin MPCs. Further investigation should be performed to assess the role of secondary ice production for the radiative properties of the Arctic MPCs.

The newly installed setup was able to measure cloud top cooling, to obtain profiles of shortwave and longwave radiation to find possible connections to the cloud microphysical properties. This demonstrates the huge potential of the combined microphysical and radiation measurements on HoloBalloon.

In addition, this analysis helped to identify possibilities to improve the setups for future measurements. (1) The use of more accurate radiation sensors correcting for the ambient temperature dependence will allow for more precise radiation measurements. (2) More frequent comparison with other radiation measurements on the ground in better controlled setup or conducting radiative transfer simulations in the field (to test the calibration of the manufacturer in the special conditions of the campaign) would be beneficial. (3) The correction of the radiation data for the response time to get higher confidence in the profiles when the temperature is changing rapidly could be useful. (4) Longer sequences above cloud top and more profiles for statistics would be needed.





# Chapter 6

## Conclusion and outlook

### 6.1 Summary and conclusion of the results

In this thesis, we investigated the cloud microphysical properties of Arctic MPCs using balloon-borne in-situ observations and ground based remote sensing instrumentation in the framework of the NASCENT campaign. The microphysical features of the Arctic MPCs observed on six days are studied to improve the process understanding of Arctic MPCs, with a particular focus on ice crystal formation and growth. The following section summarizes the main findings and conclusions of this thesis:

#### 6.1.1 Ice crystal formation from secondary ice processes

In this thesis ice crystal formation from SIP was investigated using pristine ice crystals smaller than  $106\ \mu\text{m}$  as a indicator for SIP (Chapters 2 and 3). We assume from the pristine and small nature of these ice crystals that they formed in the last 120 sec before being sampled and remained associated with their environment of origin during this time. Further, we deduce from larger concentrations of these ice crystals than of INPC that they originated from SIP processes and not from nucleation on INPs. This allows to identify regions of SIP cloud regions and to link SIP directly to the environmental conditions prevailing in these regions. In other words, this method identifies SIP occurrence in the 120 sec preceding the measurements and the pristine small ice crystals are used as tracers for the identification of the conditions favorable for SIP.

During the six days of measurements in MPCs with HoloBalloon, SIP regions were observed in 40% of the in-cloud measurements, and SIP<sub>high</sub> regions (with  $\text{ICNC}_{\text{pr}<106\ \mu\text{m}} > 10\ \text{L}^{-1}$ ) in 3.6% of the measurements. These frequencies of occurrence are considerable as only the SIP occurring maximally 120 sec prior to the measurements are considered. The frequency of occurrence of SIP attained even higher values at certain temperature ranges and reached up to 75% between  $-3\ ^\circ\text{C}$  and  $-8\ ^\circ\text{C}$  and 95% between  $-18\ ^\circ\text{C}$  and  $-23\ ^\circ\text{C}$  (Chapter 3). This highlights the necessity to incorporate SIP parametrizations at lower temperatures in numerical weather models, currently generally only including parametrization for the HM process at temperatures above  $-8\ ^\circ\text{C}$ . In one sampled MPC however, the ice crystals merely formed by nucleation on INPs at  $-16\ ^\circ\text{C}$  and no substantial contribution from SIP was observed. This suggests that a critical ICNC must be reached together with the adequate environmental conditions in order to initiate SIP which then increases the ICNC appreciably. This is in accordance with persistent supercooled liquid clouds observed in previous studies (e.g., Rosenfeld and Woodley, 2000; Silber et al., 2019). In contrary, in two MPCs, the concentration of the small pristine ice crystals suddenly increased by two orders of magnitudes from below  $1\ \text{L}^{-1}$  to  $55\ \text{L}^{-1}$  and  $92\ \text{L}^{-1}$ , respectively (Chapters 2 and 3). Both sudden increases occurred close to cloud base at temperatures between  $-3\ ^\circ\text{C}$  and  $-5\ ^\circ\text{C}$ . Comparable sudden jumps in ICNC caused by SIP have been reported in previous studies (e.g., Lawson et al., 2015; Korolev et al., 2020) and were explained by a cascading process initiated by the production of splinters by freezing droplets which then collide with other supercooled

droplets and further increase the number of droplets freezing and creating splinters (Lawson et al., 2015).

Actually, our measurements show that the occurrence of SIP was strongly connected to the freezing of drizzle drops, i.e. by the droplet shattering process, as the ratio of drizzle drops occurrence was enhanced by a factor 2 during SIP<sub>all</sub> and by a factor 4 during SIP<sub>high</sub>. Moreover, the frozen drops were measured during 87% of the SIP<sub>high</sub> observations. Previous studies linked the presence of drizzle drops to the occurrence of SIP in tropical and midlatitude convective clouds (e.g., Lawson et al., 2015, 2017; Keppas et al., 2017). In convective clouds with warm cloud base, the drizzle drops grow by collision-coalescence in updraft cores regions extending over a large portion of the troposphere (Lawson et al., 2017). In other cases, the large liquid drops responsible for the initiation of droplet shattering close to the melting layer were suggested to originate from melted ice crystals recirculating through the melting layer with convective turbulent updrafts (Korolev et al., 2020; Lauber et al., 2021). In this thesis, we propose that the formation of large drizzle drops is determined by the low CCNC observed in the pristine Arctic environment. Indeed, consistently as found in other studies (Reutter et al., 2009; Moore et al., 2013), aerosols acting as CCN were limiting the CDNC, but the fewer droplets being activated could grow to larger sizes (Chapter 2). Thus, aerosols are influencing the SIP in Arctic MPC by (1) acting as INP forming sufficient ice crystals for initiating SIP processes, and (2) providing limited CCN leading to the formation of large drops responsible for SIP.

### 6.1.2 Ice crystal habits as indicator for environmental properties

The holographic imager used in this thesis retrieved images of ice crystals, which were manually classified into habits. Their habits help to determine their histories as well as the atmospheric conditions prevailing in the clouds. Many ice crystals observed in Arctic MPCs during NASCENT showed pristine features, compared to aged or irregular habits more regularly observed in MPCs over orographic terrain (e.g., Lauber et al., 2021; Ramelli et al., 2021a). This facilitates interpretation of the history of the particles.

For example, ice crystals growing subsequently in plate and column regimes were observed. The growth as plate or column is favored depending on the ambient temperature, with plate growth being enhanced at temperatures lower than -10 °C or larger than -3 °C and column growth favored between -10 °C and -3 °C. As in-cloud temperature decreases with altitude, the variations in temperature growth environment are related to recirculation of particles through the cloud. Interestingly, the observed recirculation particles were generally not rimed. This signifies that the particles were recirculating up and down without colliding with cloud droplets. The recirculation of ice crystals is an indicator for changing updraft velocities in the cloud. A growing ice crystal is lifted by updrafts before precipitating to lower parts of the cloud when the updrafts can not sustain its weight anymore, and gets then repeatedly lifted when updrafts increase.

Other interesting ice crystal habits observed were aged rimed particles, where cloud droplets first rimed on the ice crystal and froze, then the frozen protuberance grew in the plate or columnar growth environment depending on the ambient temperatures. This creates faceted protuberances, in comparison to the smaller roundish protuberances caused by freshly rimed droplets. Aged-rimed ice crystals showing no fresh rime likely originated from regions of the cloud with higher CDNC.

A further observed ice crystal habit was ice crystals showing signs of sublimation. These ice crystals show blunt edges, consistently with previous studies (e.g., Jambon-Puillet et al., 2018) and indicated that the cloud region was subsaturated with respect to ice, which caused the ice crystals to sublimate.

Finally, droplets stuck with columns (called droplet lollipops in this thesis) were observed. These ice crystals demonstrate that large drops were freezing while colliding with columns. Because the freezing of drops is a known secondary ice process, droplet lollipops can be used as indicator of the droplet shattering process.

Ice crystal habits helps to understand the cloud microphysical processes responsible for ice crystal formation and growth, which in turn determine precipitation initiation, as well as the cloud's lifetime and radiative properties.

### 6.1.3 Arctic cloud and radiation

For the first time, the holographic imager measurements on the tethered balloon system were supplemented with in-situ radiation observations, allowing for a direct comparison between cloud microphysical and radiative properties.

Observations through the complete depth of a low-level stratocumulus MPC indicated a radiative cooling rate of  $1.5 \text{ K hr}^{-1}$  at cloud top. During another measurement day, profiling through a low level feeder MPC enabled to relate the shortwave radiative fluxes to the cloud phase properties. The measured CDNC was mostly low ( $\sim 1 \text{ cm}^{-3}$ ) in the feeder MPC. It therefore had a small optical thickness, which was mainly determined by the ice phase. In regions with enhanced ICNC, the diffuse shortwave radiation measured became nearly isotropic and the in-cloud albedo became close to unity. This highlights the importance of fluctuations in ICNC in such optically thin clouds with low CDNC.

Such increases in ICNC changing the radiative properties of MPCs can be caused by SIP processes. In optically thin cloud with low LWC, an increase in ICNC would increase the albedo leading to an enhanced cooling effect, but also increase the emissivity leading to an enhanced longwave radiative warming at the surface. In optically thicker clouds with larger LWC, an increase in ICNC would have the opposite effect. Indeed, it would favor the WBF process reducing the cloud droplet number concentration, thus reducing the albedo and the emissivity of the cloud. To quantify these complicated processes between thermodynamical phase and radiation cloud properties, more collocated measurements are needed.

In addition to the ICNC, the ice crystal habits influence the cloud radiative properties (e.g., Järvinen et al., 2018). So far, modeling studies were used to assess the influence of ice crystal habits to the cloud radiative properties (e.g. Harrington and Olsson, 2001; Liu et al., 2014). In this thesis we demonstrate the feasibility to perform collocated in-situ measurements of ice crystal habits and radiative cloud properties on the tethered balloon system HoloBalloon. The results reveal the huge potential of the combination of these measurements, but uncertainties in the radiation instrumentation should be reduced to increase the confidence of the results (Chapter 5).

## 6.2 Outlook

### 6.2.1 Further analysis of dataset from the NASCENT campaign

The unique and multidimensional set of observations obtained during the NASCENT campaign renders a holistic approach possible to study the effect of aerosol and clouds on the Arctic climate. The role of aerosol and secondary ice production processes for the phase partitioning of Arctic MPC was investigated in this thesis. Yet, the understanding of clouds and aerosols and their interactions in the Arctic climate can still be further improved. Ongoing work and analysis on the NASCENT data set is being performed.

Among others, the advantage of the proximity between in-situ airborne and cloud radar measurements for a relatively long temporal coverage in Ny-Ålesund is being used. The two techniques are complementary. While the high-resolution in-situ observations deliver detailed phased-resolved data at a given point, remote sensing observations provide information about the entire cloud structure. Thus, the in-situ measurements can be compared with the Doppler spectra at a precise point and then be related to other regions of the cloud with comparable Doppler spectra features. For example, the peakTree analysis (Radenz et al., 2019) can be used to differentiate between several cloud particle populations. With this technique, the small ice particles related

to secondary ice production could be related to the Doppler spectra and it may be possible to find other cloud regions with the same cloud particle populations. This would allow to assess the importance of SIP in the entire cloud and not solely at the precise location measured with the balloon-borne instrumentation.

Another approach is to relate the in-situ dataset and the skewness feature obtained from the Doppler spectra, which was found to be connected to the presence of multiple cloud particle populations with different fall velocities, i.e. of liquid and ice particles (e.g., Luke et al., 2010; Kalesse et al., 2016). Features in the Doppler spectrum skewness profiles that relate to changes in the partitioning between liquid and ice were found in the Doppler spectra retrieved by the cloud radar in Ny-Ålesund (Rosa Gierens, personal communication). Comparison with the in-situ cloud microphysical measurements sampled on HoloBalloon will help getting a better understanding of the observed skewness features.

Furthermore, the secondary ice production processes are poorly represented in numerical weather prediction models. The dataset obtained from the NASCENT campaign enables to prescribe the aerosol concentration, as well as ice nucleating particles and cloud condensation nuclei concentration to test secondary production parametrization and compare the results with the in-situ cloud microphysical measurements and remote sensing observations. Simulations with several models including the WRF model as discussed in Chapter 2 and the Norwegian Earth System Model (NorESM2) are planned. This will help to obtain a better representation of the ice crystal formation and phase partitioning in Arctic MPCs and thus to reduce the uncertainty related to cloud radiative feedbacks in the Arctic Amplification.

### 6.2.2 Technical improvements of HoloBalloon

First, a more robust inner bubble inside helikite should be used in future campaigns. The inner bubble is crucial for the successful measurements with HoloBalloon since it holds the helium necessary for flying. It is protected from the outside by a more resistant but not elastic outer bubble. Because of the large size and lifting capacity of HoloBalloon, the helikite was tightened to the ground between measurement flights and could not be stored in warm and protected storage rooms like other tethered balloons employed for cloud measurements. Thus, the inner bubble encountered windy and cold conditions. During previous field campaigns in Switzerland, the inner bubble resisted the atmospheric conditions (e.g. wind, temperatures). However, the inner bubble did not resist the high wind speeds ( $> 10 \text{ m s}^{-1}$ ) and/or low temperatures ( $\sim -20 \text{ }^\circ\text{C}$ ) sometimes prevailing in the Arctic. Therefore, a new and more resistant inner bubble should be used in future field campaigns if severe weather is expected.

Second, the collocated cloud microphysical and radiation measurements performed with HoloBalloon demonstrated the potential of combining these observations to study the influence of the cloud particle concentration and thermodynamical phase on the cloud radiative properties (Chapter 5). However, the comparison of the measurements obtained by the radiation sensors mounted on HoloBalloon with the radiation measurements at the BSRN field site revealed large uncertainties in the radiation measurements of the sensors mounted on HoloBalloon. The main uncertainty is related to the temperature gradient inside the instruments, i.e. to the lack of correction for the dependence on the environmental temperature of the thermal measurements. More accurate pyranometers and pyrgeometers exist, such as the ones employed at the BSRN field site. Installing such instruments on HoloBalloon would improve the accuracy of the radiation measurements taken with HoloBalloon and enable more precise investigation of the cloud radiative properties. This would be especially important when performing profiles inside clouds and at cloud top, as the environmental temperature changes rapidly with altitude, especially at cloud top. However, the weight of the payload hanging below HoloBalloon should be kept as low as possible to ensure a sufficient lifting capacity for the HoloBalloon to reach the cloud altitude. Therefore, it is important that the sensors are light. Last but not least, higher standard sensors are generally more expensive than the sensors used in this thesis. Therefore, a balance should be

found between increased accuracy, weight, and cost of the radiation instruments to be mounted on HoloBalloon in future campaigns.

Third, the spatial and temporal resolution of HOLIMO3B could be increased. HOLIMO3B has a well-defined sample volume of approximately  $45 \text{ cm}^3$ , but the number of frames per second (fps) can be varied up to 80 fps. Because of the limited storage capacity in HOLIMO3B, the choice of frame rate is a trade-off between high temporal and spatial resolutions or long time series. So far, we opted for a balance between high resolution and long temporal coverage by employing a frame rate of 5 to 6 fps. This allowed the investigation of phase partitioning on a meter scale at wind speed below  $1 \text{ m s}^{-1}$ . However, the frame rate could be increased in future campaigns to allow for the investigation of the cloud properties on an even smaller scale.

Fourth, the temperature and humidity conditions at the measurement's location are important to understand the cloud microphysical properties. In this thesis, we benefited from the frequent radiosonde launches at Ny-Ålesund to obtain the temperature, relative humidity, and wind speed and direction at the HoloBalloon's location. However, such frequent and accurate radiosonde measurements are rarely available. In Switzerland for example, two radiosondes are launched every day from the MeteoSwiss station in Payerne. A discrepancy of several degrees can prevail between the temperature observed at Payerne and the one observed more than hundred km away a few hours after the radiosonde was launched. Therefore, we would suggest to mount temperature and humidity sensors on the HoloBalloon platform. This will help to obtain an accurate description of the environmental conditions prevailing in cloud.

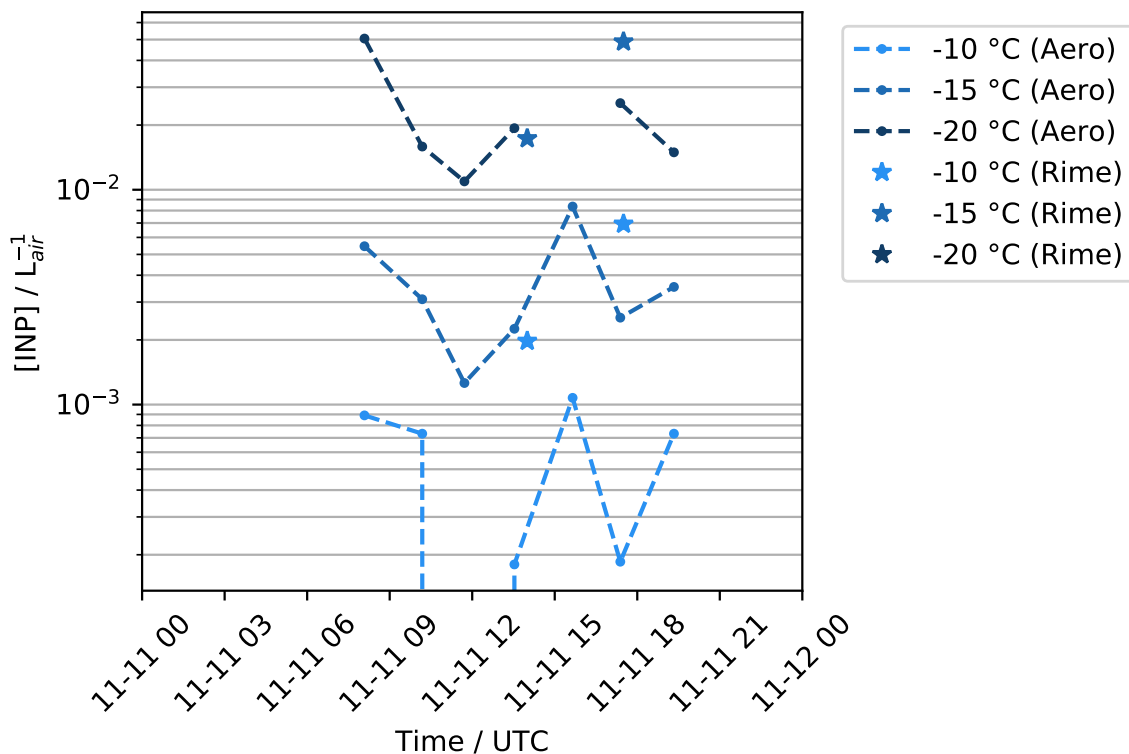


Figure 6.1: Ambient INPC measured from the inlet of the container at the Swiss Site (dashed lines) and INPC found in the melted rime converted to INPC in ambient air according to Petters and Wright (2015) assuming a cloud water content of  $0.4 \text{ g m}^{-3}$  (stars) at  $-10 \text{ }^{\circ}\text{C}$ ,  $-15 \text{ }^{\circ}\text{C}$  and  $-20 \text{ }^{\circ}\text{C}$ . Figure courtesy Jörg Wieder.

Lastly, an important improvement would be the measurements of in-cloud INPs with the HoloBalloon platform. In Chapters 2 and 3, we were limited to INP measurements on the ground at the Swiss Site with a temporal resolution of a few hours, or to INP measurements at

the Zeppelin Observatory (475 m a.s.l.) with a temporal resolution of several days. In-cloud INPC measurements would enable a more accurate differentiation between primary ice nucleation from INPs or SIP. In-cloud INPs have for example been determined using electrostatic precipitation of aerosol particles onto silicon wafers on drones, with subsequent offline analysis of the INPC (Schrod et al., 2017). A similar technique could be employed on HoloBalloon with subsequent analysis with DRINCZ (David et al., 2019a). Another possible technique to estimate the in-cloud INPC is the use of a cloud water sampler with subsequent offline analysis to retrieve the INPC. We tested this approach during the NASCENT campaign. We carefully collected rime on parts of the measurement platform after in-cloud measurements and analysed the samples with DRINCZ. An example is shown in Figure 6.1 for 11 November 2019. The INPC is about one order of magnitude higher in the rime than in the ambient air, indicating higher in-cloud INPC than the INPC sampled close to the ground. The reason for this higher concentration may be the collection of ice crystals with the cloud water. I.e. it is assumed that the rime on the probe consists of activated cloud droplets, but ice crystals could also have been colliding and staying stuck on the probe. If ice crystals were sampled together with the cloud water, it would explain the higher INPC in the rime than in the ambient air. Therefore, an instrument sampling separately ice crystals, cloud droplets, and air with subsequent determination of INPC would be ideal for comparison with the ICNC. Additionally, a cloud water content of  $0.4 \text{ g m}^{-3}$  was used in this example to convert INPC from liquid to ambient air according to Petters and Wright (2015). However, HOLIMO3B retrieved a cloud water content of  $0.1 \text{ g m}^{-3}$  on this day. Using this cloud water content for conversion of INPC from rime to ambient air would decrease the INPC by a factor of 4. In future studies, precise cloud water content derived from HOLIMO3B should be used for accurate derivation of INPC in rime.

### 6.2.3 Automatic classification of ice crystal habits

One time consuming task of this thesis was the labelling of more than 50'000 ice crystals into habits. The classification into habits was needed on the one hand to differentiate between pristine and non-pristine small ice crystals used to define SIP cloud regions and on the other hand to assess the importance of possible SIP processes (see Chapter 3). The ice crystals classified into habits will serve to train a convolutional neural network resulting in an automatic classification algorithm. This approach will save many hours in future holographic images analyses. Replacing the manual classification by an automatic one can however be delicate for three reasons. First, ice crystal habit classification depends on the goal of the study. For example frozen cloud droplets aggregated with columns were classified as 'droplet lollipops' and used as indicators for a possible occurrence of droplet shattering in this thesis. In another study, these ice crystals could be classified as aggregates or as rimed columns. Second, an ice crystal can exhibit simultaneously several habits, for example a freshly rimed column aggregated with an aged-rimed plate. The ice crystal exhibits the plate, column, aggregate, and (aged) rimed habits simultaneously. Third, the two dimensional holographic image may not be sufficient to infer the ice crystal habit in three dimensions. For example the differentiation between capped columns and two aggregated plates is difficult. Examples of ice crystals with difficult habit identification are shown in Figure 6.2, where particles that are difficultly distinguishable between capped columns and aggregated plates are highlighted with orange frames.

The use of an automatic classification algorithm would allow a more objective classification of the ice crystals into habits. However, the automatic classification would not consider specific classification goals (e.g. classification into specific habits associated with different SIP processes). We suggest in a first step to use the automatic classification for general habit classes (e.g. columns, plates, dendrites). In a second step, an automatic classifier could distinguish between e.g. pristine, rimed, or aged particles. This classification could also be done manually.



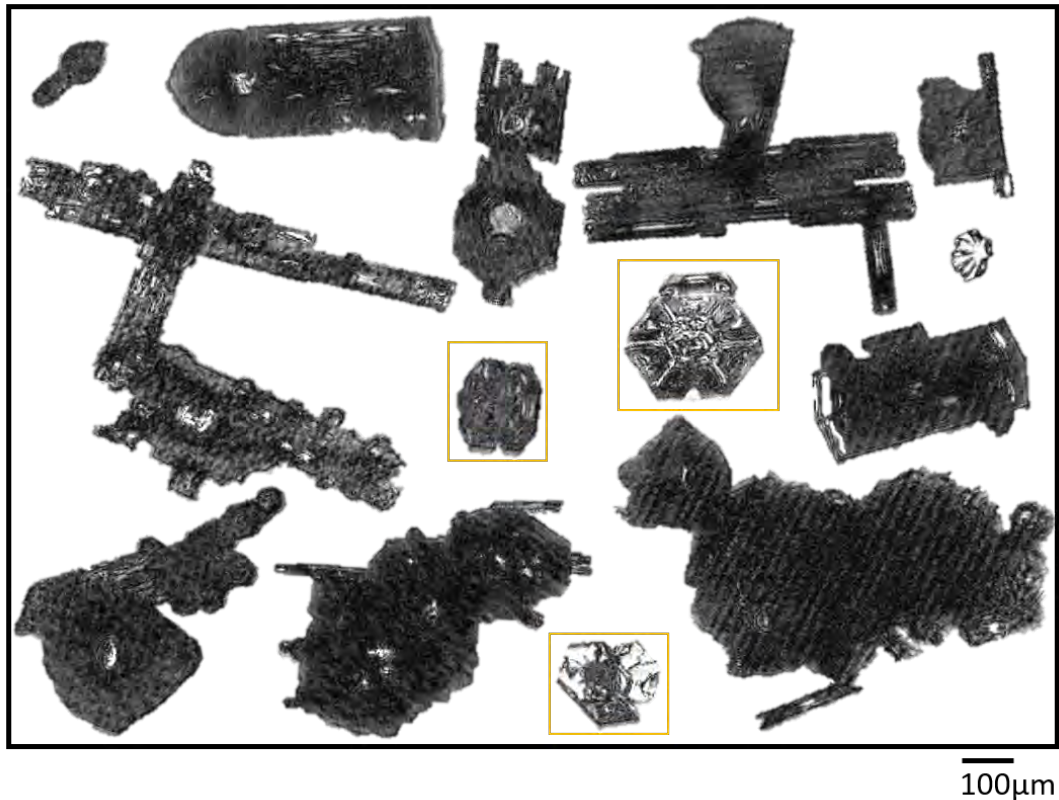


Figure 6.2: Example of ice crystals that can be classified into several habits.

#### 6.2.4 Need for a more accurate SIP process characterization

In-cloud studies highlighted the importance of SIP processes for ice crystal formation in MPCs (e.g., Lloyd et al., 2015; Lawson et al., 2017; Gayet et al., 2009; Korolev and Leisner, 2020). We consistently found that SIP largely contributed to high ICNC in the low-level Arctic MPCs measured during the NASCENT campaign. Despite the increased awareness of the importance of SIP in MPC, an accurate description of the necessary and sufficient criteria for SIP occurrence is lacking. Advanced knowledge should be gained from laboratory and field studies. Regarding the laboratory studies, contradictory results and gaps in knowledge hinder an adequate description of all SIP processes. Hence, future laboratory work should aim to acquire a precise characterization of the SIP processes, including a range of number of secondary ice crystals produced and the evaluation over the entire heterogeneous temperature range from 0 °C to -35 °C for all SIP processes. For this new instrumentation together with large cloud chambers could for example be used.

Regarding in-cloud measurements, the uncontrolled environment complicates the characterization of SIP processes. In this thesis, we investigated the atmospheric conditions prevailing during SIP. However, only a subset of the possible environmental conditions could be investigated. More in-cloud measurements should aim to assess the environmental conditions in which SIP are occurring. To this aim, a variety of state-of-the-art instrumentation could be used in an automatic way. For example, remote sensing instrumentation such as ceilometer and cloud radar could be used to determine the presence of mixed-phase clouds, and trigger the flight of a drone carrying a small and light holographic imager together with temperature, wind, and humidity sensors. The drone could perform profiles through the entire cloud layer, using real time cloud top and cloud base altitude determination from the remote sensing observations. Thereafter, the entire

data processing could be automatized and SIP regions identified and compared to the environmental conditions prevailing at these locations. Such an automatized processing from data acquisition to identification of SIP regions and environmental conditions interpretation would provide a extremely large database that would enable an accurate description environmental conditions favorable for SIP. Ny-Ålesund would be an ideal for such a project, because of (1) the high frequency of low-level MPCs at this location, (2) the minor frequency of airplane flights blocking the air space for in-cloud flights with drones, (3) the existing scientific infrastructure such as aerosol and INP concentrations monitoring, as well as remote sensing observations (and the recent installation of a polarimetric cloud radar), and (4) permanent scientific staff available for maintenance of the instrumentation on-site.

Last but not least, the results from laboratory and field measurements should be used to derive realistic SIP parametrizations over a wide temperature range. The improved SIP parametrization should be used in numerical weather prediction for improved precipitation forecasts and in climate models to reduce the uncertainty of cloud radiative feedbacks in climate projections.

## Appendix A

# Supplementary Material: The Ny-Ålesund Aerosol Cloud Experiment (NASCENT): Overview and First Results

Julie T. Pasquier (1) and R. O. David (2) and G. Freitas (3,4) and R. Gierens (5) and Y. Gramlich (3,4) and S. Haslett (3,4) and G. Li (1) and B. Schäfer (2) and K. Siegel (3,4) and J. Wieder (1) and K. Adachi (17) and F. Belosi (14) and T. Carlsen (2) and S. Decesari (14) and K. Ebell (5) and S. Gilardoni (12,13) and M. Gysel-Beer (9) and J. Henneberger (1) and J. Inoue (6) and Z. A. Kanji (1) and M. Koike (7) and Y. Kondo (6) and R. Krejci (3,4) and U. Lohmann (1) and M. Maturilli (10) and M. Mazzolla (12,13) and R. Modini (9) and C. Mohr (3) and G. Motos (11) and A. Nenes (11, 19) and A. Nicosia (14) and S. Ohata (15, 16) M. Paglione (14) and and S. Park (8) and R. E. Pileci (9,21) and F. Ramelli (1) and M. Rinaldi (14) and C. Ritter (10) and K. Sato (18) and T. Storelvmo (2) and Y. Tobo (6) and and R. Traversi (20) and A. Viola (12,13) and P. Zieger(3,4)

- (1) Institute for Atmospheric and Climate Science, ETH Zürich, Zurich, Switzerland
- (2) Department of Geosciences, University of Oslo, Oslo, Norway
- (3) Department of Environmental Science, Stockholm University, Sweden
- (4) Bolin Centre for Climate Research, Stockholm University, Sweden
- (5) Institute for Geophysics and Meteorology, University of Cologne, Cologne, Germany
- (6) National Institute of Polar Research (NIPR), Tachikawa, Tokyo, Japan
- (7) Department of Earth and Planetary Science, Graduate School of Science, University of Tokyo, Tokyo, Japan
- (8) Korea Polar Research Institute (KOPRI), Incheon, Korea
- (9) Laboratory of Atmospheric Chemistry, Paul Scherrer Institute (PSI), Villigen PSI, Switzerland
- (10) Alfred Wegener Institute, Helmholtz Centre for Polar and Marine Research (AWI), Potsdam, Germany
- (11) Laboratory of Atmospheric Processes and their Impacts, Ecole Polytechnique Fédérale de Lausanne, Lausanne, Switzerland
- (12) Institute for Polar Sciences, CNR, Bologna, Italy
- (13) Institute for Polar Sciences , CNR, Rome, Italy
- (14) National Research Council, Institute of Atmospheric Sciences and Climate, CNR-ISAC, Bologna, Italy
- (15) Institute for Space–Earth Environmental Research, Nagoya University, Nagoya, Aichi, Japan
- (16) Institute for Advanced Research, Nagoya University, Nagoya, Aichi, Japan
- (17) Meteorological Research Institute, Tsukuba, Ibaraki, Japan
- (18) Kitami Institute of Technology, Kitami, Hokkaido, Japan
- (19) Center for Studies of Air Quality and Climate Change, Institute for Chemical Engineering Sciences, Foundation for Research and Technology Hellas, Patras, Greece
- (20) Department of Chemistry, University of Florence, Florence, Italy
- (21) U-Earth Biotech Ltd, London, United Kingdom

In this supplementary material, we shortly describe the atmospheric situation on 12 November

2019 in Ny-Ålesund, Svalbard (Fig. A.1), as mainly measurements taken this day are discussed in the main manuscript. Additionally, the major instrumentation used in this manuscript or installed in the framework of the Ny-Ålesund Aerosol Cloud Experiment (NASCENT) at the Swiss Site, the Zeppelin Observatory, Gruvebadet, the Climate Change Tower, and AWIPEV are described. Finally, information about the WRF model setup are given, together with a short description of the simulation during flights 2 and 3 of HoloBalloon. Summarizing tables with the instrument parameters are included.



Figure A.1: Map of Svalbard with location of Ny-Ålesund marked with the red star (topographical data from Norwegian Polar Institute, 2014).

## A.1 Meteorological situation on 12 November 2019

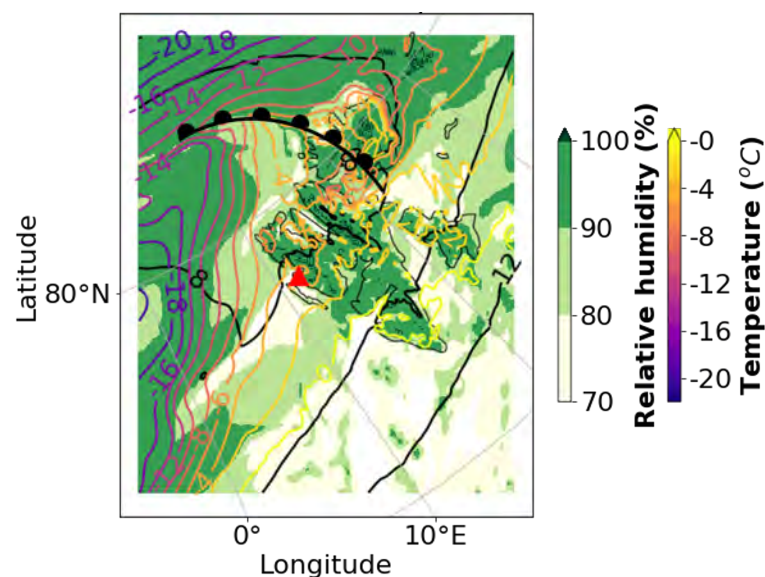


Figure A.2: Weathermap showing the relative humidity (green shading), temperature (colored lines) at 1000 hPa and the estimated location of the warm front at 0600 UTC on 12 November. The red triangle shows the location of Ny-Ålesund. The model data are from the MEPS Weathermaps Hellmuth and Hofer (2019).

A warm front passed over Ny-Ålesund on 11 November 2019. One day later, on 12 November 2019, Ny-Ålesund was located in the warm sector behind the warm front (Fig. A.2). The temperature at the ground was therefore relatively high (varying between  $0^{\circ}\text{C}$  and  $-3^{\circ}\text{C}$  and the pressure slightly increased from 1009 to 1011 hPa (not shown). Note that on this day the sun was permanently below the horizon with a minimum altitude of  $-29^{\circ}$  and a maximum altitude of  $-7^{\circ}$ . Thus no direct sunlight was shining.

On 12 November 2019, several short and intense precipitation events occurred and are recognizable as fallstreaks in the radar reflectivity (Fig. A.3a) with total precipitation summing up to about 2.4 mm (not shown). The large-scale wind measured by the radiosondes (Fig. A.8) and visible on the wind lidar measurements above 800 m a.s.l. (Fig. A.3b) was southwesterly. After 1500 UTC, a strong change in the horizontal wind direction below 500 m a.s.l. was observed, which generated strong wind shear (Fig. A.3b). The Zeppelin Observatory was in cloud for large parts of the day and three flights into clouds were performed with HoloBalloon (Fig. A.3).

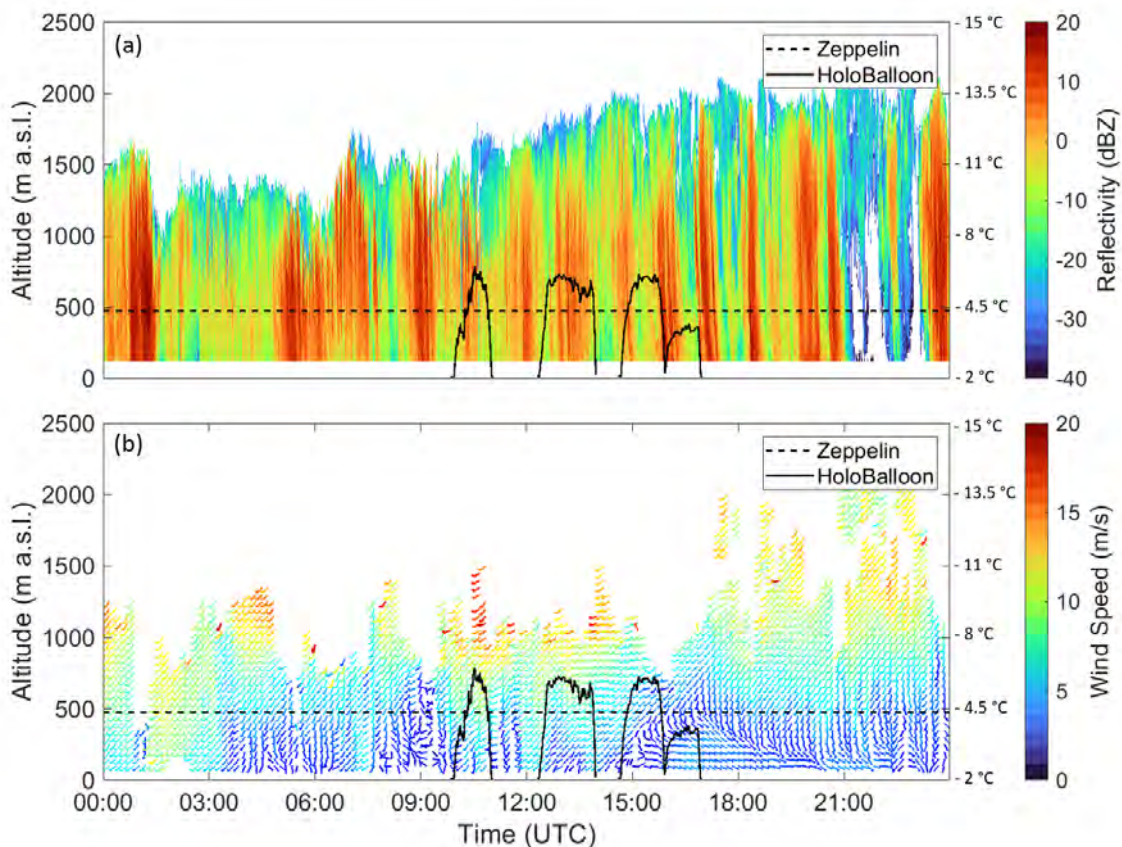


Figure A.3: Cloud radar and wind lidar measurements on 12 November 2019. (a) Cloud radar reflectivity and (b) wind lidar horizontal wind speed. The wind barbs show the wind direction and the color the horizontal wind speed. The solid black line shows the height of HoloBalloon and the dashed line the height of the Zeppelin Observatory. The black dots in (a) show the cloud base heights measured by the ceilometer. The temperature measured by the radiosonde launch at 1700 UTC is shown on the right y-axis at the corresponding altitude on the left y-axis.

## A.2 Swiss Site

### A.2.1 Aerosol measurements at the container

During October - November 2019 and March - April 2020, the temporary Swiss Site was installed at the southwestern end of Ny-Ålesund. Ambient aerosol, cloud condensation nuclei (CCN), and ice nucleating particles (INPs) were sampled through an inlet mounted on top of the observatory container. Aerosol particles were measured in the size range of 10 nm to 20  $\mu\text{m}$  using an APS, scanning mobility particles sizer (SMPS, TSI Inc., Shoreview, MN, USA), condensation particle counters (CPC, TSI Inc., Shoreview, MN, USA), and optical particle counters (OPC-N3, Alphasense). A Wideband Integrated Bioaerosol Sensor (WIBS-NEO) provided information on fluorescent properties of the particles.

To obtain a broader INP concentration - temperature spectrum, two methods were applied in parallel. INPs were monitored continuously at  $-30\text{ }^\circ\text{C}$  in the immersion freezing mode using the online technique Horizontal Ice Nucleating Chamber (HINC, Lacher et al., 2017). HINC sampled ambient air continuously at a total flow rate of  $2.83\text{ StdL min}^{-1}$ , of which 90% consists of recirculating particle-free sheath flow and the remaining 10% is compensated by aerosol flow. To account for the false positive ice count originating from the internal chamber, e.g., falling frost from the warmer plate, a motorized valve was applied to switch from sample flow to filtered air measurements regularly (5 min) before and after each sampling period (15 min) to determine a background count.

In addition, ambient aerosol particles were sampled from the heated inlet using a high flow-rate impinger (Coriolis<sup>®</sup>  $\mu$ , Bertin Instruments, France) operating at  $300\text{ L min}^{-1}$ . For one sample the impinger collected aerosol for one hour, probing a volume of  $18\text{ m}^3$ . Right after collection, each sample was analysed for INP concentration via the offline technique DRoplet Ice Nuclei Counter Zurich (DRINCZ, David et al., 2019a), which measured INP concentrations at sub-freezing temperatures down to  $-20^\circ\text{C}$ . See also Wieder et al. (2022b), where the setup and procedure are described in details.

CCN concentrations during the NASCENT campaign were measured by a cloud condensation nuclei counter (model CCNC-100), commercialized by Droplet Measurement Technologies (DMT, Longmont, CO, USA). Unfortunately, this instrument malfunctioned during periods of the campaign that include 12 November 2019. Therefore, we used a back-integrated SMPS to calculate the aerosol concentration down to a particle mobility diameter of 70 nm to estimate CCN concentrations, following the method by Koike et al. (2019). Data quality was ensured by comparing total integrated concentration with two condensation particle counters (CPC, TSI Inc., Shoreview, MN, USA) at the Zeppelin Observatory as well as another SMPS and a CPC at sea level at the Swiss Site.

Additionally, at regions near shore close to Ny-Ålesund, we used a clean glass plate withdrawn vertically from the sea surface for sea surface microlayer samples. The thin microlayer film on the plate was then transferred into sample bottles using a Teflon scraper to wipe down the glass plate. The sub-surface bulk seawater samples were sampled by directly submerging sample bottles to about 50 cm below the ocean surface.

### A.2.2 HoloBalloon

The tethered balloon system HoloBalloon (Ramelli et al., 2020) was used to perform in-situ cloud microphysical measurements. The main instrument on HoloBalloon is the HOLographic cloud Imager for Microscopic Objects (HOLIMO3B, Fig. A.4), which can image an ensemble of cloud particles in the size range from small cloud droplets (6  $\mu\text{m}$ ) to precipitation-sized particles (2 mm) in a three-dimensional sample volume (Henneberger et al., 2013; Beck et al., 2017; Ramelli et al., 2020). HOLIMO3B provides information about the phase-resolved particle size distribution and particle habits. Particles larger than 25  $\mu\text{m}$  can be differentiated between cloud droplets and ice



crystals based on their shape, whereas all particles smaller than 25  $\mu\text{m}$  are classified as cloud droplets. Because of this size threshold, the reported ice properties can be considered as a lower estimate. Cloud droplets and ice crystals larger than 25  $\mu\text{m}$  were classified using convolutional neural network trained on cloud particles from holographic imagers (Touloupas et al., 2020) and smaller cloud droplets using support vector machines. The ice particle habits were classified manually. The sampling volume of HOLIMO3B used was about 15.5  $\text{cm}^{-3}$ , and 6 frames were taken per seconds. The processed data are averaged over 60 seconds, which gives a volume of about 5.6 L per minute. The diameter used from the measurements by HOLIMO3B is the major diameter, which correspond to the major axis of an ellipse around the detected pixels of the particle. Two Optical Particle Counters (OPCs) and one 3D-sonic anemometer are furthermore mounted on the platform. Expanding on the measurement platform described in Ramelli et al. (2020), two pyranometers and pyrgeometers (Apogee SL-510/610, SP-510/610) measured upward and downward solar and terrestrial radiation (Fig. A.4) were installed on the instrument and the platform was suspended 12 m below the helikite to prevent turbulence effects.

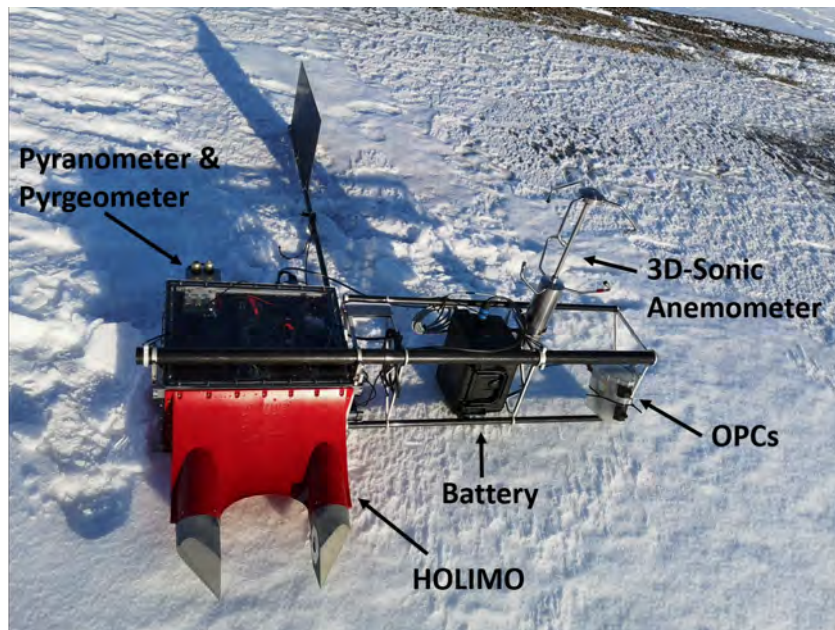


Figure A.4: HoloBalloon Platform with description of the different parts. The platform is aligning in direction of the wind thanks to the wind tail and is hanging 12 m below the helikite.

## A.3 Zeppelin Observatory

Detailed in-situ observations of clouds, aerosols, and meteorology were made at the Zeppelin Observatory. Figure A.5 presents a schematic of the set-up at the site during NASCENT which is described below.

### A.3.1 GCVI sampling and aerosol instrumentation

A ground-based counterflow virtual impactor inlet (CVI) was installed at the Zeppelin Observatory to sample ambient cloud droplets and ice crystals. The CVI is based on the technical principles described by Shingler et al. (2012). The evaluation of the ground-based version of the CVI at the Zeppelin Observatory is described in detail by Karlsson et al. (2021) and only a brief description will be given here. The CVI separates particles according to their inertia using opposing air flows. Large particles (e.g. cloud droplets or ice crystals) are sampled, while small particles with low inertia (e.g. interstitial aerosol) do not penetrate through the virtual

stagnation plate of the inlet and are not sampled. The cloud droplets or ice crystals are then dried and the remaining particles are termed cloud residuals. The residuals are then characterized by various aerosol instruments. This includes a custom-made DMPS (differential mobility particle sizer) for measuring the particle size distribution between approximately 10 and 945 nm (electrical mobility diameter) of the cloud residuals (see Karlsson et al., 2021, for more technical details). A condensation particle counter (CPC, Model 3772, TSI Inc, USA) determines the total particle number concentration. A multi-parameter bioaerosol spectrometer (MBS, University of Hertfordshire, U.K., see e.g., Ruske et al., 2017) was used to characterize the size, shape and fluorescent characteristics of particles larger than 0.5  $\mu\text{m}$  (optical diameter). The FIGAERO-CIMS (see next section) was connected to the CVI to measure the chemical composition of cloud residuals and aerosol particles. An impactor sampler (AS-24W, Arios Inc., Tokyo, Japan) was used to collect particles for a single particle analysis using a transmission electron microscope (TEM; JEM-1400, JEOL) with an energy-dispersive X-ray spectrometer (EDS; X-max 80, Oxford Instruments). The extended-range single-particle soot photometer (SP2-XR, DMT Inc., USA Stephens et al., 2003; Schwarz et al., 2006) was used to characterize the black carbon content of cloud residuals. In addition, a cloud condensation nuclei counter (CCNC, DMT Inc., USA, see Roberts and Nenes, 2005) measured the (re-)activation of cloud residuals behind the CVI.

The CVI can be operated in manual or automatic mode. In automatic mode, the readings of a visibility sensor were used to turn on the CVI (threshold was usually set to 1 km visibility). A three-way valve enables the in-situ instrumentation to sample from the whole-air inlet during non-cloudy periods, allowing additional validation with the standard aerosol instruments measuring behind the whole-air inlet.

An iodide chemical ionization high-resolution time-of-flight mass spectrometer (FIGAERO, Lopez-Hilfiker et al., 2014; Thornton et al., 2020) was coupled to a filter inlet for gases and aerosols (CIMS) using iodide-adduct ionization. The iodide-FIGAERO-CIMS is sensitive to polarizable or acidic organic aerosol components (Lee et al., 2014). The instrument was installed at the Zeppelin Observatory and connected with two separate inlet lines to ambient air. The particle phase inlet was connected via a  $\frac{1}{2}$  inch stainless steel tube to a three-way valve switching between the whole air inlet and the CVI inlet mounted at the top of the observatory. During the NASCENT campaign aerosol particles were sampled with 4 L  $\text{min}^{-1}$  on a Teflon filter for 2.5 hours. To determine the particle background, air was passed through an additional Teflon filter upstream the FIGAERO particle inlet, usually every third collection cycle. The data presented here is particle phase data of one whole-air inlet sample and one CVI inlet sample (cloud residual). The gas phase inlet was connected via  $\frac{1}{4}$  inch PTFE tubing to ambient air directly through a hole in the wall. Gases were sampled at 1 Hz with 2 StdL  $\text{min}^{-1}$ . To determine the gas phase background during the campaign, zero air was frequently injected into the instrument for 15 minutes. The FIGAERO-CIMS was installed in October 2019, and data is available from November 2019 until December 2020, with some interruptions.

In parallel, size distributions of cloud residuals and ambient aerosols were characterized using three differential mobility particle sizer instruments (see e.g. Karlsson et al., 2021), while the black carbon (BC) mass concentration was determined using an extended-range single-particle soot photometer (SP2-XR, Stephens et al., 2003; Schwarz et al., 2006), a multi-angle absorption photometer (MAAP, Petzold and Schönlinner, 2004), and a continuous soot monitoring system (COSMOS, Kondo et al., 2011). Note that the measurement of BC mass relies on operational definitions and is therefore method dependent, as discussed by Petzold et al. (2013). Note that recently, a method to harmonize Arctic BC measurements using the COSMOS as a standard instrument was developed, because COSMOS-derived BC mass concentration is traceable to a rigorously calibrated SP2 and the absolute accuracy has been demonstrated previously to be about 15 % in the Arctic (Ohata et al., 2021, submitted). The agreement between the BC mass concentration measurements obtained during NASCENT indicates that the instruments are in

accordance with this method.

On the terrace of Zeppelin Observatory, a Fine dust measurement device Fidas 200 S (FIDAS, Palas GmbH, Germany) was installed to measure the particle size distribution from around 200 nm to approx. 18  $\mu\text{m}$  (optical diameter). The instrument is installed in its own temperature-controlled stainless steel water protected cabinet. The Sigma-2 sampling head allows sampling even at high wind speed conditions. The inlet pipe is automatically heated to ensure sampling at dry conditions (controlled by an external RH/T sensor and monitored by an additional RH/T sensor within the sampling line).

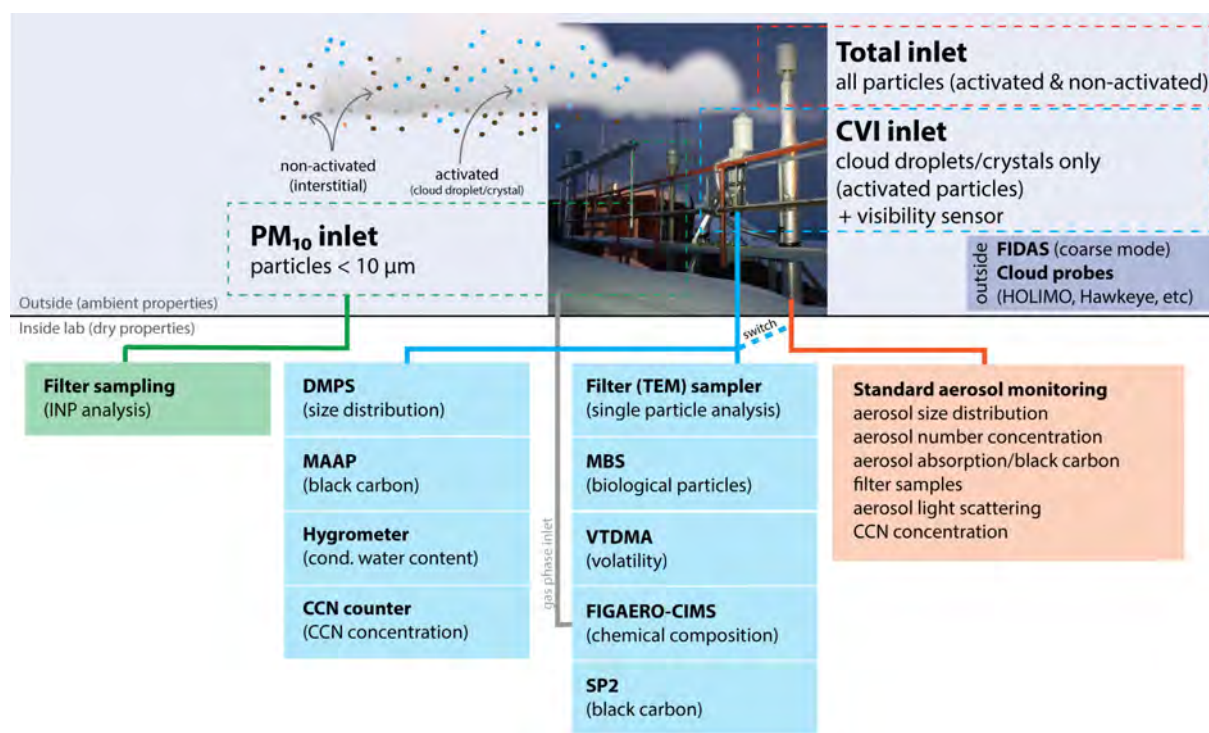


Figure A.5: Aerosol and cloud sampling at the Zeppelin Observatory during NASCENT. Various air inlet systems were used to sample particles, gas phase, cloud particles and whole air (aerosol and cloud particles) that were analysed in the laboratories below. In addition, various cloud probes and aerosol instrumentation were placed outside on the observation terrace. For further details on the CVI/whole-air inlet sampling see Karlsson et al. (2021).

### A.3.2 CRAFT

Continuous year-round measurements of atmospheric INPs active in the immersion mode at the Zeppelin Observatory were started in March 2018. Weekly aerosol sampling for measuring INPs has been performed continuously and sequentially from Sunday (0000 UTC) to Saturday (2359 UTC) using a 10-line Global Sampler (GS-10N, Tokyo Dylec Corp.) connected with a PM10 common inlet. Each sample has been collected on a precleaned Whatman Nuclepore track-etched membrane filter (47 mm in diameter and 0.2  $\mu\text{m}$  in pore size) supported by a filter cassette screen (part no 59-005147-0010, Thermo Fisher Scientific) and mounted in a NILU inline filter holder system at a flow rate of 3 L  $\text{min}^{-1}$ . The samples were analyzed using the Cryogenic Refrigerator Applied to Freezing Test (CRAFT, Tobo, 2016). The basic procedures for measuring the number concentrations of atmospheric INPs using the CRAFT system are essentially the same as those used for our previous studies (Tobo et al., 2019, 2020). As for the data obtained during the NASCENT campaign, we quantified the INP number concentrations over a temperature range down to  $-30^{\circ}\text{C}$ .

### A.3.3 Hawkeye & MPS

Continuous year-round in-situ measurements of cloud and precipitating particles were made using a fog monitor (FM-120, DMT Inc., CO USA), Meteorological Particle Sensor (MPS, DMT Inc., CO USA), and Hawkeye (SPEC Inc., CO USA), which were located on the deck of the Zeppelin Observatory (Koike et al., 2019, 2021). The MPS is an optical disdrometer, which measures the precipitating particle size distributions with radii between 12.5 and 775  $\mu\text{m}$  (12.5  $\mu\text{m}$  resolution) using an optical array detector. Particles cast a shadow on the array as they gravitationally fall through the laser. The subsequent decrease in light intensity on the diodes is recorded, and a two-dimensional image is captured. In this study a maximum width is used as the particle size. Hawkeye consists of three systems, namely, the Fast Cloud Droplet Probe (FCDP), the Two-Dimensional Stereo Particle Imaging Probe (2D-S), and the Cloud Particle Imager (CPI). The 2D-S has two optical array detectors which are orthogonal to each other and normal to the flow of particles. Each detector measures particles with radii between 10 and 1280  $\mu\text{m}$  (10  $\mu\text{m}$  resolution) and 50 and 6400  $\mu\text{m}$  (50  $\mu\text{m}$  resolution). The CPI is a particle imaging system using the CCD camera with an effective pixel size of 2.3  $\mu\text{m}$ . In this study, a maximum dimension is used as the particle size. The 2D-S and CPI measure particles, which are sucked into a straight flow tube of the Hawkeye probe using an aspiration fan. The probe is mounted on a rotating pedestal to orient it toward the wind direction.

On 12 November 2019, the 2D-S observed ice crystals consisting of column and frozen drops that we named 'droplet lollipops' in the main manuscript (Fig. A.6). Such droplet lollipops were also measured by HOLIMO3B on HoloBalloon (see Fig. 10 of the main manuscript) and by HOLIMO3G at the Zeppelin Observatory (not shown).

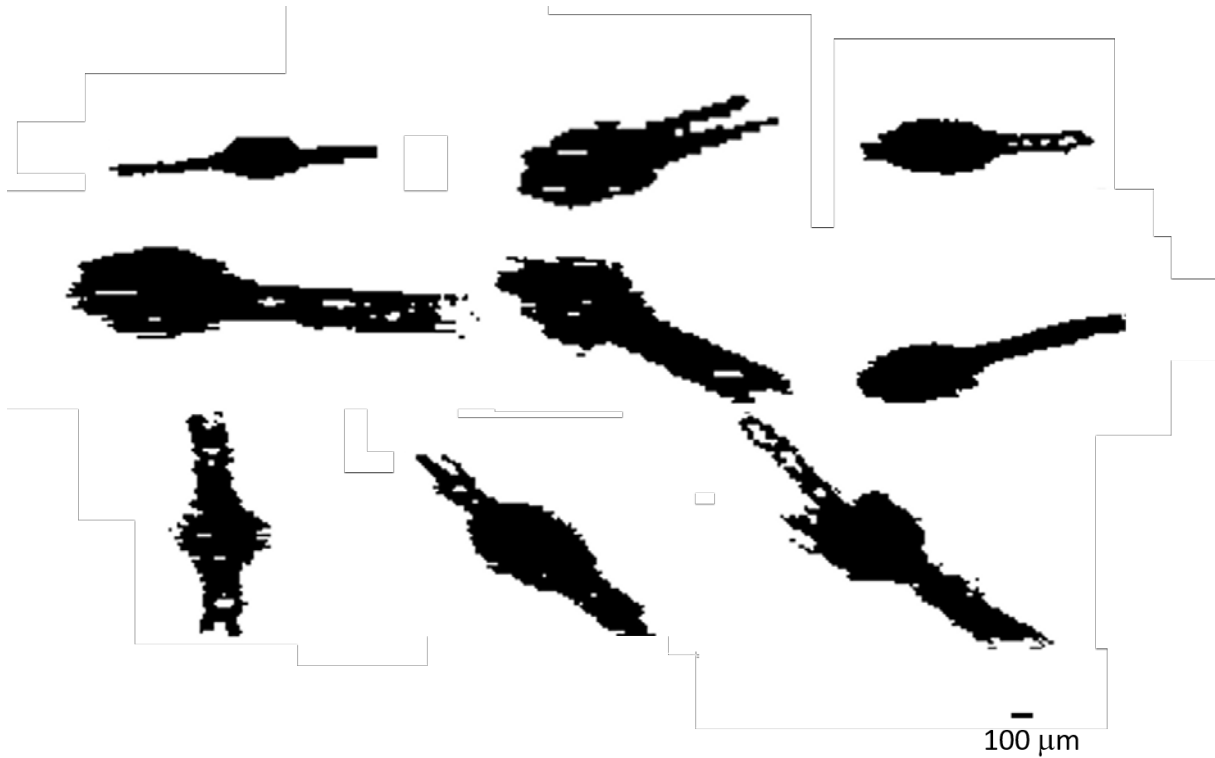


Figure A.6: Example of ice crystals classified to 'droplet lollipops' observed with the 2D-S probe at the Zeppelin Observatory.

### A.3.4 HOLIMO3G

The holographic imager HOLIMO3G (Henneberger et al., 2013; Beck et al., 2017; Lauber et al., 2021) was mounted on the platform in October - November 2019 and March - April 2020. The working principle of HOLIMO3G is identical with the one of HOLIMO3B (Section A.2.2). The sampling volume of HOLIMO3G used in this study was about  $13 \text{ cm}^{-3}$ , and 1 frame was taken per second. The processed data are averaged over 30 seconds, which gives a volume of about 0.4 L per 30 sec interval.

## A.4 AWIPEV

The German Alfred Wegener Institute for Polar and Marine Research (AWI) and the French Polar Institute Paul Emile Victor (IPEV) operate their research stations in the town of Ny-Ålesund as the joint AWIPEV Research Base. Meteorological surface measurements are sampled continuously on the measurement field south of the Ny-Ålesund village, including up- and downward short- and longwave surface radiation measurements that are performed within the Baseline Surface Radiation Network (BSRN, Maturilli et al., 2013, 2015). Radiosondes are launched at least once per day (Maturilli and Kayser, 2017), with additional launches performed during intensive measurement periods. Additionally, a suite of remote sensing instruments observe the atmosphere. In this study, we used the 94 GHz cloud radar of University of Cologne (JOYRAD-94, Kuchler et al., 2017), the ceilometer (Vaisala-CL51, Maturilli and Ebell, 2018), and the wind lidar (Windcube200). The measurements of the cloud radar, the microwave radiometer HATPRO and the ceilometer are combined with thermodynamic profiles from a numerical weather prediction model to provide continuous, standardized information on cloud properties using the Cloudnet algorithm suite (Illingworth et al., 2007). For details on the Ny-Ålesund set-up, see Nomokonova et al. (2019). Further examples of the use of the Cloudnet products in Ny-Ålesund are given in Nomokonova et al. (2020) and Gierens et al. (2020). In this work, we utilized the vertically resolved hydrometeor classification to derive the monthly frequency of occurrence for different cloud types during the NASCENT year (Section 3b, Fig. 2b). In addition to the measurements used in this study, further instrumentation for observing aerosols, water vapor, clouds and precipitation are operated at AWIPEV. Table A.1 lists the instrumentation relevant for NASCENT.

### A.4.1 CPS Sonde

Cloud particle observations using a cloud particle sensor sonde (Meisei Electric Co., Ltd.; hereafter, CPS sonde) were conducted at the French-German Arctic research base AWIPEV in Ny-Ålesund during March 2020. The CPS sonde connected to the Meisei RS-11G radiosonde can measure the vertical profile of cloud parameters (e.g., total particle count, particle phases, and particle size) and basic meteorological parameters (e.g., temperature, relative humidity, wind speed). During this campaign, 13 CPS sonde observations were made under various synoptic situations. In the lower troposphere ( $<2 \text{ km}$ ), mixed-phase and/or liquid water clouds were frequently observed, while in the middle (2-6 km) and upper troposphere ( $>6 \text{ km}$ ), ice clouds were occasionally detected, particularly in cases of low-pressure systems nearby Ny-Ålesund. The characteristics of estimated liquid water content (LWC) profiles from CPS sonde data agreed with the adiabatic retrieval of LWC obtained by a humidity and temperature profiler (HATPRO) at the AWIPEV base (Inoue et al., 2021).

### A.4.2 Forward simulation with PAMTRA

To illustrate how different hydrometeors contribute to the radar Doppler spectrum (Section 4b, Fig. 11), we utilized the Passive and Active Microwave radiative TRANSfer tool (PAMTRA

Mech et al., 2020). PAMTRA produces synthetic observations for a given atmospheric state by combining a radiative transfer model with an instrument model. In the simulations carried out for this paper, PAMTRA was run in full Doppler spectra mode for a ground based view to produce synthetic cloud radar observations resembling the JOYRAD-94 measurements. Details of the modelling framework are provided by Mech et al. (2020). In short, PAMTRA first calculates the volumetric backscattering as a function of particle size  $\eta_D$ , where  $D$  is the maximum diameter of the particle, based on the given hydrometeor properties and chosen scattering model. In the next step,  $\eta_D$  is converted to a spectral radar reflectivity as a function of particle fall velocity (e.g. the radar Doppler spectrum) by utilizing a hydrodynamic model, which provides a relationship between particle size and fall velocity. To produce radar Doppler spectra that are comparable to real observations, the radar simulator also accounts for kinematic broadening, vertical wind speed, radar receiver noise, and attenuation (Mech et al., 2020, and references therein).

In this work, the simulated radar observations were considered at a fixed altitude of 350 m, with 4 m range resolution. Further radar simulator settings corresponded to the parameters of the JOYRAD-94 measurements. The thermodynamic profile was obtained from the sounding launched at 1400 UTC. The vertical wind was set to  $0 \text{ ms}^{-1}$ , and the eddy dissipation rate to  $10^{-4} \text{ m}^2\text{s}^{-3}$ . Keeping these parameters constant is not realistic, but simplifies the interpretation of the simulated Doppler spectra as all changes can be attributed to changes in the hydrometeor properties, and changing thermodynamic conditions or range dependent factors of the radar measurement can be ignored. Additionally, attenuation was neglected for simplicity.

The description of hydrometeor particle size distributions (PSDs) and single-scattering properties, especially for frozen hydrometeors, is a general problem for forward modelling (Kneifel et al., 2018; Mech et al., 2020). Here, we took advantage of the full-bin interface of PAMTRA and used the PSDs measured by HOLIMO3B, averaged over 5 min, as input for PAMTRA. Four hydrometeor classes were used in PAMTRA: liquid, small ice ( $<106 \text{ }\mu\text{m}$ ), large ice ( $\geq 106 \text{ }\mu\text{m}$ ), and frozen droplets. For each hydrometeor class, phase (ice or liquid) and the scattering and fall-velocity models need to be defined in order to calculate the synthetic radar Doppler spectrum. Furthermore, with the full-bin interface used, the mass ( $M$ ), cross-section area ( $A$ ), density ( $\rho$ ) and aspect ratio for each size bin need to be set. For liquid droplets, the single-scattering properties were calculated using Mie-theory (Mie, 1908) and fall velocity follows Khvorostyanov and Curry (2002). The mass, area, and density were trivial to set, assuming liquid droplets are spheres with constant density of  $1000 \text{ kgm}^{-3}$ . Similarly, frozen droplets were assumed to be spheres with a constant density of  $917 \text{ kgm}^{-3}$ . The description of other ice particles (other than frozen droplets) was less trivial. The large variability in ice particle properties in the studied case (Fig. 9,10) makes it difficult to set bulk properties that describe well the entire ice particle population. For simplicity, we assumed Rayleigh scattering (Petty, 2006), meaning that particles were assumed to be spherical and backscattering only depends on the size and density of the particle. This is a crude simplification, but the difficulty to precisely estimate key particle properties hinders the use of more sophisticated scattering models. Furthermore, the purpose of the PAMTRA simulations was not to produce synthetic measurements matching the JOYRAD-94 observations, as a closure study is beyond the scope of this paper. Rather, the aim was to help the reader to gain an understanding of how different hydrometeors contribute to reflectivity and the cloud radar Doppler spectrum. The fall velocity of ice particles was estimated using the model from Heymsfield and Westbrook (2010), which calculates the fall velocity depending on the mass and area of the particle.

For ice particles (other than frozen droplets), the mass ( $M$ ) and area ( $A$ ) for each size bin were determined using power laws in the form of  $M = \alpha D^\beta$  and  $A = \gamma D^\sigma$ , where  $\alpha$ ,  $\beta$ ,  $\gamma$ , and  $\sigma$  are habit dependent coefficients (Pruppacher and Klett, 2010). All power laws used follow Mitchell (1996). For small ice ( $<106 \text{ }\mu\text{m}$ ), which consists of mostly columns, we used the coefficients for hexagonal columns smaller than  $100 \text{ }\mu\text{m}$  ( $M = 0.1677D^{2.91}$  and  $A = 0.684D^{2.00}$ , where the units of  $M$ ,  $A$  and  $D$  are  $\text{g}$ ,  $\text{cm}^2$  and  $\text{cm}$ , respectively). For larger ice ( $\geq 106 \text{ }\mu\text{m}$ ), which consists



of a mixture of mainly columns, aggregates, and irregular, partially rimed particles, we used a combination of hexagonal columns ( $M = 0.00166D^{1.91}$  and  $A = 0.0696D^{1.50}$  for  $100 \mu\text{m} < D \leq 300 \mu\text{m}$ , and  $M = 0.000907D^{1.74}$  and  $A = 0.0512D^{1.414}$  for  $D > 300 \mu\text{m}$ ) and lump graupel ( $M = 0.049D^{2.8}$  and  $A = 0.50D^{2.0}$ ). The mass and area used for large ice were calculated as a weighted average of the hexagonal column and graupel for each size bin, so that in the turbulent period (until 1545 UTC, see Section 4b and Fig. 9) a weight of 2 was given for column and 1 for graupel, and in the fallstreak period (after 1545 UTC) both were weighted equal. In this way, we could account for the shift in the ice particle population, which showed a large fraction of columns ( $>106 \mu\text{m}$ ) in the turbulent period and drops in the fallstreak period (Fig. 9f). An effective density was calculated for each size bin as  $\rho(D) = M / V(D)$ , where  $V(D)$  is the volume of a sphere with diameter  $D$ , to be consistent with the other assumptions. As all hydrometeors were essentially treated as spheres, the aspect ratio has no effect on the simulated radar Doppler spectra and could therefore be neglected.

To produce the Doppler spectra shown in Fig. 11, a simulation was run for each hydrometeor class independently. Two simulations were run for liquid hydrometeors: one for cloud droplets ( $\leq 56 \mu\text{m}$ ) and one for drizzle droplets ( $>56 \mu\text{m}$ ). Finally, a simulation including all hydrometeor classes was performed, and the resulting reflectivity showed reasonable agreement with the reflectivity measured by JOYRAD-94 (not shown).

## A.5 Gruvebadet

At Gruvebadet the long-term aerosol monitoring set of measurements active since 2010 including an SMPS + APS system (measuring the ambient aerosol size distribution) and filter-samplers deployed for the offline chemical characterization of PM10 as better described in Udusti et al. (2016); Giardi et al. (2016); Becagli et al. (2019); Turetta et al. (2021) was operational.

In addition, during NASCENT ambient PM1 was also collected on pre-baked quartz-fiber filters for the characterization of the Organic matter (OM) and Organic Nitrogen (ON) using advanced spectroscopic techniques (namely, proton-Nuclear Magnetic Resonance spectroscopy ((H-NMR, Decesari et al., 2000) and C and N elemental analysis (CN-EA, Rinaldi et al., 2007; Montero-Martínez et al., 2014). Due to the necessity of collecting sufficient amounts of samples for the subsequent detailed chemical analyses, long ( $\sim 3$ -4 days) time-integrated samplings were performed. Even if results are not available yet, multivariate statistical techniques (namely Positive Matrix Factorization, PMF, and other factor analysis methods) will be applied on OM HR-TOF-AMS and NMR with the aim of the apportionment of different OA primary and secondary sources and components (Paglione et al., 2014).

In this study, a Particle Soot Absorption Photometer (PSAP - Radiance Research) which measures light absorption coefficient at three wavelengths is used. Measurements are corrected according to Virkkula et al. (2005) and normalized at standard temperature and pressure. Equivalent BC (eBC) concentration is derived from light absorption coefficient at 660 nm.

## A.6 Climate Change Tower

The 33 m high Amundsen-Nobile Climate Change Tower (CCT) is located about 1 km south-westward of the town of Ny-Ålesund and is equipped with a consistent set of meteorological sensors installed at 10 m and 33 m and described in Mazzola et al. (2016). Additionally, a wind lidar gives information about the vertical wind profile.

## A.7 WRF Modeling

The model used is the Advanced Research WRF model (ARW), version 4.2.1 Skamarock et al. (2019). We used a nested setup with three domains, where the outermost has a resolution of

15 km, the middle domain has 5 km and the inner has 1 km resolution. The geographical extent of the domains is shown in Figure A.7.

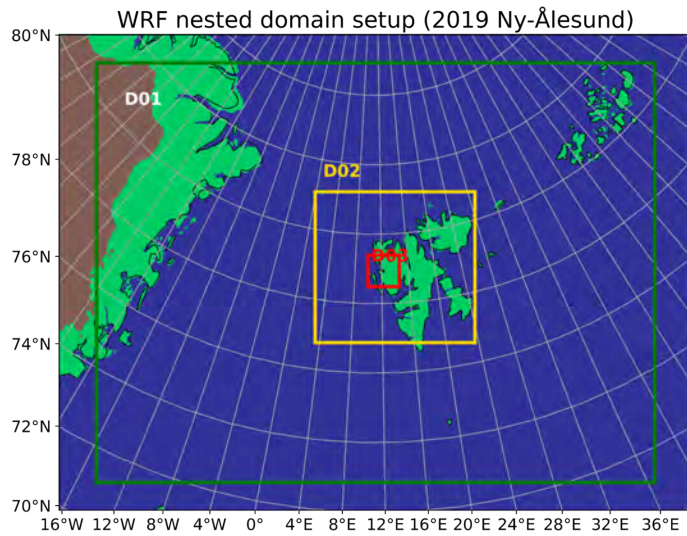


Figure A.7: Visualisation of the WRF domains with the outermost domain in green, in yellow the middle domain, and in red the inner domain.

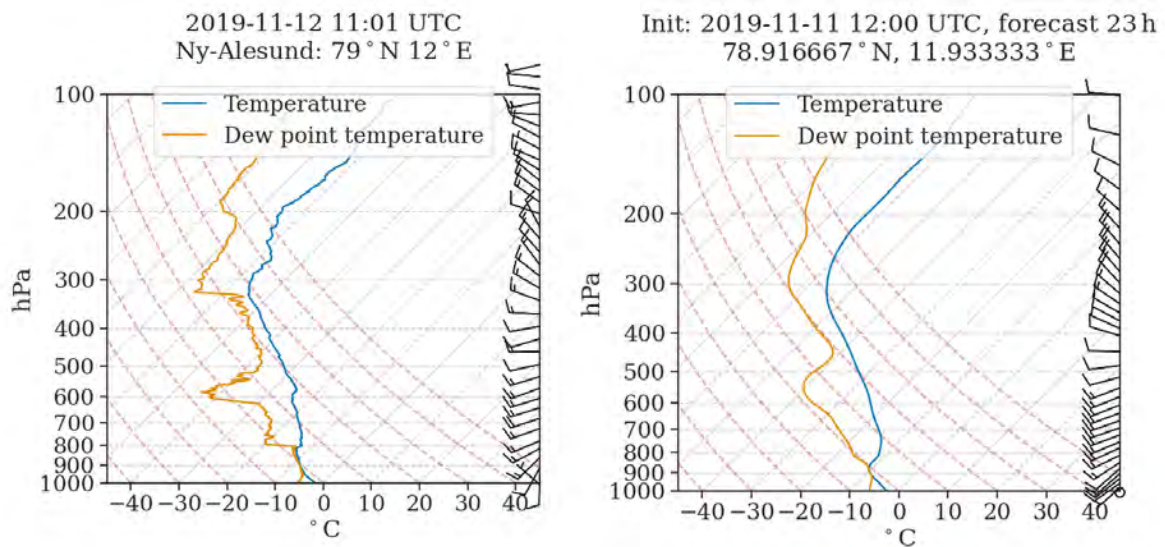


Figure A.8: Radiosounding at 1100 UTC 12 November 2019 performed at Ny-Ålesund (left) and simulated with the WRF model (right).

The number of vertical levels is 172 between the surface and 50 hPa whereof 93 are below 3 km altitude. We initialized and nudged the model with 6-hourly reanalysis input data from ERA5 on single and pressure levels (Hersbach et al., 2018a,b). The longwave and shortwave radiation were treated by the CAM scheme (Collins et al., 2004), and for boundary layer processes we used the Yonsei University (YSU) scheme (Hong et al., 2006). As a microphysics scheme we used the double moment scheme developed by Milbrandt and Yau having six different classes for cloud water and ice, rain, snow, graupel and hail (Milbrandt and Yau, 2005). Cumulus parametrization was only active on the largest domain, here we used the Grell-Freitas ensemble scheme (Grell and Freitas, 2014). We verified a satisfying model performance by comparing meteorological results

with radiosonde observations before using the model data for comparison of cloud properties (Fig. A.8). The CCN and INP concentrations were prescribed and are therefore independent of the simulated background aerosol.

To complement the description of the WRF simulation for flight 3 in Section 4.c of the main manuscript, we show here the simulated cloud properties averaged for each flights performed with HoloBalloon on 12 November 2019 (Fig. A.9). The model correctly simulated an increase in the cloud top height from flight 1 to 3 as can be seen from the increasing height where hydrometeors are observed (Fig. S9). This is in accordance with the cloud top increase measured by the cloud radar (Fig. S3,S9). It also followed observed changes in cloud base height in agreement with ceilometer retrievals, although the magnitude of the decrease before the third flight differs (Fig. A.9). In this regard, it is important to note that snowfall may have attenuated the visibility of the ceilometer below cloud base and thus led to a lower recorded liquid water cloud base than in reality.

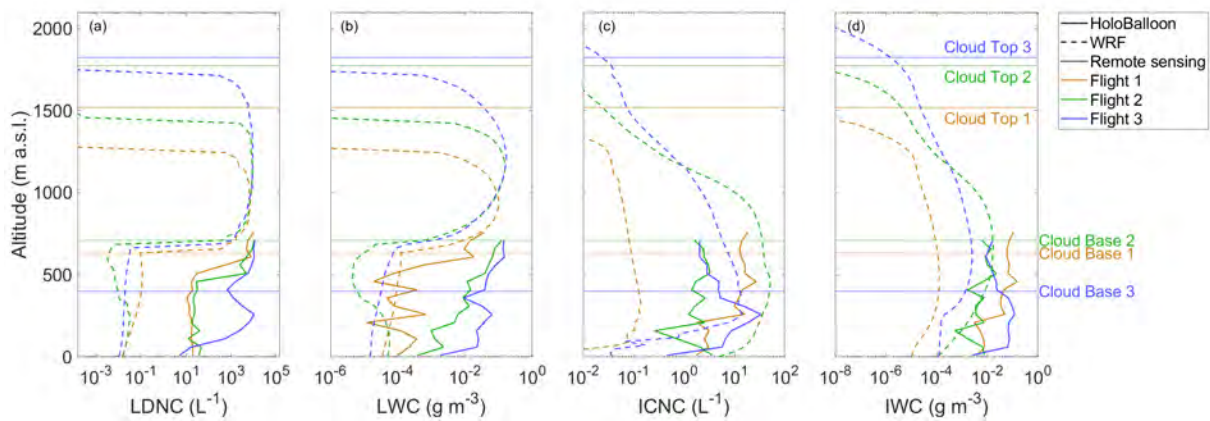


Figure A.9: The averaged vertical profiles during the three flights on 12 November 2019 (flight 1 from 1000 to 1100 UTC (yellow), flight 2 from 1215 to 1400 UTC (green), and flight 3 from 1545 to 1700 UTC (blue)) as observed by HOLIMO3B (solid lines) and simulated by WRF (dashed lines) of (a) CDNC, (b) LWC, (c) ICNC & (d) IWC. The data from HOLIMO3B are averaged over 50 m altitude bins and the WRF data over every model layer. The average cloud base and cloud top measured by the remote sensing instrumentation (ceilometer and cloud radar, respectively) are represented by the dotted horizontal lines. All frozen hydrometeor types (graupel, hail, snow and ice) from the WRF model are merged together into the ICNC and IWC calculation and the rain and cloud droplet number and mass for the CDNC and LWC calculation.

The liquid droplet number concentration (LDNC) and LWC measured by HOLIMO3B and simulated by the model are comparable between 600-750 m a.s.l (which corresponds approximately to cloud base for flights 1 and 2), whereas below this height the model underestimates the LDNC and LWC (Fig. A.9a,b). The simulated ICNC and IWC are underestimated during flight 1, whereas during flight 2 the simulated ICNC is overestimated and the simulated IWC is in the same order of magnitude as the in-situ measurements (Fig. A.9c,d).

Table A.1: Overview of all instruments and derived parameters installed in the framework of NASCENT or used in this study. Note that more instrumentation is operational at Ny-Ålesund.

<i>Location</i>	<i>Instrument</i>	<i>Derived Parameters</i>
<b>Zeppelin Observatory</b>	Ultrasonic Anemometer	Wind speed and direction
	Ground-based virtual impactor inlet (GCVI)	Operational parameters (flows, temperature, visibility, etc)
	Multiparameter Bioaerosol Sensor (MBS)	Optical parameters on particle size, shape and fluorescence (single-particle data)
	Chemical ionization mass spectrometer with filter inlet for gases and aerosols (FIGAERO-CIMS)	Mass spectra: ion signals in counts per second
	Differential Mobility Particle Sizer (DMPS 1&2)	Particle size distribution (5 to 900 nm) and particle concentration
	HOLIMO3G	Phase resolved distribution, ICNC, CDNC, IWC, LWC
	Hawkeye	Particle size distributions (3 - 50 $\mu\text{m}$ )
	MPS	Precipitating particle size distributions (12.5 - 775 $\mu\text{m}$ )
	CDP2	cloud droplet number concentration ( 2 $\mu\text{m}$ - 50 $\mu\text{m}$ )
	CRAFT	INP number concentration (immersion mode)
	Extended range Single Particle Soot Photometer (SP2-XR)	Black carbon mass concentrations and size distributions for normal ambient aerosol as well as for cloud droplet residuals (sampled from the CVI inlet)
	SP2-XR	Black carbon mass concentrations and size distributions for normal ambient aerosol as well as for cloud droplet residuals (sampled from the CVI inlet)
	MAAP	Equivalent black carbon mass concentrations
	COSMOS	Equivalent black carbon mass concentrations
CPC, DMPS, SMPS	Ambient aerosol size distribution	
Fog monitor	cloud droplet size distribution	

<b>Swiss Site</b>	<p>APS, SMPS, CPC, OPC</p> <p>Weather station Laserdisdrometer</p> <p>DRINCZ</p> <p>HINC</p> <p>WIBS-NEO</p> <p>CCN-100 Counter</p>	<p>Ambient aerosol size distribution</p> <p>Meteorological variables</p> <p>Precipitation rate, particle size and fall velocity distribution</p> <p>INP concentration in ambient air, snow, rime and snow pits</p> <p>Continuous ambient INP concentration measurement (<math>&lt; 2.5, \mu\text{m}</math>, <math>T = 243.15 \text{ K}</math>, <math>\text{RHw} = 104\%</math>)</p> <p>Size distribution and fluorescence of aerosol particles</p> <p>Count and size of CCN</p>
<b>HoloBalloon</b>	<p>HOLIMO3B</p> <p>Sonic Anemometer OPC</p> <p>Pyranometer &amp; Pyrgeometer</p>	<p>Phase resolved distribution, ICNC, CDNC, IWC, LWC</p> <p>Wind speed and direction</p> <p>Ambient aerosol size distribution</p> <p>SW &amp; LW up &amp; down</p>
<b>AWIPEV</b>	<p>94 GHz Doppler Cloud Radar JOYRAD-94 (RPG-FMCW-94-SP)</p> <p>Wind Lidar Windcube200</p> <p>Laserdisdrometer OTT Parsivel<sup>2</sup></p> <p>Vaisala CL-51 ceilometer</p> <p>Digiquarz-6000, PT100, Vaisala HMT337, Thiess combined wind sensor classic</p> <p>Radiosondes RS41</p> <p>CPS sonde</p>	<p>Radar reflectivity factor, radar Doppler spectra and its moments</p> <p>Wind direction and speed profile</p> <p>Precipitation rate, particle size and fall velocity distribution</p> <p>Attenuated backscatter, cloud base height</p> <p>Station level pressure, temperature (2 and 10 m), relative humidity (2 m), wind speed and direction (2 and 10 m)</p> <p>Profiles of T, p, RH, wind vector</p> <p>Profiles of cloud parameters (e.g., total particle count, particle phases, and particle size) and of T, p, RH, wind vector</p>
<b>Gruvebadet</b>	<p>PM10 filter sampling with subsequent offline analysis via DRINCZ</p> <p>Particle Soot Absorption Photometer (PSAP)</p> <p>PM1 filter samples with subsequent offline with H-NMR and HR-TOF-AMS</p> <p>PM1 and PM10 with subsequent offline analysis via DFPC</p>	<p>Ambient INP concentration - temperature spectrum</p> <p>equivalent Black Carbon concentration</p> <p>Organic Matter characterization</p> <p>INP concentraion (condensation freezing)</p>
<b>CCT</b>	Sonic Young Anemometer	Wind speed and direction





# List of symbols and abbreviations

$C_R$	radar constant, page 11
$K^2$	complex index of refraction, page 11
$P_r$	power received by the antenna, page 11
$Z$	radar reflectivity, page 11
AA	Arctic Amplification, page 1
AA	Arctic Amplification, page 16
CPC	Condensation particle counter, page 22
APS	Aerodynamic Particle Sizer, page 26
APS	Aerodynamic Particle Sizer, page 108
AWIPEV	Alfred Wegener Institut and Institut Paul Emile Victor, page 18
BC	Black Carbon, page 18
BSRN	Baseline Surface Radiation Network, page 13
C	Celsius, page 2
CCN	cloud condensation nucleus, page 3
CCNC	cloud condensation nucleus concentration, page 3
CDNC	cloud droplet number concentration, page 7
COSMOS	continuous soot monitoring system, page 22
COSMOS	continuous soot monitoring system, page 107
CPNC	cloud particle number concentration, page 23
CTT	Climate Change Tower, page 18
CVI	Counterflow Virtual Impactor, page 23
DDNC	drizzle drops number concentration, page 45
DDNC	drizzle drops number concentration, page 110
DMA	dimethylamine, page 27
DMA	dimethylamine, page 108
DMPS	Differential Mobility Particle Size Spectrometer, page 24
DMPS	Differential Mobility Particle Size Spectrometer, page 107
DRINCZ	DRoplet Ice Nuclei Counter Zurich, page 12
$ERF_{aci}$	Effective Radiative Forcing due to aerosol-cloud interactions, page 7
$ERF_{ari}$	Effective Radiative Forcing due to aerosol-radiation interactions, page 7
FIDAS	Fine Dust Measurement Device, page 26
FIDAS	Fine Dust Measurement Device, page 108
FIGAERO-CIMS	iodide Chemical Ionization high-resolution time-of-flight Mass Spectrometer coupled to a Filter Inlet for Gases and AEROsols coupled to a Chemical Ionization Mass Spectrometer, page 27
fps	frames per seconds, page 85
Gly	glycerol, page 27
Gly	glycerol, page 108
HINC	Horizontal Ice Nucleating Chamber, page 12
HM	Hallett-Mossop, page 4
HMSA	hydroxymethane-sulfonic acid, page 27
HMSA	hydroxymethane-sulfonic acid, page 108

HOLIMO3B	HOLographic Imager for Microscopic Objects, page 9
hr	hour, page 74
ICNC	ice crystal number concentration, page 4
ICNC <sub>pr&lt;106 μm</sub>	number concentration of pristine ice crystals smaller than 106 μ, page 42
INP	ice nucleating particle, page 2
INPC	ice nucleating particle concentration, page 4
INPC <sub>CT</sub>	ice nucleating particle concentration at cloud top temperature, page 43
INPC <sub>HB</sub>	ice nucleating particle concentration at the temperature of the measurement location of HoloBalloon, page 43
IWC	ice water content, page 32
K	kelvin, page 74
L	levoglucosan, page 27
L	levoglucosan, page 108
LDNC	liquid droplet number concentration, page 32
LIDAR	LIght Detection And Ranging, page 11
LWC	liquid water content, page 23
MAAP	multi-angle absorption photometer, page 22
MAAP	multi-angle absorption photometer, page 107
MPC	mixed-phase clouds, page 3
MSA	methane-sulfonic acid, page 27
MSA	methane-sulfonic acid, page 108
NASCENT	Ny-Ålesund AeroSol Cloud ExperimentNT, page 16
NASCENT	Ny-Ålesund Aerosol Cloud Experiment, page 13
NorESM2	Norwegian Earth System Model, page 84
OEF	occurrence enhancement factor, page 53
PAMTRA	Passive and Active Microwave radiative TRAnsfer tool, page 31
PM1	Particulate Matter smaller 1 μm, page 25
PM1	Particulate Matter smaller 1 μm, page 108
PM10	Particulate Matter smaller 10 μm, page 25
PM10	Particulate Matter smaller 10 μm, page 108
PSAP	Particle Soot Absorption Photometer, page 22
PSAP	Particle Soot Absorption Photometer, page 107
RADAR	RAdar Detection And Ranging, page 11
s	seconds, page 52
S <sub>i</sub>	saturation ratio with respect to ice, page 6
SI	Supplementary Information, page 18
SIP	Secondary Ice Production, page 4
SIP <sub>all</sub>	all measurements with secondary ice production, page 42
SIP <sub>high</sub>	high secondary ice production regions, page 42
SIP <sub>low</sub>	low secondary ice production regions, page 42
SIP <sub>mod</sub>	moderate secondary ice production regions, page 42
SIP <sub>no</sub>	measurements without secondary ice production, page 42
SMPS	Scanning Mobility Particle Sizer, page 28
T	temperature, page 6
TMA	trimethylamine, page 27
TMA	trimethylamine, page 108
WBF	Wegener-Bergeron-Findeisen process, page 6
WRF	Weather Research and Forecasting, page 13

# List of Figures

2.1	Overview of the NASCENT study set-up at Ny-Ålesund, Svalbard. Aerial photo with the five measurement locations and the respective instrumentation. The campaign logo is shown in the lower right corner. . . . .	19
2.2	Temperature and cloud seasonality observed during NASCENT. (a) Average temperatures during NASCENT compared to the climatology of 1994 to 2018 (shading represents the standard deviation) measured at the AWIPEV weather mast 10 m above ground (Maturilli et al., 2013). (b) Monthly frequency of occurrence of cloud types derived from the Cloudnet data during NASCENT. Colors represent the different cloud types, while dashed lines show all clouds in the column and solid lines the low-level clouds with cloud tops below three kilometers. Note that multiple cloud layers of different kinds are accounted for separately, so that the sum of 'liquid', 'ice', and 'mixed-phase' does not equal the frequency of 'any' clouds.	20
2.3	Wind measurements during NASCENT throughout the Ny-Ålesund area at the different locations and retrieved from radiosondes. Data is shown for the AWIPEV weather mast (10 m), the Zeppelin Observatory, the CCT (10 m), and from daily radiosondes between 3000-3500 m a.s.l.. The bar length gives the respective frequency of occurrence with the maximum frequency value specified at the end of the longest bar. Topographic map of the Ny-Ålesund region from (Norwegian Polar Institute, 2014). . . . .	21
2.4	Monthly average distributions of (a) aerosol particle number and (b) black carbon (BC) mass concentrations measured during NASCENT at Gruvebadet and at the Zeppelin Observatory in comparison to previous climatologies. The box-whisker plots show the quartiles and the 5th and 95th percentiles, respectively, while outliers are marked with diamonds. The particle number concentrations were measured using CPC's, while BC concentrations were measured by four different instruments: extended-range single-particle soot photometer (SP2-XR, Stephens et al., 2003; Schwarz et al., 2006), a multi-angle absorption photometer (MAAP, Petzold and Schönlinner, 2004), a continuous soot monitoring system (COSMOS, Kondo et al., 2011), and a Particle Soot Absorption Photometer (PSAP). . . . .	22
2.5	Cloud in-situ measurements on 12 November 2019 at Zeppelin Observatory. (a) Cloud particle number concentration and liquid water content measured by the fog monitor. The period selected for the lower panels (c) and (d) is indicated. (b) Cloud residual number concentration and ambient aerosol number concentration, together with the fluorescent particle concentration ( $\times 10^3$ ) within the cloud residuals/ambient aerosol number concentrations, and ambient visibility measured at the CVI inlet (note the reversed y-axis). The shading at the top of the figure indicates when the CVI was in operation/ON. (c) Particle number size distribution of the cloud residuals and whole-air aerosols (interstitial and activated aerosol) measured by a tandem-DMPS system. (d) Cloud residual number concentration measured by the CVI inlet, ambient ICNC ( $\times 10$ ) measured by HOLIMO3G, and CPNC measured by the fog monitor. . . . .	24

- 2.6 Overview of INPCs observed on 12 November 2019. Blue violin plots: six INP samples measured with DRINCZ between  $-10\text{ }^{\circ}\text{C}$  and  $-21\text{ }^{\circ}\text{C}$  and with HINC at  $-30\text{ }^{\circ}\text{C}$  at the Swiss Site. The red lines indicate the median and the dashed black lines the 25th and 75th percentiles. The blue dashed line shows the corresponding exponential fit ( $INPC(T) = \exp(-0.4146 \cdot T - 12.4059)$ ) (cf. Li et al., 2022)). Purple and Magenta: one filter sample collected between 0900 - 1200 UTC at Gruvebadet analyzed by the DFPC on PM1 and PM10. Orange line: one filter sample collected from 10 - 16 November 2019 at the Zeppelin Observatory analyzed by CRAFT. The error bars represent the 95% confidence interval. . . . . 25
- 2.7 (a) Particle number concentration for sizes  $\geq 0.5\text{ }\mu\text{m}$  measured by the APS (aerodynamic diameter) at the Swiss Site and by the FIDAS (optical diameter) at the Zeppelin Observatory, with a time resolution of 3 minutes for both instruments. (b) INPC and activated fraction ( $INPC/N_{0.5}$ ) at  $-12\text{ }^{\circ}\text{C}$  (left axis), and fluorescent (particle) concentration and fluorescent (particle) fraction (right axis). We select a temperature of  $-12\text{ }^{\circ}\text{C}$  to adequately evaluate the contribution from biological aerosol particles (Kanji et al., 2017, and references therein). The INPCs are measured by DRINCZ and the fluorescent particle concentration by an Wideband Integrated Bioaerosol Sensor (WIBS). The fractions are normalized to the particle fraction  $\geq 0.5\text{ }\mu\text{m}$ . . . . . 26
- 2.8 High-resolution chemical composition of (a) aerosol particles before a cloud event (whole-air inlet) and (b) of cloud residuals during the cloud measured by the FIGAERO-CIMS on 24 December 2019. Shown is the background-corrected absolute signal of individual molecules, separated by the number of carbon and oxygen atoms. (c)  $^1\text{H-NMR}$  spectra of ambient PM1 samples collected at Gruvebadet for 12 November and 24 December 2019. Specific resonances are assigned to levoglucosan (L), hydroxymethane-sulfonic acid (HMSA), methane-sulfonic acid (MSA), dimethylamine (DMA), trimethylamine (TMA) and glycerol (Gly). Unresolved mixtures of aromatic compounds and linear aliphatic chains, including possible contributions from lipids, are indicated in the spectra. The insert provides a focus on the aliphatic region of the spectra characteristic of polyols/saccharides compounds (H-C-O). Grey areas between 4.7 - 5.0 ppm and between 8 - 8.5 ppm cover the disturbance due to solvent and buffer solutions needed for the analysis. 27
- 2.9 Overview of the cloud properties observed in-situ on HoloBalloon and by the cloud radar on 12 November 2019. (a) Cloud radar reflectivity, HoloBalloon path and Zeppelin altitude. (b) Doppler spectra and mean Doppler velocity at the height of the HoloBalloon path. Positive values represent a downward velocity. (c) Cloud droplet and (d) ice crystal size distributions (color) and total CDNC and ICNC (black line) measured by HOLIMO3B. (e) Cloud droplets, drizzle drops, and ICNC for crystals smaller and larger than  $106\text{ }\mu\text{m}$ . This cut-off size is defined by the bin size closest to  $100\text{ }\mu\text{m}$ . (f) Frequency of occurrence of the ice crystal habits and total ICNC. The data are averaged over 60 sec. Note that at around 1550 UTC, HoloBalloon flew out of the cloud, which explains the decrease in CDNC and ICNC measured by HOLIMO3B (c-f) and the missing reflectivity data at the HoloBalloon height (b). . . . . 29

- 
- 2.10 Examples of ice crystals classified as typical habits observed with HOLIMO3B. Plates and (hollow) columns with a diameter smaller than 106  $\mu\text{m}$  were classified as pristine, whereas larger columns were classified separately. Droplet 'lollipop', and drops showing evidence of freezing are classified as frozen drops. All the other ice crystals, including rimed and aggregated particles are classified as 'Aged'. The scale bar in the right panel is representative for all of the panels. The respective fractions of the typical ice crystals habits to the total ICNC are displayed in Figure 2.9f. . . . . 30
- 2.11 (a-c) Measured size distributions from HOLIMO3B. (d-f) Radar Doppler spectra simulated with the PAMTRA tool using the size distribution shown in a-c. The measured size distribution and simulated Doppler spectra are shown at three characteristic time periods of 5 minutes: 1525-1530 UTC (a & d), 1600-1605 UTC (b & e), and 1625-1630 UTC (c & f). . . . . 32
- 2.12 The averaged vertical profiles during flight 3 on 12 November 2019 observed by HOLIMO3B and simulated by WRF. (a) LDNC, (b) LWC, (c) ICNC & (d) IWC. The contribution of graupel to the ICNC and IWC are shown with the colored dashed profile line in (c) and (d). The data from HOLIMO3B are averaged over 50 m altitude bins and the WRF data over every model layer. The average cloud base and cloud top measured by the remote sensing instrumentation (ceilometer and cloud radar, respectively) are represented by the black dotted horizontal lines and the HM temperature range ( $-8^{\circ}$  to  $-3^{\circ}\text{C}$ ) is highlighted in (c) and (d). . . . . 34
- 3.1 (a) Map of Svalbard with the location of Ny-Ålesund marked with the red star. (b) Map of the peninsula close to Ny-Ålesund. Ny-Ålesund, the Kronebreen and Kongsvegen glaciers, the fjord Kongsfjorden, and the Mt. Zeppelin mountain are labelled. (Topographical data from Norwegian Polar Institute, 2014). . . . . 40
- 3.2 Examples of ice crystals observed with HOLIMO classified as pristine with diameters  $< 106 \mu\text{m}$ , non-pristine ice crystals with diameters  $< 106 \mu\text{m}$ , and pristine ice crystals with diameters  $> 106 \mu\text{m}$ . The presence of pristine ice crystals with diameter  $< 106 \mu\text{m}$  was used for identification of SIP. The scale bar applies to all panels. . . . . 42

- 3.3 (a) Ambient temperature and pressure measured from the weather mast two meters above ground at the AWIPEV Observatory. (b) Horizontal wind speed measured with the wind lidar averaged over 1h30 (wind barbs) and HoloBalloon measurement height (black line). (c) Cloud radar reflectivity (color), HoloBalloon measurement height (black line), and cloud top temperatures from radiosonde launches measured during the six-day measurement period. On 8 November 2019 and 1 April 2020 the temperature is shown at an altitude of 1800 m a.s.l. because the cloud top is higher than 3000 m a.s.l.. (d) Total CDNC (black) and drizzle drops number concentration (DDNC) (orange) averaged over 5 min. The uncertainty in the concentration of cloud and drizzle is estimated to be  $\pm 6\%$ . (e) Total ICNC (black line) and  $\text{ICNC}_{\text{pr}<106\ \mu\text{m}}$  (red line) averaged over 5 min,  $\text{INPC}_{\text{CT}}$  (light blue crosses) and  $\text{INPC}_{\text{HB}}$  (dark blue crosses). For 10 November 2019, the ICNCs averaged over each flight are shown with black circles because the ICNC are too low to display a time series. On 12 November 2019, the  $\text{INPC}_{\text{HB}}$  were below the limit of detection of the INP instrumentation, therefore the limit of detection ( $1.4 \cdot 10^{-4} \text{ L}^{-1}$ ) is displayed instead ( $\text{INPC}_{\text{lim}}$ , dark blue dashed line). The uncertainty for the concentration of ice particles smaller than 100  $\mu\text{m}$  is estimated to  $\pm 5\%$  and to  $\pm 15\%$  for ice crystals larger than 100  $\mu\text{m}$ . The uncertainty for the INPC amounts to a factor of two. On 8 November 2019 and 1 April 2020, no  $\text{INPC}_{\text{CT}}$  can be provided as the cloud top temperatures were below the observable nucleation temperatures of our INP instrumentation. All data are shown from 11:00 UTC on 8 November to 18:00 UTC on 12 November 2019 and on 1 April 2020 from 05:00 to 16:00 UTC. Note that the ticks are at 12:00 UTC for each day. . . . . 45
- 3.4 Temperature (red) and relative humidity (RH) with respect to water (bright grey) and ice (dark grey) measured by the radiosonde launched at 11:00 UTC on 8 to 12 November 2019 and at 17:00 UTC on 1 April 2020. The 100% RH line is shown with the broken black line. . . . . 45
- 3.5 Representative examples of ice crystals observed with HOLIMO during the flights on (a) 8 and 9 November 2019 and (b) 10 November 2019. The scale bar applies to both panels. . . . . 46
- 3.6 Overview of the cloud properties on 11 November 2019. (a) Cloud radar reflectivity (color), HoloBalloon measurement height (black line), cloud base height measured by the ceilometer (black dots), and temperatures at the corresponding altitudes measured by the radiosonde at 11:00 UTC, 14:00 UTC, and 20:00 UTC. Note that the lowering of the cloud base to the surface detected by the ceilometer after 17:30 UTC is caused by precipitation. (b) Cloud droplet size distributions (color shading) and total CDNC (black line). The uncertainty in the concentration of cloud and drizzle is estimated to be  $\pm 6\%$ . (c) Ice crystal size distributions (color shading) and total ICNC (black line) measured by HOLIMO averaged over 1 min. The uncertainty for the concentration of ice particles smaller than 106  $\mu\text{m}$  is estimated to  $\pm 5\%$  and for the concentration of larger ice crystals to  $\pm 15\%$ . . . . 47
- 3.7 (a) Representative examples of ice crystals classified in typical habits observed with HOLIMO between 18:00 UTC and 19:00 UTC on 11 November 2019. The scale bar applies to all panels. (b) Concentrations of ice crystals classified into habits and  $\text{ICNC}_{\text{pr}<106\ \mu\text{m}}$  (black line). (c) Fraction of  $\text{ICNC}_{\text{pr}<106\ \mu\text{m}}$ , pristine ice crystals with diameter  $> 106\ \mu\text{m}$  ( $\text{ICNC}_{\text{pr}>106\ \mu\text{m}}$ ), aged ice crystals, recirculation particles, and frozen drops concentrations to ICNC. The shaded area shows when HoloBalloon flew out of the cloud. The measurements are averaged over 1 min. The uncertainty for the concentration of ice particles smaller than 106  $\mu\text{m}$  is estimated to  $\pm 5\%$  and for the concentration of ice larger crystals to  $\pm 15\%$ . . . . 49



3.8	Overview of the cloud properties on 1 April 2020. (a) Cloud radar reflectivity (color), HoloBalloon measurement height (black line), cloud base height measured by the ceilometer (black dots), and temperatures at the corresponding altitudes measured by the radiosounding at 17:00 UTC. (b) Cloud droplet size distributions (color shading) and total CDNC (black line). The uncertainty in the concentration of cloud and drizzle is estimated to be $\pm 6\%$ . (c) Ice crystal size distributions (color shading) and total ICNC (black line) measured by HOLIMO averaged over 1 min. The uncertainty for the concentration of ice particles smaller than $106 \mu\text{m}$ is estimated to $\pm 5\%$ and for the concentration of larger ice crystals to $\pm 15\%$ . . . . .	50
3.9	(a) Representative examples of ice crystals classified in typical habits observed with HOLIMO on 1 April 2020. Ice crystals with indication of broken features are highlighted with blue frames. The scale bar is representative for both panels. (b) The concentration of the ice crystals by habit and $\text{ICNC}_{\text{pr}<106\mu\text{m}}$ (black line) between 12:20 UTC and 14:40 UTC (bottom) on 1 April 2020 are shown. The uncertainty for the concentration of ice particles smaller than $100 \mu\text{m}$ is estimated to $\pm 5\%$ and for the concentration of larger ice crystals to $\pm 15\%$ . . . . .	51
3.10	Frequency of occurrence of $\text{SIP}_{\text{no}}$ ( $\text{ICNC}_{\text{pr}<106 \mu\text{m}} < 0.3 \text{ L}^{-1}$ ), $\text{SIP}_{\text{low}}$ ( $0.3 \text{ L}^{-1} < \text{ICNC}_{\text{pr}<106 \mu\text{m}} < 1 \text{ L}^{-1}$ ), $\text{SIP}_{\text{mod}}$ ( $1 \text{ L}^{-1} < \text{ICNC}_{\text{pr}<106 \mu\text{m}} < 10 \text{ L}^{-1}$ ), and $\text{SIP}_{\text{high}}$ ( $10 \text{ L}^{-1} < \text{ICNC}_{\text{pr}<106 \mu\text{m}}$ ). The numbers refer to the number of 30 s intervals observed within each SIP class. . . . .	52
3.11	(a) $\text{ICNC}_{\text{pr}<106 \mu\text{m}}$ , (b) CDNC and drizzle drop number concentrations (DDNC), (c) frozen drop number concentrations, and (d) snow crystals number concentrations retrieved with HOLIMO averaged over 30 s. The uncertainty for the concentration of cloud droplets is estimated to $\pm 6\%$ , for the concentration of ice particles smaller than $100 \mu\text{m}$ to $\pm 5\%$ and for the concentration of snow crystals and frozen drops to $\pm 15\%$ . (e) Temperature derived from the radiosondes at the HoloBalloon location. The breaks on the time axis separate measurement flights. The black dashed lines in panel (a) and (c) denote the $\text{SIP}_{\text{mod}}$ ( $1 \text{ L}^{-1}$ ) and $\text{SIP}_{\text{high}}$ ( $10 \text{ L}^{-1}$ ) limits. The white regions show the occurrence of SIP, whereas the grey shaded regions show no SIP. . . . .	54
3.12	(a) Number of measurements for each $\text{ICNC}_{\text{pr}<106\mu\text{m}}$ bin (note the log scale) for each day of measurements (color lines) and all measurements (black line). The $\text{ICNC}_{\text{pr}<106\mu\text{m}}$ regions defined as $\text{SIP}_{\text{low}}$ , $\text{SIP}_{\text{mod}}$ , $\text{SIP}_{\text{high}}$ are shown on top and $\text{SIP}_{\text{no}}$ is represented with a black box. (b) $\text{ICNC}_{\text{pr}<106\mu\text{m}}$ fraction from total ICNC for each temperature bin of $1 \text{ }^\circ\text{C}$ (color shading) and $\text{ICNC}_{\text{pr}<106\mu\text{m}}$ bin. The frequency of $\text{ICNC}_{\text{pr}<106\mu\text{m}} < 0.3 \text{ L}^{-1}$ to ICNC ( $\text{SIP}_{\text{no}}$ class conditions) is highlighted by the thick black frame. A concentration of $0.3 \text{ L}^{-1}$ was used for the calculation of $\text{ICNC}_{\text{pr}<106\mu\text{m}}$ to total ICNC when no ice crystal was measured in the 30 s interval. (c) Number of measurements ( $N_{\text{meas}}$ ) per temperature bin ( $1 \text{ }^\circ\text{C}$ ) for measurements with SIP (red bars), and for measurements with $\text{SIP}_{\text{no}}$ (black bars). (d) Number of measurements ( $N_{\text{meas}}$ ) per temperature bin for each day of measurements (colored lines). The data were averaged over 30 s for the analysis. . . . .	56
3.13	Potential temperature and wind speed and direction measured by the radiosonde launched at 11:00 UTC or 17:00 UTC on the six days of measurements. The mean cloud base (CB) measured with the ceilometer is labeled. . . . .	59
3.14	Schematic of the derivation of the maximum Doppler velocity $v_{\text{max}}$ (red star) from the Doppler spectra. $Z_{\text{min}}$ and $Z_{\text{max}}$ (green dots) are the minimum and maximum radar reflectivity (see the text for more details). . . . .	60
4.1	Examples of ice crystals observed with HOLIMO and classified manually as columns, plates, dendrites, and aged particles. The scale bar at the bottom right applies for all panels. . . . .	64

4.2	Doppler velocity (colour), HoloBalloon path (black line) and cloud base height measured by the ceilometer (black dots) on 11 November 2019. The cloud top temperature as well as the altitudes where $-3^{\circ}\text{C}$ and $-10^{\circ}\text{C}$ were measured by the radiosondes launched at 20:00 UTC are indicated. . . . .	65
4.3	Schematic of the growth of recirculation particles within clouds. See text for detailed description. Examples of recirculation particles observed with HOLIMO. An example of two aggregated recirculation particles is highlighted with the green frame, and of a recirculation particle with a missing column is highlighted with the orange frame. . . . .	65
4.4	Doppler velocity (colour) and HoloBalloon path (black line) on 1 April 2020. The temperature is indicated every 500 m in altitude as measured by the radiosondes launched at 17:00 UTC. Note that the cloud base measured by the ceilometer is not shown because its detection was obstructed by snowfall and blowing snow. . .	66
4.5	Growth of columns and plates after a droplet collided, rimed, and grew in the columnar or plate regime. These ice crystals are referred to as aged-rimed and examples of such ice crystals measured with HOLIMO are shown in the black frames on the right. An aged-rimed plate showing signs of breaking is highlighted with an orange frame. . . . .	67
5.1	Picture of HOLIMO3B located on the ground during the comparison with the BSRN measurements. . . . .	72
5.2	Comparison of radiation sensors (upward-looking configuration) with downward radiation measured by the BSRN station. . . . .	73
5.3	Longwave radiative fluxes (red arrows) along HoloBalloon path (black line) and at the BSRN station at the surface (at the bottom). The shading shows the reflectivity measured by the cloud radar and the black dots the cloud base measured by the ceilometer. . . . .	74
5.4	(a) Cloud thickness and the $F_{LW_{BSRN}}^{net}$ on 10 November 2019. (b) Cloud thickness vs. $F_{LW_{BSRN}}^{net}$ . The Pearson's correlation and the linear fit over the data is shown.	75
5.5	(a) HoloBalloon path (black line) and reflectivity measured by the cloud radar. (b) Total $F_{SW_{BSRN}}^{\downarrow}$ , $F_{SW_{BSRN,diff}}^{\downarrow}$ , and $F_{SW_{BSRN,dir}}^{\downarrow}$ measured at the BSRN field, and $F_{SW_{HoloBalloon}}^{\uparrow}$ and $F_{SW_{HoloBalloon}}^{\downarrow}$ . The downward shortwave consists of the direct and diffuse shortwave radiation. The normal component of the direct shortwave radiation was corrected with the solar zenith angle to obtain its effective component to the total downward shortwave radiation. . . . .	76
5.6	(a) HoloBalloon path (black line) and reflectivity measured by the cloud radar. (b) CDNC, ICNC and $\text{ICNC}_{<106\ \mu\text{m}}$ measured by HOLIMO3B. (c) Ice and water extinction coefficient ( $\text{m}^{-1}$ ). (d) SW ratio calculated from the $F_{SW_{HoloBalloon}}^{\uparrow}$ and $F_{SW_{HoloBalloon}}^{\downarrow}$ measured on HoloBalloon. (e) $F_{SW_{HoloBalloon}}^{\uparrow}$ and $F_{SW_{HoloBalloon}}^{\downarrow}$ . The grey shading highlight regions where the $\text{albedo}_{\text{HoloBalloon}}$ is higher than 0.9 and profile 3 is labelled. The data were averaged for 60 sec. . . . .	77
5.7	Measured cloud and radiative properties during profile 3. The data were averaged over 50 m. . . . .	78
A.1	Map of Svalbard with location of Ny-Ålesund marked with the red star (topographical data from Norwegian Polar Institute, 2014). . . . .	90
A.2	Weathermap showing the relative humidity (green shading), temperature (colored lines) at 1000 hPa and the estimated location of the warm front at 0600 UTC on 12 November. The red triangle shows the location of Ny-Ålesund. The model data are from the MEPS Weathermaps Hellmuth and Hofer (2019). . . . .	90

A.3	Cloud radar and wind lidar measurements on 12 November 2019. (a) Cloud radar reflectivity and (b) wind lidar horizontal wind speed. The wind barbs show the wind direction and the color the horizontal wind speed. The solid black line shows the height of HoloBalloon and the dashed line the height of the Zeppelin Observatory. The black dots in (a) show the cloud base heights measured by the ceilometer. The temperature measured by the radiosonde launch at 1700 UTC is shown on the right y-axis at the corresponding altitude on the left y-axis. . . . .	91
A.4	HoloBalloon Platform with description of the different parts. The platform is aligning in direction of the wind thanks to the wind tail and is hanging 12 m bellow the helikite. . . . .	93
A.5	Aerosol and cloud sampling at the Zeppelin Observatory during NASCENT. Various air inlet systems were used to sample particles, gas phase, cloud particles and whole air (aerosol and cloud particles) that were analysed in the laboratories below. In addition, various cloud probes and aerosol instrumentation were placed outside on the observation terrace. For further details on the CVI/whole-air inlet sampling see Karlsson et al. (2021). . . . .	95
A.6	Example of ice crystals classified to 'droplet lollipops' observed with the 2D-S probe at the Zeppelin Observatory. . . . .	96
A.7	Visualisation of the WRF domains with the outermost domain in green, in yellow the middle domain, and in red the inner domain. . . . .	100
A.8	Radiosounding at 1100 UTC 12 November 2019 performed at Ny-Ålesund (left) and simulated with the WRF model (right). . . . .	100
A.9	The averaged vertical profiles during the three flights on 12 November 2019 (flight 1 from 1000 to 1100 UTC (yellow), flight 2 from 1215 to 1400 UTC (green), and flight 3 from 1545 to 1700 UTC (blue)) as observed by HOLIMO3B (solid lines) and simulated by WRF (dashed lines) of (a) CDNC, (b) LWC, (c) ICNC & (d) IWC. The data from HOLIMO3B are averaged over 50 m altitude bins and the WRF data over every model layer. The average cloud base and cloud top measured by the remote sensing instrumentation (ceilometer and cloud radar, respectively) are represented by the dotted horizontal lines. All frozen hydrometeor types (graupel, hail, snow and ice) from the WRF model are merged together into the ICNC and IWC calculation and the rain and cloud droplet number and mass for the CDNC and LWC calculation. . . . .	101



# List of Tables

1.1	Typical values of radar reflectivity for various hydrometeors and precipitation types.	12
2.1	Retrieved variables at the five measurement locations. The black crosses show long-term measurements and the measurements performed only during NASCENT are represented with the symbol 'N'. Parameters that were in addition measured behind the ground-based Counterflow Virtual Impactor (CVI) inlet are marked by an asterisk (*).	36
3.1	Frequency of occurrence and OEF of the hydrometeor types cloud droplets (with concentrations larger than $5 \text{ cm}^{-3}$ ), drizzle drops, frozen drops, and snow crystals during all measurements ( $N_{\text{all}}$ ), $SIP_{\text{all}}$ , $SIP_{\text{low}}$ , $SIP_{\text{mod}}$ , and $SIP_{\text{high}}$ . Bold font signifies OEF values larger than 1, i.e. enhancements.	55
A.1	Overview of all instruments and derived parameters installed in the framework of NASCENT or used in this study. Note that more instrumentation is operational at Ny-Ålesund.	102





# Bibliography

- Albrecht, B. A., Penc, R. S., and Schubert, W. H.: An Observational Study of Cloud-Topped Mixed Layers, *Journal of Atmospheric Sciences*, 42, 800 – 822, [https://doi.org/10.1175/1520-0469\(1985\)042<0800:AOSOCT>2.0.CO;2](https://doi.org/10.1175/1520-0469(1985)042<0800:AOSOCT>2.0.CO;2), 1985.
- Ansmann, A., Tesche, M., Althausen, D., Muller, D., Seifert, P., Freudenthaler, V., Heese, B., Wiegner, M., Pisani, G., Knippertz, P., and Dubovik, O.: Influence of Saharan dust on cloud glaciation in southern Morocco during the Saharan Mineral Dust Experiment, *Journal of Geophysical Research: Atmospheres*, 113, <https://doi.org/https://doi.org/10.1029/2007JD008785>, 2008.
- Bacon, N. J., Swanson, B. D., Baker, M. B., and Davis, E. J.: Breakup of levitated frost particles, *Journal of Geophysical Research: Atmospheres*, 103, 13 763–13 775, <https://doi.org/https://doi.org/10.1029/98JD01162>, 1998.
- Bailey, M. P. and Hallett, J.: A Comprehensive Habit Diagram for Atmospheric Ice Crystals: Confirmation from the Laboratory, AIRS II, and Other Field Studies, *Journal of the Atmospheric Sciences*, 66, 2888 – 2899, <https://doi.org/10.1175/2009JAS2883.1>, 2009.
- Beaubien, D. J., Bisberg, A., and Beaubien, A. F.: Investigations in Pyranometer Design, *Journal of Atmospheric and Oceanic Technology*, 15, 677 – 686, [https://doi.org/10.1175/1520-0426\(1998\)015<0677:IIPD>2.0.CO;2](https://doi.org/10.1175/1520-0426(1998)015<0677:IIPD>2.0.CO;2), 1998.
- Becagli, S., Amore, A., Caiazzo, L., Iorio, T. D., Sarra, A. d., Lazzara, L., Marchese, C., Meloni, D., Mori, G., Muscari, G., Nuccio, C., Pace, G., Severi, M., and Traversi, R.: Biogenic Aerosol in the Arctic from Eight Years of MSA Data from Ny alesund (Svalbard Islands) and Thule (Greenland), *Atmosphere*, 10, <https://doi.org/10.3390/atmos10070349>, 2019.
- Beck, A.: Observing the Microstructure of Orographic Clouds with HoloGondel, Ph.D. thesis, ETH Zurich, <https://doi.org/10.3929/ethz-b-000250847>, 2017.
- Beck, A., Henneberger, J., Schopfer, S., Fugal, J., and Lohmann, U.: HoloGondel: in situ cloud observations on a cable car in the Swiss Alps using a holographic imager, *Atmospheric Measurement Techniques*, 10, 459–476, <https://doi.org/10.5194/amt-10-459-2017>, 2017.
- Beck, A., Henneberger, J., Fugal, J. P., David, R. O., Lacher, L., and Lohmann, U.: Impact of surface and near-surface processes on ice crystal concentrations measured at mountain-top research stations, *Atmospheric Chemistry and Physics*, 18, 8909–8927, <https://doi.org/10.5194/acp-18-8909-2018>, 2018.
- Beck, L. J., Sarnela, N., Junninen, H., Hoppe, C. J., Garmash, O., Bianchi, F., Riva, M., Rose, C., Perakyla, O., Wimmer, D., et al.: Differing mechanisms of new particle formation at two Arctic sites., *Geophysical Research Letters*, p. e2020GL091334, 2020.
- Beine, H. J., Argentini, S., Maurizi, A., Mastrantonio, G., and Viola, A.: The local wind field at Ny-alesund and the Zeppelin mountain at Svalbard, *Meteorology and Atmospheric Physics*, 78, 107–113, <https://doi.org/10.1007/s007030170009>, 2001.
- Bekryaev, R. V., Polyakov, I. V., and Alexeev, V. A.: Role of Polar Amplification in Long-Term Surface Air Temperature Variations and Modern Arctic Warming, *Journal of Climate*, 23, 3888 – 3906, <https://doi.org/10.1175/2010JCLI3297.1>, 2010.
- Bennartz, R., Shupe, M. D., Turner, D. D., Walden, V. P., Steffen, K., Cox, C. J., Kulie, M. S., Miller, N. B., and Pettersen, C.: July 2012 Greenland melt extent enhanced by low-level liquid clouds, *Nature*, 496, <https://doi.org/10.1038/nature12002>, 2013.

- Bergeron, T.: On the physics of clouds and precipitation, Report, International Union of Geodesy and Geophysics, pp. 156–180, 1935.
- Bigg, E. K. and Leck, C.: Cloud-active particles over the central Arctic Ocean, *Journal of Geophysical Research: Atmospheres*, 106, 32 155–32 166, <https://doi.org/https://doi.org/10.1029/1999JD901152>, 2001.
- Bintanja, R., van der Linden, E. C., and Hazeleger, W.: Boundary layer stability and Arctic climate change: a feedback study using EC-Earth, *Climate Dynamics*, 39, 2659–2673, <https://doi.org/10.1007/s00382-011-1272-1>, 2012.
- Boose, Y., Welti, A., Atkinson, J., Ramelli, F., Danielczok, A., Bingemer, H. G., Ploetze, M., Sierau, B., Kanji, Z. A., and Lohmann, U.: Heterogeneous ice nucleation on dust particles sourced from nine deserts worldwide–Part 1: Immersion freezing, *Atmospheric Chemistry and Physics*, 16, 15 075–15 095, 2016.
- Borys, R. D., Lowenthal, D. H., Cohn, S. A., and Brown, W. O. J.: Mountaintop and radar measurements of anthropogenic aerosol effects on snow growth and snowfall rate, *Geophysical Research Letters*, 30, <https://doi.org/10.1029/2002GL016855>, 2003.
- Boucher, O., Randall, D., Artaxo, P., Bretherton, C., Feingold, G., Forster, P., Kerminen, V.-M., Kondo, Y., Liao, H., Lohmann, U., et al.: Clouds and aerosols, in: *Climate change 2013: the physical science basis. Contribution of Working Group I to the Fifth Assessment Report of the Intergovernmental Panel on Climate Change*, pp. 571–657, Cambridge University Press, 2013.
- Brean, J., Dall’Osto, M., Simó, R., Shi, Z., Beddows, D. C. S., and Harrison, R. M.: Open ocean and coastal new particle formation from sulfuric acid and amines around the Antarctic Peninsula, *Nature Geoscience*, 14, 383–388, <https://doi.org/10.1038/s41561-021-00751-y>, 2021.
- Choi, J. H., Jang, E., Yoon, Y. J., Park, J. Y., Kim, T.-W., Becagli, S., Caiazzo, L., Cappelletti, D., Krejci, R., Eleftheriadis, K., Park, K.-T., and Jang, K. S.: Influence of Biogenic Organics on the Chemical Composition of Arctic Aerosols, *Global Biogeochemical Cycles*, 33, 1238–1250, <https://doi.org/https://doi.org/10.1029/2019GB006226>, 2019.
- Cohen, J., Screen, J. A., Furtado, J. C., Barlow, M., Whittleston, D., Coumou, D., Francis, J., Dethloff, K., Entekhabi, D., Overland, J., and Jones, J.: Recent Arctic amplification and extreme mid-latitude weather, *Nature Geoscience*, 7, 627–637, <https://doi.org/10.1038/ngeo2234>, 2014.
- Collins, W. D., Rasch, P. J., Boville, B. A., Hack, J. J., McCaa, J. R., Williamson, D. L., Kiehl, J. T., Briegleb, B., Bitz, C., Lin, S.-J., et al.: Description of the NCAR community atmosphere model (CAM 3.0), NCAR Tech. Note NCAR/TN-464+ STR, 226, 2004.
- COST: COST Action ES0702 EG-CLIMET – Final Report , URL [http://cfa.aquila.infn.it/wiki.eg-climet.org/index.php5/Final\\_Report](http://cfa.aquila.infn.it/wiki.eg-climet.org/index.php5/Final_Report), 2013.
- Croft, B., Lohmann, U., Martin, R. V., Stier, P., Wurzler, S., Feichter, J., Posselt, R., and Ferrachat, S.: Aerosol size-dependent below-cloud scavenging by rain and snow in the ECHAM5-HAM, *Atmospheric Chemistry and Physics*, 9, 4653–4675, <https://doi.org/10.5194/acp-9-4653-2009>, 2009.
- Curry, J. A., Schramm, J. L., Rossow, W. B., and Randall, D.: Overview of Arctic Cloud and Radiation Characteristics, *Journal of Climate*, 9, 1731–1764, [https://doi.org/10.1175/1520-0442\(1996\)009<1731:OOACAR>2.0.CO;2](https://doi.org/10.1175/1520-0442(1996)009<1731:OOACAR>2.0.CO;2), 1996.
- Dahlke, S. and Maturilli, M.: Contribution of Atmospheric Advection to the Amplified Winter Warming in the Arctic North Atlantic Region, *Advances in Meteorology*, 2017, 4928 620, <https://doi.org/10.1155/2017/4928620>, 2017.
- Dall’Osto, M., Tunved, P., Krejci, R., Ström, J., Hansson, H.-C., Yoon, Y., Park, K.-T., Becagli, S., Udusti, R., et al.: Arctic sea ice melt leads to atmospheric new particle formation, *Scientific Reports*, 7, 2017.
- David, R. O., Cascajo-Castresana, M., Brennan, K. P., Rösch, M., Els, N., Werz, J., Weichlinger, V., Boynton, L. S., Bogler, S., Borduas-Dedekind, N., Marcolli, C., and Kanji, Z. A.:

- Development of the DRoplet Ice Nuclei Counter Zurich (DRINCZ): validation and application to field-collected snow samples, *Atmospheric Measurement Techniques*, 12, 6865–6888, <https://doi.org/10.5194/amt-12-6865-2019>, 2019a.
- David, R. O., Marcolli, C., Fahrni, J., Qiu, Y., Perez Sirkin, Y. A., Molinero, V., Mahrt, F., Brühwiler, D., Lohmann, U., and Kanji, Z. A.: Pore condensation and freezing is responsible for ice formation below water saturation for porous particles, *Proceedings of the National Academy of Sciences*, 116, 8184–8189, <https://doi.org/10.1073/pnas.1813647116>, 2019b.
- Decesari, S., Facchini, M. C., Fuzzi, S., and Tagliavini, E.: Characterization of water-soluble organic compounds in atmospheric aerosol: A new approach, *Journal of Geophysical Research: Atmospheres*, 105, 1481–1489, <https://doi.org/https://doi.org/10.1029/1999JD900950>, 2000.
- Dedekind, Z., Lauber, A., Ferrachat, S., and Lohmann, U.: Sensitivity of precipitation formation to secondary ice production in winter orographic mixed-phase clouds, *Atmospheric Chemistry and Physics Discussions*, 2021, 1–27, <https://doi.org/10.5194/acp-2020-1326>, 2021.
- Dekhtyareva, A., Holmén, K., Maturilli, M., Hermansen, O., and Graversen, R.: Effect of seasonal mesoscale and microscale meteorological conditions in Ny-Ålesund on results of monitoring of long-range transported pollution, *Polar Research*, 37, 1508–1516, <https://doi.org/10.1080/17518369.2018.1508196>, publisher: Routledge \_eprint: <https://doi.org/10.1080/17518369.2018.1508196>, 2018.
- DeMott, P. J., Prenni, A. J., Liu, X., Kreidenweis, S. M., Petters, M. D., Twohy, C. H., Richardson, M., Eidhammer, T., and Rogers, D.: Predicting global atmospheric ice nuclei distributions and their impacts on climate, *Proceedings of the National Academy of Sciences*, 107, 11 217–11 222, 2010.
- Deser, C., Walsh, J. E., and Timlin, M. S.: Arctic Sea Ice Variability in the Context of Recent Atmospheric Circulation Trends, *Journal of Climate*, 13, 617 – 633, [https://doi.org/10.1175/1520-0442\(2000\)013<0617:ASIVIT>2.0.CO;2](https://doi.org/10.1175/1520-0442(2000)013<0617:ASIVIT>2.0.CO;2), 2000.
- Dexheimer, D., Airey, M., Roesler, E., Longbottom, C., Nicoll, K., Kneifel, S., Mei, F., Harrison, R. G., Marlton, G., and Williams, P. D.: Evaluation of ARM tethered-balloon system instrumentation for supercooled liquid water and distributed temperature sensing in mixed-phase Arctic clouds, *Atmospheric Measurement Techniques*, 12, 6845–6864, <https://doi.org/10.5194/amt-12-6845-2019>, 2019.
- Dong, X., Xi, B., Crosby, K., Long, C. N., Stone, R. S., and Shupe, M. D.: A 10 year climatology of Arctic cloud fraction and radiative forcing at Barrow, Alaska, *Journal of Geophysical Research: Atmospheres*, 115, <https://doi.org/https://doi.org/10.1029/2009JD013489>, 2010.
- Dong, Y., Oraltay, R. G., and Hallett, J.: Ice particle generation during evaporation, *Atmospheric Research*, 32, 45–53, [https://doi.org/https://doi.org/10.1016/0169-8095\(94\)90050-7](https://doi.org/https://doi.org/10.1016/0169-8095(94)90050-7), 1994.
- Doviak, R. J. and Zrnić, D. S.: Doppler radar and weather observations, Dover Publications, Inc., 3 edn., 2006.
- Duda, D. P., Stephens, G. L., and Cox, S. K.: Microphysical and Radiative Properties of Marine Stratocumulus from Tethered Balloon Measurements, *Journal of Applied Meteorology and Climatology*, 30, 170 – 186, [https://doi.org/10.1175/1520-0450\(1991\)030<0170:MARPOM>2.0.CO;2](https://doi.org/10.1175/1520-0450(1991)030<0170:MARPOM>2.0.CO;2), 1991a.
- Duda, D. P., Stephens, G. L., and Cox, S. K.: Microphysical and Radiative Properties of Marine Stratocumulus from Tethered Balloon Measurements, *Journal of Applied Meteorology*, 30, 170–186, [https://doi.org/10.1175/1520-0450\(1991\)030<0170:MARPOM>2.0.CO;2](https://doi.org/10.1175/1520-0450(1991)030<0170:MARPOM>2.0.CO;2), 1991b.
- Ebell, K., Nomokonova, T., Maturilli, M., and Ritter, C.: Radiative Effect of Clouds at Ny-Ålesund, Svalbard, as Inferred from Ground-Based Remote Sensing Observations, *Journal of Applied Meteorology and Climatology*, 59, 3–22, <https://doi.org/10.1175/JAMC-D-19-0080.1>, 2020.
- Egerer, U., Ehrlich, A., Gottschalk, M., Griesche, H., Neggers, R. A. J., Siebert, H., and Wendisch, M.: Case study of a humidity layer above Arctic stratocumulus and potential

- turbulent coupling with the cloud top, *Atmospheric Chemistry and Physics*, 21, 6347–6364, <https://doi.org/10.5194/acp-21-6347-2021>, 2021.
- Ehrlich, A. and Wendisch, M.: Reconstruction of high-resolution time series from slow-response broadband terrestrial irradiance measurements by deconvolution, *Atmospheric Measurement Techniques*, 8, 3671–3684, <https://doi.org/10.5194/amt-8-3671-2015>, 2015.
- Eleftheriadis, K., Vratolis, S., and Nyeki, S.: Aerosol black carbon in the European Arctic: Measurements at Zeppelin station, Ny-Ålesund, Svalbard from 1998–2007, *Geophys. Res. Lett.*, 36, L02 809, <https://doi.org/10.1029/2008GL035741>, 2009.
- Feltracco, M., Barbaro, E., Tedeschi, S., Spolaor, A., Turetta, C., Vecchiato, M., Morabito, E., Zangrando, R., Barbante, C., and Gambaro, A.: Interannual variability of sugars in Arctic aerosol: Biomass burning and biogenic inputs, *Science of The Total Environment*, 706, 136 089, <https://doi.org/https://doi.org/10.1016/j.scitotenv.2019.136089>, 2020.
- Field, P. R., Lawson, R. P., Brown, P. R. A., Lloyd, G., Westbrook, C., Moisseev, D., Miltenberger, A., Nenes, A., Blyth, A., Choularton, T., Connolly, P., Buehl, J., Crosier, J., Cui, Z., Dearden, C., DeMott, P., Flossmann, A., Heymsfield, A., Huang, Y., Kalesse, H., Kanji, Z. A., Korolev, A., Kirchgaessner, A., Lasher-Trapp, S., Leisner, T., McFarquhar, G., Phillips, V., Stith, J., and Sullivan, S.: Secondary Ice Production: Current State of the Science and Recommendations for the Future, *Meteorological Monographs*, 58, 7.1–7.20, <https://doi.org/10.1175/AMSMONOGRAPHS-D-16-0014.1>, 2017.
- Findeisen, W.: Kolloid-meteorologische Vorgänge bei Neiderschlags-bildung, *Meteor. Z*, 55, 121–133, 1938.
- Freud, E., Krejci, R., Tunved, P., Leaitch, R., Nguyen, Q. T., Massling, A., Skov, H., and Barrie, L.: Pan-Arctic aerosol number size distributions: seasonality and transport patterns, *Atmos. Chem. Phys.*, 17, 8101–8128, <https://doi.org/10.5194/acp-17-8101-2017>, 2017.
- Fu, S., Deng, X., Shupe, M. D., and Xue, H.: A modelling study of the continuous ice formation in an autumnal Arctic mixed-phase cloud case, *Atmospheric Research*, 228, 77–85, <https://doi.org/https://doi.org/10.1016/j.atmosres.2019.05.021>, 2019.
- Fugal, J. P., Schulz, T. J., and Shaw, R. A.: Practical methods for automated reconstruction and characterization of particles in digital in-line holograms, 20, 075 501, <https://doi.org/10.1088/0957-0233/20/7/075501>, 2009.
- Gayet, J.-F., Mioche, G., Dörnbrack, A., Ehrlich, A., Lampert, A., and Wendisch, M.: Microphysical and optical properties of Arctic mixed-phase clouds. The 9 April 2007 case study., *Atmospheric Chemistry and Physics*, 9, 6581–6595, <https://doi.org/10.5194/acp-9-6581-2009>, 2009.
- Georgakaki, P., Sotiropoulou, G., Vignon, E., Billault-Roux, A.-C., Berne, A., and Nenes, A.: Secondary ice production processes in wintertime alpine mixed-phase clouds, *Atmospheric Chemistry and Physics*, 22, 1965–1988, <https://doi.org/10.5194/acp-22-1965-2022>, 2022.
- Giardi, F., Becagli, S., Traversi, R., Frosini, D., Severi, M., Caiazzo, L., Ancillotti, C., Cappelletti, D., Moroni, B., Grotti, M., Bazzano, A., Lupi, A., Mazzola, M., Vitale, V., Abollino, O., Ferrero, L., Bolzacchini, E., Viola, A., and Udisti, R.: Size distribution and ion composition of aerosol collected at Ny-Ålesund in the spring–summer field campaign 2013, *Rendiconti Lincei*, 27, 47–58, <https://doi.org/10.1007/s12210-016-0529-3>, 2016.
- Gierens, R., Kneifel, S., Shupe, M. D., Ebell, K., Maturilli, M., and Löhnert, U.: Low-level mixed-phase clouds in a complex Arctic environment, *Atmospheric Chemistry and Physics*, 20, 3459–3481, <https://doi.org/10.5194/acp-20-3459-2020>, 2020.
- Girard, E., Dueymes, G., Du, P., and Bertram, A. K.: Assessment of the effects of acid-coated ice nuclei on the Arctic cloud microstructure, atmospheric dehydration, radiation and temperature during winter, *International Journal of Climatology*, 33, 599–614, <https://doi.org/https://doi.org/10.1002/joc.3454>, 2013.
- Gosse, H., Kay, J. E., Armour, K. C., Bodas-Salcedo, A., Chepfer, H., Docquier, D., Jonko,

- A., Kushner, P. J., Lecomte, O., Massonnet, F., et al.: Quantifying climate feedbacks in polar regions, *Nature communications*, 9, 1–13, <https://doi.org/10.1038/s41467-018-04173-0>, 2018.
- Gordon, N. D., Jonko, A. K., Forster, P. M., and Shell, K. M.: An observationally based constraint on the water-vapor feedback, *Journal of Geophysical Research: Atmospheres*, 118, 12,435–12,443, <https://doi.org/https://doi.org/10.1002/2013JD020184>, 2013.
- Graversen, R. G. and Wang, M.: Polar amplification in a coupled climate model with locked albedo, *Climate Dynamics*, 33, 629–643, <https://doi.org/10.1007/s00382-009-0535-6>, 2009.
- Grell, G. A. and Freitas, S. R.: A scale and aerosol aware stochastic convective parameterization for weather and air quality modeling, *Atmospheric Chemistry and Physics*, 14, 5233–5250, 2014.
- Hall, R. J., Hanna, E., and Chen, L.: Winter Arctic Amplification at the synoptic timescale, 1979–2018, its regional variation and response to tropical and extratropical variability, *Climate Dynamics*, 56, 457–473, <https://doi.org/10.1007/s00382-020-05485-y>, 2021.
- Hallett, J. and Mossop, S. C.: Production of secondary ice particles during the riming process, *Nature*, 249, 26–28, <https://doi.org/10.1038/249026a0>, 1974.
- Harrington, J. Y. and Olsson, P. Q.: A method for the parameterization of cloud optical properties in bulk and bin microphysical models. Implications for arctic cloudy boundary layers, *Atmospheric Research*, 57, 51–80, [https://doi.org/https://doi.org/10.1016/S0169-8095\(00\)00068-5](https://doi.org/https://doi.org/10.1016/S0169-8095(00)00068-5), 2001.
- Harrington, J. Y., Reisin, T., Cotton, W. R., and Kreidenweis, S. M.: Cloud resolving simulations of Arctic stratus: Part II: Transition-season clouds, *Atmospheric Research*, 51, 45 – 75, [https://doi.org/10.1016/S0169-8095\(98\)00098-2](https://doi.org/10.1016/S0169-8095(98)00098-2), 1999.
- Hartmann, M., Adachi, K., Eppers, O., Haas, C., Herber, A., Holzinger, R., H $\ddot{A}$ nerbein, A., J $\ddot{A}$ ckel, E., Jentsch, C., van Pinxteren, M., Wex, H., Willmes, S., and Stratmann, F.: Wintertime Airborne Measurements of Ice Nucleating Particles in the High Arctic: A Hint to a Marine, Biogenic Source for Ice Nucleating Particles, *Geophysical Research Letters*, 47, e2020GL087770, <https://doi.org/https://doi.org/10.1029/2020GL087770>, e2020GL087770 10.1029/2020GL087770, 2020.
- Hellmuth, F. and Hofer, S.: Weathermaps from MEPS latest runs, URL <https://github.com/franzihe/Weathermap>, 2019.
- Henneberger, J., Fugal, J. P., Stetzer, O., and Lohmann, U.: HOLIMO II: a digital holographic instrument for ground-based in situ observations of microphysical properties of mixed-phase clouds, *Atmospheric Measurement Techniques*, 6, 2975–2987, <https://doi.org/10.5194/amt-6-2975-2013>, 2013.
- Hersbach, H., Bell, B., Berrisford, P., Biavati, G., Horányi, A., Muñoz Sabater, J., Nicolas, J., Peubey, C., Radu, R., Rozum, I., Schepers, D., Simmons, A., Soci, C., Dee, D., and Thépaut, J.-N.: ERA5 hourly data on pressure levels from 1979 to present, Copernicus Climate Change Service (C3S) Climate Data Store (CDS) (Accessed on 19-MAR-2021), <https://doi.org/10.24381/cds.bd0915c6>, 2018a.
- Hersbach, H., Bell, B., Berrisford, P., Biavati, G., Horányi, A., Muñoz Sabater, J., Nicolas, J., Peubey, C., Radu, R., Rozum, I., Schepers, D., Simmons, A., Soci, C., Dee, D., and Thépaut, J.-N.: ERA5 hourly data on single levels from 1979 to present, Copernicus Climate Change Service (C3S) Climate Data Store (CDS). (Accessed on 21-APR-2021), <https://doi.org/10.24381/cds.adbb2d47>, 2018b.
- Heslin-Rees, D., Burgos, M., Hansson, H.-C., Krejci, R., Ström, J., Tunved, P., and Zieger, P.: From a polar to a marine environment: has the changing Arctic led to a shift in aerosol light scattering properties?, *Atmospheric Chemistry and Physics*, 20, 13 671–13 686, <https://doi.org/10.5194/acp-20-13671-2020>, 2020.
- Heymsfield, A. J.: Precipitation Development in Stratiform Ice Clouds: A Microphysical and Dynamical Study, *Journal of Atmospheric Sciences*, 34, 367 – 381, [https://doi.org/10.1175/1520-0469\(1977\)034<0367:PDISIC>2.0.CO;2](https://doi.org/10.1175/1520-0469(1977)034<0367:PDISIC>2.0.CO;2), 1977.

- Heymsfield, A. J. and Westbrook, C. D.: Advances in the estimation of ice particle fall speeds using laboratory and field measurements, *J. Atmos. Sci.*, 67, 2469–2482, <https://doi.org/https://doi.org/10.1175/2010jas3379.1>, 2010.
- Hobbs, P. V. and Rangno, A. L.: Ice Particle Concentrations in Clouds, *Journal of the Atmospheric Sciences*, 42, 2523–2549, [https://doi.org/10.1175/1520-0469\(1985\)042<2523:IPCIC>2.0.CO;2](https://doi.org/10.1175/1520-0469(1985)042<2523:IPCIC>2.0.CO;2), 1985.
- Hobbs, P. V. and Rangno, A. L.: Microstructures of low and middle-level clouds over the Beaufort Sea, *Quarterly Journal of the Royal Meteorological Society*, 124, 2035–2071, <https://doi.org/https://doi.org/10.1002/qj.49712455012>, 1998.
- Hoffer, T. E. and Braham, R. R.: A Laboratory Study of Atmospheric Ice Particles, *Journal of Atmospheric Sciences*, 19, 232 – 235, [https://doi.org/10.1175/1520-0469\(1962\)019<0232:ALSOAI>2.0.CO;2](https://doi.org/10.1175/1520-0469(1962)019<0232:ALSOAI>2.0.CO;2), 1962.
- Hong, S.-Y., Noh, Y., and Dudhia, J.: A new vertical diffusion package with an explicit treatment of entrainment processes, *Monthly weather review*, 134, 2318–2341, 2006.
- Hoose, C. and Möhler, O.: Heterogeneous ice nucleation on atmospheric aerosols: a review of results from laboratory experiments, *Atmos. Chem. Phys*, 12, 9817–9854, 2012.
- Houze Jr, R. A.: *Cloud dynamics*, Academic press, 2014.
- Illingworth, A. J., Hogan, R. J., O’Connor, E., Bouniol, D., Brooks, M. E., Delanoé, J., Donovan, D. P., Eastment, J. D., Gaussiat, N., Goddard, J. W. F., Haefelin, M., Baltink, H. K., Krasnov, O. A., Pelon, J., Piriou, J.-M., Protat, A., Russchenberg, H. W. J., Seifert, A., Tompkins, A. M., van Zadelhoff, G.-J., Vinit, F., Willén, U., Wilson, D. R., and Wrench, C. L.: Cloudnet: Continuous Evaluation of Cloud Profiles in Seven Operational Models Using Ground-Based Observations, *Bulletin of the American Meteorological Society*, 88, 883 – 898, <https://doi.org/10.1175/BAMS-88-6-883>, 2007.
- Inoue, J., Tobo, Y., Sato, K., Taketani, F., and Maturilli, M.: Application of cloud particle sensor sondes for estimating the number concentration of cloud water droplets and liquid water content: case studies in the Arctic region, *Atmospheric Measurement Techniques*, 14, 4971–4987, <https://doi.org/10.5194/amt-14-4971-2021>, 2021.
- Intrieri, J. M., Fairall, C. W., Shupe, M. D., Persson, P. O. G., Andreas, E. L., Guest, P. S., and Moritz, R. E.: An annual cycle of Arctic surface cloud forcing at SHEBA, *Journal of Geophysical Research: Oceans*, 107, <https://doi.org/10.1029/2000JC000439>, 2002.
- IPCC, 2021: *Climate Change 2021: The Physical Science Basis. Contribution of Working Group I to the Sixth Assessment Report of the Intergovernmental Panel on Climate Change* [Masson-Delmotte, V., P. Zhai, A. Pirani, S.L. Connors, C. Péan, S. Berger, N. Caud, Y. Chen, L. Goldfarb, M.I. Gomis, M. Huang, K. Leitzell, E. Lonnoy, J.B.R. Matthews, T.K. Maycock, T. Waterfield, O. Yelekçi, R. Yu, and B. Zhou (eds.)] Cambridge University Press. In Press.
- Jackson, R. C., McFarquhar, G. M., Korolev, A. V., Earle, M. E., Liu, P. S. K., Lawson, R. P., Brooks, S., Wolde, M., Laskin, A., and Freer, M.: The dependence of ice microphysics on aerosol concentration in arctic mixed-phase stratus clouds during ISDAC and M-PACE, *Journal of Geophysical Research: Atmospheres*, 117, <https://doi.org/10.1029/2012JD017668>, 2012.
- Jambon-Puillet, E., Shahidzadeh, N., and Bonn, D.: Singular sublimation of ice and snow crystals, *Nature Communications*, 9, 4191, <https://doi.org/10.1038/s41467-018-06689-x>, 2018.
- Järvinen, E., Jourdan, O., Neubauer, D., Yao, B., Liu, C., Andreae, M. O., Lohmann, U., Wendisch, M., McFarquhar, G. M., Leisner, T., and Schnaiter, M.: Additional global climate cooling by clouds due to ice crystal complexity, *Atmospheric Chemistry and Physics*, 18, 15767–15781, <https://doi.org/10.5194/acp-18-15767-2018>, 2018.
- Jiang, H., Cotton, W. R., Pinto, J. O., Curry, J. A., and Weissbluth, M. J.: Cloud Resolving Simulations of Mixed-Phase Arctic Stratus Observed during BASE: Sensitivity to Concentration of Ice Crystals and Large-Scale Heat and Moisture Advection, *Journal of*

- the Atmospheric Sciences, 57, 2105–2117, [https://doi.org/10.1175/1520-0469\(2000\)057<2105:CRSOMP>2.0.CO;2](https://doi.org/10.1175/1520-0469(2000)057<2105:CRSOMP>2.0.CO;2), 2000.
- Kalesse, H., de Boer, G., Solomon, A., Oue, M., Ahlgrimm, M., Zhang, D., Shupe, M. D., Luke, E., and Protat, A.: Understanding Rapid Changes in Phase Partitioning between Cloud Liquid and Ice in Stratiform Mixed-Phase Clouds: An Arctic Case Study, *Monthly Weather Review*, 144, 4805 – 4826, <https://doi.org/10.1175/MWR-D-16-0155.1>, 2016.
- Kanji, Z. A., Ladino, L. A., Wex, H., Boose, Y., Burkert-Kohn, M., Cziczo, D. J., and Krämer, M.: Overview of Ice Nucleating Particles, *Meteorological Monographs*, 58, 1.1 – 1.33, <https://doi.org/10.1175/AMSMONOGRAPHS-D-16-0006.1>, 2017.
- Kärcher, B. and Marcolli, C.: Aerosol–cloud interactions: the representation of heterogeneous ice activation in cloud models, *Atmospheric Chemistry and Physics*, 21, 15 213–15 220, <https://doi.org/10.5194/acp-21-15213-2021>, 2021.
- Karlsson, L., Krejci, R., Koike, M., Ebell, K., and Zieger, P.: A long-term study of cloud residuals from low-level Arctic clouds, *Atmospheric Chemistry and Physics*, 21, 8933–8959, <https://doi.org/10.5194/acp-21-8933-2021>, 2021.
- Kay, J. E. and Gettelman, A.: Cloud influence on and response to seasonal Arctic sea ice loss, *Journal of Geophysical Research: Atmospheres*, 114, <https://doi.org/10.1029/2009JD011773>, 2009.
- Keinert, A., Spannagel, D., Leisner, T., and Kiselev, A.: Secondary Ice Production upon Freezing of Freely Falling Drizzle Droplets, *Journal of the Atmospheric Sciences*, 77, 2959–2967, <https://doi.org/10.1175/JAS-D-20-0081.1>, 2020.
- Keppas, S. C., Crosier, J., Choulaton, T. W., and Bower, K. N.: Ice lollies: An ice particle generated in supercooled conveyor belts, *Geophysical Research Letters*, 44, 5222–5230, <https://doi.org/https://doi.org/10.1002/2017GL073441>, 2017.
- Khvorostyanov, V. I. and Curry, J. A.: Terminal velocities of droplets and crystals: Power laws with continuous parameters over the size spectrum, *Journal of the atmospheric sciences*, 59, 1872–1884, [https://doi.org/https://doi.org/10.1175/1520-0469\(2002\)059<1872:TVODAC>2.0.CO;2](https://doi.org/https://doi.org/10.1175/1520-0469(2002)059<1872:TVODAC>2.0.CO;2), 2002.
- King, W. D. and Fletcher, N. H.: Thermal Shock as an Ice Multiplication Mechanism. Part I. Theory, *Journal of Atmospheric Sciences*, 33, 85 – 96, [https://doi.org/10.1175/1520-0469\(1976\)033<0085:TSAAIM>2.0.CO;2](https://doi.org/10.1175/1520-0469(1976)033<0085:TSAAIM>2.0.CO;2), 1976.
- Kneifel, S., Dias Neto, J., Ori, D., Moisseev, D., Tyynelä, J., Adams, I. S., Kuo, K.-S., Benkert, R., Berne, A., Clothiaux, E. E., Eriksson, P., Geer, A. J., Honeyager, R., Leinonen, J., and Westbrook, C. D.: Summer Snowfall Workshop: Scattering Properties of Realistic Frozen Hydrometeors from Simulations and Observations, as well as Defining a New Standard for Scattering Databases, *Bulletin of the American Meteorological Society*, 99, ES55– ES58, <https://doi.org/10.1175/BAMS-D-17-0208.1>, 2018.
- Knight, C. A.: Ice Growth from the Vapor at  $-5^{\circ}\text{C}$ , *Journal of the Atmospheric Sciences*, 69, 2031 – 2040, <https://doi.org/10.1175/JAS-D-11-0287.1>, 2012.
- Koenig, L. R.: Drop Freezing Through Drop Breakup, *Journal of Atmospheric Sciences*, 22, 448 – 451, [https://doi.org/10.1175/1520-0469\(1965\)022<0448:DFTDB>2.0.CO;2](https://doi.org/10.1175/1520-0469(1965)022<0448:DFTDB>2.0.CO;2), 1965.
- Kogan, Z. N., Mechem, D. B., and Kogan, Y. L.: Assessment of variability in continental low stratiform clouds based on observations of radar reflectivity, *Journal of Geophysical Research: Atmospheres*, 110, <https://doi.org/https://doi.org/10.1029/2005JD006158>, 2005.
- Koike, M., Ukita, J., Ström, J., Tunved, P., Shiobara, M., Vitale, V., Lupi, A., Baumgardner, D., Ritter, C., Hermansen, O., Yamada, K., and Pedersen, C. A.: Year-Round In Situ Measurements of Arctic Low-Level Clouds: Microphysical Properties and Their Relationships With Aerosols, *Journal of Geophysical Research: Atmospheres*, 124, 1798–1822, <https://doi.org/10.1029/2018JD029802>, 2019.
- Koike, M., Goto-Azuma, K., Kondo, Y., Matsui, H., Mori, T., Moteki, N., Ohata, S., Okamoto, H., Oshima, N., Sato, K., Takano, T., Tobo, Y., Ukita, J., and Yoshida, A.:



- Studies on Arctic aerosols and clouds during the ArCS project, *Polar Science*, 27, 100621, <https://doi.org/https://doi.org/10.1016/j.polar.2020.100621>, arctic Challenge for Sustainability Project (ArCS), 2021.
- Kondo, Y., Sahu, L., Moteki, N., Khan, F., Takegawa, N., Liu, X., Koike, M., and Miyakawa, T.: Consistency and Traceability of Black Carbon Measurements Made by Laser-Induced Incandescence, Thermal-Optical Transmittance, and Filter-Based Photo-Absorption Techniques, *Aerosol Science and Technology*, 45, 295–312, <https://doi.org/10.1080/02786826.2010.533215>, 2011.
- Korolev, A.: Limitations of the Wegener–Bergeron–Findeisen Mechanism in the Evolution of Mixed-Phase Clouds, *Journal of the Atmospheric Sciences*, 64, 3372–3375, <https://doi.org/10.1175/JAS4035.1>, 2007.
- Korolev, A. and Isaac, G.: Phase transformation of mixed-phase clouds, *Quarterly Journal of the Royal Meteorological Society*, 129, 19–38, <https://doi.org/10.1256/qj.01.203>, 2003.
- Korolev, A. and Leisner, T.: Review of experimental studies on secondary ice production, *Atmospheric Chemistry and Physics Discussions*, 2020, 1–42, <https://doi.org/10.5194/acp-2020-537>, 2020.
- Korolev, A., Emery, E., Strapp, J., Cober, S. G., Isaac, G. A., Wasey, M., and Marcotte, D.: Small Ice Particles in Tropospheric Clouds: Fact or Artifact? Airborne Icing Instrumentation Evaluation Experiment, *Bulletin of the American Meteorological Society*, 92, 967–973, <https://doi.org/10.1175/2010BAMS3141.1>, 2011.
- Korolev, A., McFarquhar, G., Field, P. R., Franklin, C., Lawson, P., Wang, Z., Williams, E., Abel, S. J., Axisa, D., Borrmann, S., Crosier, J., Fugal, J., Krämer, M., Lohmann, U., Schlenzcek, O., Schnaiter, M., and Wendisch, M.: Mixed-Phase Clouds: Progress and Challenges, *Meteorological Monographs*, 58, 5.1–5.50, <https://doi.org/10.1175/AMSMONOGRAPHS-D-17-0001.1>, 2017.
- Korolev, A., Heckman, I., Wolde, M., Ackerman, A. S., Fridlind, A. M., Ladino, L. A., Lawson, R. P., Milbrandt, J., and Williams, E.: A new look at the environmental conditions favorable to secondary ice production, *Atmospheric Chemistry and Physics*, 20, 1391–1429, <https://doi.org/10.5194/acp-20-1391-2020>, 2020.
- Korolev, A. V., Isaac, G. A., and Hallett, J.: Ice particle habits in Arctic clouds, *Geophysical Research Letters*, 26, 1299–1302, <https://doi.org/https://doi.org/10.1029/1999GL900232>, 1999.
- Küchler, N., Kneifel, S., Löhnert, U., Kollias, P., Czekala, H., and Rose, T.: A W-Band Radar-Radiometer System for Accurate and Continuous Monitoring of Clouds and Precipitation, *J. Atmos. Ocean. Technol.*, 34, 2375–2392, <https://doi.org/10.1175/JTECH-D-17-0019.1>, 2017.
- Lacher, L., Lohmann, U., Boose, Y., Zipori, A., Herrmann, E., Bukowiecki, N., Steinbacher, M., and Kanji, Z. A.: The Horizontal Ice Nucleation Chamber (HINC): INP measurements at conditions relevant for mixed-phase clouds at the High Altitude Research Station Jungfraujoch, *Atmospheric Chemistry and Physics*, 17, 15199–15224, <https://doi.org/10.5194/acp-17-15199-2017>, 2017.
- Ladino, L. A., Korolev, A., Heckman, I., Wolde, M., Fridlind, A. M., and Ackerman, A. S.: On the role of ice-nucleating aerosol in the formation of ice particles in tropical mesoscale convective systems, *Geophysical Research Letters*, 44, 1574–1582, <https://doi.org/https://doi.org/10.1002/2016GL072455>, 2017.
- Lance, S., Shupe, M. D., Feingold, G., Brock, C. A., Cozic, J., Holloway, J. S., Moore, R. H., Nenes, A., Schwarz, J. P., Spackman, J. R., Froyd, K. D., Murphy, D. M., Brioude, J., Cooper, O. R., Stohl, A., and Burkhardt, J. F.: Cloud condensation nuclei as a modulator of ice processes in Arctic mixed-phase clouds, *Atmospheric Chemistry and Physics*, 11, 8003–8015, <https://doi.org/10.5194/acp-11-8003-2011>, 2011.
- Langham, E. J., Mason, B. J. N., and Bernal, J. D.: The heterogeneous and homogeneous nucle-

- ation of supercooled water, *Proceedings of the Royal Society of London. Series A. Mathematical and Physical Sciences*, 247, 493–504, <https://doi.org/10.1098/rspa.1958.0207>, 1958.
- Lauber, A.: In-situ observations of ice multiplication in clouds using a holographic imager and a deep learning algorithm for the classification of cloud particles, Ph.D. thesis, ETH Zurich, Zurich, <https://doi.org/10.3929/ethz-b-000474830>, 2020.
- Lauber, A., Kiselev, A., Pander, T., Handmann, P., and Leisner, T.: Secondary Ice Formation during Freezing of Levitated Droplets, *Journal of the Atmospheric Sciences*, 75, 2815–2826, <https://doi.org/10.1175/JAS-D-18-0052.1>, 2018.
- Lauber, A., Henneberger, J., Mignani, C., Ramelli, F., Pasquier, J. T., Wieder, J., Hervo, M., and Lohmann, U.: Continuous secondary-ice production initiated by updrafts through the melting layer in mountainous regions, *Atmospheric Chemistry and Physics*, 21, 3855–3870, <https://doi.org/10.5194/acp-21-3855-2021>, 2021.
- Lawrence, Z. D., Perlwitz, J., Butler, A. H., Manney, G. L., Newman, P. A., Lee, S. H., and Nash, E. R.: The Remarkably Strong Arctic Stratospheric Polar Vortex of Winter 2020: Links to Record-Breaking Arctic Oscillation and Ozone Loss, *Journal of Geophysical Research: Atmospheres*, 125, e2020JD033271, <https://doi.org/https://doi.org/10.1029/2020JD033271>, e2020JD033271 10.1029/2020JD033271, 2020.
- Lawson, P., Gurganus, C., Woods, S., and Brientjes, R.: Aircraft Observations of Cumulus Microphysics Ranging from the Tropics to Midlatitudes: Implications for a New Secondary Ice Process, *Journal of the Atmospheric Sciences*, 74, 2899 – 2920, <https://doi.org/10.1175/JAS-D-17-0033.1>, 2017.
- Lawson, R. P., Baker, B. A., Schmitt, C. G., and Jensen, T. L.: An overview of microphysical properties of Arctic clouds observed in May and July 1998 during FIRE ACE, *Journal of Geophysical Research: Atmospheres*, 106, 14 989–15 014, <https://doi.org/10.1029/2000JD900789>, 2001.
- Lawson, R. P., Woods, S., and Morrison, H.: The Microphysics of Ice and Precipitation Development in Tropical Cumulus Clouds, *Journal of the Atmospheric Sciences*, 72, 2429 – 2445, <https://doi.org/10.1175/JAS-D-14-0274.1>, 2015.
- Lee, B. H., Lopez-Hilfiker, F. D., Mohr, C., Kurtén, T., Worsnop, D. R., and Thornton, J. A.: An Iodide-Adduct High-Resolution Time-of-Flight Chemical-Ionization Mass Spectrometer: Application to Atmospheric Inorganic and Organic Compounds, *Environmental Science & Technology*, 48, 6309–6317, <https://doi.org/10.1021/es500362a>, 2014.
- Lee, H., Lee, K., Lunder, C. R., Krejci, R., Aas, W., Park, J., Park, K.-T., Lee, B. Y., Yoon, Y. J., and Park, K.: Atmospheric new particle formation characteristics in the Arctic as measured at Mount Zeppelin, Svalbard, from 2016 to 2018, *Atmospheric Chemistry and Physics*, 20, 13 425–13 441, <https://doi.org/10.5194/acp-20-13425-2020>, 2020a.
- Lee, S. H., Lawrence, Z. D., Butler, A. H., and Karpechko, A. Y.: Seasonal Forecasts of the Exceptional Northern Hemisphere Winter of 2020, *Geophysical Research Letters*, 47, e2020GL090328, <https://doi.org/https://doi.org/10.1029/2020GL090328>, e2020GL090328 10.1029/2020GL090328, 2020b.
- Li, G., Wieder, J., Pasquier, J. T., Henneberger, J., and Kanji, Z. A.: Predicting atmospheric background number concentration of ice nucleating particles in the Arctic, *Atmospheric Chemistry and Physics Discussions*, 2022, 1–27, <https://doi.org/10.5194/acp-2022-21>, 2022.
- Li, H., Möhler, O., Petäjä, T., and Moiseev, D.: Multiyear statistics of columnar ice production in stratiform clouds over Hyytiälä, Finland, *Atmospheric Chemistry and Physics Discussions*, 2021, 1–26, <https://doi.org/10.5194/acp-2021-332>, 2021.
- Libbrecht, K. G.: The physics of snow crystals, *Reports on Progress in Physics*, 68, 855–895, <https://doi.org/10.1088/0034-4885/68/4/r03>, 2005.
- Libbrecht, K. G.: Physical Dynamics of Ice Crystal Growth, *Annual Review of Materials Research*, 47, 271–295, <https://doi.org/10.1146/annurev-matsci-070616-124135>, 2017.

- Liu, C., Yang, P., Minnis, P., Loeb, N., Kato, S., Heymsfield, A., and Schmitt, C.: A two-habit model for the microphysical and optical properties of ice clouds, *Atmospheric Chemistry and Physics*, 14, 13 719–13 737, <https://doi.org/10.5194/acp-14-13719-2014>, 2014.
- Lloyd, G., Choularton, T. W., Bower, K. N., Crosier, J., Jones, H., Dorsey, J. R., Gallagher, M. W., Connolly, P., Kirchgaessner, A. C. R., and Lachlan-Cope, T.: Observations and comparisons of cloud microphysical properties in spring and summertime Arctic stratocumulus clouds during the ACCACIA campaign, *Atmospheric Chemistry and Physics*, 15, 3719–3737, <https://doi.org/10.5194/acp-15-3719-2015>, 2015.
- Lohmann, U.: A glaciation indirect aerosol effect caused by soot aerosols, *Geophysical Research Letters*, 29, 11–1–11–4, <https://doi.org/10.1029/2001GL014357>, 2002.
- Lohmann, U. and Feichter, J.: Global indirect aerosol effects: A review, *Atmospheric Chemistry and Physics*, 5, 715–737, <https://doi.org/10.5194/acp-5-715-2005>, 2005.
- Lohmann, U., Henneberger, J., Henneberg, O., Fugal, J. P., Bühl, J., and Kanji, Z. A.: Persistence of orographic mixed-phase clouds, *Geophysical Research Letters*, 43, 10, 512–10, 519, <https://doi.org/10.1002/2016GL071036>, 2016a.
- Lohmann, U., Lüönd, F., and Mahrt, F.: *Clouds*, p. 1–25, Cambridge University Press, <https://doi.org/10.1017/CBO9781139087513.002>, 2016b.
- Lopez-Hilfiker, F. D., Mohr, C., Ehn, M., Rubach, F., Kleist, E., Wildt, J., Mentel, T. F., Lutz, A., Hallquist, M., Worsnop, D., and Thornton, J. A.: A novel method for online analysis of gas and particle composition: description and evaluation of a Filter Inlet for Gases and AEROsols (FIGAERO), *Atmospheric Measurement Techniques*, 7, 983–1001, <https://doi.org/10.5194/amt-7-983-2014>, 2014.
- Luke, E. P., Kollias, P., and Shupe, M. D.: Detection of supercooled liquid in mixed-phase clouds using radar Doppler spectra, *Journal of Geophysical Research: Atmospheres*, 115, <https://doi.org/https://doi.org/10.1029/2009JD012884>, 2010.
- Luke, E. P., Yang, F., Kollias, P., Vogelmann, A. M., and Maahn, M.: New insights into ice multiplication using remote-sensing observations of slightly supercooled mixed-phase clouds in the Arctic, *Proceedings of the National Academy of Sciences*, 118, <https://doi.org/10.1073/pnas.2021387118>, 2021.
- Marcocolli, C.: Deposition nucleation viewed as homogeneous or immersion freezing in pores and cavities, *Atmospheric Chemistry and Physics*, 14, 2071–2104, <https://doi.org/10.5194/acp-14-2071-2014>, 2014.
- Mason, B. J. and Maybank, J.: The fragmentation and electrification of freezing water drops, *Quarterly Journal of the Royal Meteorological Society*, 86, 176–185, <https://doi.org/https://doi.org/10.1002/qj.49708636806>, 1960.
- Maturilli, M.: High resolution radiosonde measurements from station Ny-Ålesund (2020-04), PANGAEA, <https://doi.org/10.1594/PANGAEA.917967>, in: Maturilli, M (2020): High resolution radiosonde measurements from station Ny-Ålesund (2017-04 et seq). Alfred Wegener Institute - Research Unit Potsdam, PANGAEA, <https://doi.org/10.1594/PANGAEA.914973>, 2020a.
- Maturilli, M.: Continuous meteorological observations at station Ny-Ålesund (2020-04), PANGAEA, <https://doi.org/10.1594/PANGAEA.925612>, in: Maturilli, M (2020): Continuous meteorological observations at station Ny-Ålesund (2011-08 et seq). Alfred Wegener Institute - Research Unit Potsdam, PANGAEA, <https://doi.org/10.1594/PANGAEA.914979>, 2020b.
- Maturilli, M.: Basic and other measurements of radiation at station Ny-Ålesund (2020-04), PANGAEA, <https://doi.org/10.1594/PANGAEA.917580>, in: Maturilli, M (2020): Basic and other measurements of radiation at station Ny-Ålesund (2006-05 et seq). Alfred Wegener Institute - Research Unit Potsdam, PANGAEA, <https://doi.org/10.1594/PANGAEA.914927>, 2020c.
- Maturilli, M.: Continuous meteorological observations at station Ny-Ålesund (2011-08 et seq), URL <https://doi.pangaea.de/10.1594/PANGAEA.914979>, 2020d.

- Maturilli, M.: Continuous meteorological observations at station Ny-Ålesund (2019-11), PANGAEA, <https://doi.org/10.1594/PANGAEA.911503>, in: Maturilli, M (2020): Continuous meteorological observations at station Ny-Ålesund (2011-08 et seq). Alfred Wegener Institute - Research Unit Potsdam, PANGAEA, <https://doi.org/10.1594/PANGAEA.914979>, 2020e.
- Maturilli, M.: High resolution radiosonde measurements from station Ny-Ålesund (2019-11), PANGAEA, <https://doi.org/10.1594/PANGAEA.911039>, in: Maturilli, M (2020): High resolution radiosonde measurements from station Ny-Ålesund (2017-04 et seq). Alfred Wegener Institute - Research Unit Potsdam, PANGAEA, <https://doi.org/10.1594/PANGAEA.914973>, 2020f.
- Maturilli, M. and Ebell, K.: Twenty-five years of cloud base height measurements by ceilometer in Ny-Ålesund, Svalbard, *Earth System Science Data*, 10, 1451–1456, <https://doi.org/10.5194/essd-10-1451-2018>, 2018.
- Maturilli, M. and Kayser, M.: Arctic warming, moisture increase and circulation changes observed in the Ny-Ålesund homogenized radiosonde record, *Theoretical and Applied Climatology*, 130, 1–17, <https://doi.org/10.1007/s00704-016-1864-0>, 2017.
- Maturilli, M., Herber, A., and König-Langlo, G.: Climatology and time series of surface meteorology in Ny-Ålesund, Svalbard, *Earth System Science Data*, 5, 155–163, <https://doi.org/10.5194/essd-5-155-2013>, 2013.
- Maturilli, M., Herber, A., and König-Langlo, G.: Continuous meteorological observations at station Ny-Ålesund, 1993-08 to 2011-07, <https://doi.org/10.1594/PANGAEA.793046>, 2013.
- Maturilli, M., Herber, A., and König-Langlo, G.: Surface radiation climatology for Ny-Ålesund, Svalbard (78.9° N), basic observations for trend detection, *Theoretical and Applied Climatology*, 120, 331–339, <https://doi.org/10.1007/s00704-014-1173-4>, 2015.
- Mazzola, M., Viola, A. P., Lanconelli, C., and Vitale, V.: Atmospheric observations at the Amundsen-Nobile Climate Change Tower in Ny-Ålesund, Svalbard, *Rendiconti Lincei*, 27, 7–18, <https://doi.org/10.1007/s12210-016-0540-8>, 2016.
- McFarquhar, G. M., Ghan, S., Verlinde, J., Korolev, A., Strapp, J. W., Schmid, B., Tomlinson, J. M., Wolde, M., Brooks, S. D., Cziczo, D., Dubey, M. K., Fan, J., Flynn, C., Gultepe, I., Hubbe, J., Gilles, M. K., Laskin, A., Lawson, P., Leaitch, W. R., Liu, P., Liu, X., Lubin, D., Mazzoleni, C., Macdonald, A.-M., Moffet, R. C., Morrison, H., Ovchinnikov, M., Shupe, M. D., Turner, D. D., Xie, S., Zelenyuk, A., Bae, K., Freer, M., and Glen, A.: Indirect and Semi-direct Aerosol Campaign, *Bulletin of the American Meteorological Society*, 92, 183–201, <https://doi.org/10.1175/2010BAMS2935.1>, 2011.
- Mech, M., Maahn, M., Kneifel, S., Ori, D., Orlandi, E., Kollias, P., Schemann, V., and Crewell, S.: PAMTRA 1.0: the Passive and Active Microwave radiative TRANSfer tool for simulating radiometer and radar measurements of the cloudy atmosphere, *Geoscientific Model Development*, 13, 4229–4251, <https://doi.org/10.5194/gmd-13-4229-2020>, 2020.
- Meredith, M., Sommerkorn, M., Cassotta, S., Derksen, C., Ekaykin, A., Hollowed, A., Kofinas, G., Mackintosh, A., Melbourne-Thomas, J., Muelbert, M., et al.: Polar Regions. Chapter 3, IPCC Special Report on the Ocean and Cryosphere in a Changing Climate, 2019.
- Mertes, S., Verheggen, B., Walter, S., Connolly, P., Ebert, M., Schneider, J., Bower, K. N., Cozic, J., Weinbruch, S., Baltensperger, U., and Weingartner, E.: Counterflow Virtual Impactor Based Collection of Small Ice Particles in Mixed-Phase Clouds for the Physico-Chemical Characterization of Tropospheric Ice Nuclei: Sampler Description and First Case Study, *Aerosol Science and Technology*, 41, 848–864, <https://doi.org/10.1080/02786820701501881>, 2007.
- Mie, G.: Beiträge Zur Optik Trüber Medien, Speziell Kolloidaler Metallösungen., *Ann. Phys.(Leipzig)*, 330, 377–445, <https://doi.org/10.1002/andp.19083300302>, 1908.
- Mignani, C., Creamean, J. M., Zimmermann, L., Alewell, C., and Conen, F.: New type of evidence for secondary ice formation at around  $-15^{\circ}\text{C}$  in mixed-phase clouds, *Atmospheric Chemistry and Physics*, 19, 877–886, <https://doi.org/10.5194/acp-19-877-2019>, 2019.
- Milbrandt, J. and Yau, M.: A multimoment bulk microphysics parameterization. Part II: A

- proposed three-moment closure and scheme description, *Journal of Atmospheric Sciences*, 62, 3065–3081, 2005.
- Mioche, G., Jourdan, O., Ceccaldi, M., and Delanoë, J.: Variability of mixed-phase clouds in the Arctic with a focus on the Svalbard region: a study based on spaceborne active remote sensing, *Atmospheric Chemistry and Physics*, 15, 2445–2461, <https://doi.org/10.5194/acp-15-2445-2015>, 2015.
- Mitchell, D. L.: Use of mass-and area-dimensional power laws for determining precipitation particle terminal velocities, *Journal of Atmospheric Sciences*, 53, 1710–1723, [https://doi.org/https://doi.org/10.1175/1520-0469\(1996\)053<1710:UOMAAD>2.0.CO;2](https://doi.org/https://doi.org/10.1175/1520-0469(1996)053<1710:UOMAAD>2.0.CO;2), 1996.
- Montero-Martínez, G., Rinaldi, M., Gilardoni, S., Giulianelli, L., Paglione, M., Decesari, S., Fuzzi, S., and Facchini, M. C.: On the water-soluble organic nitrogen concentration and mass size distribution during the fog season in the Po Valley, Italy, *Science of The Total Environment*, 485–486, 103–109, <https://doi.org/https://doi.org/10.1016/j.scitotenv.2014.03.060>, 2014.
- Moore, G. W. K.: The December 2015 North Pole Warming Event and the Increasing Occurrence of Such Events, *Scientific Reports*, 6, 39 084, <https://doi.org/10.1038/srep39084>, 2016.
- Moore, R. H., Karydis, V. A., Capps, S. L., Latham, T. L., and Nenes, A.: Droplet number uncertainties associated with CCN: an assessment using observations and a global model adjoint, *Atmospheric Chemistry and Physics*, 13, 4235–4251, <https://doi.org/10.5194/acp-13-4235-2013>, 2013.
- Morrison, H., de Boer, G., Feingold, G., Harrington, J., Shupe, M. D., and Sulia, K.: Resilience of persistent Arctic mixed-phase clouds, *Nature Geoscience*, 5, <https://doi.org/10.1038/ngeo1332>, 2011.
- Mossop, S. C.: The influence of drop size distribution on the production of secondary ice particles during graupel growth, *Quarterly Journal of the Royal Meteorological Society*, 104, 323–330, <https://doi.org/10.1002/qj.49710444007>, 1978.
- Mossop, S. C.: Secondary ice particle production during rime growth: The effect of drop size distribution and rimer velocity, *Quarterly Journal of the Royal Meteorological Society*, 111, 1113–1124, <https://doi.org/https://doi.org/10.1002/qj.49711147012>, 1985.
- Mossop, S. C. and Hallett, J.: Ice Crystal Concentration in Cumulus Clouds: Influence of the Drop Spectrum, *Science*, 186, 632–634, <https://doi.org/10.1126/science.186.4164.632>, 1974.
- Murray, B., O’sullivan, D., Atkinson, J., and Webb, M.: Ice nucleation by particles immersed in supercooled cloud droplets, *Chemical Society Reviews*, 41, 6519–6554, 2012.
- Nakaya, U.: *Snow Crystals: Natural and Artificial*, Cambridge, MA: Harvard University Press, 1954.
- Nielsen, I. E., Skov, H., Massling, A., Eriksson, A. C., Dall’Osto, M., Junninen, H., Sarnela, N., Lange, R., Collier, S., Zhang, Q., Cappa, C. D., and Nøjgaard, J. K.: Biogenic and anthropogenic sources of aerosols at the High Arctic site Villum Research Station, *Atmospheric Chemistry and Physics*, 19, 10 239–10 256, <https://doi.org/10.5194/acp-19-10239-2019>, 2019.
- Nomokonova, T., Ebell, K., Löhnert, U., Maturilli, M., Ritter, C., and O’Connor, E.: Statistics on clouds and their relation to thermodynamic conditions at Ny-Ålesund using ground-based sensor synergy, *Atmospheric Chemistry and Physics*, 19, 4105–4126, <https://doi.org/10.5194/acp-19-4105-2019>, 2019.
- Nomokonova, T., Ebell, K., Löhnert, U., Maturilli, M., and Ritter, C.: The influence of water vapor anomalies on clouds and their radiative effect at Ny-Ålesund, *Atmospheric Chemistry and Physics*, 20, 5157–5173, <https://doi.org/10.5194/acp-20-5157-2020>, 2020.
- Norwegian Polar Institute: Kartdata Svalbard 1:100 000 (S100 Kartdata) / Map Data, <https://doi.org/10.21334/npolar.2014.645336c7>, 2014.
- Ohata, S., Mori, T., Kondo, Y., Sharma, S., Hyvärinen, A., Andrews, E., Tunved, P., Asmi, E., Backman, J., Servomaa, H., Veber, D., Eleftheriadis, K., Vratolis, S., Koike, M., Kanaya, Y., Yoshida, A., Moteki, N., Zhao, Y., Tobo, Y., Matsushita, J., and Oshima, N.: Estimates

- of mass absorption cross sections of black carbon for filter-based absorption photometers in the Arctic, *Atmospheric Measurement Techniques Discussions*, 2021, 1–46, <https://doi.org/10.5194/amt-2021-166>, 2021.
- Paglione, M., Saarikoski, S., Carbone, S., Hillamo, R., Facchini, M. C., Finessi, E., Giulianelli, L., Carbone, C., Fuzzi, S., Moretti, F., Tagliavini, E., Swietlicki, E., Eriksson Stenström, K., Prévôt, A. S. H., Massoli, P., Canaragatna, M., Worsnop, D., and Decesari, S.: Primary and secondary biomass burning aerosols determined by proton nuclear magnetic resonance ( $^1\text{H-NMR}$ ) spectroscopy during the 2008 EUCAARI campaign in the Po Valley (Italy), *Atmospheric Chemistry and Physics*, 14, 5089–5110, <https://doi.org/10.5194/acp-14-5089-2014>, 2014.
- Park, H.-S., Lee, S., Son, S.-W., Feldstein, S. B., and Kosaka, Y.: The Impact of Poleward Moisture and Sensible Heat Flux on Arctic Winter Sea Ice Variability, *Journal of Climate*, 28, 5030 – 5040, <https://doi.org/10.1175/JCLI-D-15-0074.1>, 2015.
- Pasquier, J. T., David, R. O., Freitas, G., Gierens, R., Gramlich, Y., Haslett, S., and et al.: The Ny-Ålesund Aerosol Cloud Experiment (NASCENT): Overview and First Results, *Bulletin of the American Meteorological Society*, in review, 2021.
- Pasquier, J. T., Henneberger, J., Ramelli, F., Korolev, A., Wieder, J., Lauber, A., Li, G., David, R. O., Carlsen, T., Gierens, R., Maturilli, M., and Lohmann, U.: Understanding the history of complex ice crystal habits deduced from a holographic imager, *Geophysical Research Letters*, in prep, 2022a.
- Pasquier, J. T., Henneberger, J., Ramelli, F., Wieder, J., Lauber, A., Li, G., David, R. O., Carlsen, T., Gierens, R., Maturilli, M., and Lohmann, U.: Conditions favorable for secondary ice production in Arctic mixed-phase clouds, *Atmospheric Chemistry and Physics*, in prep, 2022b.
- Petters, M. D. and Wright, T. P.: Revisiting ice nucleation from precipitation samples, *Geophysical Research Letters*, 42, 8758–8766, <https://doi.org/https://doi.org/10.1002/2015GL065733>, 2015.
- Petty, G.: *A First Course in Atmospheric Radiation*, 2nd Edition, Sundog Publishing, Madison, Wisconsin, 2006.
- Petzold, A. and Schönlinner, M.: Multi-angle absorption photometry—a new method for the measurement of aerosol light absorption and atmospheric black carbon, *J. Aerosol Sci.*, 35, 421–441, 2004.
- Petzold, A., Ogren, J. A., Fiebig, M., Laj, P., Li, S.-M., Baltensperger, U., Holzer-Popp, T., Kinne, S., Pappalardo, G., Sugimoto, N., Wehrli, C., Wiedensohler, A., and Zhang, X.-Y.: Recommendations for reporting "black carbon" measurements, *Atmospheric Chemistry and Physics*, 13, 8365–8379, <https://doi.org/10.5194/acp-13-8365-2013>, 2013.
- Pinto, J.: Autumnal Mixed-Phase Cloudy Boundary Layers in the Arctic, *Journal of the Atmospheric Sciences*, 55, 2016–2038, [https://doi.org/10.1175/1520-0469\(1998\)055<2016:AMPCBL>2.0.CO;2](https://doi.org/10.1175/1520-0469(1998)055<2016:AMPCBL>2.0.CO;2), 1998.
- Pithan, F. and Mauritsen, T.: Arctic amplification dominated by temperature feedbacks in contemporary climate models, *Nature Geoscience*, 7, 181–184, <https://doi.org/10.1038/ngeo2071>, 2014.
- Platt, S. M., Hov, O., Berg, T., Breivik, K., Eckhardt, S., Eleftheriadis, K., Evangeliou, N., Fiebig, M., Fisher, R., Hansen, G., Hansson, H.-C., Heintzenberg, J., Hermansen, O., Heslin-Rees, D., Holmén, K., Hudson, S., Kallenborn, R., Krejci, R., Krognnes, T., Larssen, S., Lowry, D., Lund Myhre, C., Lunder, C., Nisbet, E., Nizetto, P. B., Park, K.-T., Pedersen, C. A., Aspö Pfaffhuber, K., Röckmann, T., Schmidbauer, N., Solberg, S., Stohl, A., Ström, J., Svendby, T., Tunved, P., Tørnkvist, K., van der Veen, C., Vratolis, S., Yoon, Y. J., Yttri, K. E., Zieger, P., Aas, W., and Tørseth, K.: Atmospheric composition in the European Arctic and 30 years of the Zeppelin Observatory, Ny-Ålesund, *Atmospheric Chemistry and*

- Physics Discussions, pp. 1–80, <https://doi.org/10.5194/acp-2021-505>, publisher: Copernicus GmbH, 2021.
- Possner, A., Ekman, A. M. L., and Lohmann, U.: Cloud response and feedback processes in stratiform mixed-phase clouds perturbed by ship exhaust, *Geophysical Research Letters*, 44, 1964–1972, <https://doi.org/10.1002/2016GL071358>, 2017.
- Proske, U., Bessenbacher, V., Dedekind, Z., Lohmann, U., and Neubauer, D.: How frequent is natural cloud seeding from ice cloud layers ( $< -35\text{ }^{\circ}\text{C}$ ) over Switzerland?, *Atmospheric Chemistry and Physics*, 21, 5195–5216, <https://doi.org/10.5194/acp-21-5195-2021>, 2021.
- Pruppacher, H. and Klett, J.: *Microphysics of Clouds and Precipitation*, Springer, <https://doi.org/10.1007/978-0-306-48100-0>, 2010.
- Quinn, P., Shaw, G., Andrews, E., Dutton, E., Ruoho-Airola, T., and Gong, S.: Arctic haze: current trends and knowledge gaps, *Tellus B*, 59, 99–114, 2007.
- Radenz, M., Bühl, J., Seifert, P., Griesche, H., and Engelmann, R.: peakTree: a framework for structure-preserving radar Doppler spectra analysis, *Atmospheric Measurement Techniques*, 12, 4813–4828, <https://doi.org/10.5194/amt-12-4813-2019>, 2019.
- Ramelli, F., Beck, A., Henneberger, J., and Lohmann, U.: Using a holographic imager on a tethered balloon system for microphysical observations of boundary layer clouds, *Atmospheric Measurement Techniques*, 13, 925–939, <https://doi.org/10.5194/amt-13-925-2020>, 2020.
- Ramelli, F., Henneberger, J., David, R. O., Bühl, J., Radenz, M., Seifert, P., Wieder, J., Lauber, A., Pasquier, J. T., Engelmann, R., Mignani, C., Hervo, M., and Lohmann, U.: Microphysical investigation of the seeder and feeder region of an Alpine mixed-phase cloud, *Atmospheric Chemistry and Physics*, 21, 6681–6706, <https://doi.org/10.5194/acp-21-6681-2021>, 2021a.
- Ramelli, F., Henneberger, J., David, R. O., Lauber, A., Pasquier, J. T., Wieder, J., Bühl, J., Seifert, P., Engelmann, R., Hervo, M., and Lohmann, U.: Influence of low-level blocking and turbulence on the microphysics of a mixed-phase cloud in an inner-Alpine valley, *Atmospheric Chemistry and Physics*, 21, 5151–5172, <https://doi.org/10.5194/acp-21-5151-2021>, 2021b.
- Rangno, A. L. and Hobbs, P. V.: Ice particles in stratiform clouds in the Arctic and possible mechanisms for the production of high ice concentrations, *Journal of Geophysical Research: Atmospheres*, 106, 15 065–15 075, <https://doi.org/10.1029/2000JD900286>, 2001.
- Rauber, R. M. and Tokay, A.: An Explanation for the Existence of Supercooled Water at the Top of Cold Clouds, *Journal of Atmospheric Sciences*, 48, 1005 – 1023, [https://doi.org/10.1175/1520-0469\(1991\)048<1005:AEFTEO>2.0.CO;2](https://doi.org/10.1175/1520-0469(1991)048<1005:AEFTEO>2.0.CO;2), 1991.
- Reutter, P., Su, H., Trentmann, J., Simmel, M., Rose, D., Gunthe, S. S., Wernli, H., Andreae, M. O., and Pöschl, U.: Aerosol- and updraft-limited regimes of cloud droplet formation: influence of particle number, size and hygroscopicity on the activation of cloud condensation nuclei (CCN), *Atmospheric Chemistry and Physics*, 9, 7067–7080, <https://doi.org/10.5194/acp-9-7067-2009>, 2009.
- Rinaldi, M., Emblico, L., Decesari, S., Fuzzi, S., Facchini, M. C., and Librando, V.: Chemical Characterization and Source Apportionment of Size-Segregated Aerosol Collected at an Urban Site in Sicily, *Water, Air, and Soil Pollution*, 185, 311–321, <https://doi.org/10.1007/s11270-007-9455-4>, 2007.
- Rinaldi, M., Santachiara, G., Nicosia, A., Piazza, M., Decesari, S., Gilardoni, S., Paglione, M., Cristofanelli, P., Marinoni, A., Bonasoni, P., and Belosi, F.: Atmospheric Ice Nucleating Particle measurements at the high mountain observatory Mt. Cimone (2165 m a.s.l., Italy), *Atmospheric Environment*, 171, 173–180, <https://doi.org/https://doi.org/10.1016/j.atmosenv.2017.10.027>, 2017.
- Rinaldi, M., Hiranuma, N., Santachiara, G., Mazzola, M., Mansour, K., Paglione, M., Rodriguez, C. A., Traversi, R., Becagli, S., Cappelletti, D., and Belosi, F.: Ice-nucleating particle concentration measurements from Ny-Ålesund during the Arctic spring–summer in 2018, *Atmospheric Chemistry and Physics*, 21, 14 725–14 748, <https://doi.org/10.5194/acp-21-14725-2021>, 2021.



- Roberts, G. C. and Nenes, A.: A Continuous-Flow Streamwise Thermal-Gradient CCN Chamber for Atmospheric Measurements, *Aerosol Science and Technology*, 39, 206–221, <https://doi.org/10.1080/027868290913988>, 2005.
- Rogers, R. R. and Yau, M. K.: *A short course in cloud physics*, Pergamon, 1989.
- Rosenfeld, D. and Woodley, W. L.: Deep convective clouds with sustained supercooled liquid water down to  $-37.5^{\circ}\text{C}$ , *Nature*, 405, 440–442, <https://doi.org/10.1038/35013030>, 2000.
- Ruske, S., Topping, D. O., Foot, V. E., Kaye, P. H., Stanley, W. R., Crawford, I., Morse, A. P., and Gallagher, M. W.: Evaluation of machine learning algorithms for classification of primary biological aerosol using a new UV-LIF spectrometer, *Atmos. Meas. Tech.*, 10, 695–708, <https://doi.org/10.5194/amt-10-695-2017>, 2017.
- Santachiara, G., Di Matteo, L., Prodi, F., and Belosi, F.: Atmospheric particles acting as Ice Forming Nuclei in different size ranges, *Atmospheric Research*, 96, 266–272, <https://doi.org/https://doi.org/10.1016/j.atmosres.2009.08.004>, 15th International Conference on Clouds and Precipitation, 2010.
- Santander, M. V., Mitts, B. A., Pendergraft, M. A., Dinasquet, J., Lee, C., Moore, A. N., Cancelada, L. B., Kimble, K. A., Malfatti, F., and Prather, K. A.: Tandem Fluorescence Measurements of Organic Matter and Bacteria Released in Sea Spray Aerosols, *Environmental Science & Technology*, 55, 5171–5179, <https://doi.org/10.1021/acs.est.0c05493>, PMID: 33755426, 2021.
- Schacht, J., Heinold, B., Quaas, J., Backman, J., Cherian, R., Ehrlich, A., Herber, A., Huang, W. T. K., Kondo, Y., Massling, A., Sinha, P. R., Weinzierl, B., Zannata, M., and Tegen, I.: The importance of the representation of air pollution emissions for the modeled distribution and radiative effects of black carbon in the Arctic, *Atmospheric Chemistry and Physics*, 19, 11 159–11 183, <https://doi.org/10.5194/acp-19-11159-2019>, 2019.
- Schlenczek, O.: *Airborne and Ground-based Holographic Measurement of Hydrometeors in Liquid-phase, Mixed-phase and Ice Clouds*, Ph.D. thesis, Universitätsbibliothek Mainz, 2018.
- Schmale, J., Baccharini, A., Thurnherr, I., Henning, S., Efraim, A., Regayre, L., Bolas, C., Hartmann, M., Welti, A., Lehtipalo, K., Aemisegger, F., Tatzelt, C., Landwehr, S., Modini, R. L., Tummon, F., Johnson, J. S., Harris, N., Schnaiter, M., Toffoli, A., Derkani, M., Bukowiecki, N., Stratmann, F., Dommen, J., Baltensperger, U., Wernli, H., Rosenfeld, D., Gysel-Beer, M., and Carslaw, K. S.: Overview of the Antarctic Circumnavigation Expedition: Study of Preindustrial-like Aerosols and Their Climate Effects (ACE-SPACE), *Bulletin of the American Meteorological Society*, 100, 2260–2283, <https://doi.org/10.1175/BAMS-D-18-0187.1>, 2019.
- Schmale, J., Zieger, P., and Ekman, A.: Aerosols in current and future Arctic climate, *Nat. Clim. Chang.*, 11, 95–105, <https://doi.org/10.1038/s41558-020-00969-5>, 2021.
- Schrod, J., Weber, D., Drücke, J., Keleshis, C., Pikridas, M., Ebert, M., Cvetković, B., Nickovic, S., Marinou, E., Baars, H., Ansmann, A., Vrekoussis, M., Mihalopoulos, N., Sciare, J., Curtius, J., and Bingemer, H. G.: Ice nucleating particles over the Eastern Mediterranean measured by unmanned aircraft systems, *Atmospheric Chemistry and Physics*, 17, 4817–4835, <https://doi.org/10.5194/acp-17-4817-2017>, 2017.
- Schwarz, J. P., Gao, R. S., Fahey, D. W., Thomson, D. S., Watts, L. A., Wilson, J. C., Reeves, J. M., Darbeheshti, M., Baumgardner, D. G., Kok, G. L., Chung, S. H., Schulz, M., Hendricks, J., Lauer, A., Kärcher, B., Slowik, J. G., Rosenlof, K. H., Thompson, T. L., Langford, A. O., Loewenstein, M., and Aikin, K. C.: Single-particle measurements of midlatitude black carbon and light-scattering aerosols from the boundary layer to the lower stratosphere, *Journal of Geophysical Research: Atmospheres*, 111, <https://doi.org/10.1029/2006JD007076>, 2006.
- Screen, J. A. and Simmonds, I.: The central role of diminishing sea ice in recent Arctic temperature amplification, *Nature*, 464, 1334–1337, <https://doi.org/10.1038/nature09051>, 2010.
- Sedlar, J., Shupe, M. D., and Tjernström, M.: On the Relationship between Thermodynamic Structure and Cloud Top, and Its Climate Significance in the Arctic, *Journal of Climate*, 25, 2374 – 2393, <https://doi.org/10.1175/JCLI-D-11-00186.1>, 2012.
- Serreze, M. C., Barrett, A. P., Stroeve, J. C., Kindig, D. N., and Holland, M. M.: The

- emergence of surface-based Arctic amplification, *The Cryosphere*, 3, 11–19, <https://doi.org/10.5194/tc-3-11-2009>, 2009.
- Shank, L. M., Howell, S., Clarke, A. D., Freitag, S., Brekhovskikh, V., Kapustin, V., McNaughton, C., Campos, T., and Wood, R.: Organic matter and non-refractory aerosol over the remote Southeast Pacific: oceanic and combustion sources, *Atmos. Chem. Phys.*, 12, 557–576, <https://doi.org/10.5194/acp-12-557-2012>, 2012.
- Shaw, G. E.: The Arctic haze phenomenon, *Bulletin of the American Meteorological Society*, 76, 2403–2414, 1995.
- Shingler, T., Dey, S., Sorooshian, A., Brechtel, F. J., Wang, Z., Metcalf, A., Coggon, M., Müllmenstädt, J., Russell, L. M., Jonsson, H. H., and Seinfeld, J. H.: Characterisation and airborne deployment of a new counterflow virtual impactor inlet, *Atmos. Meas. Tech.*, 5, 1259–1269, <https://doi.org/10.5194/amt-5-1259-2012>, 2012.
- Shupe, M. D. and Intrieri, J. M.: Cloud Radiative Forcing of the Arctic Surface: The Influence of Cloud Properties, Surface Albedo, and Solar Zenith Angle, *Journal of Climate*, 17, 616–628, [https://doi.org/10.1175/1520-0442\(2004\)017<0616:CRFOTA>2.0.CO;2](https://doi.org/10.1175/1520-0442(2004)017<0616:CRFOTA>2.0.CO;2), 2004.
- Shupe, M. D., Matrosov, S. Y., and Uttal, T.: Arctic Mixed-Phase Cloud Properties Derived from Surface-Based Sensors at SHEBA, *Journal of the Atmospheric Sciences*, 63, 697–711, <https://doi.org/10.1175/JAS3659.1>, 2006.
- Shupe, M. D., Daniel, J. S., de Boer, G., Eloranta, E. W., Kollias, P., Long, C. N., Luke, E. P., Turner, D. D., and Verlinde, J.: A Focus On Mixed-Phase Clouds, *Bulletin of the American Meteorological Society*, 89, 1549–1562, <https://doi.org/10.1175/2008BAMS2378.1>, 2008a.
- Shupe, M. D., Kollias, P., Poellot, M., and Eloranta, E.: On deriving vertical air motions from cloud radar Doppler spectra, *Journal of Atmospheric and Oceanic Technology*, 25, 547–557, 2008b.
- Silber, I., Fridlind, A. M., Verlinde, J., Ackerman, A. S., Chen, Y.-S., Bromwich, D. H., Wang, S.-H., Cadeddu, M., and Eloranta, E. W.: Persistent Supercooled Drizzle at Temperatures Below  $-25^{\circ}\text{C}$  Observed at McMurdo Station, Antarctica, *Journal of Geophysical Research: Atmospheres*, 124, 10 878–10 895, <https://doi.org/https://doi.org/10.1029/2019JD030882>, 2019.
- Sinha, P. R., Kondo, Y., Koike, M., Ogren, J. A., Jefferson, A., Barrett, T. E., Sheesley, R. J., Ohata, S., Moteki, N., Coe, H., Liu, D., Irwin, M., Tunved, P., Quinn, P. K., and Zhao, Y.: Evaluation of ground-based black carbon measurements by filter-based photometers at two Arctic sites, *Journal of Geophysical Research: Atmospheres*, 122, 3544–3572, <https://doi.org/https://doi.org/10.1002/2016JD025843>, 2017.
- Skamarock, W. C., Klemp, J. B., Dudhia, J., Gill, D. O., Liu, Z., Berner, J., Wang, W., Powers, J. G., Duda, M. G., Barker, D. M., et al.: A description of the advanced research WRF model version 4, National Center for Atmospheric Research: Boulder, CO, USA, p. 145, 2019.
- Solomon, A., Feingold, G., and Shupe, M. D.: The role of ice nuclei recycling in the maintenance of cloud ice in Arctic mixed-phase stratocumulus, *Atmospheric Chemistry and Physics*, 15, 10 631–10 643, <https://doi.org/10.5194/acp-15-10631-2015>, 2015.
- Sotiropoulou, G., Sullivan, S., Savre, J., Lloyd, G., Lachlan-Cope, T., Ekman, A. M. L., and Nenes, A.: The impact of secondary ice production on Arctic stratocumulus, *Atmospheric Chemistry and Physics*, 20, 1301–1316, <https://doi.org/10.5194/acp-20-1301-2020>, 2020.
- Stapf, J., Ehrlich, A., Jäkel, E., Lüpkes, C., and Wendisch, M.: Reassessment of shortwave surface cloud radiative forcing in the Arctic: consideration of surface-albedo–cloud interactions, *Atmospheric Chemistry and Physics*, 20, 9895–9914, <https://doi.org/10.5194/acp-20-9895-2020>, 2020.
- Stephens, M., Turner, N., and Sandberg, J.: Particle identification by laser-induced incandescence in a solid-state laser cavity, *Applied Optics*, 42, 3726, <https://doi.org/10.1364/AO.42.003726>, 2003.
- Stohl, A.: Characteristics of atmospheric transport into the Arctic troposphere, *Journal of*

- Geophysical Research: Atmospheres, 111, <https://doi.org/10.1029/2005JD006888>, \_eprint: <https://agupubs.onlinelibrary.wiley.com/doi/pdf/10.1029/2005JD006888>, 2006.
- Stohl, A., Berg, T., Burkhardt, J. F., Fjaraa, A. M., Forster, C., Herber, A., Hov, Ø., Lunder, C., McMillan, W. W., Oltmans, S., Shiobara, M., Simpson, D., Solberg, S., Stebel, K., Ström, J., Tørseth, K., Treffeisen, R., Virkkunen, K., and Yttri, K. E.: Arctic smoke — record high air pollution levels in the European Arctic due to agricultural fires in Eastern Europe in spring 2006, *Atmospheric Chemistry and Physics*, 7, 511–534, <https://doi.org/10.5194/acp-7-511-2007>, 2007.
- Ström, J., Umegård, J., Tørseth, K., Tunved, P., Hansson, H., Holmén, K., Wismann, V., Herber, A., and König-Langlo, G.: One year of particle size distribution and aerosol chemical composition measurements at the Zeppelin Station, Svalbard, March 2000-March 2001, *Phys. Chem. Earth*, 28, 1181–1190, 2003.
- Sun, Z. and Shine, K. P.: Studies of the radiative properties of ice and mixed-phase clouds, *Quarterly Journal of the Royal Meteorological Society*, 120, 111–137, <https://doi.org/10.1002/qj.49712051508>, 1994.
- Susskind, J., Schmidt, G. A., Lee, J. N., and Iredell, L.: Recent global warming as confirmed by AIRS, *Environmental Research Letters*, 14, 044030, <https://doi.org/10.1088/1748-9326/aafd4e>, 2019.
- Takahashi, C. and Yamashita, A.: Shattering of Frozen Water Drops in a Supercooled Cloud, *Journal of the Meteorological Society of Japan. Ser. II*, 48, 373–376, [https://doi.org/10.2151/jmsj1965.48.4\\_373](https://doi.org/10.2151/jmsj1965.48.4_373), 1970.
- Takahashi, T., Nagao, Y., and Kushiyama, Y.: Possible High Ice Particle Production during Graupel–Graupel Collisions, *Journal of the Atmospheric Sciences*, 52, 4523–4527, [https://doi.org/10.1175/1520-0469\(1995\)052<4523:PHIPPD>2.0.CO;2](https://doi.org/10.1175/1520-0469(1995)052<4523:PHIPPD>2.0.CO;2), 1995.
- Thornton, J. A., Mohr, C., Schobesberger, S., D’Ambro, E. L., Lee, B. H., and Lopez-Hilfiker, F. D.: Evaluating Organic Aerosol Sources and Evolution with a Combined Molecular Composition and Volatility Framework Using the Filter Inlet for Gases and Aerosols (FIGAERO), *Accounts of Chemical Research*, 53, 1415–1426, <https://doi.org/10.1021/acs.accounts.0c00259>, 2020.
- Tjernström, M., Leck, C., Birch, C. E., Bottenheim, J. W., Brooks, B. J., Brooks, I. M., Bäcklin, L., Chang, R. Y.-W., de Leeuw, G., Di Liberto, L., de la Rosa, S., Granath, E., Graus, M., Hansel, A., Heintzenberg, J., Held, A., Hind, A., Johnston, P., Knulst, J., Martin, M., Matrai, P. A., Mauritsen, T., Müller, M., Norris, S. J., Orellana, M. V., Orsini, D. A., Paatero, J., Persson, P. O. G., Gao, Q., Rauschenberg, C., Ristovski, Z., Sedlar, J., Shupe, M. D., Sierau, B., Sirevaag, A., Sjogren, S., Stetzer, O., Swietlicki, E., Szczodrak, M., Vaattovaara, P., Wahlberg, N., Westberg, M., and Wheeler, C. R.: The Arctic Summer Cloud Ocean Study (ASCOS): overview and experimental design, *Atmospheric Chemistry and Physics*, 14, 2823–2869, <https://doi.org/10.5194/acp-14-2823-2014>, 2014.
- Tobo, Y.: An improved approach for measuring immersion freezing in large droplets over a wide temperature range, *Scientific Reports*, 6, 32930, <https://doi.org/10.1038/srep32930>, 2016.
- Tobo, Y., Adachi, K., DeMott, P. J., Hill, T. C. J., Hamilton, D. S., Mahowald, N. M., Nagatsuka, N., Ohata, S., Uetake, J., Kondo, Y., and Koike, M.: Glacially sourced dust as a potentially significant source of ice nucleating particles, *Nature Geoscience*, 12, 253–258, <https://doi.org/10.1038/s41561-019-0314-x>, 2019.
- Tobo, Y., Uetake, J., Matsui, H., Moteki, N., Uji, Y., Iwamoto, Y., Miura, K., and Misumi, R.: Seasonal Trends of Atmospheric Ice Nucleating Particles Over Tokyo, *Journal of Geophysical Research: Atmospheres*, 125, e2020JD033658, <https://doi.org/https://doi.org/10.1029/2020JD033658>, e2020JD033658 2020JD033658-T, 2020.
- Touloupas, G., Lauber, A., Henneberger, J., Beck, A., and Lucchi, A.: A convolutional neural network for classifying cloud particles recorded by imaging probes, *Atmospheric Measurement Techniques*, 13, 2219–2239, <https://doi.org/10.5194/amt-13-2219-2020>, 2020.

- Tunved, P., Ström, J., and Krejci, R.: Arctic aerosol life cycle: linking aerosol size distributions observed between 2000 and 2010 with air mass transport and precipitation at Zeppelin station, Ny-Ålesund, Svalbard, *Atmos. Chem. Phys.*, 13, 3643–3660, <https://doi.org/10.5194/acp-13-3643-2013>, 2013.
- Turetta, C., Feltracco, M., Barbaro, E., Spolaor, A., Barbante, C., and Gambaro, A.: A Year-Round Measurement of Water-Soluble Trace and Rare Earth Elements in Arctic Aerosol: Possible Inorganic Tracers of Specific Events, *Atmosphere*, 12, <https://doi.org/10.3390/atmos12060694>, 2021.
- Udisti, R., Bazzano, A., Becagli, S., Bolzacchini, E., Caiazzo, L., Cappelletti, D., Ferrero, L., Frosini, D., Giardi, F., Grotti, M., Lupi, A., Malandrino, M., Mazzola, M., Moroni, B., Severi, M., Traversi, R., Viola, A., and Vitale, V.: Sulfate source apportionment in the Ny-Ålesund (Svalbard Islands) Arctic aerosol, *Rendiconti Lincei*, 27, 85–94, <https://doi.org/10.1007/s12210-016-0517-7>, 2016.
- Vali, G.: Quantitative Evaluation of Experimental Results on the Heterogeneous Freezing Nucleation of Supercooled Liquids, *Journal of Atmospheric Sciences*, 28, 402 – 409, [https://doi.org/10.1175/1520-0469\(1971\)028<0402:QEOERA>2.0.CO;2](https://doi.org/10.1175/1520-0469(1971)028<0402:QEOERA>2.0.CO;2), 1971.
- Vardiman, L.: The Generation of Secondary Ice Particles in Clouds by Crystal–Crystal Collision, *Journal of Atmospheric Sciences*, 35, 2168 – 2180, [https://doi.org/10.1175/1520-0469\(1978\)035<2168:TGOSIP>2.0.CO;2](https://doi.org/10.1175/1520-0469(1978)035<2168:TGOSIP>2.0.CO;2), 1978.
- Vassel, M., Ickes, L., Maturilli, M., and Hoose, C.: Classification of Arctic multilayer clouds using radiosonde and radar data in Svalbard, *Atmospheric Chemistry and Physics*, 19, 5111–5126, <https://doi.org/10.5194/acp-19-5111-2019>, 2019.
- Verheggen, B., Cozic, J., Weingartner, E., Bower, K., Mertes, S., Connolly, P., Gallagher, M., Flynn, M., Choulaton, T., and Baltensperger, U.: Aerosol partitioning between the interstitial and the condensed phase in mixed-phase clouds, *Journal of Geophysical Research: Atmospheres*, 112, 2007.
- Virkkula, A., Ahlquist, N. C., Covert, D. S., Arnott, W. P., Sheridan, P. J., Quinn, P. K., and Coffman, D. J.: Modification, Calibration and a Field Test of an Instrument for Measuring Light Absorption by Particles, *Aerosol Science and Technology*, 39, 68–83, <https://doi.org/10.1080/027868290901963>, 2005.
- Wang, P. K.: *Physics and Dynamics of Clouds and Precipitation*, Cambridge University Press, <https://doi.org/10.1017/CBO9780511794285>, 2013.
- Wegener, A.: *Thermodynamik der Atmosphäre*, Barth, Leipzig, Germany, 1911.
- Weinbruch, S., Wiesemann, D., Ebert, M., Schütze, K., Kallenborn, R., and Ström, J.: Chemical composition and sources of aerosol particles at Zeppelin Mountain (Ny Ålesund, Svalbard): An electron microscopy study, *Atmospheric Environment*, 49, 142–150, 2012.
- Wendisch, M., Brückner, M., Burrows, J. P., Crewell, S., Dethloff, K., Lüpkes, C., Macke, A., Notholt, J., Quaas, J., Rinke, A., and Tegen, I.: Understanding causes and effects of rapid warming in the Arctic, *EOS*, 98, 22–26, <https://doi.org/10.1029/2017EO064803>, 2017.
- Wendisch, M., Macke, A., Ehrlich, A., Lüpkes, C., Mech, M., Chechin, D., Dethloff, K., Velasco, C. B., Bozem, H., Brückner, M., Clemen, H.-C., Crewell, S., Donth, T., Dupuy, R., Ebell, K., Egerer, U., Engelmann, R., Engler, C., Eppers, O., Gehrman, M., Gong, X., Gottschalk, M., Goubeyre, C., Griesche, H., Hartmann, J., Hartmann, M., Heinold, B., Herber, A., Herrmann, H., Heygster, G., Hoor, P., Jafariserajehlou, S., Jäkel, E., Järvinen, E., Jourdan, O., Kästner, U., Kecorius, S., Knudsen, E. M., Köllner, F., Kretzschmar, J., Lelli, L., Leroy, D., Maturilli, M., Mei, L., Mertes, S., Mioche, G., Neuber, R., Nicolaus, M., Nomokonova, T., Notholt, J., Palm, M., van Pinxteren, M., Quaas, J., Richter, P., Ruiz-Donoso, E., Schäfer, M., Schmieder, K., Schnaiter, M., Schneider, J., Schwarzenböck, A., Seifert, P., Shupe, M. D., Siebert, H., Spreen, G., Stapf, J., Stratmann, F., Vogl, T., Welti, A., Wex, H., Wiedensohler, A., Zanatta, M., and Zeppenfeld, S.: The Arctic Cloud Puzzle: Using ALOUD/PASCAL Multiplatform Observations to Unravel the Role of Clouds and Aerosol Particles in Arctic

- Amplification, *Bulletin of the American Meteorological Society*, 100, 841–871, <https://doi.org/10.1175/BAMS-D-18-0072.1>, 2019.
- Wieder, J., Ihn, N., Mignani, C., Haarig, M., Bühl, J., Seifert, P., Engelmann, R., Ramelli, F., Kanji, Z. A., Lohmann, U., and Henneberger, J.: Retrieving ice nucleating particle concentration and ice multiplication factors using active remote sensing validated by in situ observations, *Atmospheric Chemistry and Physics Discussions*, 2022, 1–47, <https://doi.org/10.5194/acp-2022-67>, 2022a.
- Wieder, J., Mignani, C., Schär, M., Roth, L., Sprenger, M., Henneberger, J., Lohmann, U., Brunner, C., and Kanji, Z. A.: Unveiling atmospheric transport and mixing mechanisms of ice-nucleating particles over the Alps, *Atmospheric Chemistry and Physics*, 22, 3111–3130, <https://doi.org/10.5194/acp-22-3111-2022>, 2022b.
- Wieder, J., Mignani, C., Schär, M., Roth, L., Sprenger, M., Henneberger, J., Lohmann, U., Brunner, C., and Kanji, Z. A.: Unveiling atmospheric transport and mixing mechanisms of ice-nucleating particles over the Alps, *Atmospheric Chemistry and Physics*, 22, 3111–3130, <https://doi.org/10.5194/acp-22-3111-2022>, 2022c.
- Willis, M. D., Leaitch, W. R., and Abbatt, J. P.: Processes controlling the composition and abundance of Arctic aerosol, *Reviews of Geophysics*, 56, 621–671, 2018.
- Worringen, A., Kandler, K., Benker, N., Dirsch, T., Mertes, S., Schenk, L., Kästner, U., Frank, F., Nillius, B., Bundke, U., Rose, D., Curtius, J., Kupiszewski, P., Weingartner, E., Vochezer, P., Schneider, J., Schmidt, S., Weinbruch, S., and Ebert, M.: Single-particle characterization of ice-nucleating particles and ice particle residuals sampled by three different techniques, *Atmospheric Chemistry and Physics*, 15, 4161–4178, <https://doi.org/10.5194/acp-15-4161-2015>, 2015.
- Wyser, K.: Ice crystal habits and solar radiation, *Tellus A: Dynamic Meteorology and Oceanography*, 51, 937–950, <https://doi.org/10.3402/tellusa.v51i5.14503>, 1999.
- Yi, B., Yang, P., Baum, B. A., L’Ecuyer, T., Oreopoulos, L., Mlawer, E. J., Heymsfield, A. J., and Liou, K.-N.: Influence of Ice Particle Surface Roughening on the Global Cloud Radiative Effect, *Journal of the Atmospheric Sciences*, 70, 2794 – 2807, <https://doi.org/10.1175/JAS-D-13-020.1>, 2013.
- Young, G., Jones, H. M., Choulaton, T. W., Crosier, J., Bower, K. N., Gallagher, M. W., Davies, R. S., Renfrew, I. A., Elvidge, A. D., Darbyshire, E., Marengo, F., Brown, P. R. A., Ricketts, H. M. A., Connolly, P. J., Lloyd, G., Williams, P. I., Allan, J. D., Taylor, J. W., Liu, D., and Flynn, M. J.: Observed microphysical changes in Arctic mixed-phase clouds when transitioning from sea ice to open ocean, *Atmospheric Chemistry and Physics*, 16, 13945–13967, <https://doi.org/10.5194/acp-16-13945-2016>, 2016.
- Young, G., Lachlan-Cope, T., O’Shea, S. J., Dearden, C., Listowski, C., Bower, K. N., Choulaton, T. W., and Gallagher, M. W.: Radiative Effects of Secondary Ice Enhancement in Coastal Antarctic Clouds, *Geophysical Research Letters*, 46, 2312–2321, <https://doi.org/https://doi.org/10.1029/2018GL080551>, 2019.
- Zangrando, R., Barbaro, E., Zennaro, P., Rossi, S., Kehrwald, N. M., Gabrieli, J., Barbante, C., and Gambaro, A.: Molecular Markers of Biomass Burning in Arctic Aerosols, *Environmental Science & Technology*, 47, 8565–8574, <https://doi.org/10.1021/es400125r>, 2013.
- Zuidema, P., Baker, B., Han, Y., Intrieri, J., Key, J., Lawson, P., Matrosov, S., Shupe, M., Stone, R., and Uttal, T.: An Arctic Springtime Mixed-Phase Cloudy Boundary Layer Observed during SHEBA, *Journal of the Atmospheric Sciences*, 62, 160–176, <https://doi.org/10.1175/JAS-3368.1>, 2005a.
- Zuidema, P., Westwater, E. R., Fairall, C., and Hazen, D.: Ship-based liquid water path estimates in marine stratocumulus, *Journal of Geophysical Research: Atmospheres*, 110, <https://doi.org/https://doi.org/10.1029/2005JD005833>, 2005b.



# Acknowledgments

The successful completion of this PhD project would not have been possible without the contribution and support of many people. Specifically, I would like to thank:

- Ulrike Lohmann for providing me the opportunity to work on this unique research project, for trusting and supporting me during the organisation and accomplishment of the NASCENT campaign in Ny-Ålesund, and for her enthusiastic guidance throughout this project.
- Jan Henneberger for his scientific and technical support, for many scientific and non-scientific discussions, for the fun time during the RACLETS and NASCENT campaigns, and for being a great and enthusiastic supervisor.
- Alexis Berne for agreeing to be my external co-examiner and taking the time to read this thesis.
- Peter Isler and Hans-Heini Vogel for helping me with all my computer related requests and issues.
- Moni for helping with the organization of the NASCENT campaign and efficiently dealing with all the administrative tasks.
- Michael, for manufacturing some extra parts of HOLIMO3B, and especially, for digging out the winch from the snow with me in Ny-Ålesund.
- Paul, Claudia, Zamin, Jan, Radek, and Ulrike for giving me the opportunity to take the lead of the NASCENT overview paper.
- The team of the Swiss Common Center (SCC) with Rob, Tim, Jörg, and Guangyu for scientific and moral support during the campaigns and for helping performing the HoloB-alloon measurements in the dark, cold, windy, and wet environment in Ny-Ålesund. For the many evenings at the SCC and the amazing time in the northernmost settlement of the world.
- The Ny-Ålesund resident for the accepting us as part of their community during the campaigns and for dancing on the helicopter song with us.
- The AWIPEV team with Greg, Gwen, Fieke, Wilfried, and Ingo for their essential technical support, but also for the long evenings with or without sun in Ny-Ålesund and an unforgettable cabin trip. As well as Marion Maturilli and Roland Neuber for their support before and during the campaigns.
- The Kingsbay team, including Espen, Marine, Blix, Andrea, Svein-Harald, Christer, for their great technical support, their flexibility and the motivating working atmosphere in such a remote settlement.
- The NPI team with Christelle, Vera, Christer, Filip, Tor, Jon, and Helge for their help in organizing the NASCENT campaign, for monitoring HoloGondel at the Zeppelin and for



bringing me safe up and down the Zeppelin mountain with the smallest cable car I was ever in.

- Rosa Gierens and Kerstin Ebell for answering my questions related to remote sensing instrumentation with enthusiasm and helping with the interpretation of the remote sensing data.
- Fabi, Rob, Jörg, and Tim for their scientific inputs and constructive feedbacks, and for proofreading parts of this thesis.
- Annika and Fabiola for helping me to come around with the HoloSuite Software, but also for always having an open ear for me, and for all the good time spent together at the IAC, in Davos, or in many other places.
- Jörg, Guangyu, Kungfeng, Mayur, Anina, and Fabian, for having been such great office mates and for having made P11 such a nice working environment.
- The whole Atmospheric Physics group at IAC for the scientific support for a very friendly atmosphere. Especially Jörg the fun time spent together in the office, in Ny-Ålesund, or even in a strange Russian city. Cyril for scientific and non-scientific advises and for bringing me to the Jungfrauoch. Bernat for being the best unofficial member of the wolke group. Émilie for speaking about life in french and for proofreading my abstract. Colin for the spontaneous Feierabend evenings. Steffen for discussions at lunch or coffee times and the mountain trips. Anina for the great veggie evening. And all the other wolke members for the funny time during BBQs, group retreats, and lunch breaks.
- All my friends from Fribourg and Zurich for being here for me at any time in my life, supporting me in difficult times and cheering with me in good times. Especially Marina for the skitouring trips. Laura for being around in Zurich when it was most needed. Salome for always being emotionally synchronized with me. Marie, Christina & Elena for amazing trips and evenings. Audrey, Fanny, & Vinch for being around since childhood. Saskia for her craziness. Laura for her openness, spontaneity, and enthusiasm. The Schnappspatrouilleurs team as well as Fanny, Christina, and Laura for amazing races in the Alps. And many others!
- Mes neveux Matteo, Luca, Marco et Florent pour me faire beaucoup rire.
- Mes parents, Marie-Claire et Simon et mes frères Samuel, Bruno et Aurélien pour leur soutien durant toutes ces années, merci!
- Jonas, für sein offenes Ohr und seine hilfreiche Ratschläge wenn es Schwierigkeiten gab und sein Enthusiasmus wenn Sachen wieder gut gelaufen sind. Du warst eine riesige Unterstützung, danke!

# Julie Pasquier

## Curriculum Vitae

Forchstrasse 62

8008 Zurich

+41 76 307 71 16

✉ julie.pasquier@env.ethz.ch

Date of birth: 05.03.1993



## Education

- 09/2018 - 12/2021 **Doctoral Candidate**, *Institute for Atmospheric and Climate Science, ETHZ, Zurich*
- Title: "Towards solving the puzzle of ice crystal formation and growth in Arctic mixed-phase clouds"
  - Doctoral examination successfully defended on December 22, 2021
  - Supervision: Prof. Ulrike Lohmann & Dr. Jan Henneberger
  - Organisation and lead of two field campaigns (NASCENT) in Ny-Ålesund, Svalbard
  - Participation to the RACLETS campaign in Davos
  - Analysis and interpretation of holographic imager, remote sensing, and weather data
  - Writing of scientific publications including the overview paper of the NASCENT campaign
- 09/2015 - 10/2017 **Master in Environmental Sciences**, *ETHZ, Zurich, Final grade – 5.27*
- Major in Atmospheric and Climate Science
- 11/2016 - 12/2016 **Antarctic Circumnavigation Expedition (ACE) Maritime University**, *Swiss Polar Institute & Russian Geographic Society, Akademik Treshnikov*
- 01/2015 - 06/2015 **Semester Abroad**, *Lancaster University, Lancaster, England*
- 09/2012 - 06/2015 **Bachelor in Environmental Sciences**, *ETHZ, Zurich, Final grade – 5.02*
- Specialisation in Atmospheric and Climate Science
- 08/2008 - 07/2012 **High-school**, *College St-Michel, Fribourg*

## Work Experience

- 2018 – 2020 **Teaching Assistant**, *Atmospheric Physics Group, Institute for Atmospheric and Climate Science, ETHZ*
- Cloud microphysics course (MSc level) & Cloud dynamics course (MSc level)
  - Supervision of a Bachelor thesis
- 06/2017 - 05/2018 **Internship**, *Federal Office of Meteorology and Climatology MeteoSwiss, Payerne & Zurich Airport.*
- Performed project on the automation of the cloud cover detection with remote sensing
- 10/2015 - 12/2015 **Research Assistant**, *Atmospheric Dynamics Group, Institute for Atmospheric and Climate Science, ETHZ*
- Analysis and interpretation of satellite imagery & determination of weather regimes over the North Atlantic

## Engagement

- 2020 - 2022 **Early Career Researcher Representative**, *FORCeS Project*
- Organisation of annual meeting 2021 and communication with FORCeS executive boards
- 2019 **Girlsday Organisation Lead**, *Institute for Atmospheric and Climate Science, ETHZ*
- Organisation of laboratory experiments for children in the framework of the "Ferienplausch" by Projuventute
- 2011 – 2017 **Artistic Gymnastics Coach**, *Freiburgia, Fribourg*

## Skills

- Computer Advanced: MATLAB, L<sup>A</sup>T<sub>E</sub>X, MS Office and InDesign. Intermediate: Git, R, PYTHON, Linux, LabVIEW, Javascript, HTML, ArcGIS, NCL. Basic: C++, ODV.
- Languages French (native), German (fluent), English (fluent)
- Hobbies Trail-running, skitouring, climbing, artistic gymnastics, violin

## Peer Reviewed Publications

**Pasquier J. T.**, Henneberger J., Ramelli F., Lauber A., David R. O., Wieder J. et al.: Conditions favorable for secondary ice production in Arctic mixed-phase clouds. *Atmospheric Chemistry and Physics Discussion*. [preprint], <https://doi.org/10.5194/acp-2022-314>, in review, 2022.

**Pasquier J. T.**, David R. O., Freitas G., Gierens R., Gramlich Y., Haslett S. et al.: The Ny-Ålesund Aerosol Cloud Experiment (NASCENT): Overview and First Results. *Bulletin of the American Meteorological Society*, in review, 2022.

**Pasquier J. T.**, Henneberger J., Korolev A., Ramelli F., Wieder J., Lauber A. et al.: Understanding the history of complex ice crystal habits deduced from a holographic imager. *Geophysical Research Letters*, in prep, 2022.

Li G., Wieder J., **Pasquier J. T.**, Henneberger J., Kanji Z. A.: Predicting atmospheric background number concentration of ice nucleating particles in the Arctic, *Atmospheric Chemistry and Physics Discussion*. [preprint], <https://doi.org/10.5194/acp-2022-21>, in review, 2022.

Ramelli F., Henneberger J., David R. O., Lauber A., **Pasquier J. T.**, Wieder J., Bühl J., Seifert P., Engelmann R., Hervo M., and Lohmann U. (2021). Influence of low-level blocking and turbulence on the microphysics of a mixed-phase cloud in an inner-Alpine valley. *Atmospheric Chemistry and Physics*, 21, 5151–5172, <https://doi.org/10.5194/acp-21-5151-2021>

Ramelli F., Henneberger J., David R. O., Bühl J., Radenz M., Seifert P., Wieder J., Lauber A., **Pasquier J. T.**, Engelmann R., Mignani C., Hervo M., and Lohmann U. (2021). Microphysical investigation of the seeder and feeder region of an Alpine mixed-phase cloud. *Atmospheric Chemistry and Physics*, 21, 6681–6706, <https://doi.org/10.5194/acp-21-6681-2021>

Lauber A., Henneberger J., Mignani C., Ramelli F., **Pasquier J. T.**, Wieder J., Hervo M., and Lohmann U. (2021). Continuous secondary-ice production initiated by updrafts through the melting layer in mountainous regions. *Atmospheric Chemistry and Physics*, 21, 3855–3870, <https://doi.org/10.5194/acp-21-3855-2021>

**Pasquier, J. T.**, Pfahl, S., & Grams, C. M. (2019). Modulation of atmospheric river occurrence and associated precipitation extremes in the North Atlantic Region by European weather regimes. *Geophysical Research Letters*, 46, 1014–1023. <https://doi.org/10.1029/2018GL081194>

## Conferences and Meeting Presentations

**Pasquier J. T.**, Henneberger J., Wieder J., David R. O., Zieger P., Lohmann U., et al. (2022): Secondary ice production in Arctic mixed-phase clouds during the NASCENT campaign. Oral presentation, QuIESCENT workshop, Tromsø, Norway.

**Pasquier J. T.**, Wieder J., Li G., David R. O., Ramelli F., Henneberger J., et al. (2021): Arctic Mixed-Phase Clouds: 5 Days Case Study with HoloBalloon. Poster presentation, International Conference on Cloud and Precipitation (ICCP), India, Online.

**Pasquier J. T.**, Wieder J., Ramelli F., David R. O., Zieger P., and Lohmann U. (2021): Arctic Mixed-Phase Clouds: 5 Days Case Study with HoloBalloon. Oral presentation, Arctic Science Summit Week (ASSW), Portugal, Online.

**Pasquier J. T.**, Wieder J., Li G., David R. O., Ramelli F., Henneberger J., et al. (2021): Ny-Ålesund AeroSol Cloud Experiment (NASCENT). Virtual Member Meeting, Association of Polar Early Career Scientists, APECS Switzerland, Online.

**Pasquier J. T.**, Wieder J., Li G., David R. O., Carlsen T., Gierens R., and Lohmann U. (2020): Arctic Mixed-Phase Clouds: The NASCENT 5-Days Case Study with HoloBalloon. Poster presentation, AGU Fall Meeting 2020, USA, Online.

**Pasquier J. T.**, Wieder J., Henneberger J., Ebell K., Zieger P. and Lohmann U. (2019): Comparison of Microphysical Processes in Alpine and Arctic Mixed-Phase Clouds. Oral presentation, Arctic Science Summit Week (ASSW), Arkhangelsk, Russia.